Direct and inverse nonlinear Fourier transform based on the Korteweg-deVries equation (KdV-NLFT)

- A spectral analysis of nonlinear surface waves in shallow water -

Von der

Fakultät Architektur, Bauingenieurwesen und Umweltwissenschaften

der Technischen Universität Carolo-Wilhelmina

zu Braunschweig

zur Erlangung des Grades eines

Doktoringenieurs (Dr.-Ing.)

genehmigte

Dissertation

von

Markus Brühl

geboren am 7. November 1973

aus Braunschweig

Eingereicht am 15. November 2013

Disputation am 28. Februar 2014

Berichterstatter Prof. Hocine Oumeraci

Prof. Alfred R. Osborne

2014

Man kann sich die Wissenschaft
als einen runden Raum mit lauter Türen vorstellen.
Manche sind offen, manche sind geschlossen.
Und jede Zeit hat ihre eigenen Schlüssel,
um ein paar der Türen neu zu öffnen.

You can imagine science
as a round room with nothing but doors.
Some are open, some are closed.
And every time has its own keys
to newly open some of these doors.

Marie Methfessel

In this life,
there is a road that you must follow,
to the left or the right.
One is wide, but the other is hard and narrow,
take this one, and you can call it your own;
there will be so many voices trying to turn you round,
take a moment just to listen, then carry on.

Go Where Your Heart Believes,
Chris de Burgh

Acknowledgements

This thesis war performed during my employment as teaching assistant and research associate at Leichtweiß-Institute for Hydraulic Engineering and Water Resources (LWI), Dept. of Hydromechanics and Coastal Engineering, Technische Universität Braunschweig. The initial research that led to the results presented here was executed within the research project 'Time-frequency domain analysis of water waves with special respect to their non-stationary and nonlinear properties – Nonlinear Fourier transform (NLFT)' that was funded by the German Research Foundation (DFG, projects Ou 1/9-1 and Ou 1/9-2). The financial support by the DFG that made this research and, finally, this thesis possible is gratefully acknowledged.

My deep gratitude goes to Prof. Dr.-Ing. Hocine Oumeraci. His passion for hydromechanics given by his lectures made me as an undergraduate student choose coastal engineering for my major studies and special field. Furthermore, Professor Oumeraci proposed to me this fascinating and ambitious NLFT topic, which turned out to be a real challenge for many years to follow. Starting from my Diploma thesis I was able to benefit from his brilliant expertise, his extensive experience, his strive for perfection and his clear conceptions of how a research project must be structured, executed and completed. With his proven patience and endurance this thesis resulted in a very successful study.

I hold a deep gratitude, as well, for Professor Alfred R. Osborne from Torino, Italy, the leading expert in the nonlinear Fourier transform. He introduced me into the wonderful world of Jacobi theta- and Riemann Theta- functions. His publications, the compact course he gave in Braunschweig in 2011 and especially the personal discussions with him significantly improved my understanding of the nonlinear wave analysis. Without his support, the results shown here would never have been obtained. I am very grateful that he accepted the part of the second reviewer for my thesis defense.

Furthermore, I would like to thank Prof. Manfred Krafczyk and Prof. Klaus Thiele, both from TU Braunschweig, to complete the board of examiners during my disputation.

Working, teaching and researching at an institute for so many years is not possible without the support by colleagues, hiwis, students, and of course my friends. I would like to thank Mike Lieske, who was the only other 'expert' on the KdV-NLFT that I could share my works and results with, and Matthias Kudella for all the inspiring discussions on wave analysis details. Thanks also to Darshana (Dassa) Dassanayake for all the constructive discussions, often at late night hours or during the weekend. Juan Carlos Alcérreca Huerta, Andreas Burzel, Hisham El Safti, Peter Geisenhainer, Kerstin Hinze, Andreas Kortenhaus, Juan Recio and Sina Reimann also gave me an ear for my questions and problems. Rainer Kvapil solved most of my technical problems in the lab or with the equipment. From the hiwis and students I would like to thank Telse Bartens, Maiu Castelar, Anja Gossel, Anja Hoppe, Natcha Kosolkamolmas, Nora Neuert and Regina Sopper. It was always my great pleasure to work with you. Thank you for the wonderful inspiring time together.

The support of the following persons and institutions is gratefully acknowledged:

Numerical simulations within this thesis are performed with the CFD programme COBRAS-UC from the University of Cantabria, Santandér, Spain. Prof. Inigo Losada and Dr. Javier

Lara gave me a two-week introduction to that software in 2008. Thank you very much for providing the software and the support.

Prof. Norden E. Huang gave me the chance to visit his Research Center for Adaptive Data Analysis (RCADA) in Chungli, Taiwan, for ten weeks in 2011. Our discussions, some together with Chien-Chung Chang and other colleagues from the National Central University (NCU) sharpened my knowledge of the nonlinearity of waves. For the social part, Hsiao-Lan Wang's support made my stay in Taiwan an unforgettable experience and I will always be thankful for the great hospitality. Until today my memories are often in Taiwan.

In 2012 I attended a PhD course at Aalborg University, Denmark. Peter Frigard and Thomas Lykke Andersen introduced me to the analysis and generation of waves in basins and flumes. The results were so impressive that I applied one of the time series measured there in this thesis. Thank you very much for the advanced introduction to wave analysis and generation.

The German Academic Exchange Service (DAAD), the German Port Technology Association (HTG), the Braunschweigischer Hochschulbund (BHB) and the Outreach for Engineers Forum at the OMAE conference supported several participations at international conferences. These fundings were always very much appreciated.

Indeed, my research projects and finally the Phd could not have been accomplished without other most valuable people to me. Therefore, I want to thank Gabi Fournier very, very much. She is the heart and soul of the institute office, and a true friend. Gabi, thank you very much for your amicable and encouraging, as well as serious and awakening words, and especially for your consolatory words. Thank you for the indestructible faith in my thesis.

Last, but not least, my very deepest and most cordial thanks go to my family, especially my wife Danuta and my children Benjamin and Sebastian. Danuta, more than any other person, proved an incredible understanding and patience for many years. When I was busy at work and concentrated on the doctoral thesis, she and especially her parents, kept things ticking over. Thank you for all the unconditional support throughout this time. I will always love you.

When I was young, my parents imparted to me those human values that became very important during my entire education and scientific work. Until now I have benefitted from that, not only for completing my doctoral thesis but also in believing in my academic future. I thank you so very much.

Finally, I want to mention my friends who not grew tired of asking me again and again about the progress of this thesis. Thereby, I was remembered again and again that writing a doctoral thesis is not just a personal matter, but significantly affects also my whole environment, including my friends. Thank you very much for all support.

Salzgitter, November 2014 Markus Brühl

Abstract

Direct and inverse nonlinear Fourier transform based on the Korteweg-deVries equation (KdV-NLFT)

- A spectral analysis of nonlinear surface waves in shallow water -

In the conventional analysis methods such as fast Fourier (FFT), wavelet (WT) and Hilbert-Huang transform (FFT) the spectral decomposition of the original data does not consider possible effects of the relative water depth on the shape, stability or nonlinearity of the determined spectral components. In the KdV-NFLT cnoidal waves are used as basis for the spectral decomposition of the original data. This allows the consideration of the water depth as a governing parameter for the analysis and the original surface data are decomposed adaptively into those nonlinear physical oscillatory waves and solitary waves that really occur in shallow water. Furthermore, the real nonlinear wave-wave interactions between the nonlinear cnoidal waves are considered and calculated explicitly in the KdV-NLFT.

The main topics of the thesis are: (i) The numerical implementation and verification of the implemented inverse and direct scattering transform (IST and DST) of the Korteweg-deVries equation as a generalized Fourier transform (KdV-NLFT). (ii) The practical application of the implemented KdV-NLFT to selected shallow-water problems such as the reliable identification of solitons from signals measured over and behind submerged reefs (soliton fission) and the analysis of the nonlinear propagation of long-period waves in shallow water. (iii) A comparative analysis using KdV-NLFT and conventional analysis methods such as the linear fast Fourier transform (FFT) in the frequency domain and the Hilbert-Huang transform (HHT) in the time-frequency domain. (iv) Then, based on the results of these comparative analyses recommendations will be given for the practical application of the nonlinear KdV-NLFT and the conventional methods FFT and HHT for the spectral analysis of nonlinear shallow-water time and space series.

Finally, the results of the thesis clearly show that the KdV-NLFT provides a decisive insight into the underlying nonlinear processes of the analysed shallow-water wave problems that cannot be obtained by application of the conventional analysis methods.

Kurzfassung

Die direkte und inverse nichtlineare Fourier-Transformation auf Grundlage der Korteweg-deVries-Gleichung (KdV-NLFT)

- Eine Spektralanalyse nichtlinearer Wellen im Küstenbereich -

In den herkömmlichen Analysemethoden schnelle Fourier- (FFT), Wavelet- (WT) und Hilbert-Huang-Transformation (HHT) erfolgt die spektrale Zerlegung von Originalsignalen ohne eine Berücksichtigung des möglichen Einflusses der relativen Wassertiefe auf die Form, die Stabilität oder die Nichtlinearität der gewählten spektralen Komponenten. In der KdV-NLFT werden cnoidalen Wellen als Basis für die spektrale Zerlegung der gegebenen freien Wasseroberfläche verwendet. Hierdurch geht die Wassertiefe als maßgebender Parameter in die Analyse ein, wodurch die Zerlegung adaptiv in die im Küstenbereich tatsächlich auftretenden physikalischen nichtlinearen oszillierenden und solitären Flachwasserwellen erfolgt. Zusätzlich werden die zwischen den cnoidalen Wellen auftretenden nichtlinearen Wellen-Wellen-Interaktionen in der KdV-NLFT explizit berücksichtigt und berechnet.

Die Schwerpunkte der Arbeit sind: (i) Die numerische Implementierung und Verifizierung der implementierten Inversen und Direkten Streuungs-Transformation (IST und DST) für die Korteweg-deVries-Gleichung als eine generalisierte nichtlineare Fourier-Transformation (KdV-NLFT). (ii) Die beispielhafte praktische Anwendung der implementierten KdV-NLFT auf ausgewählte Problemstellungen aus dem Küsteningenieurwesen wie z.B. die zuverlässige Identifizierung von Solitonen in Signalen über und hinter getauchten Riffen (soliton fission) und die Analyse der nichtlinearen Ausbreitung langer Wellen im Flachwasser. (iii) Eine vergleichende Analyse zwischen der KdV-NLFT sowie den herkömmlichen Frequenz- und Zeit-Frequenz-Analyseverfahren FFT und HHT. (iv) Die Erarbeitung von Empfehlungen für die praktische Anwendung der KdV-NLFT sowie der herkömmlichen Verfahren FFT und HHT für die spektrale Analyse von nichtlinearen Daten im Flachwasser auf Grundlage der Ergebnisse der Vergleichsanalysen.

Die in dieser Arbeit erzielten Ergebnisse zeigen eindeutig, dass die KdV-NLFT für die untersuchten Fragestellungen weitreichende Einblicke in die zugrundeliegenden nichtlinearen Prozesse und Eigenschaften der Wellen im Flachwasser liefert, die mit den herkömmlichen Methoden nicht erzielt werden können.

Contents

List of figures

List of tables

Nomenclature

Latin capital letters

A	[m]	soliton amplitude
A_j	[m]	soliton amplitude
A_n	[m]	amplitude of added white noise in the EEMD
B	[-]	Riemann matrix element
B_{ii}	[-]	constants for the calculation of Stokes 5th order wave
B_{ii}	[-]	diagonal Riemann matrix elements
B_{ij}, B_{ji}	[-]	off-diagonal Riemann matrix elements
C	[m/s]	nonlinear wave celerity
C	[-]	coefficient
C_d	[-]	dissipation coefficient
$C_{m0,d}$	[-]	dissipation coefficient from spectral wave height H_{m0}
$C_{m0,r}$	[-]	reflection coefficient from spectral wave height H_{m0}
$C_{m0,t}$	[-]	transmission coefficient from spectral wave height H_{m0}
C_r	[-]	reflection coefficient
C_t	[-]	transmission coefficient
C_g	[m/s]	linear group celerity
E	[J/m²]	wave energy
E	[m^4]	eigenvalue
E_{2j},E_{2j+1}	[m^4]	band edges in the Floquet discriminant $\Delta(E)$
E_d	[J/m²]	dissipated wave energy
E_i	[J/m²]	wave energy of incident wave
E_{kin}	[J/m²]	kinetic wave energy
E_{max}	[m^{-2}]	maximum value of Eigenvalue vector, low pass value in DST
E_{min}	[m^{-2}]	minimum value of Eigenvalue vector, high pass value in DST
E_{pot}	[J/m²]	potential wave energy
E_r	[J/m²]	wave energy of reflected wave
E_{ref}	[m^{-2}]	reference level in DST
E_t	[J/m²]	wave energy of transmitted wave
E_{tot}	[J/m²]	total wave energy from FFT spectrum
$E_{tot,cn}$	[J/m²]	total wave energy of a cnoidal wave
$E_{tot,cn,d}$	[J/m²]	total wave dissipated wave energy from KdV-NLFT
$E_{tot,cn,i}$	[J/m²]	total wave energy of the initial cnoidal wave from KdV-NLFT
$E_{tot,cn,r}$	[J/m²]	total wave energy of the reflected cnoidal wave from KdV-NLFT
$E_{tot,cn,t}$	[J/m²]	total wave energy of the transmitted cnoidal wave from KdV-NLFT
$E_{tot,d}$	[J/m²]	total dissipated wave energy from FFT
$E_{tot,i}$	[J/m²]	total wave energy of the incident wave from FFT
$E_{tot,int}$	[J/m²]	total wave energy of the nonlinear wave-wave interactions
$E_{tot,r}$	[J/m²]	total wave energy of the reflected wave from FFT
$E_{tot,t}$	[J/m²]	total wave energy of the transmitted wave from FFT
F	[Hz]	soliton frequency
H	[m]	wave height
H_d	[m]	wave height of “dissipated” wave
H_i	[m]	wave height of incident wave
$H_{i,sol}$	[m]	wave height of incident solitary wave
H_{m0}	[m]	spectral wave height
H_{nom}	[m]	nominal wave height
H_r	[m]	wave height of reflected wave

H_t	[m]	wave height of transmitted wave
I	[-]	soliton index, also denoted as modulus m
J	[-]	number of nonlinear partial interaction terms
K	[m^{-1}]	soliton wave number
$K(m)$	[-]	complete elliptical integral of the first kind as function of modulus m
$K'(m)$	[-]	function of $K(m)$, $K'(m)=K(1-m)$
$K(q)$	[-]	complete elliptical integral of the first kind as function of nome q
L	[m]	wave length
L_0	[m]	wave length in shallow water
$L_{(h)m}$	[m]	wave length in the specified water depth h, e.g. L_{20m}
L_i	[m]	wave length of incident (solitary) wave
L_{sp}	[m]	spatial period
L_{sp}	[m]	width of the analysis window
L_w	[m]	width of the analysis window
M	[-]	integer
M	[-]	number of expected solitons from formulae by Germain (1984) and Kabbaj (1985)
N	[-]	integer
N	[-]	number of wave components that are superposed in cnoidal wave Generation
N_{sol}	[-]	number of transmitted solitons
N_{wn}	[-]	number of cycles of white noise addition in the EEMD
P		Polynomial in the DST, $P_n(\lambda_e)$
P		Cauchy principal value in the Hilbert transform
R		function in the hyperelliptic function representation of KdV-NLFT
S		element in the monodromy matrix **S** in the DST
$S(f)$	[m^2]	spectral energy density in FFT power spectrum
T	[s]	wave period
T_{nom}	[s]	nominal wave period
U_g	[-]	generalized Ursell number
Ur	[-]	Ursell number
$W(c,s)$		Wronskian with basis set (c,s)
X_i	[-]	phase argument, $X_i(x,t)=k_ix-\omega_it+\varphi_i$
X	[-]	dimensionless ordinate in the DS equation
Y	[-]	dimensionless ordinate in the DS equation
Z		analytical signal in the Hilbert transform, $Z(t)$

Latin small letters

a	[m]	wave amplitude of oscillatory waves, radiation amplitude
a		element in the quadratic matrix **A** in the DST
a		element in the monodromy matrix **S** in the DST
a_i	[m]	incident wave amplitude
a_j	[m]	oscillatory wave amplitude
a, a_{HT}	[m]	instantaneous, time-dependent amplitude in HT, $a(t)$ or $a(x)$
a_t	[m]	transmitted wave amplitude
a_z	[m]	zero-crossing amplitude of a local whole wave in HHT
$\overline{a_z}$	[m]	mean zero-crossing amplitude of a local whole wave in HHT
b	[-]	hyperbolic term in Stokes 5th order wave generation, $b = \cosh(kh)$
b		element in the monodromy matrix **S** in the DST
b_r	[m]	reef width

c	[m/s]	linear wave celerity
c	[-]	hyperbolic term in Stokes 5th order wave calculation, c = cosh(kh)
c		basis of the solution to the Schroedinger eigenvalue problem
c_0	[m/s]	wave celerity in shallow water , $c_0 = \sqrt{gh}$
c_i		cnoidal wave component within a transient wave
c_{ij}		cnoidal wave component within a transient wave c_i
c'_0	[m/s]	modified wave celerity for the tKdV equation
cn_i		*i-th* cnoidal wave in the KdV-NLFT spectrum
d	[m]	water depth, preferably denoted as h
d_r	[m]	submergence depth, water depth over the reef
e	[-]	Euler's number
f	[Hz]	frequency of oscillatory waves, radiation frequency
f_{const}	[Hz]	constant frequency of a linear Airy wave
$f_{cos,i}$	[Hz]	frequency of a cosine wave
f_{inst}	[Hz]	instantaneous, time-dependent frequency in HT, $f_{inst}(t)$
g	[m/s²]	acceleration due to gravity
h	[m]	water depth
h_r	[m]	reef height
h_{ref}	[m]	reference level water depth for soliton propagation
i	[-]	imaginary number, $i = \sqrt{-1}$
i	[-]	integer
j	[-]	integer
k	[m^{-1}]	wave number
k_0	[m^{-1}]	deep water wave number
k_{inst}	[Hz]	instantaneous, time-dependent wave number in HT, $k_{inst}(x)$
l	[-]	integer
m	[-]	integer
m	[-]	modulus, also denoted as soliton index I
m	[-]	bottom slope $1{:}m$
m_0	[-]	spectral moment of order Zero
m_j	[-]	modulus, also denoted as soliton index I
$m(q)$	[-]	modulus m as function of nome q
n	[-]	integer
n	[-]	order of the basic wave component in cnoidal wave calculation
n	[m]	white noise in the EEMD, $n(x,t)$
q	[-]	nome, used for cnoidal wave calculation
s	[-]	hyperbolic term in Stokes 5th order wave calculation, s = sinh(kh)
s		basis of the solution to the Schroedinger eigenvalue problem
s		eigenfunctions in the DST, $s(x)$
t	[s]	time
t'	[s]	time after wave evolution, $t'=t+\Delta t$
u	[m^4]	variable used in the KdV-NLFT, $u(x,t)=\lambda\eta(x,t)$
$u(x)$	[m]	current wave form (= the free surface within one wave period)
v_s	[kn]	ship speed
y	[m]	ordinate/position transverse to wave propagation
y		function
x	[m]	ordinate/position in direction of wave propagation
x'	[s]	position after wave evolution, $x'=x+\Delta x$
x_o	[m]	arbitrary base point in the periodic interval $0 \le x_o \le L_w$
z	[m]	ordinate/position in vertical direction

Greek capital letters

$\Delta(E)$		*Delta*, Floquet discriminant in DST
Δf	[Hz]	*Delta*, frequency resolution in FFT
Δt	[s]	*Delta*, time increment
Δx	[m]	*Delta*, space increment
Θ	[-]	*Theta*, denotes the Riemann Θ-function
Φ	[rad]	*Phi*, soliton phase
Φ	[rad]	*Phi*, normalized slowly varying part of the velocity potential in the Davey-Stewartson equation, $\Phi(x,y,t)$
Ψ	[m]	*Psi*, normalized complex envelope function in the Davey-Stewartson equation, $\Psi(x,y,t)$

Greek small letters

α	[s^{-1}]	*alpha*, nonlinearity parameter
α		*alpha*, element in the monodromy matrix $\boldsymbol{\alpha}$
α'	[s^{-1}]	*alpha*, modified nonlinearity parameter for the tKdV equation
β	[m^3/s]	*beta*, dispersion parameter
β'	[m^3/s]	*beta*, modified dispersion parameter for the tKdV equation
η	[m]	*eta*, water surface elevation
η'	[m]	*eta*, water surface elevation after wave evolution, $\eta'(x',t')$
η^*	[m]	*eta*, modified data in the EEMD
$\overline{\eta}$	[m]	*eta*, mean surface elevation, $\overline{\eta}(x,t)$
$\eta_{cos,i}$	[m]	cosine wave
η_i	[m]	*i*-th [m] component in superposition of water surface elevations
η_{ref}	[m]	*eta*, water surface at reference level
θ	[-]	*theta*, denotes the Jacobi θ-function
λ	[m^3]	*lambda*, relation between nonlinearity α and dispersion β, $\lambda = \alpha/\beta$
λ'	[m^3]	*lambda*, modified relation λ for the tKdV equation, $\lambda' = \alpha'/\beta'$
λ_e	[m^3]	*lambda*, eigenvalue in the DST
μ	[-]	*mu*, coefficient in the DS equation
μ	[-]	*mu*, coefficient in the NLS equation
μ, μ_j	[m^4]	*mu*, hyperelliptic function, μ-function
υ	[-]	*nu*, coefficient in the NLS equation
π	[-]	*pi*, circular constant, $\pi = 3.1415\ldots$
ρ	[kg/m^3]	*rho*, density
σ	[-]	*sigma*, Riemann sheet index
τ	[-]	*tau*, dimensionless time in the DS equation
φ	[rad]	*phi*, wave phase
$\varphi_{cos,i}$	[rad]	*phi*, wave phase of a cosine wave
ϕ	[m^2/s]	*phi*, velocity potential
ϕ	[-]	*phi*, eigenfunction, $\phi(x;x_o,k)$
ϕ, ϕ_{HT}	[-]	instantaneous, time-dependent phase in HT, $\phi(t)$
ϕ_x	[-]	*phi*, partial derivative of eigenfunction, $\phi_x(x_o;x_o,k)=ik$
ϕ^*	[-]	*phi*, complex conjugate eigenfunction, $\phi^*(x_o;x_o,k)=1$
ϕ^*_x	[-]	*phi*, partial derivative of eigenfunction, $\phi^*_x(x_0;x_0,k)=-ik$
χ	[-]	*chi*, arbitrary function
χ , χ_0	[-]	*chi*, coefficient in the DS equation

ψ	[m]	*psi*, complex envelope function in the nonlinear Schroedinger equation, $\psi(x,t)$ or $\psi(x,y,t)$
ψ	[m²/s]	*psi*, stream function in the stream function theory, $\psi(x,z,t)$
ω	[s^{-1}]	*omega*, angular frequency
ω_0	[s^{-1}]	*omega*, angular deep water frequency

Symbols

∂	partial derivative
∞	infinity

Mathematical functions

arctan	[-]	inverse tangent, arctangent
cn	[-]	cnoidal function, one of the Jacobian elliptic functions
cos	[-]	cosine function
cosh	[-]	hyperbolic cosine function
ln	[-]	natural logarithm
sech	[-]	hyperbolic secant
sin	[-]	sine function
sinh	[-]	hyperbolic sine function
sgn	[-]	signature, sign of a variable, $\mathrm{sgn}(\chi)=\chi/\lvert\chi\rvert$
tan	[-]	tangent function
tanh	[-]	hyperbolic tangent function

Matrices and vectors

$\mathbf{A}$	soliton amplitude vector
$\mathbf{A}$	quadratic matrix of type (n,n) in the DST
$\mathbf{A}$	*alpha*, monodromy matrix
$\mathbf{B}$	Riemann matrix
$\mathbf{B}$	quadratic matrix of type (n,n) in the DST
$\mathbf{E}$	n-column unit matrix
$\mathbf{F}$	soliton frequency vector
$\mathbf{K}$	soliton wave number vector
$\mathbf{Q}$	matrix in the similarity transformation in the DST
$\mathbf{S}$	monodromy matrix, $\mathbf{S}(x_o,k)$
$\mathbf{f}$	oscillatory wave frequency vector
$\mathbf{k}$	oscillatory wave number vector
$\mathbf{m}$	modulus vector
$\mathbf{n}$	integer vector
$\bar{\mathbf{x}}$	eigenvector in the DST
$\mathbf{\Phi}$	*Phi*, soliton phase vector
$\mathbf{\Phi}$	*Phi*, eigenfunctions matrix in the DST, $\mathbf{\Phi}(x;x_o,k)$
$\boldsymbol{\varphi}$	*phi*, oscillatory wave phase vector
$\boldsymbol{\omega}$	*omega*, oscillatory wave angular frequency vector

Superscripts

T	transposed matrix
*	complex conjugate

Subscripts

I	'the imaginary part of'
N	integer, number of spectral basic components
R	'the real part of'
cn	cnoidal wave
const	constant
cos	cosine wave
i	integer
i	integer for oscillatory waves
inst	instantaneous
int	nonlinear interactions
j	integer
j	integer for solitons
kin	kinetic
n	integer
norm	normalized
pot	potential
t	partial derivative with respect to time *t*
tot	total
x	partial derivative with respect to position *x*
y	partial derivative with respect to position *y*

Abbreviations

1+1	propagation of the wave in the *x-z* plane $\eta(x,t)$, also denoted as 2D wave propagation
2+1	propagation of the wave in the *x-y-z* space $\eta(x,y,t)$, also denoted as 3D wave propagation
2D	propagation of the wave in the *x-z* plane $\eta(x,t)$, also denoted as wave motion in *1+1* dimensions
3D	propagation of the wave in the *x-y-z* space $\eta(x,y,t)$, also denoted as wave motion in *2+1* dimensions
BAW	Bundesanstalt für Wasserbau, Dienststelle Hamburg
BHB	Braunschweigischer Hochschulbund
CH	Camassa-Holm equation
COBRAS	CFD software, Cornell breaking waves and structures
COBRAS-UC	CFD software, modification of COBRAS at the University of Cantabria, Santandér, Spain
DAAD	German Academic Exchange Service
DFG	German Research Foundation
dKdV-NLFT	direct KdV-NLFT
DN	degree of nonlinearity in the HHT
DS	Davey-Stewartson equations
DS-NLFT	nonlinear Fourier transform, based on the DS equation

DST	direct scattering transform
EEMD	ensemble empirical mode decomposition
EMD	empirical mode decomposition
FFT	fast Fourier transform
FT	Fourier transform
HHT	Hilbert-Huang transform
HT	Hilbert transform
HTG	German Port Technology Association
iKdV-NLFT	inverse KdV-NLFT
IMF	intrinsic mode function
IST	inverse scattering transform
KdV	Korteweg-deVries
KdV-NLFT	nonlinear Fourier transform, based on the KdV equation
KP	Kadomtsev-Petviashvili equation
KPII	KP equation without influence of surface tension
KP-NLFT	nonlinear Fourier transform, based on the KP equation
LWI	Leichtweiß-Institute for Hydraulic Engineering and Water Resources
mKdV	modified KdV equation
NLFT	nonlinear Fourier transform
NLS	nonlinear Schroedinger equation
NLS-NLFT	nonlinear Fourier transform, based on the NLS equation
ODE	ordinary differential equation
OMAE	Offshore Mechanics and Arctic Engineering
PDE	partial differential equation
PDST	periodic direct scattering transform
PIST	periodic inverse scattering transform
RANS	Reynolds-averaged Navier-Stokes equations for fluid flow
RCADA	Research Center for Adaptive Data Analysis
sKdV	space-like Korteweg-deVries equation
STFT	short-time Fourier transform
Stokes2	Stokes 2nd order wave theory
Stokes5	Stokes 5th order wave theory
SWL	still water level
tKdV	time-like Korteweg-deVries equation
TU	Technische Universität
VOF	volume-of-fluid method for free-surface modelling
W2	second Whitham equation
WG	wave gauge
WT	wavelet transform

1 Introduction

In the following sections the motivation, the objectives and the methodology of this thesis are presented.

1.1 Motivation

The primary objective of wave research in coastal engineering is to analyse and to better understand the underlying physical processes as the waves interact with the sea bed, sea bed forms as well as with natural and man-made barriers. Based on this improved understanding, description and prediction models for these processes are developed. Unfortunately, most properties of real sea state and the connected hydraulic processes, e.g. around a submerged structure, cannot be detected by visual observation. To overcome these restrictions, the application of data analysis techniques is required which provide information on the time, frequency or joint time-frequency properties of the measured time or space series. Depending on the selected analysis methods, the analysis algorithms, the determined parameters as well as the spectral representations vary (s. Fig. 1.1).

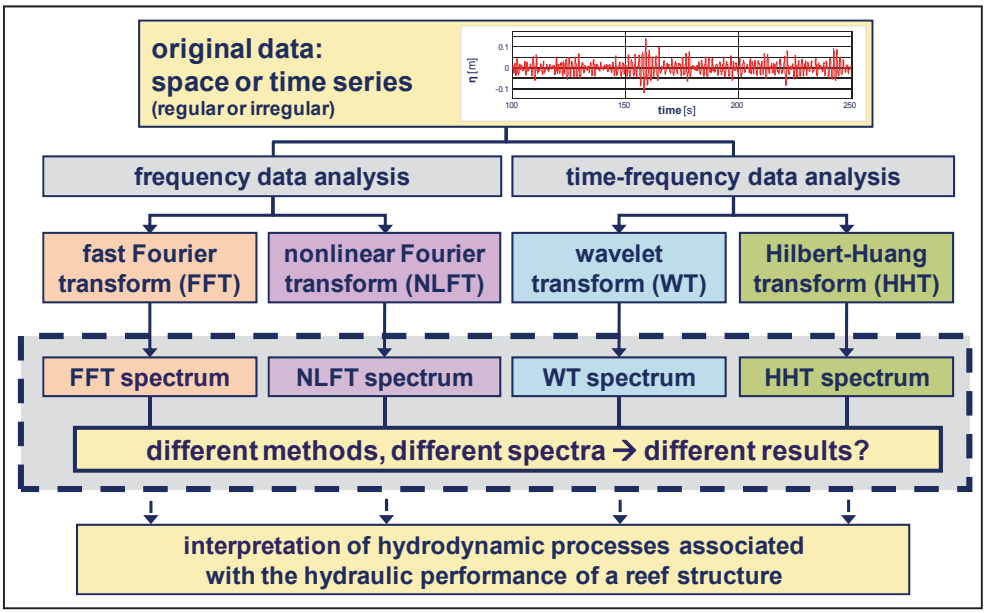

Fig. 1.1: Motivation for the implementation of the nonlinear Fourier transform and the comparative analysis using different data analysis methods in time and time-frequency domain.

Since these analysis results are used for the identification of the hydrodynamic processes that are associated with the hydraulic performance of a reef structure, the following questions arise:

(i) If different analysis methods provide different spectral representations, do these representations provide different results?

(ii) And if the analysis results differ, how does that affect our understanding and interpretation of the physical processes?

(iii) What are the qualitative and quantitative effects of different analysis method on the design formulae that are determined based on those analysis results, e.g. what is the difference between empirical factors determined with different methods from the same data sets?

When Jean Baptiste Fourier published his pioneering book *Théorie analytique de la chaleur* (Fourier, 1822) he opened a completely new view on the hidden spectral properties of experimental data. With the *fast Fourier transform (FFT*) any arbitrary data can be regarded as a linear superposition of sine and cosine waves with different amplitudes, frequencies or wave numbers and phases. This innovative approach of understanding waves led the way from time domain towards frequency domain analysis, and later by application of windowing methods such as the short-time Fourier transform (STFT) also towards time-frequency domain analysis of time and space series. From today's perspective, this idea seems relatively simple, the theoretical background can easily be understood and the numerical calculation can be performed very fast. However, due to the limited water depth near-shore waves differ from a sinusoidal shape and rather follow either the nonlinear Stokes (Stokes, 1847), cnoidal (Korteweg & deVries, 1895) or solitary wave theory (Boussinesq, 1871). Therefore, in the algorithm of the FFT additional higher harmonic components are required to reconstruct the measured time series. When applying the FFT, we always have to keep in mind that initially this method was developed for periodic, linear and stationary signals and that it has some serious drawbacks if applied to nonlinear and/or non-stationary shallow-water wave data. Strictly speaking, the FFT is not valid for nonlinear and non-stationary signal analysis. However, in daily practice the FFT is the standard analysis method even for these kinds of shallow-water wave data. Depending on the special application and the nonlinear and non-stationary character of the analysed waves, the effects of these drawbacks are either be neglected or considered to a certain extent in the application of the FFT and in the interpretation of the Fourier spectrum. Examples for this are

(i) the definition of suitable time windows for the analysis of non-stationary data, and

(ii) the definition and identification of bound and free harmonics in the linear FFT spectrum.

These are the reasons why nearly 200 years after its development the FFT still remains the standard analysis method for wave data in ocean and coastal engineering (Goda, 2000; 2002).

In the last decades, the *wavelet transform (WT)* (Daubechies, 1992) represents the most widely used joint time-frequency analysis method. More recently, based on the *empirical mode decomposition* (EMD) introduced by Huang et al. (1998), the *Hilbert-Huang transform (HHT)* became increasingly popular for the analysis of oceanic and coastal data in the time-frequency domain. The localised basic components in WT, the wavelets, have to be defined a priori (before the analysis) and it is known that the selected type of wavelet strongly influences the analysis results. Therefore some experience in data analysis is required to choose the adequate wavelet for the given type of data. HHT is the most adaptive method as it uses the so-called *intrinsic mode functions (IMF)* as basic components. The latter, which do not necessarily represent physical wave forms, are not defined a priori but are adaptively derived directly from the original data by a sifting process called EMD or the more advanced *ensemble empirical mode decomposition (EEMD)* (Wu & Huang, 2004).

The most serious drawback of the conventional analysis methods FFT, WT and HHT is that none of these approaches explicitly considers the effects of the relative water depth on the shape, stability or nonlinearity of the basic wave components. Therefore, the decomposition of the original data into pre-defined wave types or adaptive modes within these conventional approaches cannot consider the real nonlinear wave shapes in the limited water depths near shore. A very good example for the problem of how to interpret the results of the conventional analysis methods when applied to shallow-water problems is the harmonic generation during the evolution of periodic waves over a constant depth (Mei et al., 2005). Osborne (2010) shows that this harmonic generation only exists in the sinusoidal wave basis of the decomposition in FFT. If the signal is decomposed into the higher-order cnoidal basic components no energy shift from one frequency component to higher-order components in the FFT spectrum (which is denoted as *resonance*) occurs and no harmonic generation is observed.

These examples clearly show that as a matter of fact different analysis methods provide different spectra with different spectral properties in time or time-frequency domain as assumed in Fig. 1.1. Therefore, based on the available literature on different analysis methods the question in the figure has to be answered this way: Yes, the application of different methods on the same data and the interpretation of different spectral representations provide significantly different analysis results. Moreover, especially for the consideration and identification of nonlinear waves and their nonlinear wave-wave interactions in shallow water, the available and well-established conventional analysis methods are not sufficient. Therefore, additional mathematical approaches have been developed in the past to explicitly calculate the interactions between a few numbers of nonlinear waves. For sea state calculations numerical models are used that usually start with linear boundary conditions and then automatically allow the generation of nonlinear wave-wave interactions after the waves have propagated a few periods or wave lengths.

The human brain is trained to interpret data in the time domain and, therefore, is not able to extract the spectral properties of the original data. Consequently, the analyses of data in frequency and time-frequency domain are assumed to be reliable even if the results might be strongly influenced by the selected analysis method and its underlying assumptions. Furthermore, most of the wave-wave and wave-structure interactions in shallow-water and the coastal areas are affected or even governed by nonlinear processes which are not *explicitly* considered in the conventional analysis methods. This latter problem is often neglected when the results of these linear analysis methods are used for the determination of prediction formulae for diverse processes and the design of coastal structures. Therefore, in this thesis, the *KdV-based nonlinear Fourier transform (KdV-NLFT)* is applied as an alternative analysis method for the spectral decomposition of shallow-water wave data. The KdV-NLFT is an application of the periodic inverse scattering transform (PIST) for the solution of the Korteweg-deVries (KdV) equation that follows the basic idea that the original free surface data can be decomposed into real existing physical nonlinear cnoidal shallow-water waves and their mutual nonlinear wave-wave interactions (Osborne, 1991a; Osborne, 1991b; Osborne, 2010; Provenzale & Osborne, 1991).

In the KdV-NLFT only cnoidal waves are used as nonlinear basis for the decomposition of the shallow-water wave data. In contrast, in coastal engineering a system of mainly four dif-

ferent conventional wave theories has been established to generate all types of waves in the coastal region: Airy, Stokes, cnoidal and solitary wave theories (for details see sections 2.3 and 2.4.1). By means of diagrams (such as in Fig. 2.3) and wave input parameters (wave height, period or length and water depth) the best-fit theory for the given boundary conditions can be determined. Within this classification the cnoidal wave theory is applied only in a small application area for the calculation of strongly nonlinear waves that are beyond the limits of Stokes waves but not solitary waves yet. But in the mathematical and physical sense the cnoidal wave equation is not restricted to these narrow limitations that arise from practical advisement. By applying the cnoidal wave equation and variation of the modulus *m* all wave shapes of the conventional wave theories can be generated. Nevertheless, for practical purposes the Airy, Stokes and solitary wave theories are much easier to understand and apply.

Cnoidal waves in the general mathematical and physical sense span the range from linear Airy-shaped waves over weakly nonlinear Stokes-shaped waves up to highly nonlinear solitons. So the spectral cnoidal components of the NLFT represent the *real* physical shallow-water wave types, and one of the most important limitations of the conventional analysis methods can be overcome: nonlinear waves - even solitary waves - can be considered explicitly as basic components in the analysis and be represented in the nonlinear spectrum. Finally, the influence of these nonlinearities can be included in the interpretation of the analysed processes and in the development of prediction formulae for coastal processes which are needed for the design of coastal structures. Consequently, the KdV-NLFT will be implemented and applied within this thesis to analyse and understand even highly nonlinear processes such as the decomposition of an initial long cosine wave in very shallow-water (see Fig. 1.2a) into a periodic train of solitons (see Fig. 1.2b) that cannot be explained by the conventional approaches. Up to date, this new KdV-NLFT approach is only used in physical oceanography for the analysis of ocean wave data (Osborne, 2010) and internal solitons in the ocean (Christov, 2009). Software for the application of the KdV-NLFT is not yet available, neither as commercial software nor as published rudimentary research codes. Therefore, the numerical implementation of the method has to be performed as an integral part of this thesis before any practical application can be executed.

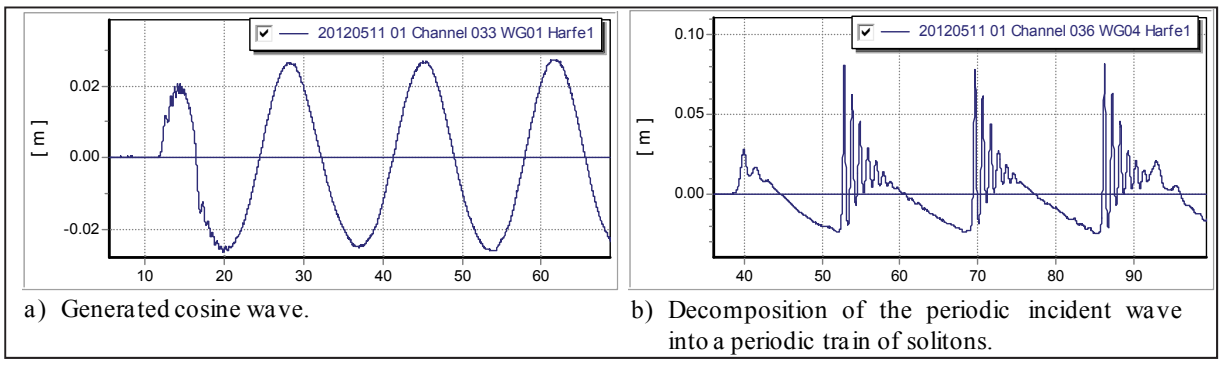

a) Generated cosine wave.

b) Decomposition of the periodic incident wave into a periodic train of solitons.

Fig. 1.2: Measurements of long cosine waves generated in the wave flume at LWI with *h=0.21m*, *H=0.05m* and *T=16.67s*. a) Generated periodic cosine-shaped wave profile measured at *x=1.05m*. b) Measured data at *x=41.26m*: The incident periodic sinusoidal wave is decomposed into periodic trains of solitons.

The application of the KdV-NLFT for the spectral decomposition of wave trains into real nonlinear shallow-water waves and their nonlinear interactions will lead to a completely new

insight for the interpretation of diverse nonlinear processes associated with wave propagation in the coastal zone as well as with wave-wave and wave-structure interactions. With the KdV-NLFT solitons can reliably be identified from measured time or space series, thus allowing one to better indentify and physically interpret the governing coastal processes as well as to explicitly consider the nonlinear nature of shallow-water waves in the prediction formulae which are generally needed for the design of coastal structures.

1.2 Objectives

The main objectives of the thesis are (see Fig. 1.3):

(i) the numerical implementation and validation of the KdV-based nonlinear Fourier transform (KdV-NLFT) as a non-conventional nonlinear analysis method for coastal engineering problems which uses nonlinear shallow-water waves as spectral basic components and explicitly considers their nonlinear wave-wave interactions in the analysis algorithm,

(ii) the practical application of the nonlinear Fourier transform exemplarily to selected shallow-water wave problems such as the identification of solitons from time and space series and the analysis of the underlying nonlinear wave-wave interactions and the propagation of relatively long waves in shallow water,

(iii) a comparative analysis using KdV-NLFT and the conventional frequency and time-frequency analysis methods fast Fourier (FFT) and Hilbert-Huang transform (HHT) and,

(iv) based on the results of these comparative analyses, recommendations will be given for the practical application of the nonlinear KdV-NLFT and the conventional methods FFT and HHT for the spectral analysis of nonlinear shallow-water time and space series.

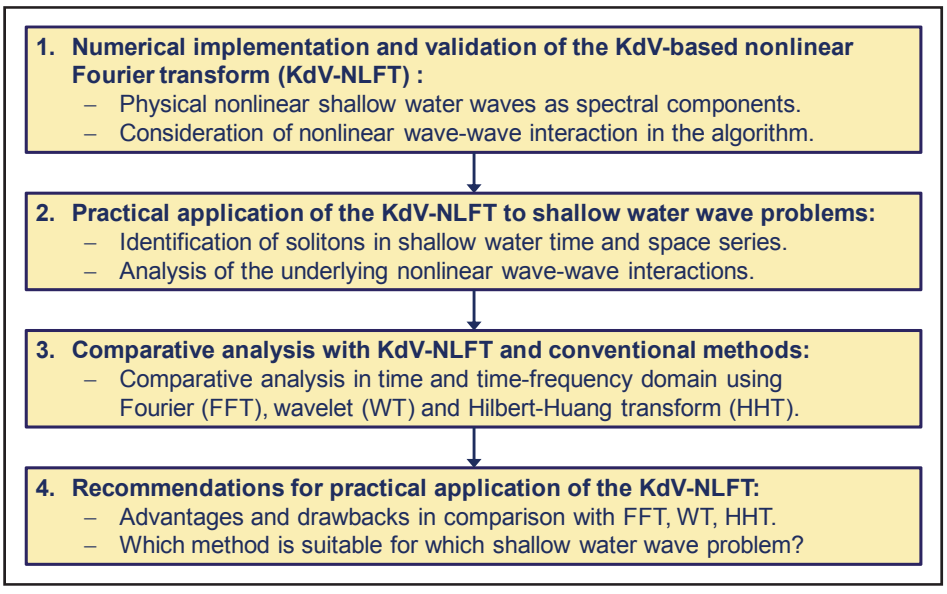

Fig. 1.3: Overview on the objectives of this thesis.

1.3 Methodology

The methodology adopted in this research includes the following six steps:

First, the theoretical background related to nonlinear water wave equations, linear and nonlinear wave theories, the periodic direct inverse scattering transform (PIST) of the Korteweg-deVries (KdV) equation and conventional wave analysis methods is briefly described (chapter 2).

Second, the numerical implementation of the two parts of the nonlinear KdV-based Fourier transform (KdV-NLFT) is described: (i) the inverse scattering transform (IST) and (ii) the direct scattering transform (DST), followed by examples from the verification of the implemented code by analysis of generated data using hydraulic model testing and numerical simulations (chapter 2).

Third, data from hydraulic model tests and numerical simulations on soliton fission over and behind submerged reefs with different widths are analysed comparatively using the implemented KdV-NLFT and the conventional analysis methods FFT and HHT (chapter 4).

Forth, data from hydraulic model tests and numerical simulations on the propagation and transmission of waves in flumes and over submerged reefs are analysed comparatively using the implemented KdV-NLFT and the conventional FFT in order to analyse the effects of harmonic generation (chapter 5).

Fifth, the new implemented KdV-NLFT code is applied to a set of different coastal and shallow-water wave problems such as long waves in shallow-water and ship wave analysis (chapter 5).

Finally, the results of the implementation, verification and application of the new KdV-NLFT code as well as those of the comparative analyses with FFT and HHT are summarised and conclusions are drawn. Furthermore, recommendations are given for the application of the KdV-NLFT and the conventional methods FFT and HHT, including the outline of possible future research topics (chapter 7).

2 Theoretical background

In the following section a general overview on the procedure of the KdV-NLFT is given, followed by a brief description of the theoretical background related to nonlinear water wave equations, linear and nonlinear wave theories, the periodic direct inverse scattering transform (PIST) of the Korteweg-deVries (KdV) equation and conventional wave analysis methods.

2.1 Procedure of the KdV-NLFT

The KdV-NLFT is the solution of *the partial differential Korteweg-deVries (KdV) equation* (Korteweg & deVries, 1895) by application of a mathematical procedure called *inverse scattering transform (IST)* (Zabusky & Kruskal, 1965). For periodic travelling-wave boundary conditions the KdV equation is solved by so-called *cnoidal waves* (Korteweg & deVries, 1895) that are physical representations of nonlinear shallow-water waves. Therefore, cnoidal waves provide a perfect basis for the spectral decomposition of coastal wave data. In engineering terminology the IST of the KdV equation might be considered as an extension or - even better - as a substitute of the conventional linear Fourier transform (FT) by a generalized nonlinear Fourier transform (NLFT) for shallow-water waves. Since the KdV-NLFT is based on the KdV equation, it is valid for relative values $kh<1.36$ ($h/L<0.22$). These values describe the range of validity of the KdV equation (Osborne, 2010). The non-conventional KdV-based nonlinear Fourier transform (KdV-NLFT) uses the real existing nonlinear cnoidal shallow-water waves for the nonlinear decomposition. For larger relative water depths with $kh\geq1.36$ the solution of the nonlinear Schroedinger equation (NLS equation) by the IST (NLS-NLFT) has to be applied which is not discussed in this study (for more details see Osborne (2010)).

The most important and fascinating feature of the KdV-NLFT approach is its ability to decompose given measured or simulated shallow-water surface wave data $\eta(x,t)$ *explicitly* into N constitutive nonlinear cnoidal waves components $\eta_{cn,i}(x,t)$ *and* the sum of their nonlinear wave-wave interactions $\eta_{int,j}(x,t)$ (Osborne, 1995b):

$$\eta(x,t)=\sum_i \eta_{cn,i}(x,t)+\sum_j \eta_{int,j}(x,t)\,. \tag{2.1}$$

The procedure of the inverse and direct KdV-NLFT is summarised in Fig. 2.1. The details on the theoretical background and the equations used in the figure are discussed in sections 2.2 to 2.5.

The procedure of the KdV-NFLT can be categorized as follows:

(1) The KdV equation governs the propagation of waves in shallow-water with $kh<1.36$. Each spectral basic component of the KdV-NLFT has to be solution of the KdV equation (section 2.2.1).

(2) Cnoidal waves $\eta_{cn}(x,t)$ are solutions of the KdV equation for periodic travelling-wave boundary conditions (Korteweg & deVries, 1895) and can therefore be used as nonlinear spectral basic components (sections 2.3.2 and 2.4).

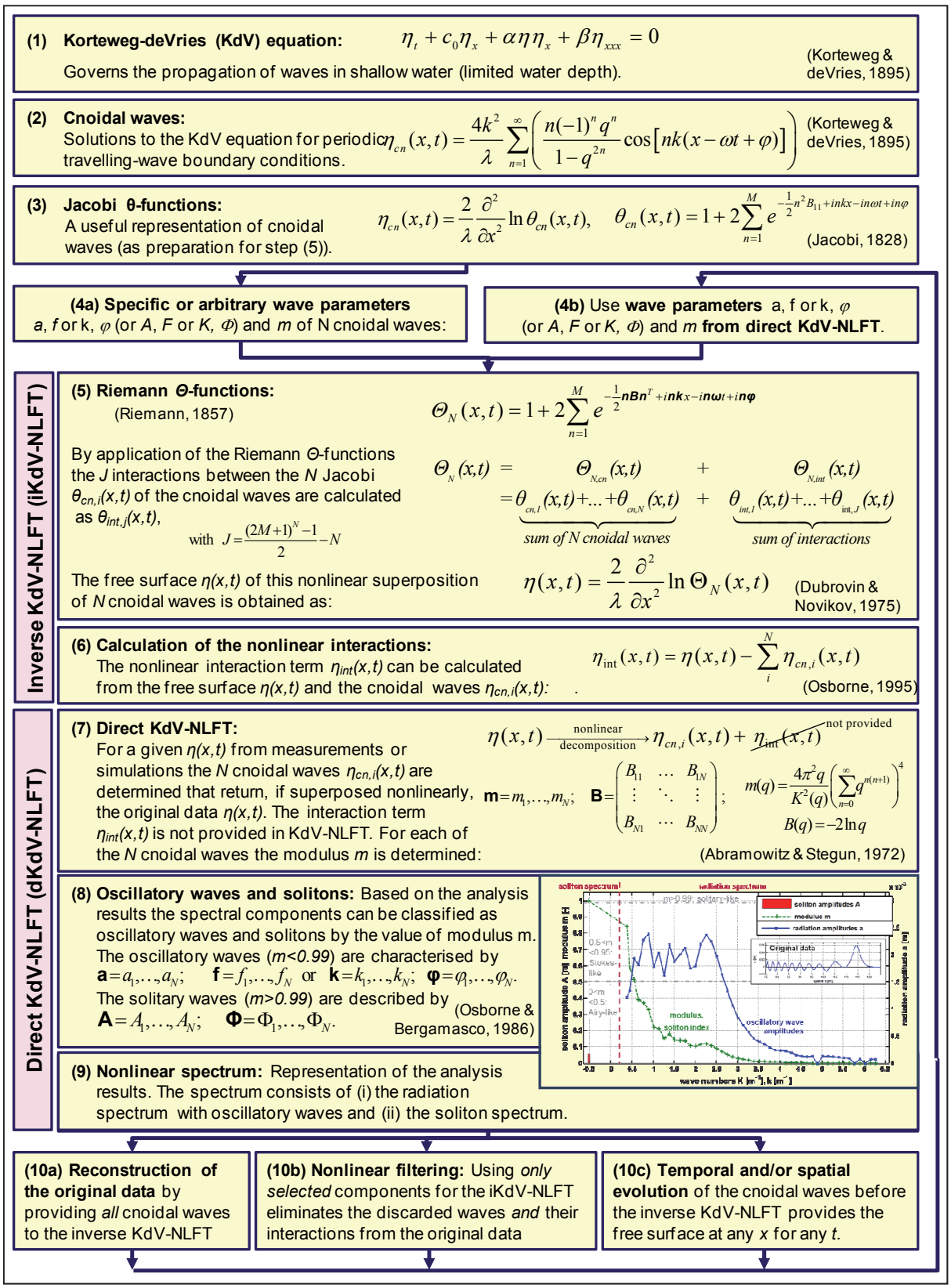

Fig. 2.1: Overview on the procedures of the direct and inverse KdV-NLFT.

(3) Jacobi θ-functions $\theta_{cn}(x,t)$ (Jacobi, 1828) are useful representations of cnoidal waves for the KdV-NLFT (as preparation for step (5)). The cnoidal wave is obtained by the second partial derivation of $\ln\theta_{cn}(x,t)$ and subsequent scaling by $2/\lambda$ (section 2.4.2).

(4a) For the nonlinear superposition of N cnoidal waves $\eta_{cn,i}(x,t)$ in the inverse KdV-NLFT the parameters amplitude a, frequency f or wave number k, modulus m and phase φ of each of these waves have to be defined. These values can be specific (with respect of the purpose of the superposition) or arbitrary values.

(4b) For the reconstruction of a given original signal in the inverse KdV-NLFT the values a, f or k, φ (or A, F or K, Φ for solitons) and m are obtained from the direct KdV-NLFT (see steps (10a) to (10c)).

(5) If N nonlinear cnoidal waves are superposed (with $N>1$), then mutual nonlinear wave-wave interactions between each of these N components occur and $[(2M+1)^N-1]/2-N$ interaction terms have to be added in the nonlinear superposition. If these N cnoidal waves are written in terms of Jacobi θ-functions, then the application of Riemann Θ-functions (Riemann, 1857) directly provides the superposition of these $\theta_{cn,i}$ and automatically calculates their mutual wave-wave interactions $\theta_{int,j}$. The result of this nonlinear superposition is the free surface $\eta(x,t)$ (section 2.4.4). This procedure of linear superposition of Jacobi θ-functions (which are representations of cnoidal waves) and their mutual nonlinear wave-wave-interactions for the calculation of the free surface is denoted as the inverse KdV-NLFT (iKdV-NLFT) (section 2.5.1).

(6) From the free nonlinear surface $\eta(x,t)$ and the N cnoidal waves $\eta_{cn,i}(x,t)$ which have been superposed nonlinearly to obtain $\eta(x,t)$ the nonlinear interaction term $\eta_{int}(x,t)$ can be calculated. It is, however, not possible (for $N>2$) to determine the mutual interactions between two or more specified waves separately (section 2.4.4).

Steps (5) and (6) can be applied for specific or arbitrary cnoidal waves (step (4a)). In order to reproduce a given original free surface in shallow-water (e.g. from measurements or simulations) first, the direct KdV-NLFT has to be applied in order to identify the underlying cnoidal waves, the interaction term, and the correct wave parameters so that the waves, if superposed nonlinearly in the inverse KdV-NLFT, return the original data (see step (4b)).

(7) In the direct KdV-NLFT (dKdV-NLFT, or direct scattering transform (DST)) a given signal $\eta(x,t)$ is decomposed into a set of N cnoidal waves $\eta_{cn,i}(x,t)$ such that the nonlinear superposition of these cnoidal waves in the iKdV-NLFT returns the original data (section 2.5.2). The interaction term $\eta_{int}(x,t)$ is not provided by the dKdV-NLFT, but can be determined by subsequent application of the iKdV-NLFT (see step (10a)). For each of the N cnoidal waves the modulus m is calculated. For application in the iKdV-NLFT the modulus has to be converted into the value B_{ii} (section 2.4.3).

(8) Based on the individual modulus m each of the cnoidal waves can be classified as oscillatory waves with the values a, f or k, φ and m, or solitons with A, F or K, Φ and m.

(9) The nonlinear spectrum presents the cnoidal wave parameters determined by the dKdV-NLFT in a representation that is very close to the well-known conventional FFT spectrum. The nonlinear spectrum consists of the radiation spectrum (right part of the spectrum in step (9) in Fig. 2.1) with the oscillatory waves and the soliton spectrum (left part of the spectrum in Fig. 2.1) (section 2.5.2).

(10a) For the reconstruction of the original data $\eta(x,t)$ all basic components from the dKdV-NLFT have to be provided to the iKdV-NLFT.

(10b) If selected wave components or specific frequency/wave number ranges are removed from the nonlinear spectrum, then these components *and* their nonlinear wave-wave interactions are removed from the original data in the iKdV-NLFT. This process is called *nonlinear filtering* (section 2.5.1).

(10c) Before the application of the iKdV-NLFT the cnoidal waves $\eta_{cn,i}(x,t)$ can be evolved in time $t'=t+\Delta t$ and/or space $x'=x+\Delta x$. The subsequent application of the iKdV-NLFT to these evolved waves $\eta'_{cn,i}(x',t')$ provides the calculated free surface $\eta'(x',t')$ for space x' and time t'. Since the interactions are *local properties* of the phases they may change significantly when the waves are evolved.

In the following sections, *first* an overview is given on the available nonlinear water wave equations including a clear definition of the range of applicability for the KdV-NLFT method.

Second, the most important conventional linear and nonlinear wave theories are presented, including the cnoidal wave theory.

Third, in a separate section the so-called *cnoidal wave equation* is introduced and it is explained, (i) why the interpretation of a cnoidal wave within this thesis strongly differs from the common applications of cnoidal-theory waves used in coastal engineering - and (ii) what is the advantage of this new approach.

Forth, the theoretical background of the direct and inverse KdV-NLFT is briefly discussed.

Fifth, the most important conventional wave analysis methods in frequency (fast Fourier transform, FFT) and time-frequency analysis (Hilbert-Huang transform, HHT) are introduced and their most important features and characteristics are compared to that of the KdV-NLFT.

Finally, the implications on the objectives and the methodology that are adopted within this thesis are specified.

2.2 Nonlinear water wave equations

The propagation of water surface waves can be described by different nonlinear water wave equations that have to be selected depending on the boundary conditions and the purpose of the analyses. Tab. 2.1 gives an overview on the relevant equations for the description and evolution of waves in the coastal region. The focus of this thesis is on the solution of the Korteweg-deVries equation that describes the propagation of waves in shallow-water for the 2D case (evolution of the surface elevation in direction z, $\eta(x,t)$, in direction x and time t, also denoted as wave motion in *1+1* dimensions).

Tab. 2.1: Available nonlinear water wave equations for 2D and 3D cases (equations from (Osborne, 2010)).

	dimensions	
relative water depth	2D or (*1+1*)	3D or (*2+1*)
$kh < 1.36$	Korteweg-deVries (KdV)	Kadomtsev-Petviashvili (KP)
$h/L < 0.22$	$\eta_t + c_0\eta_x + \alpha\eta\eta_x + \beta\eta_{xxx} = 0$	$\frac{\partial}{\partial x}\left[\eta_t + c_0\eta_x + \alpha\eta\eta_x + \beta\eta_{xxx}\right] + \frac{c_0}{2}\eta_{yy} = 0$
$kh \geq 1.36$	nonlinear Schroedinger (NLS)	Davey-Stewartson (DS)
$h/L \geq 0.22$	$i\left(\psi_t + C_g\psi_x\right) + \mu\psi_{xx} + \nu\lvert\psi\rvert^2\psi = 0$	$i\Psi_\tau + \lambda\Psi_{XX} + \mu\Psi_{YY} + \chi\lvert\Psi\rvert^2\Psi = \chi_0\Phi_X\Psi$ $\alpha\Phi_{XX} + \Phi_{YY} = -\beta\left(\lvert\Psi\rvert^2\right)_X$

2.2.1 The Korteweg-deVries (KdV) equation

The Korteweg-deVries equation was found by Korteweg and deVries (1895) for the description of the evolution of the free surface *η(x,t)* of long, unidirectional surface waves in shallow-water (*h/L<0.22*) in space and time. It can be found by a singular perturbation expansion of the Euler equations for $k \approx 0$ in 2D. The KdV equation is integrable by the inverse scattering transform (IST). Cnoidal waves as given in Eq. (2.24) are found by Korteweg and deVries (1895 to be exact solutions of the KdV equation for periodic travelling-wave boundary conditions.

For the analysis of *space series* and the Cauchy problem *η(x,0)* (initial value problem) the space-like KdV (sKdV) equation is applied. The dimensional form as presented in Tab. 2.1 is given by (Miles, 1980; Osborne, 1995a; Whitham, 1974):

$$\eta_t + c_o\eta_x + \alpha\eta\eta_x + \beta\eta_{xxx} = 0, \quad 0 \leq x \leq L_w, \tag{2.2}$$

where *η(x,t)* is the elevation (or amplitude) of the free surface as a function of space *x* and time *t*, $\eta_t = \partial\eta/\partial t$ the vertical velocity of *η(x,t)*, $\eta_x = \partial\eta/\partial x$ the gradient of *η(x,t)* in wave direction *x*, η_{xxx} the third-order partial derivative of *η(x,t)*, $\alpha\eta\eta_x$ the nonlinear convective term and $\beta\eta_{xxx}$ the dispersive term. The subscripts in Eq. (2.2) refer to partial derivatives of the surface elevation *η(x,t)* with respect to the variables *x* and *t*. The wave celerity or linear phase speed in shallow-water c_0, the coefficients α for nonlinearity and β for dispersion and the relation λ between nonlinearity and dispersion strongly depend on the particular physical application and the boundary conditions, especially on the water depth *h*. For surface waves in space domain as in Eq. (2.2) applies

$$\begin{aligned} c = c_0 = \sqrt{gh}, \qquad & \alpha = 3c_0 / (2h), \\ \beta = c_0 h^2 / 6, \qquad & \lambda = \alpha / (6\beta) = \frac{3}{2h^3}. \end{aligned} \tag{2.3}$$

with $g = 9.81\ m/s^2$ the acceleration due to gravity. Since periodic travelling-wave boundary conditions are assumed, the variable x varies from 0 to the length L_w of the analysis window.

Eq. (2.2) has the linear dispersion relation

$$\omega = c_0 k - \beta k^3 . \tag{2.4}$$

For the analysis of *time series* and the boundary value problem $\eta(0,t)$ the time-like KdV (tKdV) equation is applied that is derived from the space-like KdV equation by changing the space and time variables $x \to t$, $t \to x$, $k \to \omega$ and $\omega \to k$ (Osborne, 1993a; 1993b; 1993c 1993d; 1993e):

$$\eta_x + c_o' \eta_t + \alpha' \eta \eta_x + \beta' \eta_{xxx} = 0, \quad 0 \le x \le T_w, \tag{2.5}$$

with the modified time-domain coefficients

$$\begin{aligned} c_0' = 1/c_0 = 1/\sqrt{gh}, \qquad & \alpha' = -\alpha / c_0^2, \\ \beta' = -\beta / c_0^4, \qquad & \lambda' = \alpha' / (6\beta') = \frac{3c_0^2}{2h^3}. \end{aligned} \tag{2.6}$$

The KdV equation, like all other wave equations, provides an approximation to the real physical behaviour of water waves in shallow-water, but unfortunately, it does not provide an exact solution for every case. By adding further approximation terms to the KdV equations other KdV-based nonlinear water wave equations like the second Whitham (W2) equation (Whitham, 1974), the Camassa-Holm (CH) equation (Camassa & Holm, 1993; 1994), the modified KdV (mKdV) equation (Ablowitz & Segur, 1981), the Gardner equation (McKean, 1981) or the Ostrovsky equation (Ostrovsky, 1978) and the Boussinesq equation (Boussinesq, 1871; 1872; McKean, 1981) can be derived.

By application of the θ-function representation for the cnoidal waves in Eq. (2.35) instead of the conventional notation in Eq. (2.24) it is possible to separate the cnoidal basic components and their nonlinear interactions as shown in Eq. (2.41). This is the most important reason to use this rather complex approach for the solution of the KdV equation (Osborne, 1995b; 1995c):

$$\eta(x,t) = \underbrace{\sum \eta_{cn,i}(x,t)}_{\substack{\text{linear superposition} \\ \text{of cnoidal waves}}} + \underbrace{\eta_{int}(x,t)}_{\substack{\text{nonlinear interactions} \\ \text{between the cnoidal waves}}}, \tag{2.7}$$

with $\eta_{int}(x,t) = \sum_j \eta_{int,j}(x,t)$ the linear superposition of all nonlinear interaction terms between the N cnoidal waves $\eta_{cn,i}(x,t)$.

2.2.2 The Kadomtsev-Petviashvili (KP) equation

The Kadomtsev-Petviashvili equation is a generalisation of the KdV equation for the calculation of $\eta(x,y,t)$ for the 3D or (*2+1*) case. In the KP equation directional spreading of shallow-water waves for small motion in y direction (transverse to the main motion in x direction) is considered. For water depths larger than one centimetre the surface tension can be neglected and then the KP equation is denoted as KPII (Osborne, 2010):

$$\left(\eta_t + c_0\eta_x + \alpha\eta\eta_x + \beta\eta_{xxx}\right)_x + \frac{c_0}{2}\eta_{yy} = 0. \tag{2.8}$$

The definition of the parameters α, β and c_0 is the same as given in Eq. (2.3) for the KdV equation. When the directional spreading is insignificant, then the KPII reduces to the KdV equation.

2.2.3 The nonlinear Schroedinger (NLS) equation

The nonlinear Schroedinger (NLS) equation describes the 2D or (*1+1*) wave dynamics in deep-water conditions ($h/L \geq 0.22$). The NLS equation is given as (Osborne, 2010; Yuen & Lake, 1982):

$$i\left(\psi_t + C_g\psi_x\right) + \mu\psi_{xx} + \nu|\psi|^2\psi = 0, \tag{2.9}$$

where C_g is the linear group speed and μ and ν coefficients which are defined as

$$C_g = \frac{\omega_0}{2k_0}, \quad \mu = -\frac{\omega_0}{8k_0^2}, \quad \nu = -\frac{\omega_0 k_0^2}{2}, \tag{2.10}$$

with $\omega_0^2 = gk_0$ the linear deep-water dispersion relation, ω_0 the phase, k_0 the wave number and g the acceleration due to gravity.

The function $\psi(x,t)$ describes the complex envelope function of a narrow-banded wave train whose amplitude $\eta(x,t)$ is given by (Osborne, 2010)

$$\eta(x,t) = \psi(x,t)e^{ik_0x - i\omega_0 t} + \text{complex conjugate}. \tag{2.11}$$

Therefore, the deepwater free surface $\eta(x,t)$ is described by the complex modulation $\psi(x,t)$ of a carrier wave $e^{ik_0x - i\omega_0 t}$ that also considers the Benjamin-Feir instability. The NLS equation that is valid for deep-water is neither implemented nor applied within this thesis which concentrates on the analysis of coastal wave data in shallow water. Nevertheless, this short outline shows that the underlying physical processes that govern the evolution of the free surface in deep water (NLS equation) are completely different from those in shallow-water (KdV and KP equation).

2.2.4 The areas of validity for the introduced nonlinear water wave equations

In order to determine the areas of validity of the Korteweg-deVries and the nonlinear Schroedinger equation, Osborne (2010) uses a generalized Ursell number U_g that is derived from the Fourier expansion of the nonlinear Schroedinger equation (NLS):

$$U_g = \frac{H\left[3 - \tanh^2(k_0 h)\right]k_0}{8\tanh^3(k_0 h)}, \tag{2.12}$$

where H is the wave height, k_0 the wave number and h the water depth.

This generalised Ursell number U_g is applied in Fig. 2.2 for plotting the nonlinearity of wave trains as a function of the wavelength-to-depth ratio L/h for different amplitude-to-depth ratios between $a/h=0.01$ to 0.32. Note that the ratio L/h is given in the figure as function of both the wave number k as well as of the wave period T by transformation of the wavelength L from space to time domain by the relation

$$L = \frac{2\pi}{k} = cT = \frac{2\pi c}{\omega}. \tag{2.13}$$

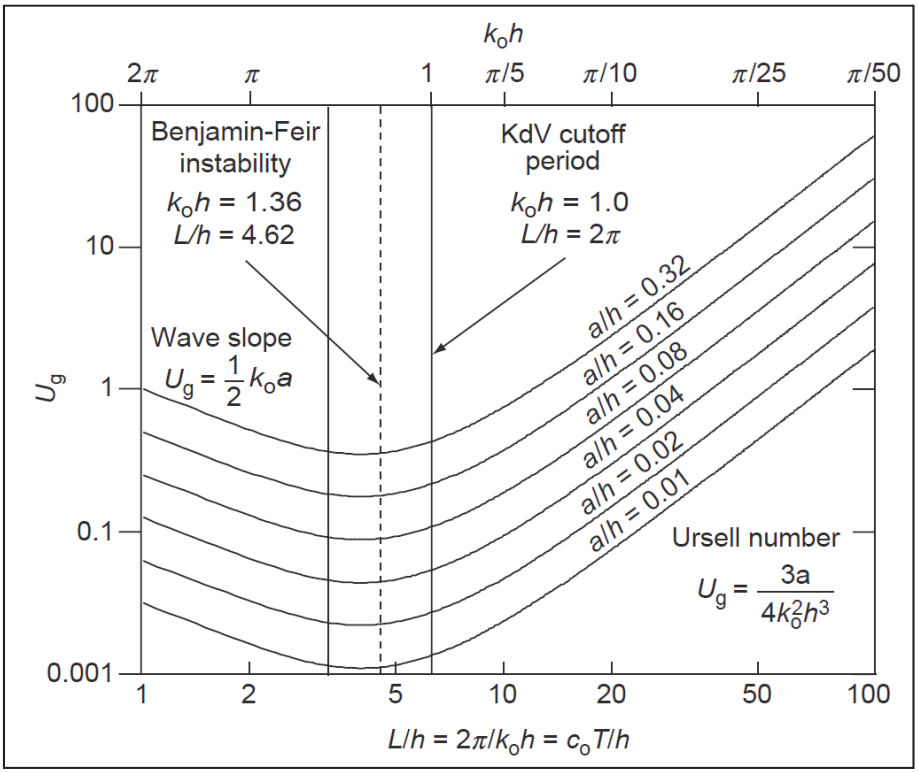

Fig. 2.2: Ursell number diagram illustrating how nonlinear a wave train is as a function of depth (Osborne, 2010).

Fig. 2.2 also clearly shows the KdV cut-off period at $k_0h=1.0$ and the beginning of the Benjamin-Feir instability starting from $k_0h\geq1.36$. These two values are very important for the practical application of the KdV-NLFT: For waves with values $kh\leq1.0$ the KdV equation is valid and the KdV-NLFT provides reliable results. This range can be extended with good approximation up to $kh<1.36$. Starting with this latter value, $kh\geq1.36$, different physical wave

interaction processes, especially the Benjamin-Feir instability, will occur and, finally, the KdV-NLFT is not able to provide correct calculations of the nonlinear wave-wave interactions for these relative water depths.

2.3 Linear and nonlinear wave theories

In coastal and ocean engineering different conventional linear and nonlinear analytical and numerical stream function wave theories are applied for the calculation of linear and nonlinear waves in shallow and intermediate water depths. Depending on the boundary conditions (wave steepness *H/L* and relative water depth *h/L*) either the Airy or Stokes (see section 2.3.1), cnoidal (2.3.2) or solitary wave theory (2.3.3) provides the best-fit results for the calculation of the free surface profile $\eta(x,t)$ of regular waves (see Fig. 2.3a). The stream function theory (2.3.4) covers a wider range of validity (see Fig. 2.3b), but is more complex, includes iterations and therefore has to be executed numerically.

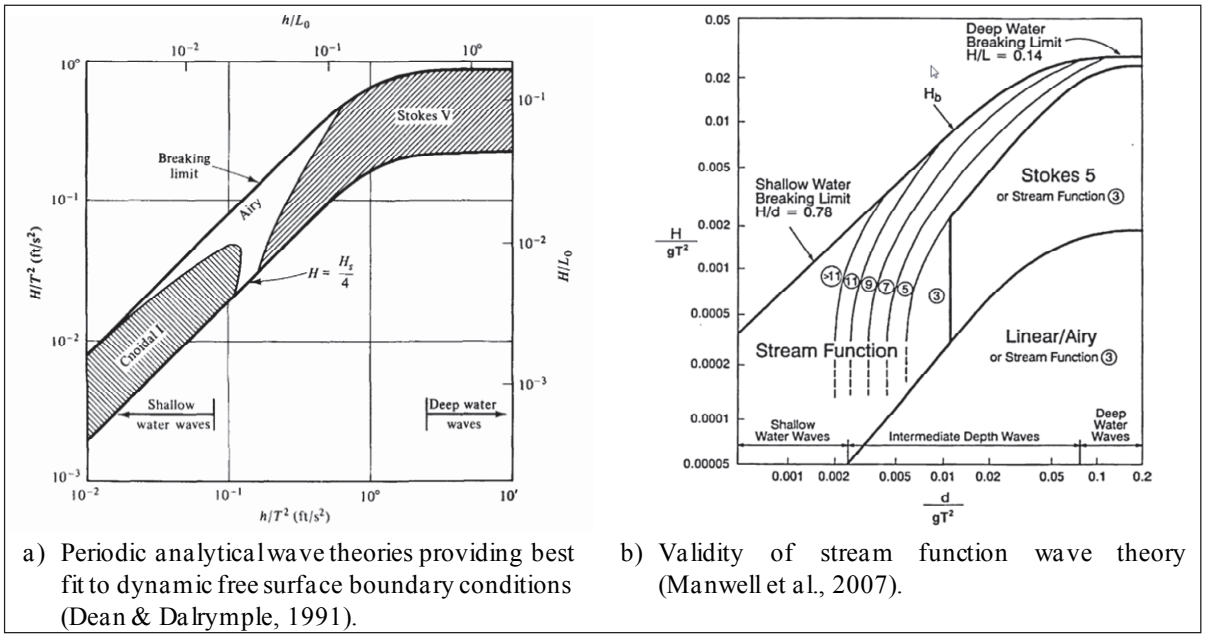

a) Periodic analytical wave theories providing best fit to dynamic free surface boundary conditions (Dean & Dalrymple, 1991).

b) Validity of stream function wave theory (Manwell et al., 2007).

Fig. 2.3: Periodic wave theories providing best fit to dynamic free surface boundary conditions (DFSBC, analytical and stream function theories).

2.3.1 Airy and Stokes wave theory

All wave theories that are presented here for the description of surface waves in ocean and coastal engineering are derived from the Laplace equation for the motion of incompressible fluids with constant density ρ (LeMéhauté, 1976):

$$\frac{\partial^2 \phi}{\partial x^2} + \frac{\partial^2 \phi}{\partial y^2} + \frac{\partial^2 \phi}{\partial z^2} = 0, \tag{2.14}$$

with $\phi(x,y,z)$ the velocity potential.

The simplest theory is the linear Airy wave theory (Airy, 1845). Progressive linear waves can easily be calculated from (Dean & Dalrymple, 1991)

$$\eta(x,t) = a\cos(kx - \omega t + \varphi), \tag{2.15}$$

where $\eta(x,t)$ is the free surface as function of position x and time t, $a=H/2$ the wave amplitude, H the wave height, $k=2\pi/L$ the wave number, L the wavelength, $\omega=2\pi/T$ the angular frequency, T the wave period and φ the phase angle.

For the derivation of Eq. (2.15) from the Laplace equation (2.14) the waves are assumed to be of small amplitude a compared to the wavelength L ($a<<L$) and therefore all terms of higher order in the kinematic and free surface boundary conditions can be neglected. The shape of the waves is not influenced by the water depth but only a function of amplitude a, wave number k, angular frequency ω and phase φ.

If the wave height increases or if the water depth decreases, then the waves are affected by water depth and wave steepness, and two different opposed effects occur: dispersion and nonlinearity. The Ursell parameter (or Ursell number) Ur combines these effects (Massel, 1996; Osborne, 2010):

$$Ur = \frac{3}{8}\frac{Hk}{(kh)^3} = \frac{3}{32\pi^2}\frac{H}{L}\left(\frac{h}{L}\right)^{-3} = \frac{3}{32\pi^2}\frac{H}{h}\left(\frac{h}{L}\right)^{-2}. \tag{2.16}$$

In these two different notations the terms H/L (wave steepness) and H/h (relative wave height with respect to the water depth) represent the *nonlinear* properties and the term h/L (relative water depth) describes the *dispersive* nature of the wave. For a given wavelength L, the Ursell number Ur increases with increasing wave height H and/or decreasing water depth h, and thus the nonlinear character of the wave is increasing. The consequence for the practical application is: frequently, the real observed water waves with higher wave steepness or in shallow water significantly differ from the linear theory. In the case of weakly nonlinear effects due to increased wave steepness the Stokes wave theory (Stokes, 1847) is applied which superposes additional sinusoidal terms of higher harmonic order for the calculation of the velocity potential and the free surface. Depending on the order of the added nonlinear components, the wave theory is denoted as Stokes second-, third- or fifth-order wave theory. The equation for a second order Stokes wave is given by (Dean & Dalrymple, 1991):

$$\begin{aligned}\eta(x,t) &= \eta_1(x,t) + \eta_2(x,t) \\ &= a\cos(kx - \omega t) + \frac{a^2 k}{4}\frac{\cosh kh}{\sinh^3 kh}(2 + \cosh 2kh)\cos 2(kx - \omega t)\end{aligned} \tag{2.17}$$

where $\eta_1(x,t)$ is the first-order (Airy) wave component, $\eta_2(x,t)$ the second-order component and a the amplitude of the first-order wave.

If the addition of second-order terms is not sufficient to represent the wave's nonlinear character, then a fifth order Stokes wave representation can be applied as given by Skjelbreia and Hendrickson (1961):

$$\begin{aligned} k\eta &= k\eta_1(x,t) + k\eta_2(x,t) + k\eta_3(x,t) + k\eta_4(x,t) + k\eta_5(x,t) \\ &= ka\cos(kx-\omega t) + \left[(ka)^2 B_{22} + (ka)^4 B_{24}\right]\cos 2(kx-\omega t) \\ &+ \left[(ka)^3 B_{33} + (ka)^5 B_{35}\right]\cos 3(kx-\omega t) \\ &+ (ka)^4 B_{44}\cos 4(kx-\omega t) + (ka)^5 B_{55}\cos 5(kx-\omega t). \end{aligned} \tag{2.18}$$

The constants B_{22}, B_{24}, B_{33}, B_{35}, B_{44} and B_{55} are functions of the hyperbolic terms $s=\sinh kh$ and $c=\cosh kh$:

$$\begin{aligned} B_{22} &= \frac{(2c^2+1)}{4s^3}, \qquad B_{24} = \frac{c(272c^8 - 504c^6 - 192c^4 + 322c^2 + 21)}{384s^9}, \\ B_{33} &= \frac{3(8c^6+1)}{64s^6}, \\ B_{35} &= \frac{-21816c^6 - 6264c^4 - 54c^2 - 81}{12288s^{12}(6c^2-1)} \\ &+ \frac{88128c^{14} - 202224c^{12} + 70848c^{10} + 54000c^8}{12288s^{12}(6c^2-1)}, \\ B_{44} &= \frac{c(768c^{10} - 448c^8 - 48c^6 + 48c^4 + 106c^2 - 21)}{384s^9(6c^2-1)}, \\ B_{55} &= \frac{192000c^{16} - 262720c^{14} + 83680c^{12} + 20160c^{10}}{12288s^{10}(6c^2-1)(8c^4-11c^2+3)} \\ &+ \frac{-7280c^8 + 7160c^6 - 1800c^4 - 1050c^2 + 225}{12288s^{10}(6c^2-1)(8c^4-11c^2+3)} \end{aligned} \tag{2.19}$$

Stokes wave theory covers steep waves in intermediate water depth and deep water. For further decrease of the water depth the cnoidal wave theory provides the best results for the free surface $\eta(x,t)$ (see Fig. 2.3a).

The relation between the angular frequency ω and the wave number k is defined by the dispersion relation. For Airy and Stokes 2nd-order waves the dispersion relation is linear and only a function of water depth h (Dean & Dalrymple, 1991):

$$\omega^2 = gk\tanh(kh). \tag{2.20}$$

As already shown, in the Ursell number in Eq. (2.16) in addition to the depth-depending dispersion an additional term for the nonlinear influence of the wave height H is introduced. Starting from Stokes 3rd-order waves, the influence of this nonlinearity has to be considered and the wave dispersion now is a function of water depth h *and* wave height H. This influence of the wave amplitude leads to the *nonlinear dispersion relation* in Eq. (2.27), that is valid for Stokes waves higher than 3rd-order and for cnoidal waves.

The potential, kinematic and total energies E_{pot}, E_{kin} and E_{tot} of an Airy wave are calculated as (Dean & Dalrymple, 1991):

$$E_{pot} = \frac{1}{16}\rho g H^2, \tag{2.21}$$

$$E_{kin} = \frac{1}{16}\rho g H^2, \tag{2.22}$$

$$E_{tot} = E_{pot} + E_{kin} = \frac{1}{8}\rho g H^2. \tag{2.23}$$

These wave energies are given as the energies per unit surface area in *[J/m²]*. In order to obtain the energies for one wave length and unit width the Eqs. (2.21) to (2.23) have to be simply multiplied with the wave length *L*. Dean and Dalrymple (1991 clearly state that "neither the average (over a wave length) potential nor kinetic energy per unit area depends on water depth or wave length, but each is simply proportional to the square of the wave height."

2.3.2 Cnoidal wave theory (elliptical functions)

The cnoidal-theory wave is a function of the Jacobian elliptic integral cn and can be noted in different forms (see Dean & Dalrymple, 1991; Dingemans, 1997a; Osborne, 2010). In order to show the variety of existing notations, the two following forms are selected (Osborne, 2010):

$$\eta(x,t) = \frac{4k^2}{\lambda}\sum_{n=1}^{\infty}\left(\frac{n(-1)^n q(m)^n}{1-q^{2n}}\cos\left[nk_n(x-C_n t)+\varphi_n\right]\right), \tag{2.24a}$$

$$\eta(x,t) = H\mathrm{cn}^2\left(\left[\frac{K(m)}{\pi}\right][kx-\omega t+\varphi];m\right) \tag{2.24b}$$

with λ as defined in Eq. (2.3), *N* the order of the partial wave component, *q(m)* the nome, *C* the nonlinear wave celerity (see Eq. (2.28)), the dispersion relation *ω=Ck, H* the wave height of the cnoidal-theory wave, cn*(m)* the Jacobian elliptic function (cosinus amplitudinis) with *m* the modulus (Osborne, 2010):

$$mK^2(m) = 2\pi^2\frac{3a}{4k^2h^3} = 2\pi^2\mathrm{Ur} \tag{2.25}$$

where *a=H/2* is the cnoidal-theory wave amplitude. The nome *q* is defined as (Osborne, 2010):

$$q(m) = e^{-\pi K'(m)/K(m)}, \tag{2.26}$$

where *K(m)* is the complete elliptic integral of the first kind and *K'(m)=K(1-m)*.

The formulation in Eq. (2.24a) represents the generation of cnoidal waves by linear superposition of an infinite number of higher-order cosine waves with decreasing amplitudes to cover the nonlinear properties of the shallow-water waves. A limitation of the number of cnoidal-theory wave components in Eq. (2.24a) to *N* instead of ∞ leads to the Stokes wave theory of order *N* whereas the simpler notation in Eq. (2.24b) is closer to the notations given in the Airy and Stokes wave theories.

Wave numbers k_n and frequencies ω_n of the cnoidal-theory waves are related by the nonlinear dispersion relation $\omega_n = \omega_n(k_n)$:

$$\omega_n = k_n C = k_n c \left\{ 1 + \frac{2a}{h} - \frac{2k_n^2 h^2 K^2(m)}{3\pi^2} \right\} \tag{2.27}$$

where C is the nonlinear wave celerity of the cnoidal-theory wave:

$$C = c \left\{ 1 + \frac{2a}{h} - \frac{2k^2 h^2 K^2(m)}{3\pi^2} \right\}. \tag{2.28}$$

The potential, kinematic and total energies E_{pot}, E_{kin} and E_{tot} of a cnoidal wave are calculated as (Dingemans, 1997b)

$$E_{pot,cn} = \frac{1}{2}\rho g H^2 \left(-\frac{1}{3m} + \frac{2}{3m}\left(1+\frac{1}{m}\right)\left(1-\frac{E(m)}{K(m)}\right) - \frac{1}{m^2}\left(1-\frac{E(m)}{K(m)}\right)^2 \right), \tag{2.29}$$

$$E_{kin,cn} = \frac{C^2}{gh} E_{pot,cn}, \tag{2.30}$$

$$E_{tot,cn} = E_{pot,cn} + E_{kin,cn}, \tag{2.31}$$

where E*(m)* is the complete elliptic integral of the second kind.

The different energy parts of cnoidal waves are depending on the water depths. While the energy fractions $E/(\rho g H^2)=1/16$ are constant for Airy waves (see Eqs. (2.21) and (2.22)) they are variable for nonlinear cnoidal waves. Dingemans (1997b) shows that for the limit $m \rightarrow 0$ Eq. (2.29) reduces to Eq. (2.21) and that in case of linear waves applies $E_{kin,cn}=E_{kin}$. For nonlinear waves always applies $C^2>gh$ since the nonlinear waves are faster than the celerity of linear waves in shallow-water. Therefore, for nonlinear waves also applies $E_{kin}>E_{pot.}$ He also shows that in case of nonlinear cnoidal waves the energy fractions of cnoidal waves always are smaller than 1/16 as applies for Airy waves. With increasing modulus the cnoidal wave energy fractions decrease further (see Fig. 2.4). Note that Dingemans (1997b) uses the formulation $E/(0.5\rho g H^2)=1/8$, leaves out the term *'0.5ρg'* in the notation and therefore determines $E/H^2=0.125$ for both E_{pot} and E_{kin} for linear waves instead of the original values $E/(H^2)=1/16 \cdot \rho g$.

As shown in Fig. 2.3 and Fig. 2.5 for the practical application and calculation of periodic surface waves the cnoidal wave theory is used only where other, simpler theories do not provide acceptable results. The reasons - most likely - are the complex theoretical background, the unfamiliar function cn, the difficulty to operate with the unusual modulus *m* and, most important, the fact that for many practical applications Airy, Stokes and solitary wave theories are sufficient within the engineering accuracy. Cnoidal waves that are applied within the limits of the *cnoidal wave theory* as shown in Fig. 2.3 are denoted within this thesis as *cnoidal-theory waves*. The term *cnoidal wave* is used for waves that are generated and interpreted within the definitions of the *cnoidal wave equation* in section 2.4.

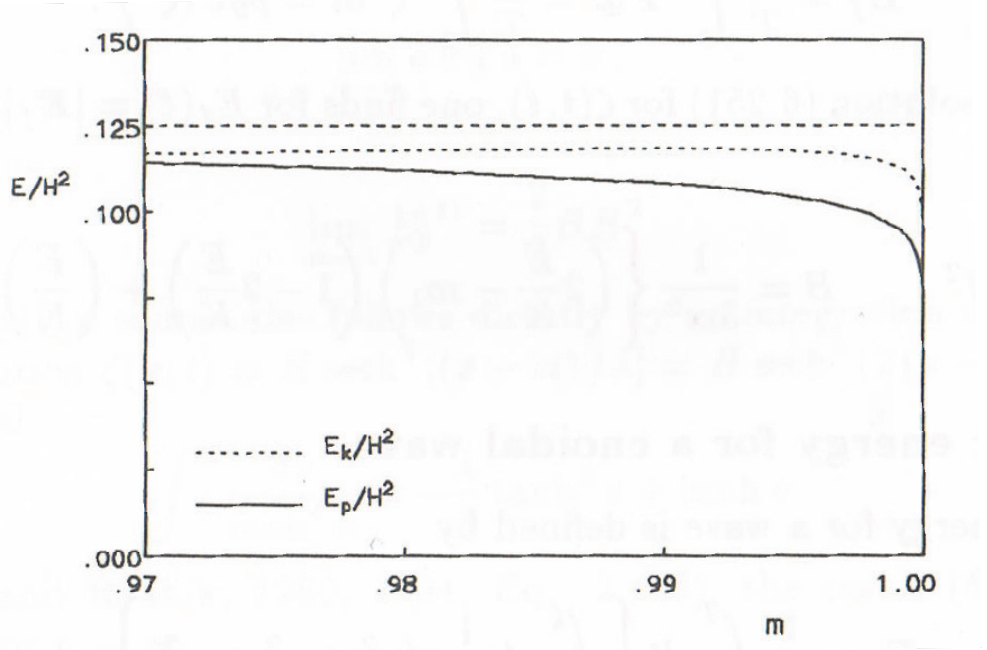

Fig. 2.4: The potential and kinetic energy densities E/H^2 for cnoidal waves, Eq. (2.29) for $E_{pot}=E_p$ and Eq. (2.30) for $E_{kin}=E_k$ (Dingemans, 1997b).

2.3.3 Solitary wave theory

The Airy, Stokes and cnoidal wave theories cover the range of linear, weakly nonlinear and strongly nonlinear periodic waves in the coastal zone. In extreme shallow-water conditions non-periodic, non-stationary solitary waves (or solitons) occur and can be calculated by the solitary wave theory (Miles, 1980):

$$\eta(x) = H \operatorname{sech}^2 \sqrt{\frac{3}{4}\frac{H}{h^2(h+H)}}(x-ct), \tag{2.32}$$

where $\operatorname{sech} = 1/\cosh$ is the hyperbolic secant. For solitary waves applies wave height equals wave amplitude: $H=a$. The wave celerity of a solitary wave is determined from the shallow-water wave celerity as

$$c = \sqrt{g(h+H)}\,. \tag{2.33}$$

The denotation *solitary wave* is used within this thesis for a single soliton. If more than one of these waves occur within a time or space series they are referred to as *solitons*.

2.3.4 Stream function theory

For further decreasing water depths with $h/L<0.1$ the Stokes fifth-order waves do not provide sufficient accuracy for periodic waves and theories of even higher order are required. Instead of developing complex analytical solutions, numerical iterative theories as the stream function theory by Dean (1965), Dalrymple (1974) and Dalrymple and Cox (1976) can be applied. These approaches include numerical iterations to provide approximate solutions to the gov-

erning partial differential equation (PDE) while the boundary conditions are fulfilled exactly at the free surface $z(x,t)=\eta(x,t)$ which, wherever it is, is a streamline by definition (Dean & Dalrymple, 1991; Brorsen, 2007):

$$\psi(x,z,t)=-\frac{H}{2}\frac{g}{\omega}\frac{\sinh k(h+z)}{\cosh kh}\cos(kx-\omega t+\varphi)\,, \tag{2.34}$$

where $\psi(x,z,t)$ is the stream function.

Since the stream function wave theory includes all terms up to order *N*, it covers not only shallow-water conditions but also provides correct waves in deep-water where the higher-order waves can be neglected. Therefore, it often is applied for the calculation of the free surface for wave generation in flumes and basins or to obtain the wave kinematics for further applications. Regarding Fig. 2.3 it can be stated that the stream function theory provides numerical solutions for the whole range of conventional wave theories. For a 'classification' of the nonlinearity of the waves the Ursell number *Ur* can be calculated.

2.4 Cnoidal waves as spectral basic components for the KdV-NLFT

The cnoidal wave equation which is introduced and discussed within this section provides the nonlinear spectral basic components for the nonlinear decomposition and superposition of the original data in the KdV-NLFT. First, the significant difference between the interpretation and application of cnoidal waves in the conventional cnoidal wave theory on the one hand and in the KdV-NLFT on the other hand is discussed. Then, the notation of cnoidal waves in terms of Jacobi θ-functions and their nonlinear superposition by application of Riemann Θ-functions are presented. Finally, the governing parameters of the cnoidal waves and a short introduction into the notation of cnoidal waves in terms of μ-functions are given.

2.4.1 Cnoidal waves and cnoidal-theory waves

For the understanding of the concept and procedures of the direct and inverse transforms within the KdV-NLFT that are applied within this thesis, it is of major significance to distinguish between the interpretation of cnoidal waves from the physical point of view (i.e. the *cnoidal wave equation* as applied within the KdV-NLFT) and the limitation of the range for the practical application of cnoidal waves in the *cnoidal wave theory* as one of four conventional wave theories. The shape and the nonlinear character of the cnoidal wave in Eq. (2.24b) are governed by the Jacobian elliptic integral cn which is a function of the modulus *m*. For $m\to 0$ follows $cn\to\cos$ and the nonlinear cnoidal wave approaches the linear Airy wave in Eq. (2.15). For $m\to 1$ follows $cn\to\operatorname{sech}$ and the cnoidal wave becomes a solitary wave as given in Eq. (2.32). If the modulus is allowed to vary within the limits $0\le m\le 1$ then the cnoidal wave equation provides waves that span the whole range from Airy over Stokes and cnoidal-theory waves up to solitary wave theory (see Fig. 2.5).

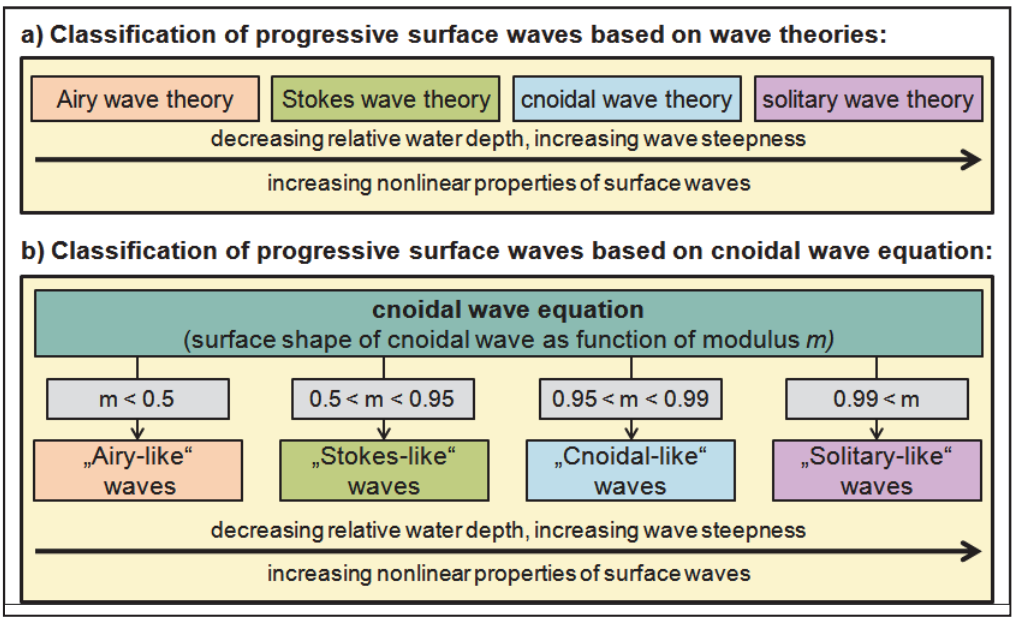

Fig. 2.5: a) Conventional classification of progressive surface waves using different wave theories. b) Classification of progressive surface waves based on the cnoidal wave equation using the modulus *m* as governing parameter for the nonlinear shape of the free surface (Brühl & Oumeraci, 2012).

A selection of cnoidal wave profiles for different values of *m* is plotted in Fig. 2.6. This universal physical interpretation of cnoidal waves is applied within the KdV-NLFT. In the *cnoidal wave theory* as usually applied for engineering applications the cnoidal waves are used only within a limited range for nonlinear shallow-water waves that are out of the scope of higher-order Stokes wave theory but not yet solitary waves (see Fig. 2.3). A 'typical' cnoidal wave used within the cnoidal wave theory to fill the existing gap between higher-order Stokes and solitary wave theory has a typical crest-to-trough-elevation ratio of 2:1, but this restriction does *not* apply to the unrestricted approach as the cnoidal waves are applied within the KdV-NLFT. Within this thesis the following denotation is used to avoid misunderstandings: *Airy, Stokes* and *solitary waves* are respectively generated by Airy, Stokes and solitary wave theory as used in the conventional classification of waves as given in sections 2.3.1 and 2.3.3. *Cnoidal-theory waves* are generated by the equations given in section 2.3.2 and used within the field of applications specified in the same section. By application of the same equation as used in the cnoidal wave theory (and which now is denoted as *cnoidal wave equation*) the *cnoidal waves* are generated, but they are interpreted and applied in a basically different way, as shown in Fig. 2.5. However, the equations for the generation of *cnoidal-theory waves* and *cnoidal waves* are the same. Cnoidal waves generated from the cnoidal wave equation that are similar to Airy waves are denoted as *Airy-like*. If they are alike Stokes waves they are designated as *Stokes-like*, etc.

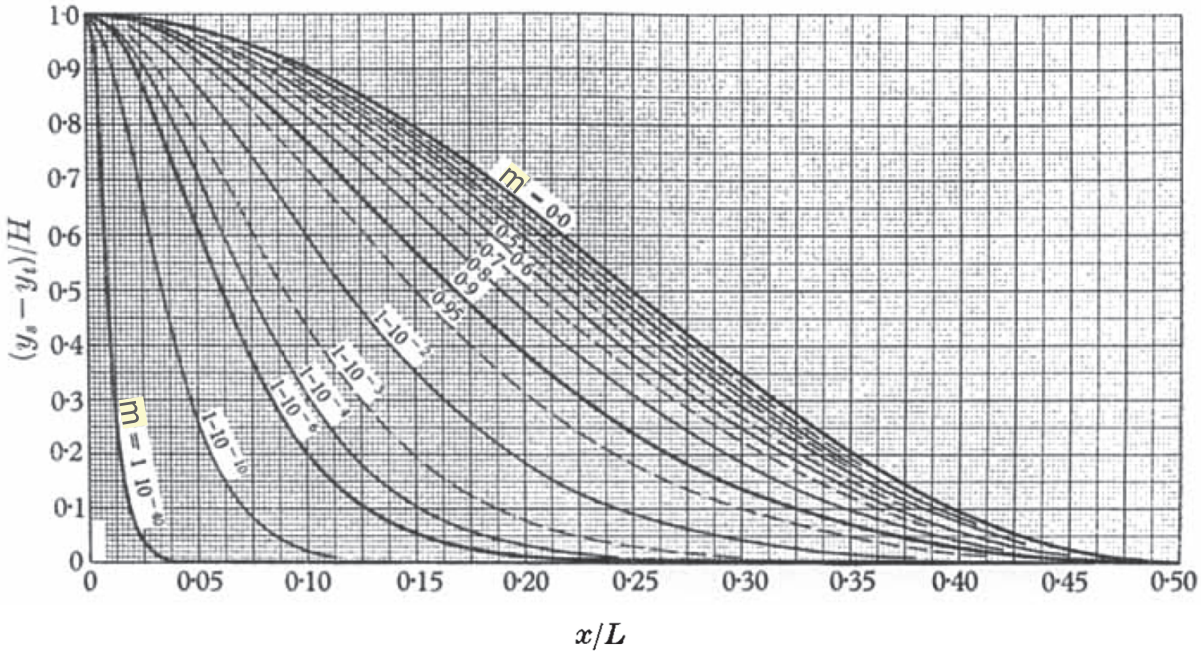

Fig. 2.6: Surface profiles of cnoidal waves as function of modulus m (after Wiegel, 1960).

2.4.2 Cnoidal waves in terms of Jacobi θ-functions

For the generation of a single cnoidal wave $\eta_{cn}(x,t)$ from the cnoidal wave equation in Eq. (2.24) the representation in terms of Jacobi θ-functions (θ = 'theta') is very useful (Jacobi, 1828; Bronstein et al., 2001; Osborne, 2010):

$$\eta_{cn}(x,t) = \frac{2}{\lambda}\frac{\partial^2}{\partial x^2}\ln\theta(x,t), \tag{2.35}$$

with

$$\theta(x,t) = 1 + 2\sum_{n=1}^{\infty} e^{-\frac{1}{2}n^2 B_{11} + ink x - in\omega t + in\varphi}, \tag{2.36}$$

$$\theta(x,t) = 1 + 2\sum_{n=1}^{M} e^{-\frac{1}{2}n^2 B_{11}} \cos\left[n(kx - \omega t + \varphi)\right]. \tag{2.37}$$

The θ-function in Eq. (2.36) can be regarded as a conventional Fourier series with an unlimited number of partial θ-components and k, ω and φ being the wave number, angular frequency and phase as known from conventional wave theories. For practical applications, the number of components can be limited to M instead of ∞, as done in Eq. (2.37). The notation in Eq. (2.37) shows that the θ-function can also be written as a conventional Fourier series in terms of cosine functions. The amplitudes of the Fourier components are functions of n^2B_{11} (with B_{11} the Riemann matrix element that defines the amplitude of the cnoidal wave) and decrease (i) with decreasing nonlinearity of the cnoidal wave (increasing values of B_{11}) and (ii) with increasing values of order n of the Fourier components, just similar as for the decreasing wave amplitudes of the higher-order components in Stokes wave theory in Eqs. (2.17) and (2.18). After the linear superposition of the M (instead of ∞) partial θ-functions in

Eqs. (2.36) or (2.37), the successive application of the natural logarithm $\ln\theta(x,t)$, the second partial derivative $\partial^2 / \partial x^2$ with respect to x, and finally a scaling of the data by $2/\lambda$ provides the single cnoidal wave $\eta_{cn}(x,t)$ in Eq. (2.35). An example for a cnoidal wave with $B_{11}=2.6$ ($m=0.992$, this value corresponds to a solitary wave) in a water depth of $h=0.60m$ is given in Fig. 2.7.

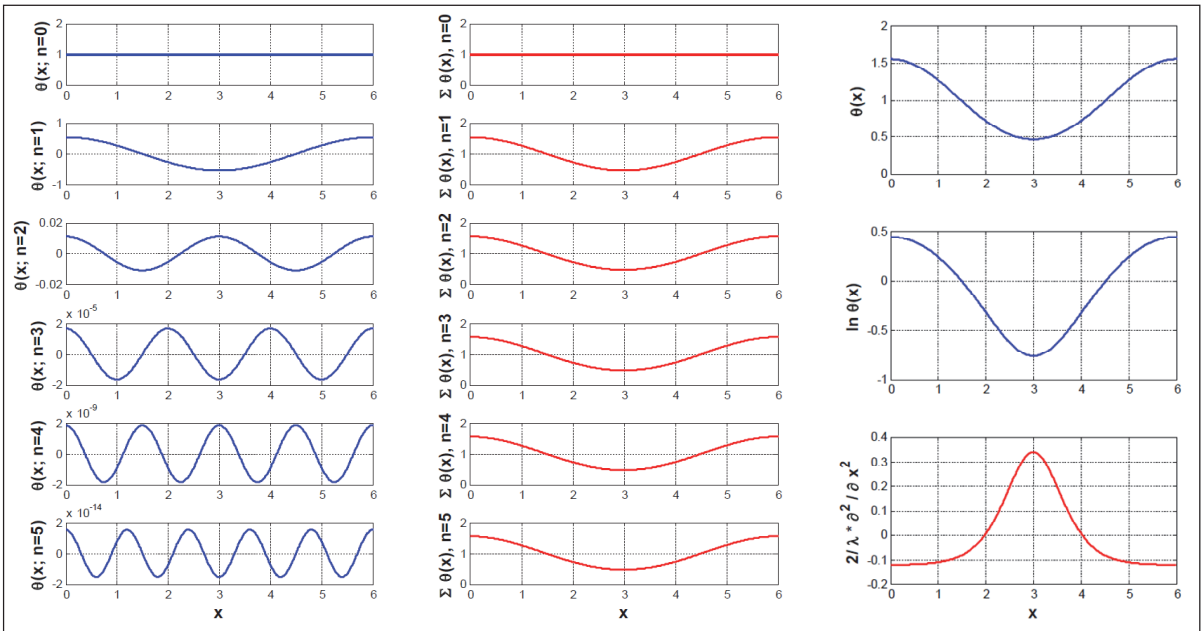

a) Convergence of the theta function for B_{11}=2.6 (modulus $m=0.992$) and $M=5$. The left plots in blue show the partial theta terms for $n=0$ to $n=5$. The right plots in red show the linear superposition of the partial terms for given values of n.

b) θ-function from figure (a); logarithm, second derivative and scaling by $2/\lambda$ provides the cnoidal soliton-shaped wave $\eta_{cn}(x,t)$ (red curve).

Fig. 2.7: Generation of a cnoidal wave by superposition of partial θ-functions.

The application of the θ-function is a much more complicated way to provide the same waves that might be obtained much easier from the conventional analytical or stream function wave theories given in section 2.3. But the major and most important difference is that the application of θ-functions provides only those cnoidal waves that are *solutions of the KdV equation*. So the cnoidal wave that is obtained for a given the combination of amplitude a (which is implicitly defined by the nonlinearity parameters m or B_{11} in Eqs. (2.36) and (2.37)), wavelength L or period T and water depth h is unique since a, m and B_{11} are not independent. Therefore, for the generation of a cnoidal wave with a given period or length in a given water depth, either the amplitude *or* the nonlinearity (represented by m and B_{11}) can be given as input parameter. This means, that the amplitude of the determined wave is adapted automatically to the desired nonlinearity. Vice versa, the nonlinearity and therefore the shape of the free surface are automatically adapted to the desired wave amplitude. Hence, by application of the θ-functions it is not possible to generate multiple waves with identical length, modulus (and therefore identical nonlinearity) but different wave heights in the same water depth, because this does not represent the real physics of these waves. The implications of this fact will be discussed further in sections 3, 4 and 5.

Another significant property of the cnoidal waves is their spectral behaviour. In Fig. 2.8 four cnoidal waves with different modulus are presented (left column) with their conventional FFT spectra (centre) and the nonlinear spectra obtained from KdV-NLFT (right column). In the FFT spectra, an increasing number of higher-harmonic components are observed. This corresponds to the generation of cnoidal waves in Eq. (2.24a) by linear superposition of cosine waves. In contrast to the conventional FFT, the KdV-NLFT considers a cnoidal wave to be just *one* component, as presented in the nonlinear spectra in the right column of the figure. The implication of this for the interpretation of the results in the following chapters is important: (i) this representation opens a completely new perspective on the interpretation of the spectral properties of nonlinear shallow-water wave trains and (ii) since no higher harmonics are present, in the nonlinear spectra the cnoidal waves can evolve easily in time and space independently of their shape by application of the cnoidal wave equations without distinguishing between free and bound harmonic components. Further details on this are given in chapter 3.

The nonlinear dispersion relation of a cnoidal wave is identical to that given for the cnoidal-theory wave in Eq. (2.27):

$$\omega_n = k_n C = k_n c \left\{ 1 + \frac{2a}{h} - \frac{2k_n^2 h^2 K^2(m)}{3\pi^2} \right\}. \tag{2.27}$$

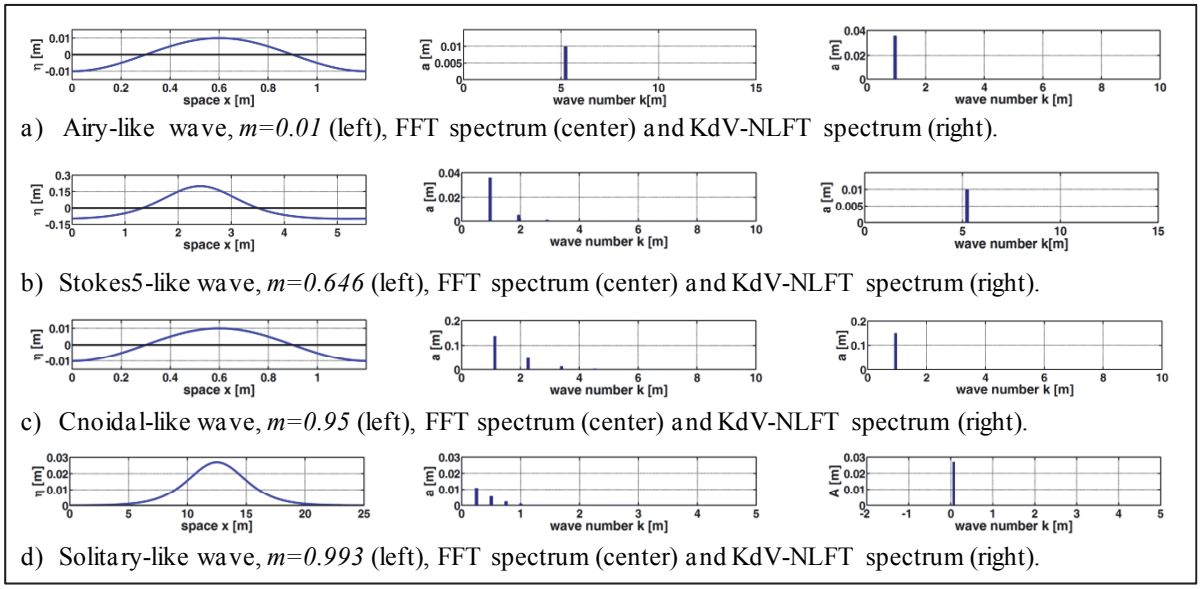

a) Airy-like wave, *m=0.01* (left), FFT spectrum (center) and KdV-NLFT spectrum (right).

b) Stokes5-like wave, *m=0.646* (left), FFT spectrum (center) and KdV-NLFT spectrum (right).

c) Cnoidal-like wave, *m=0.95* (left), FFT spectrum (center) and KdV-NLFT spectrum (right).

d) Solitary-like wave, *m=0.993* (left), FFT spectrum (center) and KdV-NLFT spectrum (right).

Fig. 2.8: Wave profiles, conventional FFT spectra and nonlinear spectra from KdV-NLFT for different wave types generated from cnoidal wave equation (water depth *h=0.6m*).

2.4.3 The governing parameters of the θ-functions

The cnoidal waves in Eq. (2.24a) are governed by the nome *q(m)* and the modulus *m* which are measures of the nonlinearity of the generated free surface wave. The values of *m*, *q* and B_{11} are related by the following equations (Osborne, 2010):

$$m = m(q) = \frac{4\pi^2 q}{K^2(q)} \left(\sum_{n=0}^{\infty} q^{n(n+1)} \right)^4, \tag{2.38a}$$

$$q = q(m) = \epsilon + 2\epsilon^5 + 15\epsilon^9 + 150\epsilon^{13} + 1707\epsilon^{17} + \ldots, \tag{2.38b}$$

$$\epsilon = \frac{1}{2}\left(\frac{1-(1-m)^{1/4}}{1+(1-m)^{1/4}}\right), \tag{2.38c}$$

$$B_{11} = B_{11}(q) = -2\ln q\,. \tag{2.38d}$$

Some examples for corresponding values of m, q, B_{11} and the complete elliptic integral of the first kind $K(q)$ with respect to the nome $q(m)$ are given in Tab. 2.2. Since for high values of m the θ-functions are very sensitive to even very small changes of the modulus, the values of the Riemann matrix element B_{11} are used in Eqs. (2.36) and (2.37). Fig. 2.9 shows the values of m as function of B_{11}. The figure also shows the limits of the different parameters for the classification of the wave shapes as used in Fig. 2.5: e.g. a cnoidal-like wave is obtained for $0.95<m<0.99$ and $2.676<B_{11}<3.463$.

Tab. 2.2: Table of parameters m, q, B_{11} and $K(q)$ for the one degree-of-freedom θ-function. Selected values from Osborne (2011 with i the number of the line in the original table.

i	m	q	B_{11}	$K(q)$
1	0.1022051404	0.006737946999	10.00000000	1.613417366
55	0.8032531310	0.1002588437	4.600000000	2.264660987
63	0.9150716364	0.1495686192	3.800000000	2.655210307
100	1.000000000	0.9512294245	0.1000000000	98.69604401

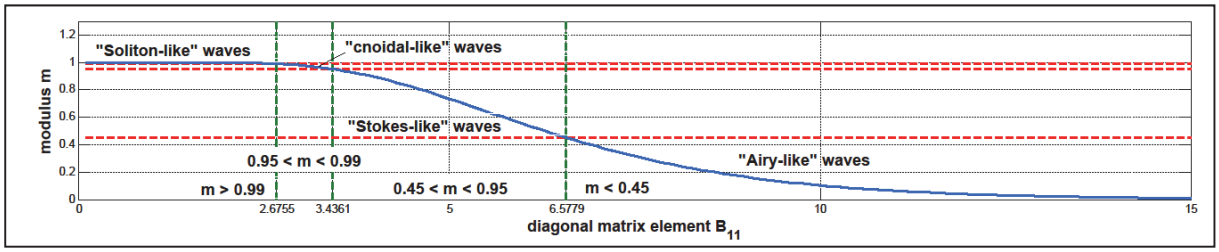

Fig. 2.9: Modulus m of the θ-function as function of the Riemann matrix element B_{11}.

2.4.4 Riemann Θ-functions and nonlinear wave-wave interactions

Cnoidal waves which are generated by the Jacobi θ-function representation in Eq. (2.35) are solutions to the KdV equation and therefore are physical representations of stable nonlinear shallow-water waves. They are strongly depending on the values for water depth h (represented by the coefficient λ), wavelength L and the nonlinearity which is represented by the modulus m or the Riemann matrix element B_{11}. If near-shore 2D sea states shall be represented by the superposition of $N>1$ of such nonlinear cnoidal waves (denoted as *nonlinear spectral basic components*), then mutual wave-wave interactions (denoted as *primary interactions*) between each of these N waves occur and affect the resulting free surface. Furthermore, if $N>2$ then more complex additional mixed-term interactions (denoted as *secondary interac-*

tions) have to be considered that are caused by the mutual interactions of cnoidal waves and the primary interactions of other cnoidal waves and by the mixed interactions between different secondary interaction terms. Finally, the free surface $\eta(x,t)$ can be regarded to be a linear superposition of the underlying cnoidal waves $\eta_{cn,i}(x,t)$ on the one hand, and their primary and secondary interactions on the other hand. The sum of all interactions is denoted as *interaction term* $\eta_{int}(x,t)$:

$$\eta(x,t) = \underbrace{\sum \eta_{cn,i}(x,t)}_{\substack{\text{linear superposition}\\ \text{of cnoidal waves}}} + \underbrace{\eta_{int}(x,t)}_{\substack{\text{nonlinear interactions}\\ \text{between the cnoidal waves}}}. \tag{2.7}$$

The Riemann Θ-functions (Theta-functions) as introduced by Riemann (1857allow the superposition of Jacobi θ-functions (single cnoidal waves) and the calculation of the nonlinear primary and secondary interaction term by simply exchanging the variables in the exponent of Eq. (2.36) against vectors of length N and a NxN *Riemann,* or *period matrix* as shown in Eq. (2.39) (Osborne, 2010). Finally, the obtained function Θ_N is a linear superposition of the *Riemann spectral term* $\Theta_{N,cn}(x,t)$ that contains the N cnoidal waves in terms of θ-functions and the *Riemann interaction term* $\Theta_{N,int}(x,t)$ that contains all resulting $J=((2M+1)^N)/2-N$ nonlinear interactions (including the $N(N-1)$ primary interactions):

$$\Theta_N(x,t) = 1 + 2\sum_{\mathbf{n}=1}^{M} e^{-\frac{1}{2}\mathbf{n}\mathbf{B}\mathbf{n}^T + i\mathbf{n}\mathbf{k}x - i\mathbf{n}\boldsymbol{\omega}t + i\mathbf{n}\boldsymbol{\varphi}}, \tag{2.39}$$

$$\Theta_N(x,t) = 1 + 2\sum_{\mathbf{n}=-M}^{0^-} e^{-\frac{1}{2}\mathbf{n}\mathbf{B}\mathbf{n}^T} \cos\left[\mathbf{n}\mathbf{k}x - \mathbf{n}\boldsymbol{\omega}t + \mathbf{n}\boldsymbol{\varphi}\right], \tag{2.40}$$

with

$$\begin{aligned} \Theta_N(x,t) &= \theta_{cn,1}(x,t) + \ldots + \theta_{cn,N}(x,t) &&+ \theta_{int,1}(x,t) + \ldots + \theta_{int,J}(x,t),\\ &= \underbrace{\Theta_{N,cn}(x,t)}_{\substack{\text{sum of N cnoidal waves}\\ \text{(Riemann spectral term)}}} &&+ \underbrace{\Theta_{N,int}(x,t)}_{\substack{\text{sum of } J \text{ nonlinear interactions}\\ \text{(Riemann interaction term)}}}, \end{aligned} \tag{2.41}$$

where $\mathbf{n} = [n_1, n_2, \ldots, n_N]$ are the integers of the sum, $\mathbf{k} = [k_1, k_2, \ldots, k_N]$ the wave numbers, $\boldsymbol{\omega} = [\omega_1, \omega_2, \ldots, \omega_N]$ the angular frequencies and $\boldsymbol{\varphi} = [\varphi_1, \varphi_2, \ldots, \varphi_N]$ the phases of the N cnoidal waves. The interactions are introduced by the NxN Riemann matrix $\mathbf{B}$. The diagonal matrix elements B_{ii} (with B_{ij}, $i=1,2,...,N$, $j=1,2,...,N$ and $i=j$) represent the N cnoidal basic components, the off-diagonal elements B_{ij} with $i \neq j$ represent the $N(N-1)$ primary interactions. In case of just one single cnoidal wave ($N=1$) no interactions occur and the Riemann Θ-function in Eq. (2.39) reduce to the Jacobi θ-function in Eq. (2.36).

The free surface $\eta(x,t)$ that is generated by the nonlinear superposition of N cnoidal waves $\eta_{cn,i}(x,t)$ is then obtained from

$$\eta(x,t) = \frac{2}{\lambda}\frac{\partial^2}{\partial x^2}\ln\Theta_N(x,t). \tag{2.42}$$

For the numerical implementation and calculation of the Θ-function the vectors and the matrix in the exponents in Eq. (2.39) have to be written in terms of variables which leads to N nested summations (Osborne, 2010):

$$\Theta_N(x,t) = 1 + 2\sum_{l_1=1}^{M}\sum_{l_2=1}^{M}\ldots\sum_{l_N=1}^{M}\exp\left[i\sum_{i=1}^{N} n_i X_i(x,t) + \frac{1}{2}\sum_{i=1}^{N}\sum_{j=1}^{N} n_i n_j B_{ij} \right], \tag{2.43}$$

with $X_i(x,t) = k_i x - \omega_i t + \varphi_i$. As can be seen from the equation, the number of required summations is N^{2M}, each for the whole series over space x and/or time t. Due to this extremely high numerical expenses the practical application of this approach is strongly connected with the development of fast computers within the last years. Further details for the numerical implementation of this multiple summations for practical applications are given in section 3.

The off-diagonal Riemann matrix elements $B_{ij}=B_{ji}$ with $i \neq j$ are obtained from the wave number of the two interacting cnoidal waves (Osborne, 2010):

$$B_{ij} = B_{ji} = \ln\left[\left(\frac{k_i - k_j}{k_i + k_j} \right)^2 \right], \quad i \neq j \tag{2.44}$$

Unfortunately, as will be shown in chapter 3, the nested summations cause mixed terms with primary and secondary interactions so that for $N>2$ the nonlinear mutual interactions between two specified cnoidal waves (the primary interactions) cannot be calculated separately. Another result from the multiple summations is that during the nonlinear interaction of two waves with wave numbers k_i, k_j or frequencies f_i, f_j the *subharmonic* (k_i-k_j or f_i-f_j) and the *superharmonic* (k_i+k_j or f_i+f_j) components are added automatically within the Θ-functions (for a simple example with two cnoidal waves see Fig. 2.10, for details see chapter 3).

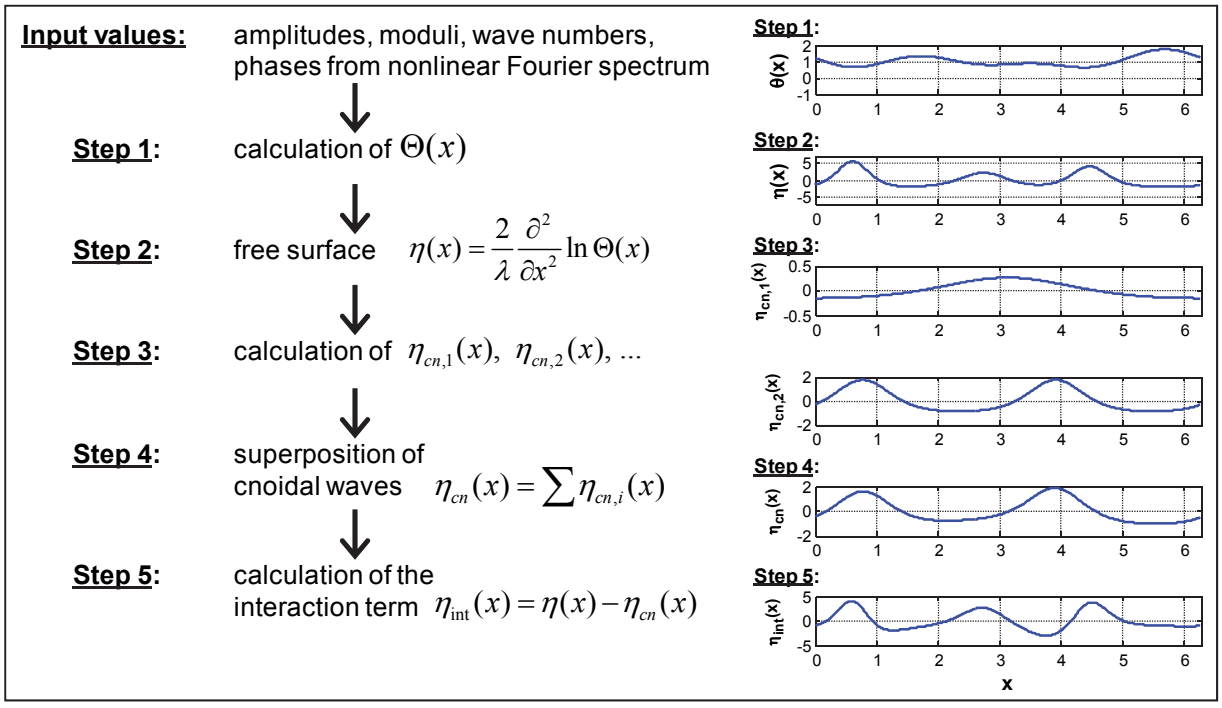

Fig. 2.10: Overview on the procedure of calculation of the cnoidal basic components $\eta_{cn,i}(x)$, the nonlinear interaction term $\eta_{int}(x)$ and the free surface $\eta(x)$.

The diagonal elements B_{ii} of the *NxN* Riemann matrix have to be known before the inverse transform, because they characterize amplitude and nonlinearity of the *N* cnoidal waves $\eta_{cn,i}(x,t)$ that are to be calculated and superposed linearly. The calculated free surface $\eta(x,t)$ from Eq. (2.42) contains both the cnoidal waves $\eta_{cn,i}(x,t)$ and their nonlinear interactions $\eta_{int}(x,t)$. Therefore, the interaction term can be obtained by simple subtraction of the cnoidal waves from the free surface:

$$\eta_{int}(x,t) = \eta(x,t) - \sum \eta_{cn,i}(x,t)\,. \tag{2.45}$$

Finally, Fig. 2.10 shows the procedure for the calculation of the free surface $\eta(x,t)$, the cnoidal basic components $\eta_{cn,i}(x,t)$ and the nonlinear interaction term $\eta_{int}(x,t)$. As can be seen from this example, the amplitudes of the interaction terms can reach the order of magnitude of the cnoidal wave amplitudes and therefore – as shown in the example - can govern the final shape of the free surface, i.e. they cannot be neglected a priori without verification.

2.4.5 Cnoidal waves in terms of μ-functions

Another way to describe the free surface of nonlinearly interacting waves is the generalisation of the Fourier series in terms of μ-functions (mu-functions). In this formulation the original data $\eta(x,t)$ is assumed to be composed of linearly superposed nonlinear hyperelliptic functions $\mu_j(x;x_o,t)$ (Osborne, 2010):

$$\lambda\eta(x,t) = -E_1 + \sum_{j=1}^{N}\Big[2\mu_j(x;x_0,t) - E_{2j} - E_{2j+1}\Big], \tag{2.46}$$

with λ as given in Eq. (2.3), E_{2j}, E_{2j+1} are constant eigenvalues of the main spectrum of the periodic inverse scattering transform of the KdV equation (2.2) (see chapter 3 for details) and x_o is referred to as an arbitrary base point in the periodic interval $0 \le x_o \le L_w$. Further details on the calculation and application of the μ-functions are given in chapter 3.

When Osborne started to implement practical applications of the inverse scattering transform in the early 1980s he used these μ-functions for the decomposition of the original data. Since 1995 he started to work on the representation in terms of Riemann Θ-functions as described in the previous sections, but only few papers were published on the results of his work. When the work within this thesis was begun, the μ-functions represented the state-of-the-art in the decomposition of nonlinear shallow-water waves. Finally, in Osborne (2010) the results of the research on the Θ-functions were finally published in more detail, showing that this new approach represents a substantial advance in the state-of-the-art related to the spectral decomposition of nonlinear water waves. Therefore, the focus of this thesis moved towards the application of the θ-/Θ-functions as the spectral basic components of the KdV-NLFT. Nevertheless, large parts of the numerical implementations are identical for μ- and Θ-functions so that further details of the μ-function approach can be found in chapter 3.

2.5 Nonlinear KdV-based Fourier transform (KdV-NLFT): The periodic inverse scattering transform (PIST) of the KdV equation

The *inverse scattering transform* (IST) or *nonlinear Fourier transform* (NLFT) is a mathematical method to solve nonlinear partial differential equations (Zabusky & Kruskal, 1965). If it is applied with periodic boundary conditions (as here in this thesis), then it is denoted as *periodic inverse scattering transform* (PIST). Among the equations that can be solved by the IST are the Korteweg-deVries (KdV), the Kadomtsev-Petviashvili (KP) and the nonlinear Schroedinger (NLS) equation. The IST can be regarded as a general extension of the conventional linear Fourier transform (FT) to the analysis of nonlinearly interacting waves (Ablowitz et al., 1974; Ablowitz & Segur, 1981) although the mathematical background of the IST is much more complex and the physical approach is completely different from that of the conventional FFT. In case of only linear waves without wave-wave interactions, the results of the nonlinear IST reduce to those of the ordinary linear FT (still with much more mathematical complexity and numerical effort).

Within this thesis, the PIST is applied for the solution of the KdV equation that governs the propagation of waves in shallow-water with relative water depths $kh \leq 1.36$. Therefore, the method is denoted as KdV-NLFT. For a detailed overview on the history and applications of the IST for the analysis of ocean waves see Osborne (2010).

2.5.1 The inverse KdV-NLFT (iKdV-NLFT)

The inverse KdV-NLFT provides the superposition (the free surface $\eta(x,t)$) of N cnoidal waves $\eta_{cn,i}(x,t)$ and their nonlinear interactions $\eta_{int}(x,t)$. If the cnoidal waves $\eta_{cn,i}(x,t)$ are given by Jacobi θ-functions (see section 2.4.2), then the application of Riemann Θ-functions provides the nonlinear superposition $\eta_{int}(x,t)$ (see section 2.4.4), and finally the free surface $\eta(x,t)$. The procedure is presented in Fig. 2.1 and Fig. 2.10. A detailed description of the implemented numerical algorithms, examples and a first verification of the implemented code and the method are given in chapter 3. The application to different physical shallow-water wave problems is presented in chapters 4 and 5.

The spectral cnoidal basic components for the nonlinear superposition have to be defined before the application of the iKdV-NLFT. For arbitrary time or space series the moduli m_i, frequencies f_i or wave numbers k_i, angular frequencies ω_i and phases φ_i are chosen randomly. If the direct KdV-NLFT (dKdV-NLFT) has been applied to a given original signal $\eta(x,t)$before, then the inverse transform can reproduce the original signal by superposition of the underlying spectral cnoidal basic components and their nonlinear interactions by using the spectral parameters provided by the dKdV-NLFT. If the data from the dKdV-NLFT is filtered in frequency or wave number range before applying the iKdV-NLFT then not only the deleted spectral components are removed in the calculated data $\eta(x,t)$, but also their primary and secondary interactions, including their subharmonics and superharmonics. Therefore, by application of this *nonlinear filtering,* additional frequency components *outside* the applied filter range in the super- and subharmonic range are eliminated from the data. Examples for super- und subharmonic wave components are given in chapter 3, and examples for the nonlinear filtering can be found in Osborne (2010). The essential advantage of the KdV-NLFT in comparison to the conventional FFT is its ability to distinguish *explicitly* between the nonlinear

spectral basic components and their nonlinear interactions. The latter are strongly dependent on the local phase differences between the cnoidal waves, and are therefore local properties of the original data $\eta(x,t)$. By application of the direct KdV-NLFT the interactions are eliminated from the original data and the underlying cnoidal waves $\eta_{cn,i}(x,t)$ are revealed. In a next step, the evolution of these basic components in *time and/or space* provides the phase information at position $x+\Delta x$ and/or time $t+\Delta t$. Finally, in the inverse KdV-NLFT these evolved cnoidal waves can be superposed with their new local interactions $\eta_{int}(x+\Delta x,\ t+\Delta t)$. This procedure is illustrated in Fig. 2.11. The details of the numerical implementation are provided in chapter 3.

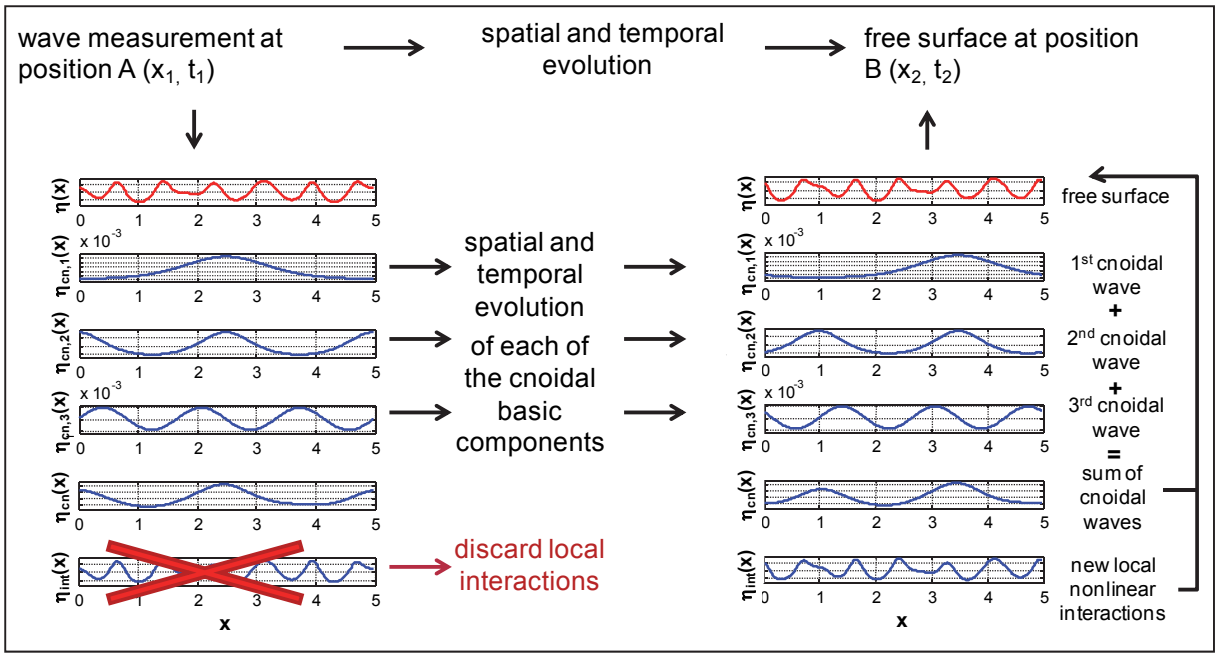

Fig. 2.11: Application of the KdV-NLFT for the temporal and spatial evolution of the original data.

2.5.2 The direct KdV-NLFT (dKdV-NLFT)

In the direct KdV-NLFT (dKdV-NLFT or *direct scattering transform* (DST)) a given original signal $\eta(x,t)$ is decomposed into a set of N cnoidal waves $\eta_{cn,i}(x,t)$ such that the nonlinear superposition of these cnoidal waves in the inverse KdV-NLFT returns the original data $\eta(x,t)$. The interaction term $\eta_{int}(x,t)$ is not provided by the dKdV-NLFT, but can be determined by subsequent application of the Riemann Θ-functions within the nonlinear iKdV-NLFT (see sections 2.4.4 and 2.5.1).

The underlying spectral structure of this set of cnoidal-wave basic components cannot be obtained (except for $N=1$) directly from the free surface $\eta(x,t)$. Therefore the original data is subject to a mathematical procedure called the solution of the Schroedinger eigenvalue problem that finally provides the so-called Floquet discriminant $\Delta(E)$ of the original data as the trace of the monodromy matrix. This procedure is constant for all kinds of input data, but the results are strongly depending on the characteristics of $\eta(x,t)$ (see Fig. 2.12). From the Floquet discriminant $\Delta(E)$ the number N of the determined cnoidal waves, their moduli, amplitudes, wave numbers or frequencies and phases are determined directly. Based on the determined values of m_i, the cnoidal waves can be separated into oscillatory waves (with moduli $m_i \leq 0.99$) with the values a_i, k_i or f_i and φ_i or solitons with A_j, K_j or F_j and Φ_j (for $m_i > 0.99$).

In order to better distinguish between oscillatory waves and solitons, the wave parameters of the latter are denoted by capital letters.

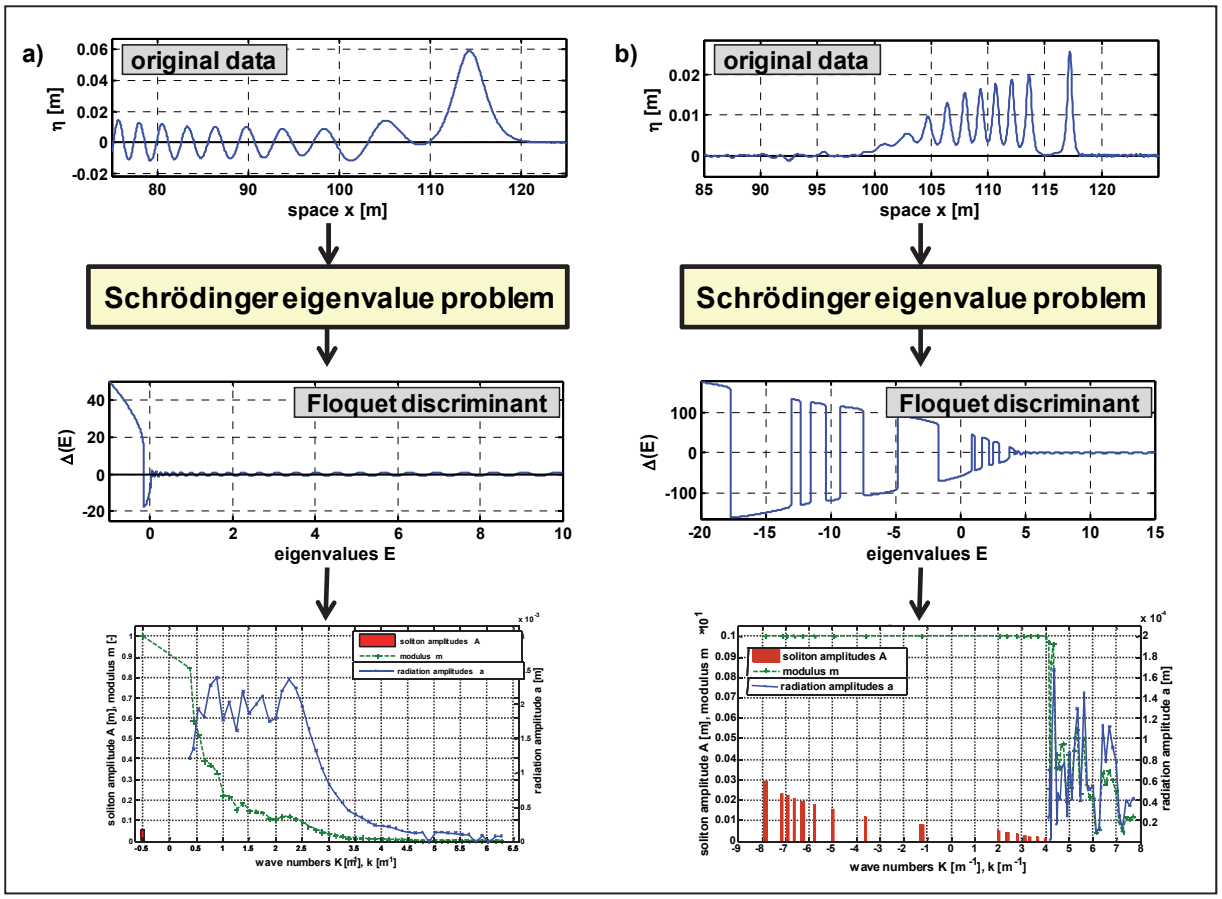

Fig. 2.12: Examples for individual solutions of the Schroedinger eigenvalue problem within the direct KdV-NLFT for different data: a) a solitary wave and some oscillatory waves provide a nonlinear spectrum with only one soliton and oscillatory waves, b) a train of solitons that evolved from a bore provides a soliton-dominated nonlinear spectrum.

The nonlinear spectrum (see the last row in Fig. 2.12a, b) illustrates the analysis results in a representation that is very close to the conventional FFT spectrum. The nonlinear spectrum consists of the radiation spectrum (right part) with the oscillatory waves and the soliton spectrum (left part). To avoid mixing of oscillatory and solitary waves in the spectrum, the latter are plotted with negative frequencies F or wave numbers K. The values of F and K have no physical meaning since $F=1$ and $K=1$ applies for all solitons in the spectrum, but they sort the amplitudes within the spectrum. The nonlinear character of each cnoidal basic component $\eta_{cn,i}(x,t)$ is defined by its modulus m_i. With increasing values of k_i and f_i the relative water depth h/L_i for each oscillatory component increases and therefore the nonlinearity decreases with increasing k_i or f_i, and the trend of the modulus m_i in general is decreasing. Details of the mathematical background are given in section 2.5.3, the numerical implementation and several examples are given in chapter 3. Further details are given in Osborne (2010).

2.5.3 Mathematical background of the KdV-NLFT

The *inverse scattering transform (IST) of the KdV equation* or *the KdV-based nonlinear Fourier transform (KdV-NLFT)* can be described by a generalization of the Fourier series in terms of the hyperelliptic μ-functions. The original data $u(x,t)$ is decomposed into linearly superposed hyperelliptic functions $\mu_j(x;x_o,t)$. 'The general spectral solution to the periodic KdV equation [(2.2)] may be written as a *linear superposition of nonlinearly interacting, nonlinear waves* that are referred to as *hyperelliptic functions*, $\mu_j(x;x_o,t)$' (Osborne, 2010). This is represented by the first so-called *trace formula of the KdV equation* (Dubrovin & Novikov, 1975; Flaschka & McLaughlin, 1976; McKean & Trubowitz, 1976; Osborne & Bergamasco, 1985; 1986; Osborne, 1994):

$$\lambda\eta(x,t) = u(x,t) = -E_1 + \sum_{j=1}^{N}\left[2\mu_j(x;x_0,t) - E_{2j} - E_{2j+1}\right], \tag{2.47}$$

with λ as given in Eq. (2.3), and the E_{2j}, E_{2j+1} are constant eigenvalues of the main spectrum of the periodic inverse scattering transform of the KdV equation (2.2): The variable x_o is referred to as an arbitrary base point in the periodic interval $0 \le x_o \le L_{sp}$. The μ_j are the nonlinear Fourier (oscillation) modes of the periodic KdV equation and they are, thereby, analogous to the sine waves of the linear Fourier analysis (Osborne, 1995a).

For a better understanding of the nature of the KdV-NLFT and the analogy to the ordinary, conventional Fourier transform, note the following facts (Osborne & Segre, 1990):

- The amplitudes of the spectral nonlinear Fourier components $\mu_j(x,t)$ (which are given by the j open spectral bands of the Floquet discriminant, see section 3.2.1) are constants in time because the KdV-NLFT provides a time-domain analysis (as the conventional Fourier transform).
- In the absence of mutual nonlinear wave-wave interactions between the basic components, each nonlinear spectral component $\mu_j(x,t)$ reduces to the cnoidal wave $\eta_{cn}(x,t)$. Absence of nonlinear interactions is given (i) if there is only one wave component in the original data $\eta(x,t)$ or (ii) if the original data is composed by linear sinusoidal waves that show no wave-wave interactions.
- For the small-amplitude limit the trace formula in Eq. (2.47) reduces to an ordinary linear Fourier series, since in this limit the following expression applies

  $$\mu_j(x,t) \sim a_j \cos\left(k_j x - \omega_j t\right) \qquad \text{(for the small-amplitude limit)}, \tag{2.48}$$

  and the μ-function representation may therefore be interpreted as a nonlinear spectral Fourier representation for general solutions of the periodic KdV equation.

Considering these facts, Eq. (2.47) can 'be called a nonlinear Fourier series with the hyperelliptic functions $\mu_j(x,t)$ as nonlinear oscillation modes of the periodic KdV equation. The latter can be regarded as nonlinear counterpart to the sinusoidal waves in the linear Fourier series; they are non-sinusoidal in shape and implicitly contain the nonlinear dynamics of the soliton and radiation solutions of periodic KdV' (Osborne, 1995a).

The spatial evolution of the hyperelliptic functions $\mu_j(x;x_o,t)$ in Eq. (2.47) is governed by the following coupled ordinary differential equations (ODEs) for a fixed time $t=0$:

$$\frac{d\mu_j}{dx} = \frac{2i\sigma_j R^{1/2}(\mu_j)}{\prod_{\substack{k=1 \\ j\neq k}}^{N}(\mu_j - \mu_k)} \tag{2.49}$$

and

$$R(\mu_j) = \prod_{k=1}^{2N+1}(\mu_j - E_k)\,. \tag{2.50}$$

The variable $\sigma=\pm 1$ specifies the signs of the square root of the function $R(\mu_j)$. The nonlinear functions $\mu_j(x,0)$ are located on two-sheeted Riemann surfaces, each specified by the signs σ_j. The branch points that connect the surfaces (i.e. the points where the Floquet discriminant intersects the values ± 1, see Fig. 3.15) are called *band edges* E_{2j} and E_{2j+1}. The $\mu_j(x,0)$ lie in the intervals $E_{2j} \leq \mu_j \leq E_{2j+1}$, i.e. inside *open bands*, and oscillate between these limits as x and t vary (see Fig. 3.15). The distance between the band edges defines the oscillation amplitude of the hyperelliptic functions (see section 3.2.1). When a $\mu_j(x,0)$ reaches a band edge (either E_{2j} or E_{2j+1}) then the associated index σ_j changes its sign and the motion moves to the other Riemann sheet (Osborne, 1994). The fact that the motion lies on two Riemann sheets, together with the strong, stiff nonlinear coupling which occurs among the μ_j presents considerable difficulties in numerical integrations of Eq. (2.47) (Osborne & Segre, 1990). These difficulties have been largely circumvented by the methods used in Osborne (1994) for the time series analysis of nonlinear wave trains.

The *temporal evolution* of the μ_j is governed by the following ODEs:

$$\frac{d\mu_j}{dt} = 2\left[-u(x,t) + 2\mu_j\right]\frac{d\mu_j}{dx} \tag{2.51}$$

or

$$\frac{d\mu_j}{dt} = 2\left[-\lambda\eta(x,t) + 2\mu_j\right]\frac{d\mu_j}{dx}\,, \tag{2.52}$$

where $d\mu_j/dx$ is given by Eq. (2.49) and $u(x,t)$ is given by Eq. (2.47). The Eq. (2.51) is self-contained (Osborne & Segre, 1990).

Osborne and Segre (1990) denote the equations given in Eq. (2.49) to Eq. (2.52) as the defining equations for the μ_j. These ODEs for space and time evolve the hyperelliptic functions in space and time. The idea is to decompose the given original data for a given time $t=0$ (Cauchy problem for the space series) or a given position $x=0$ (boundary value problem for a given time series) into hyperelliptic functions for that given time or position. This procedure is called the direct scattering transform (DST) and analogue to the direct Fourier transform. The determined basic components μ_j then are developed in time and space respectively using the evolution equations Eq. (2.49) to Eq. (2.52). In the next step, the evolved hyperelliptic basic components are superposed and the free surface for time $t\neq 0$ or position $x\neq 0$ is determined. This latter procedure is called the inverse scattering transform (IST). Osborne (1993a, 1994, 1995a and 2010) give numerical methods for the computation of the nonlinear oscillation

modes $\mu_j(x,0)$ of the KdV equation at the particular time $t=0$ or alternatively $\mu_j(0,t)$ at the particular spatial position $x=0$. The presented numerical methods are denoted as the nonlinear Fourier analysis procedures for space or time series (Osborne, 1995a).

The periodic direct scattering transform (PDST) decomposes the original data $\eta(x,t)$ into nonlinear hyperelliptic functions $\mu_j(x;x_o,t)$ and provides the spectral information in terms of the main spectrum that contains the constant eigenvalues E_i with $1 \le i \le 2N+1$, and the auxiliary spectrum that contains the hyperelliptic functions $\mu_j(x_o;x_o,t)$ and the Riemann signs $\sigma_j=\pm 1$ with $1 \le j \le 2N$. After these information are given, the periodic inverse scattering transform (PIST) evolves the nonlinear hyperelliptic basic components $\mu_j(x;x_o,t)$ to the required time t or the position x and superposes them to obtain the free surface $\eta(x,t)$ for that time and position. Finally, this procedure provides solutions to the space-like or time-like KdV equations (2.2) or (2.5).

Since the temporal evolution of the μ_j in Eqs. (2.51) and (2.52) contain the spatial evolution $d\mu_j/dx$, Osborne and Segre (1990) concentrate on this procedure and state that 'once the problems related to the spatial integration are solved, the temporal integration follows in a straightforward manner' by application of Eq. (2.51). For the solution of the direct spectral problem of the KdV equation the second-order Schroedinger eigenvalue problem has to be solved. The Schroedinger eigenvalue problem usually is associated with quantum mechanics problems and therefore some notations that are used here are derived from quantum mechanics. The term *radiation* which denotes the oscillatory wave components is an example for that. In quantum mechanics particles and radiation can be measured. In water wave mechanics, these notations refer to solitons ('particles') and oscillatory waves ('radiation') respectively. Another example is the term 'potential'. The given original time or space series $\eta(x,t)$ is denoted as 'potential function', where potential might be any kind of energy in quantum mechanics.

The *Schroedinger eigenvalue problem* is given by Osborne (2010) as

$$\psi_{xx} + \left[\lambda \eta(x) + k^2 \right] \psi = 0, \quad (k^2 = E) \tag{2.53}$$

where the potential function, $\eta(x)=\eta(x,0)$, is the solution to the sKdV equation (2.2) at arbitrary time $t=0$, $\lambda = \alpha/(6\beta)=3/(2h^3)$ from Eq. (2.3) is the scaling factor of the free surface in $u(x,t)=\lambda\eta(x,t)$, k is the spectral wave number and E is the 'energy'. Due to the periodic spatial boundary conditions, it is assumed that $\eta(x,t)=\eta(x+L_w,t)$, with L_w the spatial period or width of the analysis window (Osborne, 1994). If the initial potential $\eta(x,t)$ is given, then the Schroedinger eigenvalue problem (2.53) is to be solved for $\Psi(x,E)$ and its properties (Osborne, 1995a).

A generalized eigenvalue problem is described as the search for a vector $\bar{\mathbf{x}}$ that satisfies

$$\mathbf{A}\bar{\mathbf{x}} = \lambda_e \, \mathbf{B}\bar{\mathbf{x}}, \tag{2.54}$$

with **A**, **B** quadratic matrices of type (n,n). The variable λ_e is called the eigenvalue, $\bar{\mathbf{x}}$ is the eigenvector. If **B**=**E** with **E** an n-column unit matrix, then the generalized eigenvalue problem is reduced to the characteristic eigenvalue problem

$$\mathbf{A}\bar{\mathbf{x}} = \lambda_e \bar{\mathbf{x}} \quad \text{or} \quad \left(\mathbf{A} - \lambda_e \, \mathbf{E}\right)\bar{\mathbf{x}} = 0\,. \tag{2.55}$$

The Eq. (2.55) describes a homogenous linear system of equations with a non-trivial solution $\bar{\mathbf{x}} \neq 0$ in case of

$$\det\left(\mathbf{A} - \lambda_e \, \mathbf{E}\right) = 0\,, \tag{2.56}$$

$$\det\left(\mathbf{A} - \lambda_e \, \mathbf{E}\right) = \begin{vmatrix} a_{11} - \lambda_e & a_{12} & a_{13} & \cdots & a_{1n} \\ a_{21} & a_{22} - \lambda_e & a_{23} & \cdots & a_{2n} \\ \vdots & \vdots & \vdots & \vdots & \vdots \\ a_{n1} & a_{n2} & a_{n3} & \cdots & a_{nn} - \lambda_e \end{vmatrix}, \tag{2.57}$$

$$\det\left(\mathbf{A} - \lambda_e \, \mathbf{E}\right) = P_n(\lambda_e) = (-1)^n \lambda_e^n + a_{n-1}\lambda_e^{n-1} + \cdots + a_1\lambda_E + a_0 = 0. \tag{2.58}$$

The determinant of the eigenvalue problem is written as the characteristic polynomial $P_n(\lambda_e)$. The roots (the points at which the polynomial becomes zero) are the eigenvalues of the matrix **A** (Bronstein et al., 2001).

The procedure to solve the periodic scattering problem given in Eq. (2.53) starts with choosing a basis of eigenfunctions $\phi(x;x_o,k)$ such that $\phi(x_o;x_o,k)=1$, $\phi_x(x_o;x_o,k)=ik$, $\phi^*(x_o;x_o,k)=1$, $\phi_x^*(x_0;x_0,k)=-ik$. The superscript * denotes the complex conjugate, the subscript x the partial derivative and x_o is an arbitrary base point in the interval $0 \leq x_o \leq L_w$. If ϕ is a complex function $\phi=x+iy$, then its complex conjugate ϕ^* is defined as $\phi^*=x-iy$. According to the periodic spatial boundary conditions for the free surface wave train $\eta(x,t)$, one assumes that the eigenfunctions one spatial period to the right, $\phi(x+L_w;x_0,k)$, are linear combinations of the solutions $\phi(x;x_0,k)$ (Osborne, 1994, 2010). The matrix $\mathbf{\Phi}(x;x_o,k)$ of independent eigenfunctions is given as

$$\mathbf{\Phi}(x;x_0,k) = \begin{pmatrix} \phi & \phi_x \\ \phi^* & \phi_x^* \end{pmatrix}. \tag{2.59}$$

Using the periodic spatial boundary conditions, the matrix $\mathbf{\Phi}(x;x_o,k)$ can be written as

$$\mathbf{\Phi}\left(\mathrm{x} + \mathrm{L_w}; \mathrm{x_o}, \mathrm{k}\right) = \mathbf{S}\left(\mathrm{x_o}, \mathrm{k}\right) \mathbf{\Phi}\left(\mathrm{x}; \mathrm{x_o}, \mathrm{k}\right), \tag{2.60}$$

with $\mathbf{S}(x_o,k)$ the so-called monodromy matrix and a, b complex numbers (Osborne, 1994, 2010):

$$\mathbf{S}(x_o,k) = \begin{pmatrix} a & b \\ b^* & a^* \end{pmatrix}. \tag{2.61}$$

The function of the monodromy matrix **S** is to carry the solutions of Eq. (2.53) one period from the point x to the point $x+L_w$ (Osborne, 2010).

The main spectrum of the direct scattering transform consists of the set of real constants $\{E_k\}$, $(1 \leq k \leq 2N+1)$, where N the integer number of degrees of freedom (which is the number of nonlinear hyperelliptic oscillation modes and the number of the nonlinear basic components of the spectral decomposition) of a particular solution to the KdV equation (Osborne, 2010). The $\{E_k\}$ are solutions to the relation

$$\left|a_R(E)\right| = 1 \quad \text{(with subscript 'R' = 'the real part of')}. \tag{2.62}$$

The auxiliary spectrum $\{\mu_j(x_o,t)\}$, with $(1 \le j \le N)$, is described by the solution to

$$(a_I + b_I)(E) = 0 \quad \text{(with subscript 'I' = 'the imaginary part of')}. \tag{2.63}$$

The vector $\{E_k\}$ consists of the eigenvalues corresponding to Bloch eigenfunctions which are either periodic or anti-periodic on the period L_w. The 'signs' of the spectrum are given by the Riemann sheet indices σ_j as

$$\sigma_j = \operatorname{sgn}\left[b_R(E)\right]_{\mu_j} = \pm 1 \tag{2.64}$$

with $\operatorname{sgn}(\chi)=\chi/|\chi|$ that gives the signature of the arbitrary function χ (Osborne, 1994).

The phase information for the hyperelliptic function representation of KdV, $\mu_j(x,t)$, can be determined from the auxiliary spectrum $\{\mu_j;\ \sigma_j\}$ (Osborne, 1993a) by application of algebraic-geometric loop integrals (see Osborne, 2010). The complete spectrum $\{E_k\};\ \{\mu_j;\ \sigma_j\},(1 \le k \le 2N+1;\ 1 \le j \le N)$, constitutes the direct scattering transform (DST) of a wave train $\eta(x,t)$ with N degrees of freedom. These spectral components are the relevant information that has to be computed from a space or time series in order to obtain the nonlinear spectrum.

For the numerical implementation of these algorithms Osborne (1995a, 2010) consider a different basis of solutions (c,s) of the Schroedinger eigenvalue problem in Eq. (2.53) such that (Flaschka & McLaughlin, 1976):

$$\begin{pmatrix} (x_o) & c'(x_o) \\ s(x_o) & s'(x_o) \end{pmatrix} = \begin{pmatrix} 1 & 0 \\ 0 & 1 \end{pmatrix}. \tag{2.65}$$

'The symbol 'c' might be read as 'cosine' and the 's' as 'sine', but this identification is not rigorous, just informative' (Osborne, 2010).

The Wronskian $W(c,s)=1$ and therefore (c,s) is a basis set of Eq. (2.53). A system of n solutions $(y_1, y_2, ..., y_n)$ of a homogeneous linear differential equation is called a basic set if these functions are linearly independent. If the system is linearly independent, then the linear combination $C_1y_1+C_2y_2+...+C_ny_n$ does vanish identically, this means for all values of x in the considered interval, only if $C_1=C_2=...=C_n=0$. The solutions $(y_1, y_2, ..., y_n)$ in linear homogenous differential equations are a basic set, if their Wronskian determinant

$$W = \begin{vmatrix} y_1 & y_2 & \cdots & y_n \\ y_{1'} & y_{2'} & \cdots & y_{n'} \\ \cdots & \cdots & \cdots & \cdots \\ y_1^{n-1} & y_2^{n-1} & \cdots & y_n^{n-1} \end{vmatrix} \tag{2.66}$$

is different from zero (Bronstein et al., 2001). So if the Wronskian of the solutions of the Schroedinger eigenvalue problem is $W(c,s)=1$, then the solutions are linearly independent and provide a basis set.

In analogy to the monodromy matrix **S** in Eq. (2.60), the matrix **α** carries the solution matrix from point x to point $x+L_w$:

$$\begin{pmatrix} c(x+L_w) & c'(x+L_w) \\ s(x+L_w) & s'(x+L_w) \end{pmatrix} = \begin{pmatrix} \alpha_{11} & \alpha_{12} \\ \alpha_{21} & \alpha_{22} \end{pmatrix} \begin{pmatrix} (x_0) & c'(x_0) \\ s(x_0) & s'(x_0) \end{pmatrix}, \tag{2.67}$$

with **α** determined from the monodromy matrix **S** by the similarity transformation

$$\boldsymbol{\alpha} = \mathbf{Q}^{-1}\ \mathbf{S}\ \mathbf{Q}, \text{ with } \mathbf{Q} = \begin{pmatrix} 1 & ik \\ 1 & -ik \end{pmatrix}. \tag{2.68}$$

The matrix **α** is the monodromy matrix in the *(c,s)* representation. It may be regarded as the fundamental matrix **Φ** of the periodic spectral theory for the KdV equation in Eq. (2.60) because it contains all required spectral information about the KdV equation in the wave number domain. The main spectrum of the KdV equation consists of the E_k ($1 \le k \le 2N+1$) which are the eigenvalues of the Bloch eigenfunction solutions of the nonlinear Schroedinger equation for a considered period L_w (Osborne, 1994, 1995a). The auxiliary spectrum is defined as the eigenvalues for which the eigenfunctions *s(x)* have the fixed boundary conditions $s_0(x_o+L_w)=s(x_o)$. From this the special spectral definitions may be summarized (Osborne & Bergamasco, 1985; Osborne et al., 1986; Osborne, 1995a, 2010):

Main spectrum $\{E_k\}$:
$$\frac{1}{2}\left(\alpha_{11}+\alpha_{22}\right) = \frac{1}{2}\left(S_{11}+S_{22}\right) = \pm 1, \tag{2.69}$$

Auxiliary spectrum $\{\mu_j\}$:
$$\alpha_{21} = -\frac{i}{2k}\left(S_{11}+S_{12}-S_{21}-S_{22}\right) = 0, \tag{2.70}$$

Riemann sheet indices $\{\sigma_j\}$:
$$\begin{aligned} \sigma_j &= \operatorname{sgn}\left[\alpha_{11}(E)-\alpha_{22}(E)\right]_{E=\mu_j} \\ &= \operatorname{sgn}\left[S_{11}(E)-S_{22}(E)\right]_{E=\mu_j} \end{aligned}. \tag{2.71}$$

Finally, the solution to the direct scattering problem of the KdV equation is given by Eqs. (2.69) to (2.71) (Osborne, 1994, 2010). The eigenvalues $\{E_k;\ \mu_j;\sigma_j\}$ constitute the direct scattering transform of a discrete wave train of N spatial points (or degrees of freedom), such that $(1 \le k \le 2N+1;\ 1 \le j \le N)$. The inverse scattering transform, Eqs. (2.47) to (2.52) then allows the construction of broadband (in the spectral sense) wave train solutions of the KdV equation (Osborne, 1995a).

For the derivation of the algorithm, the solution of the trace formula in Eq. (2.47) is determined for an arbitrary base point x_o in the considered interval $0 \le x \le L_w$. The PIST spectrum as represented by Eqs. (2.69) to (2.71) corresponds to an arbitrary base point. To start with the IST, x_o has to be set to a particular base point, in general this is the beginning of the original data $x_o=0$. Therefore, the main and auxiliary spectra are obtained for this particular point at $x_o=0$: $\{E_k,\mu_j(0,0)\}$. In order to obtain the $\mu_j(x,0)$ for all base points x_o in the interval $0 \le x \le L_w$, the auxiliary spectrum is first computed for a nearby point $x_o=\Delta x<<L$, $\mu_j(\Delta x,0)$, in the *associated periodic interval* $\Delta x \le x \le L_w+\Delta x$, then at $x_o=2\Delta x$, $\mu_j(2\Delta x,0)$ and so on until $x_o=L_w+\Delta x$. 'To carry out this procedure it is enough to notice that by considering the wave train $\eta(x,0)$ to be on the associated periodic interval $(\Delta x \le x \le L_w+\Delta x)$ we find $\mu_j(\Delta x,0)$ by application of Eq. (2.70). Then for $\eta(x,0)$ on the interval $(2\Delta x \le x \le L_w+2\Delta x)$ Eq. (2.70) yields $\mu_j(2\Delta x,0)$, etc. In this way the hyperelliptic functions $\mu_j(x,0)$ for all x can be determined by iterating the *direct problem* in Eqs. (2.69) to (2.71) for the potential $\eta(x,0)$ on successive intervals

$[x_o, x_o+L_w]=[n\Delta x, (n+M-1)\Delta x]$, where $L_w=(M-1)\Delta x$ is the spatial period (or the width of the analysis window), $x_o=n\Delta x$ is an arbitrary base point, and n is an integer on $0 \leq n \leq M-1$' (Osborne, 2010). Once the $\eta_j(x,0)$ are determined for all points in the interval, the original data $\eta(x,0)$ can be reconstructed using the linear superposition law for $\mu_j(x,0)$ in Eq. (2.47). Therefore, instead of numerically solving the spatial evolution of the ODEs in Eqs. (2.49) and (2.50) (which are numerically ill-conditioned), the direct scattering problem is simply repeated for each desired spatial point in the function $\mu_j(x,0)$ (which is numerically well-conditioned). This approach is a substantial improvement over the numerical problems encountered in the solution to Eq. (2.49).

Linear superposition of all hyperelliptic functions provides the original data. If the superposition is performed only for a selected range of wave numbers k_j, then the original time series is filtered nonlinearly (Osborne, 1994).

Since $t=0$, the temporal evolution of the μ_j are not considered in the descriptions for the space-like KdV (Osborne, 1994, 2010). But usually, experimental test data are provided as time series where the surface elevation $\eta(x,t)$ is recorded at a function of time t at a fixed point $x=0$. The recording of a space series with sufficient spatial resolution requires the installation of a high number of measurement devices. Usually financial aspects exclude this approach. Furthermore, it is difficult to measure the free surface elevation with wave gauges that are very close together without disturbing the surface by the measurement equipment. Therefore, procedures for the IST were developed that also provide the scattering transform of time series $\eta(0,t)$. To this end one may apply the time-like KdV equation (tKdV) (2.5) (Ablowitz & Segur, 1981; Karpman, 1975; Osborne, 1995a).

The tKdV is here viewed as solving a boundary value problem: given the temporal evolution $\eta(0,t)$ at a fixed spatial location $x=0$, Eq. (2.5) specifies the motion over all space as a function of time $\eta(x,t)$. The temporal variable is assumed to obey periodic boundary conditions $\eta(x,t)=\eta(x,t+T_w)$. The scattering transform approach for the time-like KdV equation (tKdV) is thereby consistent with the same periodicity assumption used for linear Fourier algorithms (discrete and fast Fourier transforms). Due to recent advances in numerical methods the tKdV may now be routinely applied to the time series analysis of experimental data (Osborne et al., 1991; Osborne, 1991a, 1991b). All solutions of the sKdV in Eq. (2.2) may be easily mapped to all solutions of the tKdV in Eq. (2.5) by a simple transformation given by Prentice-Hall (1961) and Osborne et al. (1991). Hence the scattering transform of Eq. (2.5) may be easily expressed in terms of the scattering transform of Eq. (2.2). For present purposes it is only necessary to note that if the IST for the dKdV equation is given, then the IST for the tKdV equation may be easily determined (Osborne, 1991a).

2.6 Conventional wave analysis methods in frequency and time-frequency domain

Wave analysis methods in frequency and time-frequency domain are applied to determine the underlying spectral properties of measured or simulated data that cannot be determined by visual observation of the waves or the application of time-domain analysis methods. During the analysis the original data is decomposed into such a set of different spectral components that, if superposed again, returns the original data. In frequency-domain analysis the time in-

formation is not preserved. The spectral components are presented in amplitude-frequency or energy-frequency spectra that illustrate the characteristic frequency distribution within the data. The determined frequencies are assumed to exist as stationary oscillations which last permanently over the whole analysis window. In time-frequency domain analysis the occurrence of the frequency information is preserved and presented in a time-frequency-amplitude or time-frequency-energy spectrum. Here the determined components may exist over the whole analysis window as stationary component or as non-stationary event with shorter duration. The conventional fast Fourier transform (FFT) provides spectral analyses in frequency domain, the Wavelet (WT) and Hilbert-Huang transform (HHT) are time-frequency domain analysis techniques.

The descriptions that are given here focus on a short introduction of the methods, the most important equations for practical applications and the advantages and disadvantages of the presented approaches with respect to the time-domain KdV-NLFT (section 2.5). Further details on the FT and its further applications can be found e.g. in Cohen (1995) and Flandrin (1999), for wavelets (which are not discussed further within this thesis) in Daubechies (1992) and MathWorks (2006), and for the Hilbert-Huang transform in Huang et al. (1998; 1999).

2.6.1 Conventional fast Fourier transform (FFT)

Since its introduction by Fourier (1822) the conventional Fourier transform (FT), nowadays usually applied as fast Fourier transform (FFT), has become the standard method for the spectral frequency-domain analysis of data not only in ocean and coastal engineering. The idea if the FFT is quite simple: Any arbitrary time or space series data $\eta(x,t)$ can be decomposed by the direct Fourier transform into N sinusoidal basic components (sine and cosine waves), each defined by its characteristic amplitude a_i, wave number k_i or frequency f_i (or angular frequency ω_i) and phase φ_i. The linear superposition of these sinusoidal waves returns the original data in the inverse FFT. Since the spectral basic components of this decomposition are linear non-interacting waves, no nonlinear wave-wave interactions occur or have to be considered neither during the decomposition nor in the superposition. In analogy to the simple cosine terms in Airy wave theory, in coastal engineering very often the following notation for the inverse Fourier transform is applied:

$$\eta(x,t) = a_0 + \sum_{i=1}^{N} a_i(f)\cos(k_i x - \omega_i t + \varphi_i). \tag{2.72}$$

with a_0 being the mean of the original data.

The results of the FFT usually are presented as amplitude-frequency or energy-frequency spectrum. The latter uses the energy density $S(f)$ to represent the wave energy of each of the determined spectral components:

$$S(f) = \int \frac{a(f)^2}{2 \cdot \Delta f} df \tag{2.73}$$

with $a(f)$ the frequency-dependent amplitude of the spectral component and Δf the frequency resolution. Finally, the representation of the FFT results is completed by the phase-frequency spectrum.

The conventional Fourier transform has become the standard analysis method for water waves in coastal engineering although it only provides an approximate solution to the problems that arise with the analysis of nonlinear waves in shallow-water. The most important advantages of the FFT are: (i) the method is fast and can be easily implemented; (ii) the method is descriptive and can easily be understood; (iii) although the method is determined for periodic, stationary linear waves, it provides good approximate results within the engineering accuracy for many applications of real water waves, especially in larger water depths.

The most important limitations of the FFT are that (i) the method is limited to sinusoidal waves as spectral basic components and therefore decomposes every signal in terms of linear sine and cosine waves; (ii) for nonlinear or non-stationary waves additional higher harmonic components are used for the reconstruction of the original data that not necessarily are based on real physical processes, but are mathematical artefacts that are required within the mathematical algorithm to represent the original data correctly; (iii) the time information is lost during the analysis.

Examples for the application of the FFT to data from the nonlinear superposition of cnoidal waves are given in chapter 3. More detailed discussions of the advantages and disadvantages of this method and comparative analyses with HHT and KdV-NLFT will be given in chapters 3 to 6.

2.6.2 Hilbert-Huang transform (HHT)

The Hilbert transform (HT) is a well-established time-frequency domain analysis method for the determination of amplitudes and instantaneous frequencies of narrow-banded signals (Huang et al., 1998):

$$HT(t) = \frac{1}{\pi} P \int_{-\infty}^{\infty} \frac{\eta(t')}{t - t'} dt' , \tag{2.74}$$

with P the Cauchy principal value. The values $\eta(t)$ and $HT(t)$ form a complex conjugate pair and an analytical signal $Z(t)$ can be written as (Huang et al., 1998)

$$Z(t) = \eta(t) + iHT(t) = a(t) e^{i\phi_{HT}(t)} \tag{2.75}$$

with the instantaneous (time-dependent) values for amplitude $a(t)$ and Hilbert phases $\phi_{HT}(t)$ (Huang et al., 1998):

$$a(t) = \left[\eta^2(t) + HT^2(t) \right]^{1/2}, \quad \phi_{HT} = \arctan\left(\frac{HT(t)}{\eta(t)} \right). \tag{2.76}$$

Unfortunately, the HT cannot be applied to broad-banded signals like irregular sea states. In order to solve that problem, Huang et al. (1998; 1999) introduced a sifting method called *empirical mode decomposition* (EMD) that decomposes broad-banded signals into narrow-banded so-called *intrinsic mode functions* (IMF) (see Fig. 2.13) and applied the HT to each of these IMF. The combination of data pre-processing using the EMD and the subsequent analysis of the IMFs using the HT is called *Hilbert-Huang transform* (HHT). Later Wu and Huang (2004 improved the sifting algorithm by addition of white noise within the so-called *ensemble*

empirical mode decomposition (EEMD). The linear superposition of the determined IMFs provides the original data, and the linear superposition of the individual Hilbert spectra of all IMFs provides the Hilbert spectrum of the original signal. The IMFs are derived adaptively from the original data by application of a mathematical procedure within the EMD or the EEMD. They are not based on physical processes or any kind of wave theory; therefore they can be regarded as adaptive non-stationary nonlinear oscillation modes.

The HHT analyses within this thesis are performed with the EEMD (if not mentioned otherwise).

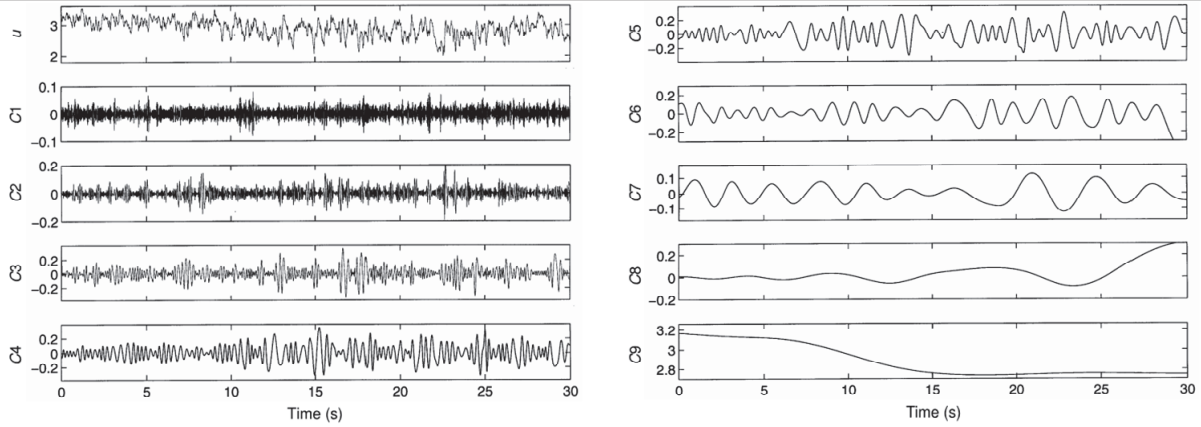

a) The original data u and the IMFs c_1 *to* c_4.

b) The IMFs c_5 to c_9. Notice the last component, c_9, is not an oscillatory IMF; it is the residual or trend.

Fig. 2.13: The resulting empirical mode decomposition components (IMFs) from wind data (Huang et al., 1998).

The HHT is called a 'nonlinear' domain time-frequency domain analysis method, because it determines the instantaneous frequencies f_{inst} of the IMFs and allows the variation of this frequency within each of the oscillations of the data (intra-wave nonlinearity):

$$f_{inst} = \frac{d\phi_{HT}}{dt}. \tag{2.77}$$

For linear cosine waves the instantaneous frequency f_{inst} is constant over the period, for nonlinear cnoidal waves with modulus $m>0$ the values of f_{inst} vary: the highest frequencies are obtained at the crest, the lowest in the wave trough (see Fig. 2.14). These nonlinear instantaneous frequencies are not considered explicitly within the KdV-NLFT. Nevertheless, the KdV-NLFT uses cnoidal waves that already implicitly contain varying instationary frequencies. Nonlinear wave-wave interactions (inter-wave interactions) as discussed in section 2.4.4 for the Riemann Θ-functions are not explicitly considered within the HHT. Hence, the linear superposition of the IMFs (which may be more or less nonlinear) returns the original data. Although both methods, HHT and KdV-NLFT are denoted as *nonlinear* analysis methods the *definition of nonlinearity* strongly differs for HHT and KdV-NLFT. Thus, the KdV-NLFT explicitly considers both, intra- *and* inter-wave nonlinearity, and the HHT is limited to intra-wave nonlinearity.

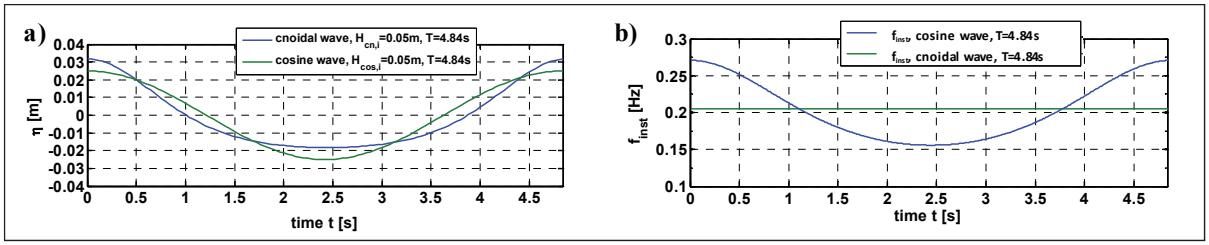

Fig. 2.14: Examples for cosine and cnoidal waves and their instantaneous frequencies.

By application of the EMD or the EEMD the original broad-banded free surface data are decomposed into different narrow-banded oscillation modes (IMFs). The definitions for these IMFs are derived from the requirements for the subsequent application of the HT. For practical application, the conditions for IMFs are: (i) 'in the whole data set, the number of extrema and the number of zero crossings must either be equal of differ at most by one', and (ii) 'at any point, the mean value of the envelope defined by the local maxima and the envelope defined by the local minima is zero' (Huang et al., 1998). By application of cubic-spline envelopes for the decomposition of the data, adaptive modes are determined whose shape can be irregular and only depends on the characteristics of the original data. Unlike in the Fourier transform or the wavelet transform the characteristics of the basic components are not defined a priori before executing the analysis. If the local extrema are used to define the scale of the decomposition, then the determined IMF might be affected by so-called mode mixing. As a consequence, the determined IMFs might contain oscillations from different frequency or wave number bands (see Fig. 2.13). This disadvantage can be avoided by application of the ensemble empirical mode decomposition (EEMD) in which white noise is added to the original data (Wu & Huang, 2004). The algorithm of the EEMD is applied and discussed in chapter 4, for a detailed introduction see Huang et al. (1998; 1999) and Wu and Huang (2004).

By the addition of numerically generated Gaussian white noise $n(x,t)$ to the original data $\eta(x,t)$ before applying the EMD to the modified data $\eta^*(x,t) = \eta(x,t) + n(x,t)$, an external scale for the decomposition of the data in time or space is applied (Flandrin et al., 2004; Wu & Huang, 2004). Based on that scale the different wave components of $\eta^*(x,t)$ are separated by frequency of wave number and assigned to different IMF, so that mode mixing within the IMFs is avoided.

Wu and Huang (2004) stated that the inevitable noise $n(x,t)$ within the data might have many causes. It can arise from the sensors and recording systems, it can have a natural source and it can be generated by 'local and intermittent instabilities and sub-grid phenomena' or it can be 'part of the concurrent phenomena in the environment where the investigations where conducted'. The latter might lead to the following analogue: The cnoidal waves $\eta_{cn,i}(x,t)$ are the true basic components we seek for. The nonlinear wave-wave interactions $\eta_{int}(x,t)$ might be regarded as an additional natural source of noise and therefore are considered during the analysis as part of a modified the noise term $n^*(x,t)$:

$$\eta^*(x,t) = \eta_{cn}(x,t) + n^*(x,t) = \sum \eta_{cn,i}(x,t) + \left[\eta_{int}(x,t) + n(x,t)\right]. \tag{2.78}$$

The nonlinear interaction term $\eta_{int}(x,t)$ is inevitable if nonlinear waves interact. Theoretically, these interactions might be separated from the 'true' signal $\sum \eta_{cn,i}(x,t)$ by application of the EEMD. If during the process of the EEMD the previously added white noise $n(x,t)$ is can-

celled out, the interaction term $\eta_{int}(x,t)$ might be obtained. Nevertheless, right at the beginning Wu and Huang (2004 also stated, that this approach will fail in the *'most complicated cases, when the processes are nonlinear and the noises also have the same time-scale as the signal; their separation becomes impossible'*. This explicit limitation has serious implications on the application of the HHT for the possible identification of nonlinear wave-wave interactions. If the range of the frequencies or wave numbers of the nonlinear waves overlap, even though to some extent, with those of the corresponding wave-wave interactions (as will be shown in Fig. 3.12), then the EEMD will not be able to reliably separate all the interactions from the cnoidal waves. For a possible application of the method follows that, if possible, a control routine has to be implemented that checks the ranges of frequencies or wave numbers for possible interference. Generally, in EEMD the data are decomposed empirically by their scale (in frequency or space), not by their wave shape. The IMFs are purely mathematical modes that are determined adaptively from the data by a purely mathematical algorithm; they are not based on physical wave theories or wave equations.

Further, Wu and Huang (2004) recognized that the analysis gets more complicated if the level of the noise in the data is not known, especially if the noise might contain any physical information such as the nonlinear interactions as assumed in Eq. (2.78). In the latter case, 'knowing the characteristics of the noise is an essential first step' before any significance can be attached 'to the signal eventually extracted from the data' (Wu & Huang, 2004) . This statement seems to be an inconsistency to the most important advantage of the HHT: its adaptive nature that does not require any knowledge of the data or a priori definition of the basic components. Actually, for the proper identification and interpretation of *nonlinear interaction noise* eventually contained in the IMFs, a detailed knowledge of the spectral characteristics of the nonlinear interactions is required. This physical knowledge about wave interactions cannot be provided by the adaptive HHT, so that this method has to be combined with a method that provides the required background data for the physical interpretation of the mathematically determined HHT analysis results.

As an additional feature Huang et al. (2013) presented the application of the Hilbert transform for the quantification a *degree of nonlinearity* (*DN*) based on the nonlinear intra-wave modulations. The basic idea of this approach is simple: The instantaneous frequency of a linear cosine wave is constant. The instantaneous frequency of a (even slightly) nonlinear wave profile is varying within one oscillation (intra-wave modulation, see Fig. 2.14). By comparison of the instantaneous frequencies within the wave oscillation with the constant frequency of a linear wave with the same period, the nonlinearity can be measured by terms of the degree of nonlinearity (Huang et al., 2013):

$$DN = \sqrt{\frac{1}{n-1}\sum_{i=1}^{n}\left[\left(\frac{f_{i,inst}-f_{const}}{f_{const}}\right)\cdot\frac{a_{i,z}}{\overline{a_z}}\right]^2}\ \text{, with } 0 \le DN \le 1\text{,} \tag{2.79}$$

with f_{inst} the instantaneous frequency, f_{const} the constant frequency of a linear wave with the same period, a_z the 'zero-crossing amplitude of a local whole wave' (Huang et al., 2013) and its mean value $\overline{a_z}$ in the denominator, indicated by the overline. For the values of the degree of nonlinearity substantially applies $0 \le DN \le 1$. For sinusoidal waves applies $DN=0$; and DN is increasing with increasing nonlinearity of the analysed wave profile. The consideration of

the amplitudes in this equation ensures that the influence of the nonlinear wave amplitudes is considered and high nonlinear waves have a higher contribution to *DN* than low waves. This definition of *DN* is valid only for narrow-banded data.

However, the HHT will be applied within this thesis for a comparative wave analysis using Fourier transform, HHT and the KdV-NLFT to evaluate the strengths and limitations of the different methods as well as their ranges of applicability (see chapters 3 to 6).

2.6.3 Comparison of basic features and characteristics of FFT, HHT and KdV-NLFT

The most important features and characteristics of FFT, HHT and KdV-NLFT that have implications on the further application of these methods within this thesis are summarised in Tab. 2.3.

Tab. 2.3: Comparison of the most important features and characteristics of FFT, HHT and KdV-NLFT.

feature	FFT	HHT	KdV-NLFT
analysis domain	frequency	time-frequency	frequency
type of basic component	sinusoidal waves	intrinsic mode functions (IMFs)	cnoidal waves
adaptivity of basic components	a priori definition	adaptive IMFs determined in EMD	partly adaptive (within range $0 \le m \le 1$ of cnoidal waves)
consideration of intra-wave nonlinearity	no	yes	yes
explicit consideration of inter-wave nonlinearity	no	no	yes
consideration of water depth	no	no	yes
explicit consideration of non-stationary data	no	yes	partly (in terms of solitons)

2.7 Specifications of objectives and methodology of this study

Based on the results of the analysis of the current knowledge related to the implementation and applications of the nonlinear KdV-based Fourier transform (KdV-NLFT) the objectives and methodology as tentatively formulated in chapter 1 have been confirmed. Moreover, they can be specified more precisely as follows:

(1) Implementation of the direct and inverse KdV-NLFT for time and space series, identification of the nonlinear interaction terms and validation and verification of the implemented algorithms.

Since no code for the practical application of the KdV-NLFT has yet been published and no software is available, the algorithms have first to be developed/implemented as an integral part of this thesis (chapter 3). To proceed further, the approach in terms of Jacobi θ- and Rie-

mann Θ-functions is applied. Overall, after the implementation and a first verification of the KdV-NLFT the method will be applicable for the practical analysis of data from hydraulic model tests and numerical simulations within the following four main objectives:

(2) Consistent identification of the nonlinear processes involved in the wave-structure interaction, exemplarily for submerged reefs.

First, selected characteristic nonlinear wave-structure interactions of the spectral basic components of KdV-NLFT are analysed (see Fig. 2.15a). Second, the nonlinear wave-wave interactions are determined from laboratory and numerical test data (see Fig. 2.15b). The required data for the analyses will be provided from both laboratory tests and numerical simulations. Overall, the results of these tasks are expected to reveal the effects of nonlinear wave-structure interactions and nonlinear wave-wave interactions in the actual nonlinear spectra of the transmitted waves which are determined by application of the KdV-NLFT (chapter 5).

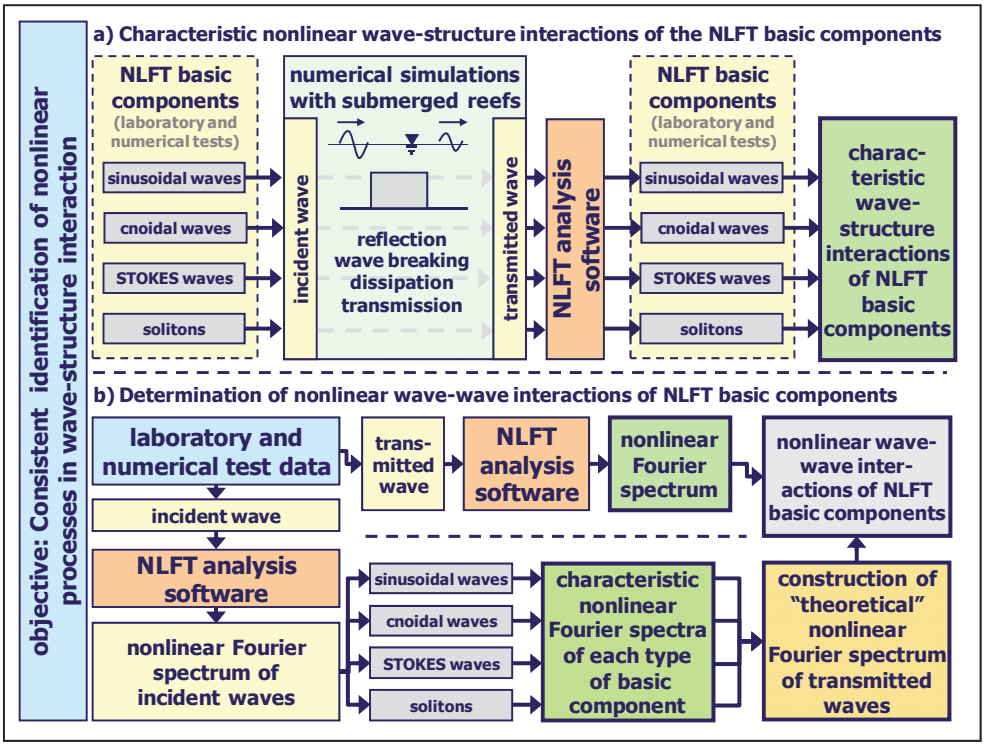

Fig. 2.15: Consistent identification of the nonlinear processes involved in the wave-structure interaction, exemplarily for submerged reefs.

(3) Proper identification of the number of solitons from wave fission in the transmitted wave trains over and behind submerged reefs.

Second, implications will be drawn for the analysis of the highly nonlinear wave fission and the evaluation of the capability of HHT to describe the nonlinear processes involved in the wave-structure interaction. One of the major problems in the analysis of wave fission at LWI in the past was the uncertain identification of the number of solitary waves in the transmitted wave train behind submerged reefs with finite width. The difficulties consist of the reliable distinction between solitons and oscillatory waves. With the nonlinear Fourier transform a powerful analysis method is available that explicitly considers solitons and oscillatory waves as basic components. Application of KdV-NLFT to the transmitted waves behind the reef,

even in the far field, will allow us to distinctly separate solitons and oscillatory waves (chapter 4). The required data for the analyses will be provided from both laboratory tests and numerical simulations. Overall, the results of these tasks are expected to substantially advance the knowledge of the mechanisms governing the highly nonlinear processes of solitary wave fission which are still not fully understood.

(4) Evaluation of the capability of the Hilbert-Huang transform (HHT) to describe the nonlinear processes involved in the wave structure interaction.

Third, the adaptive HHT will be applied for comparative analyses of the given nonlinear data (chapters 3 to 5). Based on the analysis results, recommendations will be given for both the applicability and limitations of the HHT. The advantages of the nonlinear KdV-NLFT analysis and the fast and effective HHT algorithm should be merged in a combined algorithm for nonlinear analysis. Overall, depending on the recommendations for applying HHT as an alternative to KdV-NLFT for defined boundary conditions, this combined algorithm shall apply the appropriate method for each particular case.

(5) Determination of the wave damping efficiency of submerged reefs on the basis of a wave energy balance analysis using FFT, HHT and KdV-NLFT.

Forth, the wave damping efficiency of submerged reefs can be expressed in terms of the wave energy balance around the reef. First, the energy of the oscillatory waves (sinusoidal, cnoidal and Stokes waves) and the energy of the identified solitons will be calculated based on the nonlinear spectra of incident, reflected and transmitted waves using available equations and approaches. Second, an approach will be developed for the consideration of the energy of the non-stationary and nonlinear interaction term (chapter 5). Additionally, the implications of the existence of local, non-stationary solitons for the energy balance shall be derived. Overall, the results of these tasks are expected to reveal the implications of the non-stationary properties of the cnoidal waves, the nonlinear interaction terms on the wave damping performance of submerged reefs and the wave energy balance. Based on the results of KdV-NLFT, prediction formulae for reflected, transmitted and dissipated wave energies E_r, E_t and E_d shall be derived.

3 Numerical implementation of the KdV-based inverse and direct nonlinear Fourier transform (KdV-NLFT)

First, the implementation of the cnoidal wave calculation is described in terms of Jacobi θ-functions, followed by a detailed description of the spectral properties of these cnoidal waves in terms of the conventional linear fast Fourier transform (FFT) and the time-frequency domain Hilbert-Huang transform (HHT). The temporal and spatial evolution of cnoidal waves and especially the advantages compared to the conventional approach with bound and free harmonics are then presented. Finally, the numerical nonlinear superposition of the Jacobi θ-functions is described in terms of Riemann Θ-functions, including the nonlinear interactions (see section 3.1).

Second, the direct and the inverse KdV-NLFT are numerically implemented. The procedures and equations for the determination of the spectral parameters are given. Examples for the practical application and construction of the nonlinear spectrum are presented (see section 3.2).

Third, the implemented direct KdV-NLFT is applied for the spectral analysis of cnoidal waves (see section 3.3).

Finally, a brief summary is given and the implications for the objectives and methodology to be adopted in this study are discussed.

Like in chapter 2, first the inverse KdV-NLFT is discussed for more clearness. The aim is to determine the physical properties and the numerical implementation of the cnoidal spectral components, of the nonlinear interaction terms and of their nonlinear superposition. Then, the function of the direct KdV-NLFT is just to determine the required specific spectral parameters so that in the inverse KdV-NLFT the given original signal is reproduced. Nevertheless, for the spectral analysis of a given signal first the direct KdV-NLFT is applied.

3.1 Numerical implementation of the inverse KdV-NLFT

3.1.1 Generation of cnoidal waves with Jacobi θ-functions

For the practical numerical generation and superposition of N cnoidal waves $\eta_{cn,i}(x,t)$ by application of Jacobi θ- and Riemann Θ-functions the Eqs. (2.39) and (2.42) are applied. The wave numbers k_i, angular frequencies ω_i and phases φ_i of the N cnoidal waves are given as vectors $\mathbf{k}$, $\boldsymbol{\omega}$ and $\boldsymbol{\varphi}$. The amplitudes of the cnoidal waves are represented by the diagonal elements B_{ii} in the NxN Riemann matrix $\mathbf{B}$. The off-diagonal elements B_{ij} with $i=1,...,N$, $j=1,...,N$ and $i \neq j$ represent the nonlinear interactions. The vector $\mathbf{n}$ contains the integers $-M \leq n_i \leq 0$ for $i < N$ and $-M \leq n_N \leq -1$ for the N-th element (notation 0^- in Eq. (2.40)). An example for the detailed numerical implementation of Eq. (2.41) is given in Tab. 3.1 for $\eta(x,t=0)$ with $N=2$ and $M=2$. The terms with the exponents already consider that $B_{ij} = B_{ji}$ (see Eq. (2.44)) and the terms with the cosine arguments the relation $\cos(x) = \cos(-x)$. This example and further details are also discussed in Osborne (2010.

Originally, the *Θ*-functions are calculated by

$$\Theta_N(x,t) = \sum_{\mathbf{n}=-M}^{M} e^{-\frac{1}{2}\mathbf{nBn}^T} \cos\left[\,\mathbf{nk}x - \mathbf{n}\omega t + \mathbf{n}\varphi\right]. \tag{3.1}$$

This leads, for the example with *N=2* and *M=2*, to the superposition of a total of $(2M+1)^N = 25$ so-called *partial θ-functions* in the sum. For the single case that all $M_i=0$ follows $e^0=1$. This case is excluded from the sum and added as discrete term (see Eq. (2.39)). Application of the relation *cos(x)=cos(-x)* shows that always two of the partial *θ*-functions are identical. Therefore, the computational effort can be reduced by a factor of *'2'* by reducing the summations from *-M* to *0* and introducing a factor of *'2'* in front of the sum. Since the case all $M_i=0$ is already considered by the summand *'1'* it has to be excluded in the remaining summation by introducing the notation 0^- in the equations (see Eqs. (2.39) and (2.40)). Further details, derivations and examples for the numerical implementation of the *θ*- and *Θ*-functions are given in Osborne (2010).

Tab. 3.1: Example for the numerical implementation of Eq. (2.39) for an example space series *η(x,t=0)* with *N=2*, *M=2*, considering $B_{ij}=B_{ji}$ for $i \neq j$ and *cos(x)=cos(-x)*.

no.	$\mathbf{n} = (m_1, m_2)$	$e^{-\frac{1}{2}\mathbf{nBn}^T}$	$\cos\left[\mathbf{nk}x + \mathbf{n}\varphi\right]$
1	(-2, -2)	$e^{-\frac{1}{2}(4B_{11}+8B_{12}+4B_{22})}$	$\cos\left[(2k_1+2k_2)x+(2\varphi_1+2\varphi_2)\right]$
2	(-2, -1)	$e^{-\frac{1}{2}(4B_{11}+4B_{12}+1B_{22})}$	$\cos\left[(2k_1+k_2)x+(2\varphi_1+\varphi_2)\right]$
3	(-2, 0)	$e^{-\frac{1}{2}(4B_{11})}$	$\cos\left[2k_1x+2\varphi_1\right]$
4	(-2, 1)	$e^{-\frac{1}{2}(4B_{11}-4B_{12}+B_{22})}$	$\cos\left[(2k_1-k_2)x+(2\varphi_1-\varphi_2)\right]$
5	(-2, 2)	$e^{-\frac{1}{2}(4B_{11}-8B_{12}+4B_{22})}$	$\cos\left[(2k_1-2k_2)x+(2\varphi_1-2\varphi_2)\right]$
6	(-1, -2)	$e^{-\frac{1}{2}(B_{11}+4B_{12}+4B_{22})}$	$\cos\left[(k_1+2k_2)x+(\varphi_1+2\varphi_2)\right]$
7	(-1, -1)	$e^{-\frac{1}{2}(B_{11}+2B_{12}+B_{22})}$	$\cos\left[(k_1+k_2)x+(\varphi_1+\varphi_2)\right]$
8	(-1, 0)	$e^{-\frac{1}{2}(B_{11})}$	$\cos\left[k_1x+\varphi_1\right]$
9	(-1, 1)	$e^{-\frac{1}{2}(B_{11}-2B_{12}+B_{22})}$	$\cos\left[(k_1-k_2)x+(\varphi_1-\varphi_2)\right]$
10	(-1, 2)	$e^{-\frac{1}{2}(B_{11}-4B_{12}+4B_{22})}$	$\cos\left[(k_1-2k_2)x+(\varphi_1+2\varphi_2)\right]$
11	(0, -2)	$e^{-\frac{1}{2}(4B_{22})}$	$\cos\left[2k_2x+2\varphi_2\right]$
12	(0, -1)	$e^{-\frac{1}{2}(B_{22})}$	$\cos\left[k_2x+\varphi_2\right]$

Due to the notation $\mathbf{nBn}^T$ the amplitudes of the partial *θ*-functions are functions of the Riemann matrix elements B_{ij} and the integers $m_1,\ldots,m_N$. For the diagonal elements B_{ii} that represent the superposed cnoidal waves, this implies that the higher the nonlinear character of the cnoidal wave, the higher the modulus *m,* the smaller the value of B_{11}, and finally, the higher the amplitude of the wave (see Fig. 2.9). The off-diagonal elements B_{ij} represent the interac-

tion terms and depend on the wave numbers k_i and k_j of the interacting waves (see Eq. (2.44)). Tab. 3.1 shows that the notation $\mathbf{nBn}^T$ provides a number of mixed terms including the N values of B_{ii} (here: B_{11} and B_{22}) and their interaction terms B_{ij} (here: B_{12} and B_{21} with $B_{12}=B_{21}$). The higher the value of M, the higher is the number of partial Θ-terms, the higher the values of the exponents and, therefore, the smaller is the resulting amplitude of these partial θ-components. For example, if $M=3$ then exponents with $\exp\left(-0.5\left(9B_{11}+18B_{12}+9B_{22}\right)\right)$ are obtained that lead to very small amplitudes in comparison to the exponent No. 1 in Tab. 3.1. For optimal computational effort, the value of M should be kept as small as possible.

Unfortunately, if M is selected too small, no oscillatory or solitary wave $\eta(x,t)$ is generated in Eq. (2.42). For optimisation of the calculation time, Fig. 3.1 shows the determined number of M as function of B_{11} that is required to obtain partial θ-amplitude values $a<10^{-16}m$ for *single cnoidal waves* $\eta(x,t)$. For the values in the figure the assumption is made that for practical application partial θ-functions with amplitudes smaller than $a<10^{-16}m$ do not provide any significant contribution to the final free surface of the cnoidal wave and therefore can be neglected. If the selected value of M for a given B_{11} is smaller than the M given in Fig. 3.1, then significant partial θ-functions might be missing in the superposition and the obtained $\eta(x,t)$ might not be correct.

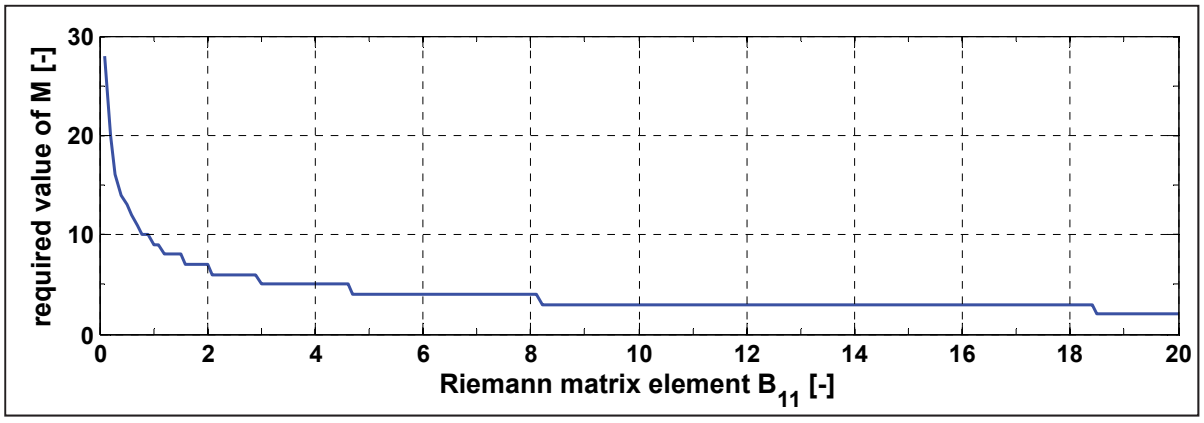

Fig. 3.1: Required value of M as function of B_{11} for the generation of cnoidal waves. The given values of M provide partial θ-amplitudes with $a<10^{-16}m$.

As can be seen in Eqs. (2.37) and (2.40) the amplitudes of the partial θ-components are not given explicitly, but they are defined by a function of B_{11} and M (the latter defines the values of n and **n** in the exponent). Furthermore, the cnoidal wave $\eta_{cn}(x,t)$ that is obtained from Eq. (2.35) is not a direct function of amplitude a or wave height H, but of B_{11} and M. Since $\theta(x,t)$ is obtained by linear superposition of partial θ-functions and $\eta_{cn}(x,t)$ is calculated as the second partial derivative of $ln\ \theta(x,t)$ the wave height of the cnoidal wave cannot explicitly be entered in or obtained from the given equations. The cnoidal wave from Eq. (2.35) can be written in the following way:

$$\lambda\eta_{cn}(x,t)=2\frac{\partial^2}{\partial x^2}\ln\theta(x,t) \tag{3.2}$$

In this notation, the term on the right hand side is independent of the water depth because only λ (which is now on the left hand side) is a function of h. For a given wave length L or wave number $k=2\pi/L$, the amplitude of the wave on the right-hand side in Eq. (3.2) is only defined

by B_{11}. The smaller B_{11} the higher the nonlinear character, the higher the modulus m, and the larger is the wave height. This can be illustrated by a simple example: For $k=1.0$ and $B_{11}=11.75$ applies the constant value $\lambda H=0.0225$ which is valid for all water depths h. For $h_1=0.10m$, $h_2=1.00m$ and $h_3=1.50$m follows $\lambda_1=12.0$, $\lambda_2=1.50$ and $\lambda_3=0.44$, respectively, and finally $H_1=0.002m$, $H_2=0.015m$ and $H_3=0.051m$. The final shapes of the free surface in the different water depths are derived by simply scaling the right hand side of Eq. (3.2) by $1/\lambda$, as shown in Eq. (2.35). For the direct generation of cnoidal wave with a specific desired wave height the nomograms in Fig. 3.2 and Fig. 3.3 can be applied. The nomograms are generated within this study to simplify the selection of appropriate input settings for the desired cnoidal waves. The figures show the scaled wave height λH in logarithmic scale $\ln(\lambda H)$ for different wave numbers k and Riemann matrix elements B_{11}. For a better visualisation, the logarithm of λH is used and the figures show different wave number ranges ($0\leq k\leq 10$ in Fig. 3.2 and $5\leq k\leq 100$ in Fig. 3.3). Furthermore, in Fig. 3.2 the ranges of B_{11} are subdivided into $2.0\leq B_{11}\leq 20$ in Fig. 3.2a and $0.7\leq B_{11}\leq 2.0$ in Fig. 3.3b.

The relations between the modulus m and B_{11} are shown in Fig. 2.9. To determine the required value of B_{11} for a desired cnoidal wave with wave height $H=0.05m$ in a water depth of $h=0.5m$ and wave number $k=1m^{-1}$ the following procedure is applied:

(i) Calculate $\lambda=3/(2h^3)=3/(2\cdot 0.5^3)=12m^{-3}$.

(ii) Calculate $\ln(\lambda H)=\ln(12\cdot 0.05)=-0.511$.

(iii) Determine the value of B_{11} for $k=10^0m$ and $\ln(\lambda H)=-0.511$ from Fig. 3.2a: $B_{11}=5.2$. If desired, determine the corresponding modulus m from Fig. 2.9 or Eq. (2.38): $m=0.698$.

(iv) Generate the cnoidal wave from Eq. (2.35) using the given (H, k, h) and determined (B_{11}) wave parameters.

The result is a cnoidal wave in water depth $h=0.5m$ with $k=1m^{-1}$ and $H=0.05m$. The modulus is $m=0.698$ ($B_{11}=5.2$) which refers to a Stokes-like wave (see Fig. 2.5b).

With increasing nonlinearity the shape of cnoidal waves changes from sinusoidal-shaped to solitary-shaped waves. This is already presented in Fig. 2.6. Unfortunately, the figure only shows profiles that are normalised for wave length L and wave height H and therefore neither does represent the real relation between sinusoidal-shaped and solitary-shaped wave height nor do they show the decrease of the reference level of the solitary waves. Therefore, the evolution of the shape of cnoidal waves in a water depth of $h=0.5m$ as a function of the Riemann matrix element B_{11} is visualized in Fig. 3.4 for $k=1m^{-1}$. The upper row (Fig. 3.4a, b) shows the plan view with contour plots of the free surface; the lower row (Fig. 3.4c, d) shows rotated views that illustrate the cnoidal wave shapes much better. The plots in the left column (Fig. 3.4a, c) for range $4\leq B_{11}\leq 20$ show that for high values of B_{11} the amplitudes are very small and the waves are very close to linear cosine waves. With decreasing B_{11} the amplitude increases and the wave becomes more and more nonlinear. The cnoidal wave for $B_{11}=5.2$ from the example above is plotted as a black line in Fig. 3.4a and c. For very small values of B_{11} (right column) the soliton amplitudes strongly increase. Note that due to the second derivative in Eq. (2.35) cnoidal and Airy waves are phase-shifted by π. The plots show the mathematical solutions of cnoidal wave generation. The breaking of waves which limits the maximum possible wave height is not considered in the plots in the right column.

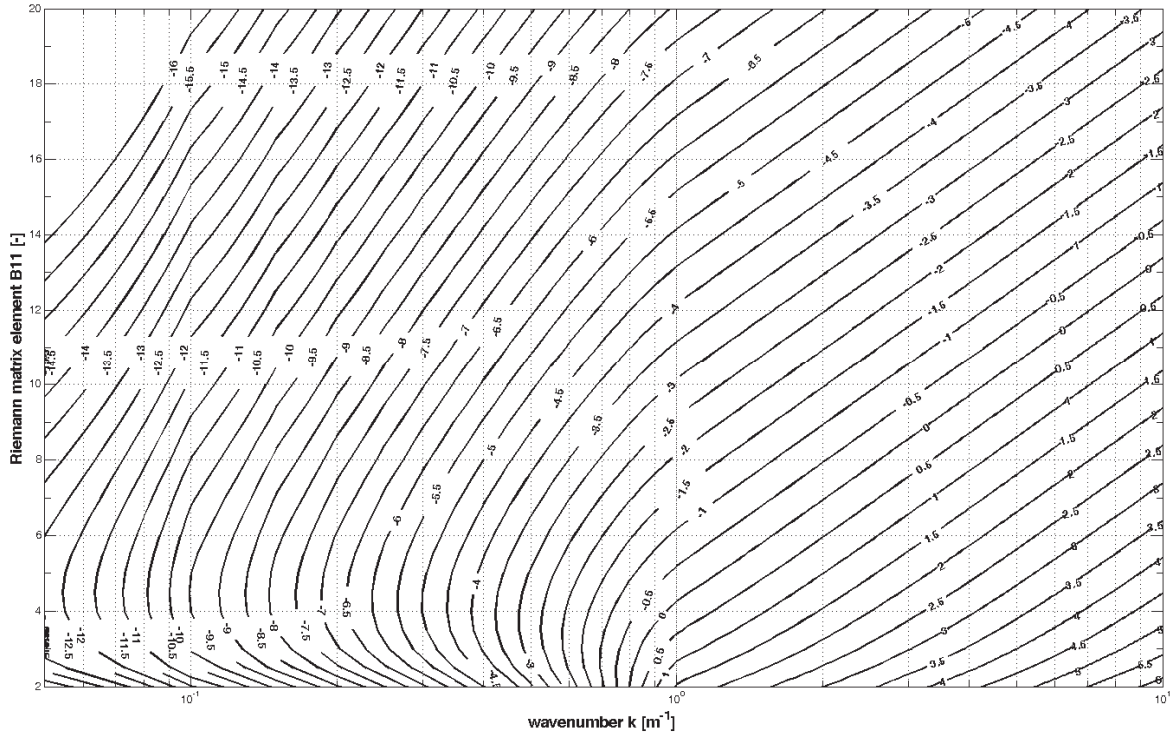

a) Nomogram with the scaled wave height in logarithmic scale ln(λH) as function of wave number $0 \le k \le 10$ and Riemann matrix element $2 \le B_{11} \le 20$.

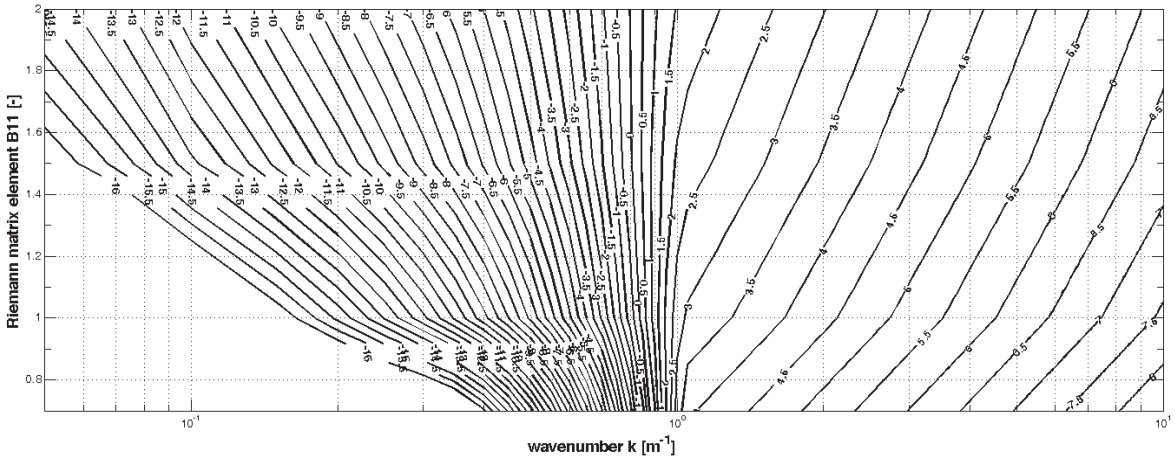

b) Nomogram with the scaled wave height in logarithmic scale ln(λH) as function of wave number $0 \le k \le 10$ and Riemann matrix element $0.7 \le B_{11} \le 2.0$.

Fig. 3.2: Nomograms with the scaled wave height in logarithmic scale ln(λH) as function of wave number $0 \le k \le 10$ and Riemann matrix element $0.7 \le B_{11} \le 20$.

Solitary waves have a steep wave crest but no wave trough and therefore the wave crest propagates on a plane of water. Nevertheless, as can be seen in Fig. 3.4b and d this plane is different from the still water level (SWL) and lying below SWL. The reason is simple: Just imagine a wave is generated within a box with limited width with a given volume of water. If a wave crest is generated at one position, due to the limited volume a depression is generated at the same time at positions to the left and right of the crest. The mean value of the generated wave within the box is the still water level, but the wave crest lies above and the infinite horizontal wave troughs of the solitary wave are below SWL. The mean of the free surface $\eta(x,t)$

(=SWL) is denoted as the reference level upon which the solitary waves propagates, even if the areas left and right from the soliton are below that value. Note that in the implementation of the KdV-NLFT periodic boundary conditions are assumed. The larger the width of the analysis window, the smaller is the depression to the right and left of the soliton.

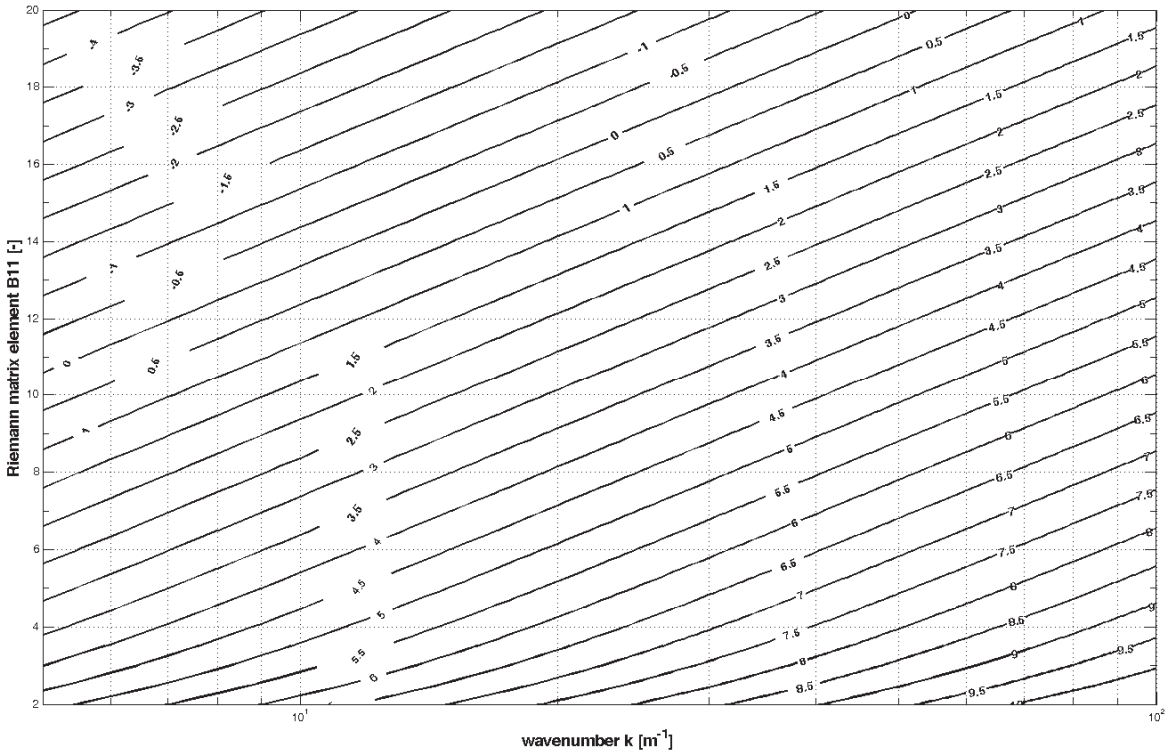

Fig. 3.3: Nomogram with the scaled wave height $\ln(\lambda H)$ in logarithmic scale as function of wave number $5 \leq k \leq 100$ and Riemann matrix element $0.7 \leq B_{11} \leq 20$.

Another important aspect of the generation of nonlinear waves is the selection of the correct dispersion relation. The conventional waves from Airy to 2nd-order Stokes are frequency dispersive and follow the linear dispersion relation in Eq. (2.20). Starting from 3rd-order Stokes the influence of the wave amplitude on the wave celerity becomes significant and a nonlinear dispersion relation has to be applied. For cnoidal-theory waves, the nonlinear relation in Eq. (2.27) is applied which is also valid for cnoidal waves in terms of Jacobi θ-functions. It can be shown in Fig. 3.5 that the nonlinear dispersion relation for cnoidal waves is a general approach that includes the relation for the linear case with small wave amplitudes and $B_{11}>18$. For very small wave amplitudes the additional terms vanish and the result is the same as for the linear dispersion relation. Therefore, no distinction between small-amplitude and nonlinear waves is required for the selection of the appropriate dispersion relation. Fig. 3.5 shows the evolution of ω in logarithmic scale $\ln(\omega)$ as function of B_{11} for the cnoidal waves in Fig. 3.4. The blue curve shows the linear dispersion relation from Eq. (2.20) which is constant for the given wave number $k=1m^{-1}$ of the cnoidal waves and the constant depth $h=0.5m$. The red curve shows the angular frequency $\ln(\omega)$ calculated with the nonlinear dispersion relation (2.27) for cnoidal waves. For high values of B_{11} and therefore small amplitudes, the values from linear and nonlinear dispersion are identical. Starting from $B_{11}<18$ (see the detail in Fig. 3.5) the red curve increases due to the influence of the increasing amplitudes. For linear Airy waves applies $\omega=2.129s^{-1}$ ($\ln(\omega)=0.76$). Application of the nonlinear approach provides slightly smaller values for $B_{11}>18.5$. For decreasing values of B_{11}, the values of ω are increas-

ing. Tab. 3.2 shows the results for selected values of B_{11} according to the results from Fig. 3.6 in section 3.1.2.1.

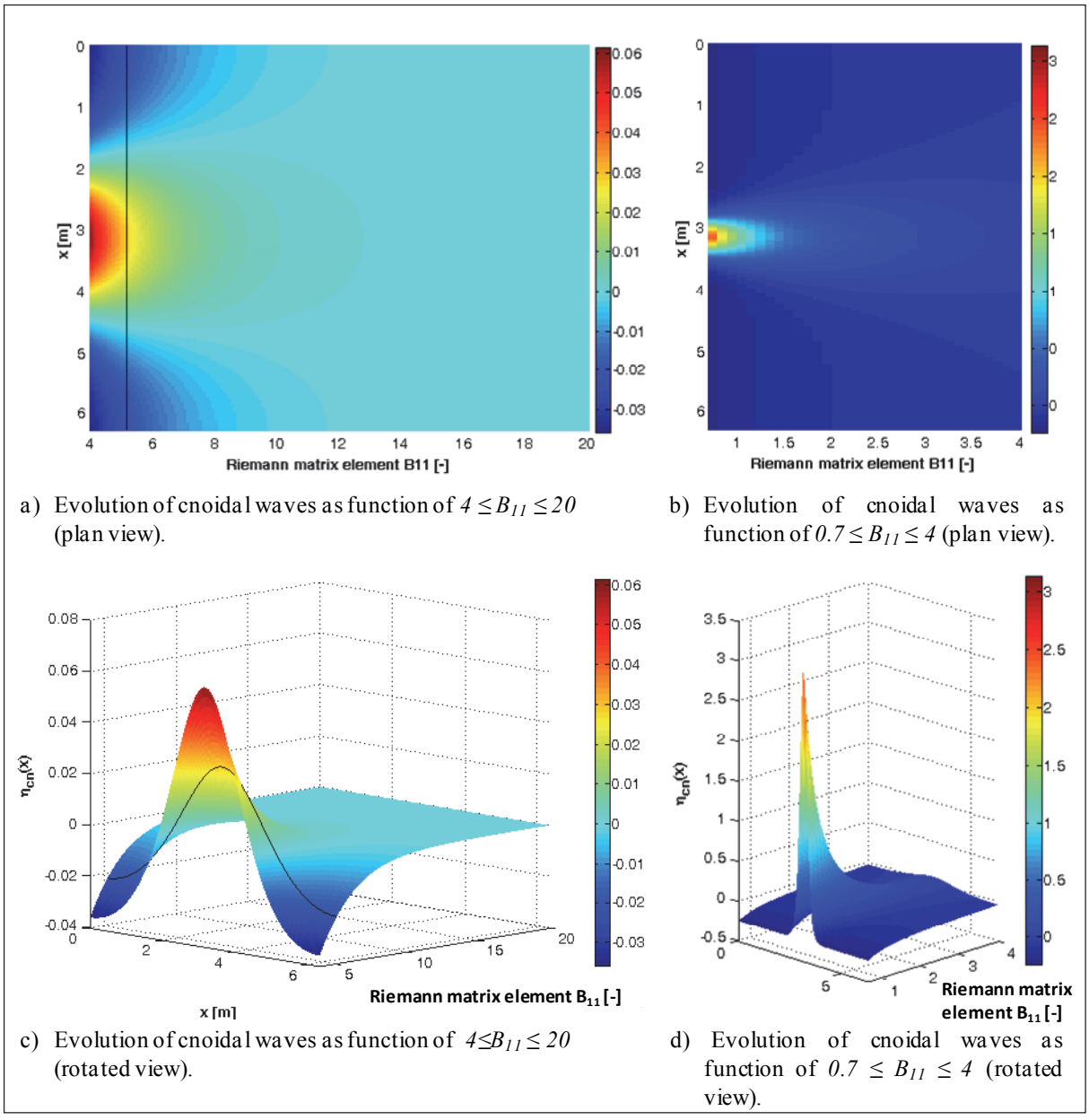

a) Evolution of cnoidal waves as function of $4 \leq B_{11} \leq 20$ (plan view).

b) Evolution of cnoidal waves as function of $0.7 \leq B_{11} \leq 4$ (plan view).

c) Evolution of cnoidal waves as function of $4 \leq B_{11} \leq 20$ (rotated view).

d) Evolution of cnoidal waves as function of $0.7 \leq B_{11} \leq 4$ (rotated view).

Fig. 3.4: Evolution of cnoidal waves $\eta_{cn}(x)$ in water depth $h=0.5m$ as function of B_{11}.

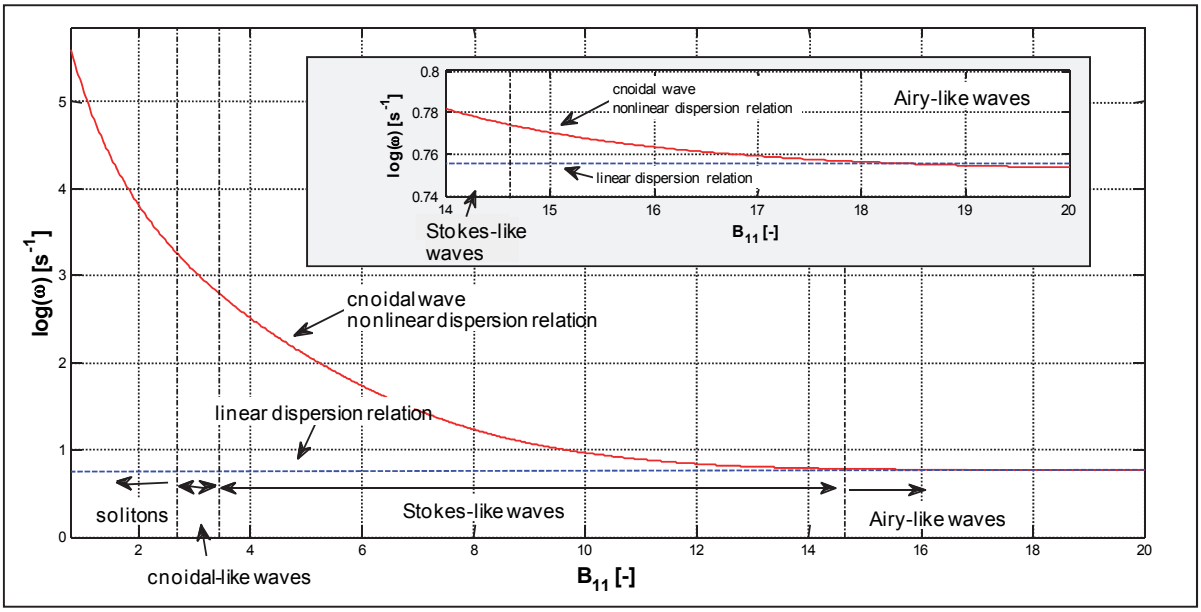

Fig. 3.5: Evolution of *log(ω)* from the nonlinear dispersion relation (2.27) of the cnoidal waves from Fig. 3.4 compared to the linear dispersion relation of Airy waves with detailed view on the range of Airy-like waves.

Tab. 3.2: Evolution of ω of cnoidal waves calculated from the nonlinear dispersion relation in Eq. (2.27) (selected values).

B_{11}	$\omega_{nonlinear}$	$\frac{\omega_{nonlinear}}{\omega_{linear}}$	remark
20.00	2.126	0.9986	nonlinear dispersion slightly smaller than linear value
18.50	2.129	1.0000	equal values for linear and nonlinear dispersion
14.63	2.169	1.0188	2nd-order amplitude larger than $0.001 \cdot a_{k=1}$
10.55	2.481	1.1650	2nd-order amplitude larger than $0.01 \cdot a_{k=1}$
8.12	3.330	1.5640	3rd-order amplitude larger than $0.001 \cdot a_{k=1}$
5.98	5.688	2.8090	2nd-order amplitude larger than $0.1 \cdot a_{k=1}$
3.43	16.430	7.7170	beginning of cnoidal-like waves
2.68	26.020	12.2220	beginning of solitary-like waves

3.1.2 Spectral properties of cnoidal waves

By applying the cnoidal wave equation, shallow-water waves with different nonlinearities can be generated. The evolution of the free surface wave shapes for decreasing values of the Riemann matrix element B_{11} (or increasing modulus m) is shown in Fig. 3.4. The conventional Stokes wave theory in Eqs. (2.17) and (2.18) and the cnoidal wave theory in Eq. (2.24a) consider the increasing nonlinearity of the waves by superposition of higher-harmonic linear cosine waves with increasing order. If the wave shape can be represented by a single cosine

wave, the linear Airy wave theory can be applied and provides the best-fit result. For higher nonlinearity in the Stokes 2nd to 5th order theories higher-order cosine waves are added to generate nonlinear waves with higher and narrower crest and lower and wider trough, which is the characteristic trait of nonlinear surface waves. Note, that for small nonlinearity the higher-order Stokes waves reduce to linear cosine waves (Stokes first-order waves), because the amplitudes of the higher-order components become negligible. On the other limit, if the number of higher-order components is increased, then first cnoidal-theory waves can be obtained (see Eq. (2.24a)), and finally, for N components a soliton-shaped wave is obtained. And this is the reason why the cnoidal wave equation provides the complete range of wave shapes, from linear ($N=1$) to soliton-shaped ($N>>1$ components). And furthermore, this also explains some of the results presented in these chapters and sections.

In the following sections, the results of the application of the fast Fourier transform (FFT) and the Hilbert transform (HT) on the cnoidal waves from Fig. 3.4 are presented. Since the generated cnoidal surface elevations are already narrow-banded single-component waves, the preprocessing by empirical or ensemble empirical mode decomposition (EMD or EEMD) before applying the Hilbert transform (HT) is not necessary.

3.1.2.1 **Fast Fourier transform (FFT) of cnoidal waves**

Since nonlinear waves in the conventional approaches (Stokes and cnoidal wave theories, Eqs. (2.17), (2.18) and (2.24a)) are generated by superposition of harmonic higher-order cosines, the conventional Fourier spectrum decomposes these waves back into these harmonic components. This effect is already shown in Fig. 2.8 for selected cnoidal waves. Now conventional FFT spectra for each of the cnoidal waves in Fig. 3.4 are presented in Fig. 3.6b. The figure shows the FFT amplitudes in logarithmic scale $\ln(a_j)$ as colour plot as function of B_{11} over normalized wave number k/k_i (which does not have any effect in this figure since here applies $k=1m^{-1}$. The contour plot confirms that for decreasing values of B_{11} (= increasing modulus m) the first order amplitude increases which can already be derived qualitatively from Fig. 3.4. Furthermore, the figure shows that for values $B_{11}\geq 14.5$, the second-order component starts to show significant amplitudes. The smaller B_{11} the more higher-order components have to be superposed to obtain the cnoidal wave. The amplitudes of the different higher-order waves are also increasing with decreasing B_{11}. This is also in agreement with the generation of waves in Eqs. (2.17), (2.18) and (2.24a). For solitary-like waves with $B_{11}\leq 2.65$ at least 15 cosines are required to generate these strongly nonlinear cnoidal waves.

In Fig. 3.6a and Fig. 3.6c the FFT amplitudes for wave numbers $k=0.1m^{-1}$ and $k=10.0m^{-1}$ are given. The comparison shows that the amplitudes strongly depend on the wave number of the cnoidal wave. The higher the wave number (i.e. the shorter the wave) the higher are the obtained amplitudes for a given nonlinearity in terms of B_{11} or modulus m. Furthermore, as already shown in Eq. (3.2) the amplitudes are, due to the factor λ, functions of the water depth. To eliminate these influences, Fig. 3.6d shows the plot with normalized Fourier amplitudes $a_j/a_{k=1}$. By normalization of the amplitudes with $a_{k=1}$ at $k=1m^{-1}$ for every value of B_{11} the relative higher-order amplitudes are given with respect to the first-order Airy component. This eliminates the influence of the water depth and the wave number on the FFT amplitudes. After normalisation, each of the plots in Fig. 3.6 a) to c) provides the identical result shown in Fig. 3.6d. Finally, for a classification of cnoidal waves in terms of conventional wave theories

the number of required higher-order components can be derived from Fig. 3.6d and the detailed view in Fig. 3.6e.

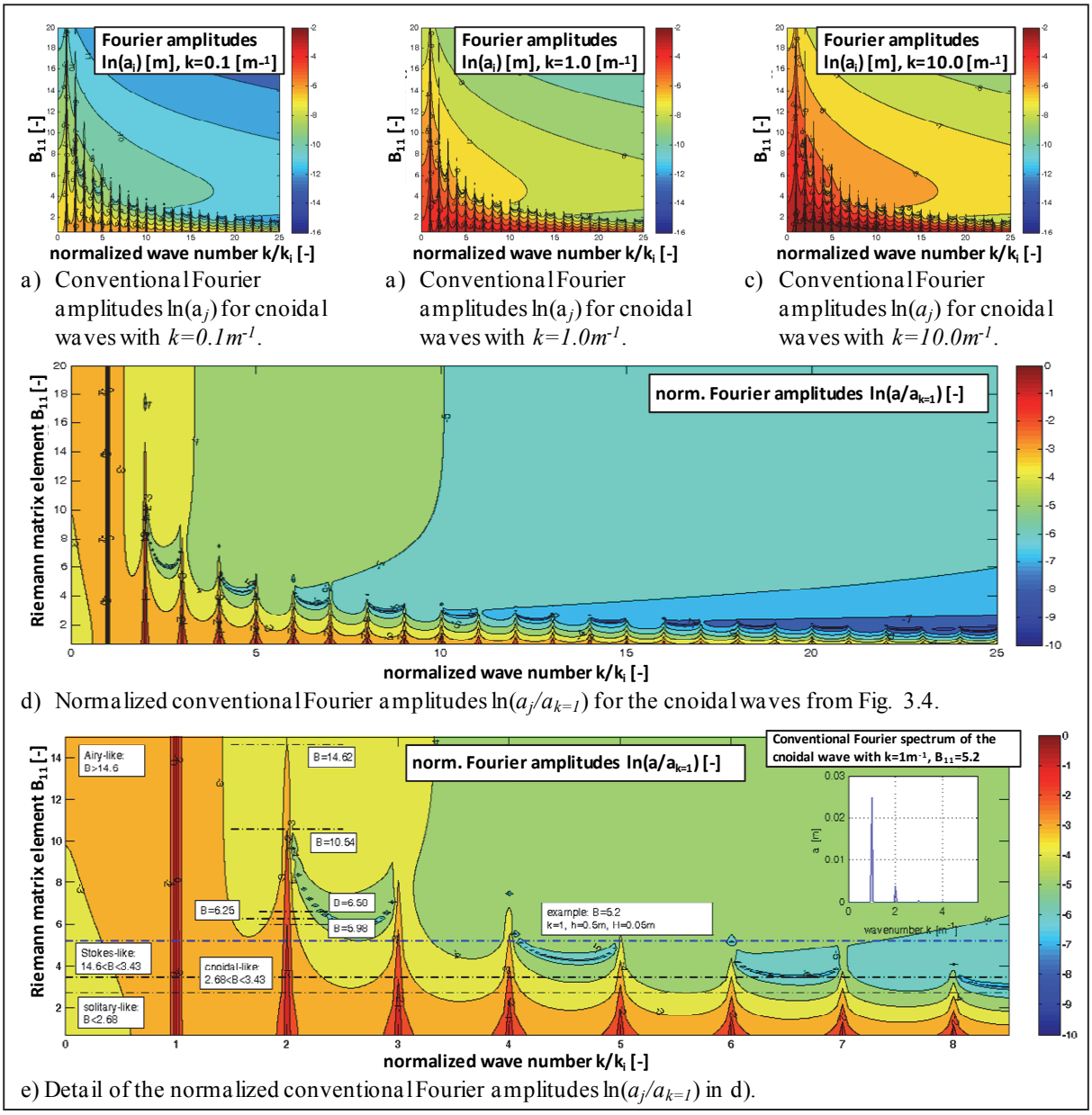

a) Conventional Fourier amplitudes $\ln(a_j)$ for cnoidal waves with $k=0.1m^{-1}$.

a) Conventional Fourier amplitudes $\ln(a_j)$ for cnoidal waves with $k=1.0m^{-1}$.

c) Conventional Fourier amplitudes $\ln(a_j)$ for cnoidal waves with $k=10.0m^{-1}$.

d) Normalized conventional Fourier amplitudes $\ln(a_j/a_{k=1})$ for the cnoidal waves from Fig. 3.4.

e) Detail of the normalized conventional Fourier amplitudes $\ln(a_j/a_{k=1})$ in d).

Fig. 3.6: Conventional Fourier spectra and normalized spectra of the cnoidal waves in water depth $h=0.5m$ from Fig. 3.4.

For an easier introduction into Fig. 3.6e the blue dash-dotted line represent the cnoidal wave from the previous example with $B_{11}=5.2$, $k=1m^{-1}$ and $h=0.5m$ which is plotted in Fig. 3.4 as black curve. The corresponding conventional Fourier amplitude-frequency spectrum of this particular wave is given on the right side within the figure: In the FFT spectrum this wave is represented by a first-order amplitude with $a_1=0.02487m$ and higher-order amplitudes $a_2=0.00366m$, $a_3=0.000408m$ and $a_4=0.00004m$. After normalization by the first-order amplitude a_1 the modified values are $a_1/a_1=1$, $a_2/a_1=0.1472$, $a_3/a_1=0.0164$ and $a_4/a_1=0.0016$. Note that these values are plotted in the contour plot in logarithmic scale. The second-order ratio is larger than 10^{-1}, the third-order value larger than 10^{-2} and the forth-order component larger than 10^{-3}. These values can (quantitatively) also be determined by following the blue dash-

dotted line in the figure from $k=1$ to the right. The example wave is generated for a water depth of $h=0.5m$, but from Eq. (3.2) follows that the scaling of η_{cn} by λ will be neutralised by the normalisation $a_i/a_{k=1}$ so that the normalised plots in Fig. 3.6d and Fig. 3.6e are valid for all water depths.

After this first introduction into the contour plots, the application for a classification of cnoidal waves based on the spectral properties obtained from the conventional FFT is discussed. The detailed view in Fig. 3.6e shows that the definition of a threshold value of B_{11} for Airy-like and Stokes-like waves based in the FFT spectra is difficult. For values of $B_{11}>14.6$ ($m=0.011$) only the first-order Airy wave amplitude a_1 is required to describe the cnoidal waves if second-order waves with $a_2<0.001a_1$ are regarded as negligible. If $B_{11}>14.6$, then for the second-order amplitude applies $a_2>0.001a_1$, if $B_{11}>10.54$ the relation is $a_2>0.01a_2$. Osborne (2010) gives a value of $m=0.5$ ($B_{11}=6.25$) as threshold to distinguish between Airy and Stokes waves, Brühl and Oumeraci (2012) used $m=0.45$ ($B_{11}=6.58$). As can be seen in the spectrum none of the latter values can be confirmed by the spectral properties shown in the Fourier spectra, but they are close to the value for $a_2>0.1a_1$ at $B_{11}=5.98$ ($m=0.55$). At this point no value will be declared to be the 'correct' threshold of B_{11}, but starting from $B_{11}=14.6$ ($m=0.011$) the second-order component can be clearly observed in the normalized FFT spectra. Stokes waves of 5th order consist of the basic Airy (Stokes first-order) frequency that is superposed by 4 higher-harmonic components. If we assume the 6th-order component to be negligible if $a_6<0.001a_1$, then starting from $B_{11}=3.43$ ($m=0.95$) the Stokes5 approach is not sufficient anymore and the waves become cnoidal-like. The threshold value for the definition of solitons is $m>0.99$ ($B_{11}=2.68$) (Osborne, 2010) which is also marked by a line in Fig. 3.6e.

Finally, the conventional FFT analysis of the cnoidal waves in Fig. 3.6 shows very clearly how the increasing nonlinearity of the free surface with decreasing values of B_{11} is considered in this linear representation: The higher the nonlinearity of the waves, the more higher-order components are required to represent the waves in the conventional Fourier spectrum, and the higher the higher-order wave amplitudes. By definition of threshold values based on the Fourier amplitudes of the harmonics, the number of required higher-order components for the cnoidal waves can be obtained and the waves can be classified in terms of B_{11} or the modulus m as shown in Fig. 3.6.

3.1.2.2 **Hilbert transform (HT) of cnoidal waves**

Depending on the objectives of the nonlinear data analysis and the different available analysis methods, different definitions of nonlinearity are applied (intra-wave and inter-wave nonlinearity). The Hilbert transform within the Hilbert-Huang transform (HHT) provides instantaneous frequencies (or wave numbers) that will vary within each oscillation of the nonlinear waves (see Fig. 2.14). This approach defines nonlinearity as an intra-wave modulation. Although the intra-wave nonlinearity of the waves is revealed, the decomposition of the data in intrinsic mode functions (IMF) within the empirical mode decomposition (EMD) is a linear process since the linear superposition of these IMFs returns the original data. Inter-wave nonlinearity is not explicitly considered. Unlike the HHT, the direct and inverse NLFT are nonlinear analysis methods that consider both intra-wave nonlinearity and inter-wave interactions between the basic components that are caused by inter-wave modulations (see Fig. 2.10). As shown in section 2.6.2, the instantaneous frequency obtained by the HT and especially the degree of nonlinearity (DN) in Eq. (2.79) can be used to quantify the nonlinear

character of a wave. In the following, the DN approach from section 2.6.2 is applied for the analysis of the cnoidal waves from Fig. 3.4. These cnoidal waves are generated using the cnoidal wave equation and therefore are monochromatic in terms of nonlinear cnoidal waves (not in terms of the FFT spectrum). These waves already are IMFs and the application of the empirical mode decomposition (EMD) is not necessary to pre-process the data before applying the HT to the cnoidal waves.

In a first step, the Hilbert transform from Eq. (2.74) is applied to the cnoidal waves shown in Fig. 3.4 with $0.7 \leq B_{11} \leq 20$, $k=1m^{-1}$ and $h=0.5m$. The different instantaneous Hilbert transform parameters amplitude a_{HT}, phase ϕ_{HT} and wave number $k_{inst}/(2\pi)$ are presented Fig. 3.9. Note that for space series $\eta(x)$ the HT provides instantaneous wave numbers $k_{inst}/(2\pi)$ instead of frequencies f_{inst}. The plots in Fig. 3.9a and b show the instantaneous Hilbert amplitudes a_{HT} as defined in Eq. (2.76). The Hilbert amplitudes provide the instantaneous radius of the Hilbert transform figure in the imaginary plane and therefore the values are all positive. The minimum and maximum values of a_{HT} represent the absolute values of the surface elevation in the wave trough and wave crest, respectively. The result of the Hilbert transform can be plotted on the imaginary plane with $\eta(x)$ as the real and $HT(x)$ as the imaginary part as shown in Fig. 3.7. For each position x (or timestep t in time series data) the instantaneous phase ϕ_{HT} can be calculated (see Eq. (2.76)). Due to the varying values of $\eta(x)$ and $HT(x)$ the values of ϕ_{HT} are also varying within one oscillation (intra-wave modulation). Finally, the instantaneous wave number $k_{inst}/(2\pi)$ is obtained as the spatial derivative of the phase $\phi_{HT}(x)$ (analogous to the frequency f_{inst} in Eq. (2.77) for time series). For Airy-like waves the Hilbert transform in the imaginary plane is a circle with center $(0,0)$ and therefore the values of $a_{HT}(x)$ are constant, $\phi_{HT}(x)$ is linearly increasing and $k_{inst}/(2\pi i)=d\phi_{HT}/dx$ is constant. This can be seen in Fig. 3.9 for high values of B_{11}.

The higher the nonlinear character of the cnoidal wave, the higher the deviation of the instantaneous phase from linear behaviour (see Fig. 3.9c and d). By spatial derivation of the phases $\phi_{HT}(x)$ the instantaneous wave numbers $k_{inst}/(2\pi)$ are obtained (Fig. 3.9e and f). These figures clearly show that the evolution of the wave numbers with decreasing values of B_{11} qualitatively correlates with the evolution of the free surface $\eta(x)$ of the cnoidal wave in Fig. 3.4. For high values of B_{11} the cnoidal waves have very small amplitudes and are very similar to linear Airy waves and therefore, the Hilbert transform provides nearly constant (Airy-like) frequencies. With decreasing B_{11} and therefore increasing nonlinearity the maximum frequency also increases and the frequency curves follow the nonlinear shape of the cnoidal waves (seeFig. 3.9).

For further proceeding it can be shown that the Hilbert amplitudes a_{HT} and wave numbers $k_{inst}/(2\pi)$ can easily be normalized by division with the (constant) wave number $k=k_{const}=2\pi/L$ of the cnoidal wave (which is the wave number of the linear wave with same length as the cnoidal wave):

$$a_{HT,norm} = a_{HT} k, \quad k_{inst,norm} / 2\pi = \frac{k_{inst} / 2\pi}{k}. \tag{3.3}$$

Finally, the normalised wave numbers can be used to calculate the degree on nonlinearity as given in Eq. (2.79). Since the influence of the amplitudes is assumed to be important only for irregular wave trains with amplitude modulated wave components (Huang et al., 2013) the

following equation is applied here for the calculation of a modified degree of nonlinearity *DN'* from the frequencies:

$$DN' = \sqrt{\frac{1}{n-1}\sum_{i=1}^{n}\left[\left(\frac{k_{i,inst}/(2\pi) - k_{const}}{k_{const}}\right)\right]^2} \tag{3.4}$$

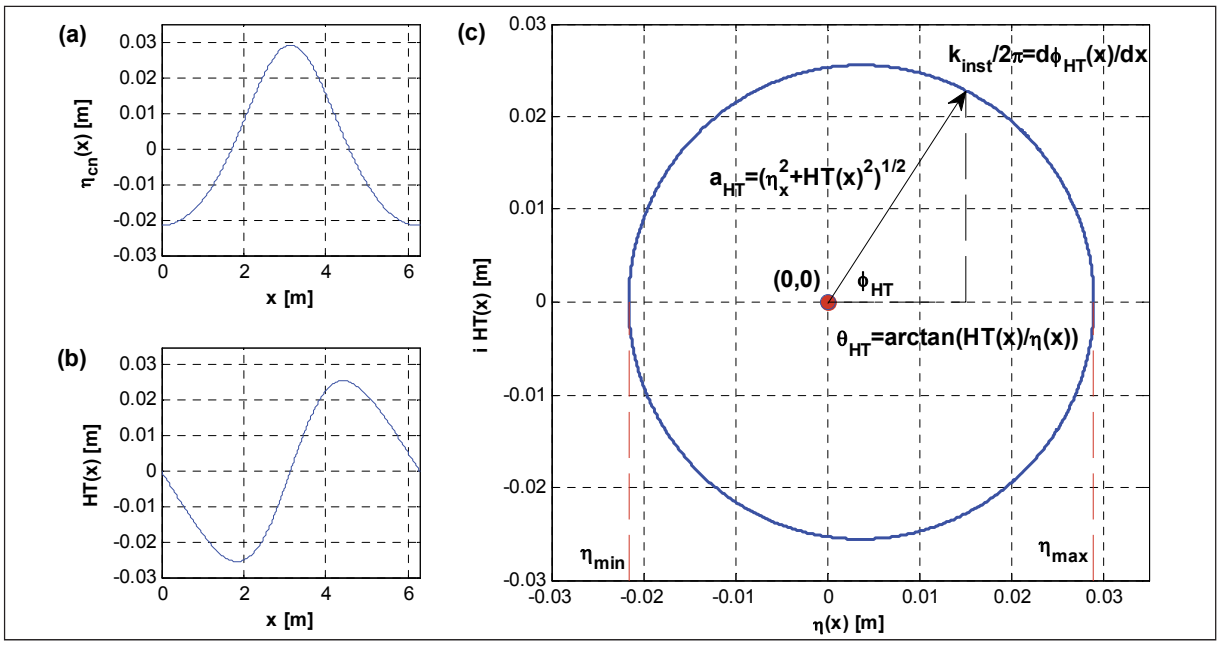

Fig. 3.7: Hilbert transform of the example wave (black line in Fig. 3.4): (a) real part $\eta_{cn}(x)$, (b) imaginary part *i HT(x)* and (c) Hilbert transform in the imaginary plane with $\eta_{cn}(x)$ and *i HT(x)*.

In the previous sections, two different approaches and definitions for the nonlinear character were introduced: (i) the Riemann matrix element B_{11} from the θ-function approach for cnoidal waves as function of the modulus and (ii) the degree of nonlinearity *DN* which is derived from the instantaneous Hilbert frequencies. If both definitions are applied to the same cnoidal waves, then an exponential relation between B_{11} and DN can be found (see Fig. 3.8):

$$DN = \exp(0.3177 - 0.4987 B_{11}), \quad \text{for } 2 \le B_{11} \le 20, \tag{3.5}$$

$$\ln DN = 0.3177 - 0.4987 B_{11}, \quad \text{for } 2 \le B_{11} \le 20. \tag{3.6}$$

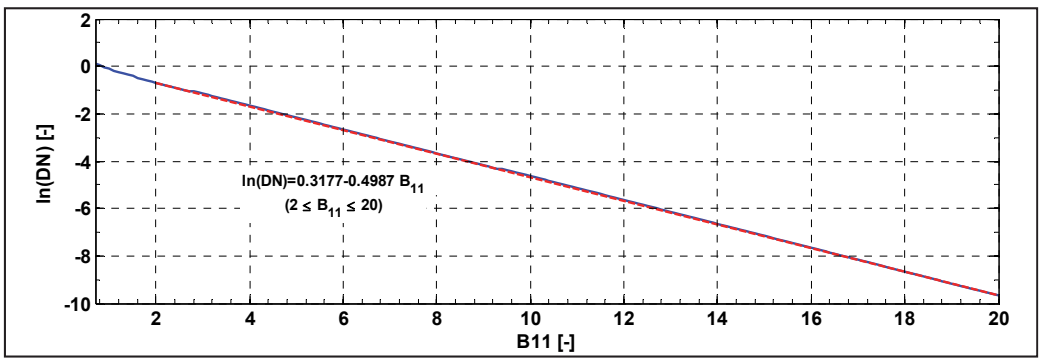

Fig. 3.8: Linear Relation between the logarithm of the degree of nonlinearity ln*(DN)* (based on the Hilbert transform) and the Riemann matrix elements B_{11} that were used in the θ-function approach to generate the cnoidal waves.

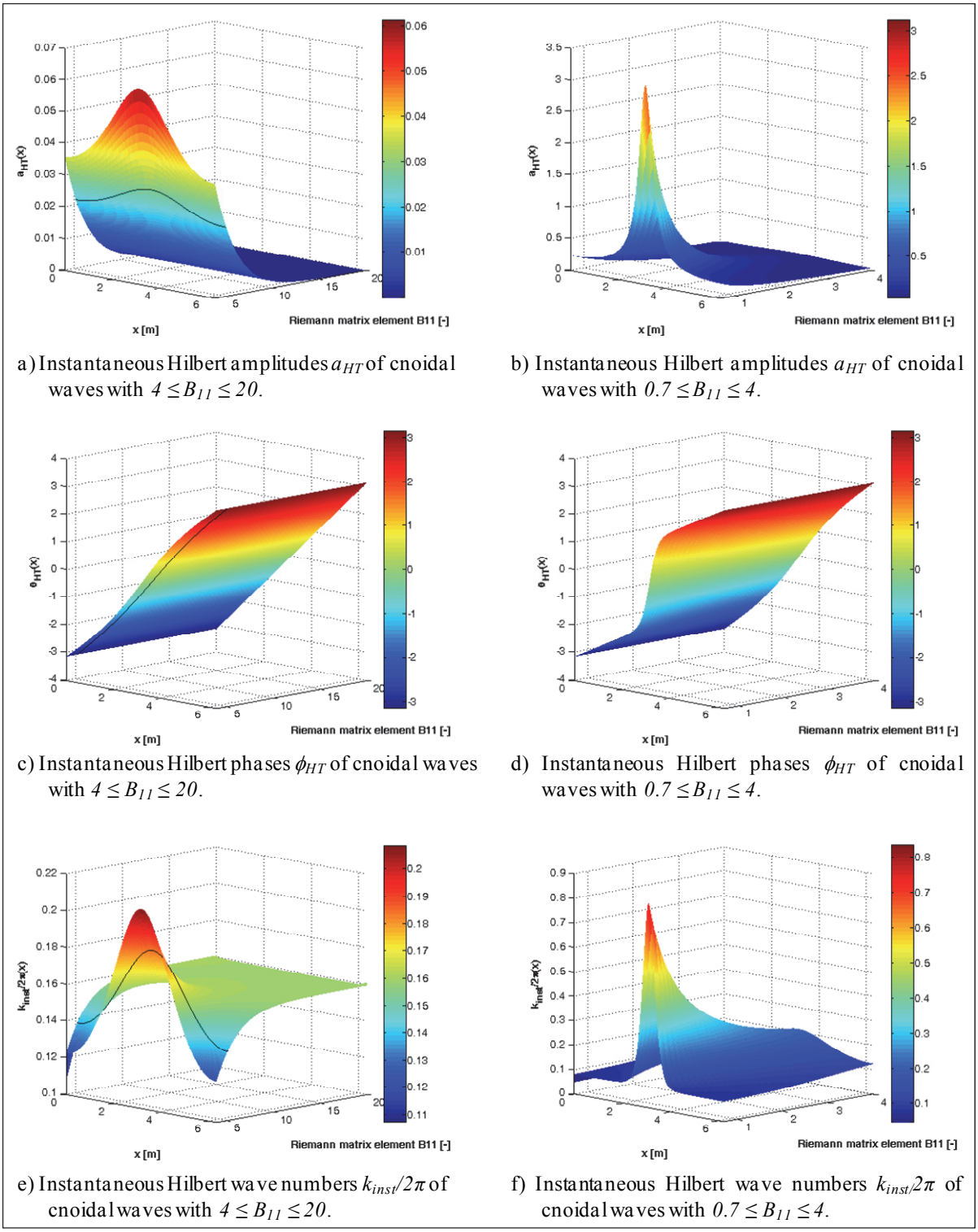

a) Instantaneous Hilbert amplitudes a_{HT} of cnoidal waves with $4 \leq B_{11} \leq 20$.

b) Instantaneous Hilbert amplitudes a_{HT} of cnoidal waves with $0.7 \leq B_{11} \leq 4$.

c) Instantaneous Hilbert phases ϕ_{HT} of cnoidal waves with $4 \leq B_{11} \leq 20$.

d) Instantaneous Hilbert phases ϕ_{HT} of cnoidal waves with $0.7 \leq B_{11} \leq 4$.

e) Instantaneous Hilbert wave numbers $k_{inst}/2\pi$ of cnoidal waves with $4 \leq B_{11} \leq 20$.

f) Instantaneous Hilbert wave numbers $k_{inst}/2\pi$ of cnoidal waves with $0.7 \leq B_{11} \leq 4$.

Fig. 3.9: Hilbert transform parameters of the cnoidal waves $\eta_{cn}(x)$ in Fig. 3.4 with $k=1m^{-1}$ in water depth $h=0.50m$ as function of B_{11}.

3.1.3 Temporal and spatial evolution of cnoidal waves

Cnoidal waves can easily be evolved in time and/or space by simply changing the values for x and/or t in Eqs. (2.35) to (2.37). Fig. 3.10 shows two examples for (a) the spatial evolution (constant time window and varying x) and (b) the temporal evolution (constant x range and varying t) of the cnoidal wave from the blue dash-dotted example in Fig. 3.4 with $B_{11}=5.2$,

H=0.05m, $k=1m^{-1}$ and *h=0.5m*. Although this wave is nonlinear and is decomposed in the conventional FFT into several cosine waves (see Fig. 3.6d)), as a *cnoidal waves* it propagates as *one single wave* in space and time without dispersion. If the waves are not generated by Eq. (2.35) but by linear superposition of the cosine components (e.g. in the inverse FFT), wave dispersion has to be considered. Then the linear higher-order components from FFT must not be allowed to propagate as free waves but have to be defined as phase-locked bound harmonics and their celerity must be the same as that of the first-order component. Fig. 3.11 shows the temporal evolution of the free (Fig. 3.11a) and phase-locked cosine components (Fig. 3.11b). Only the phase-locked propagation of the higher-order components provides the correct wave evolution.

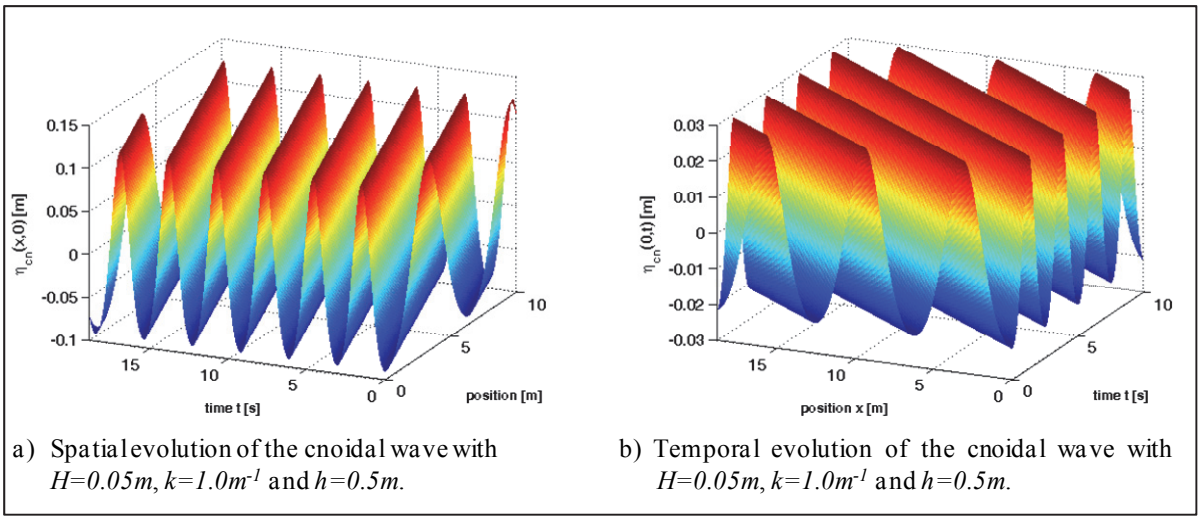

a) Spatial evolution of the cnoidal wave with *H=0.05m*, $k=1.0m^{-1}$ and *h=0.5m*.

b) Temporal evolution of the cnoidal wave with *H=0.05m*, $k=1.0m^{-1}$ and *h=0.5m*.

Fig. 3.10: Temporal and spatial evolution of the cnoidal wave with *H=0.05m*, $k=1.0m^{-1}$ and *h=0.5m*.

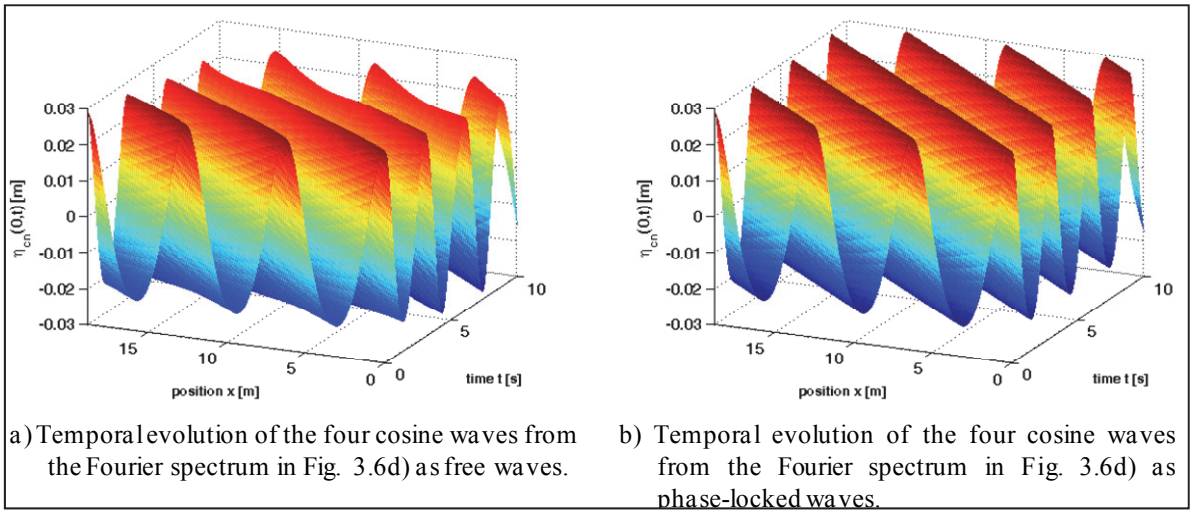

a) Temporal evolution of the four cosine waves from the Fourier spectrum in Fig. 3.6d) as free waves.

b) Temporal evolution of the four cosine waves from the Fourier spectrum in Fig. 3.6d) as phase-locked waves.

Fig. 3.11: Temporal evolution of the four cosine waves from the Fourier spectrum in Fig. 3.6d) as free and bound (phase-locked) waves.

This simple but very descriptive example shows that cnoidal waves evolve in space and time as only *one* wave component, described by only one term - the cnoidal wave equation in Eq. (2.35). The identification and distinction between free and bound harmonics is *not necessary* in the KdV-NLFT approach.

For very small values of modulus m cnoidal waves have cosine shape and therefore can be represented by a single cosine wave as in the Airy wave theory (Airy-like cnoidal waves). With increasing modulus the cnoidal wave changes from sinusoidal to higher-order wave shape. Since the conventional description of water surface waves in the Airy and Stokes wave theories is based on sinusoidal wave, additional harmonics are required to generate the nonlinear waves. Despite its harmonic representation in the FFT spectra in Fig. 3.6, a cnoidal waves has to be regarded to be just a monochromatic wave that is generated by only one frequency in terms of cnoidal waves. Therefore, it propagates as a monochromatic cnoidal wave without dispersion effects. Higher harmonic (phase-locked or bound) components as obtained in the FFT analysis are a mathematical tool to describe the nonlinear wave in terms of linear cosine waves. As was already shown in Fig. 3.11 and will be discussed further in section 3.2, by application of the nonlinear Fourier transform these mathematical harmonic artefacts are unnecessary. Furthermore, the examples in Fig. 3.10 and Fig. 3.11 show that the approach of phase-locked harmonics is a result of the limitations of the Fourier transform to really consider nonlinear waves. This drawback can be overcome by application of the cnoidal wave equation for the generation and evolution of shallow-water surface waves.

3.1.4 Nonlinear superposition of cnoidal waves with Riemann Θ-functions

By applying the Riemann Θ-function approach in Eqs. (2.39) to (2.42) the Jacobi θ-functions can be superposed nonlinearly, including the calculation of the nonlinear wave-wave interactions. This superposition is implemented within this thesis as a MATLAB code that directly uses the vector and matrix notations given in the equations. The following examples show the results of the nonlinear superposition of two Stokes-like waves and of two solitons, respectively.

The first example in Fig. 3.12 shows the nonlinear superposition of two cnoidal Stokes-like waves. The wave parameters are given in the caption of the figure. The subfigures show in the left column from top to bottom the first and the second cnoidal wave $\eta_{cn,1}(x)$ and $\eta_{cn,2}(x)$, their linear superposition $\eta_{cn,1+2}(x)$, the nonlinear interaction term $\eta_{int}(x)$and, finally, the free surface $\eta(x)$ which is the linear superposition of the two cnoidal waves and the interactions. The right column shows the conventional Fourier spectra of each of these components. For better clarity, the Fourier amplitudes are given in logarithmic scale. The FFT of the first cnoidal wave shows a total of seven clear peaks at $k=0.4m^{-1}$ and its integer multiples. The first two amplitudes are larger than 10^{-3} so that, based on the definitions used in section 3.1.2.1, this waves is classified as a Stokes2-like wave. Nevertheless, in the logarithmic representation given here five additional components with minor amplitudes are present.

The second wave has a higher value of B_{11}, but a shorter wave length so that its nonlinear character is slightly smaller than that of the first wave. As a consequence, the Fourier spectrum shows only five components whereof two have amplitudes higher than 10^{-3}. This wave also is also classified as a Stokes2-like wave. The third row in Fig. 3.12 shows the linear superposition of the two waves. The corresponding Fourier spectrum is determined directly from the superposed space series on the right, but is identical to the linear superposition of the two spectra shown in a) and b). Due to the high base line in spectrum b) some of the small amplitudes for higher k in spectrum a) are not visible. Note that the superposition spectrum in

c) only contains the frequency components that are already observed in the two spectra above, but no additional frequencies.

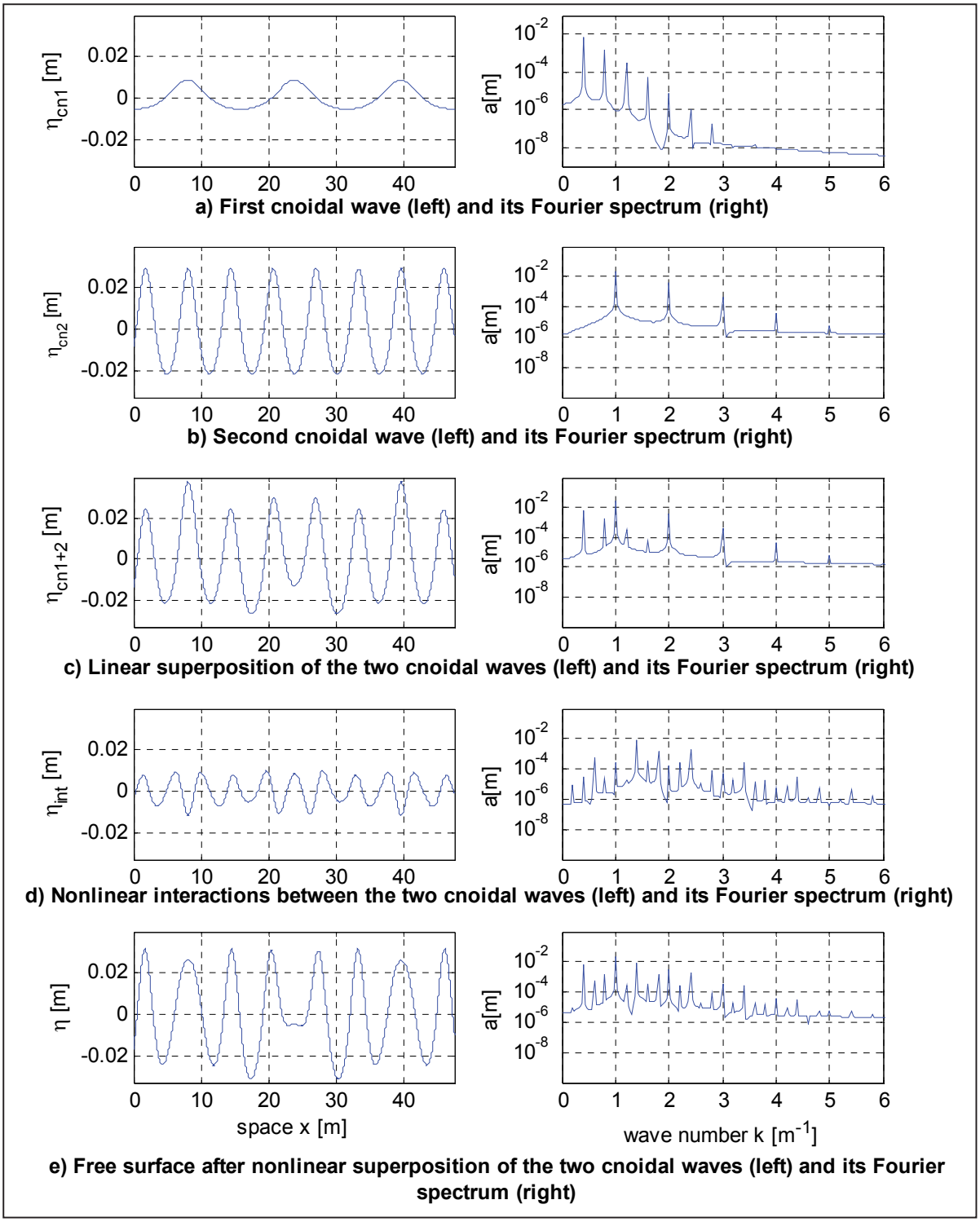

Fig. 3.12: Components of the nonlinear superposition of two Stokes-like waves with $B_{11,1}=4.2$, $k_1=0.4m^{-1}$, $\varphi_1=0rad$, $B_{11,2}=5.4$, $k_1=1\ m^{-1}$, $\varphi_1=\pi/2\ rad$ and $h=0.5m$.

In the nonlinear superposition by Riemann Θ-functions, the generation of sub- and superharmonic wave components is automatically considered and executed (see section 2.4.4). Therefore, the Fourier spectrum of the nonlinear interaction term in Fig. 3.12d contains several peaks at wave numbers that were not determined in the FFT spectra of the two basic waves in

Fig. 3.12a and b. Tab. 3.3 shows the wave number components of the two cnoidal waves and of all resulting sub- and superharmonics contained in the superposition spectrum in Fig. 3.12e. The wave numbers of the cnoidal waves are denoted as k_{1i} and k_{2j}, the wave numbers of the interactions as $k_{1i\pm2j}$. The first component in the spectrum in Fig. 3.12a is denoted as $k_{11}=0.4m^{-1}$, the second one as $k_{12}=0.8m^{-1}$, and so on. The subharmonic interaction between the first peak in spectrum a) and the third peak in spectrum b) is denoted as $k_{13\text{-}21}=1.2\text{-}1.0=0.2m^{-1}$, the corresponding superharmonic component is $k_{13+21}=1.2+1.0=2.2m^{-1}$.

The amplitudes for wave numbers $k<6$ can be observed in the Fourier spectra, for larger values of k the values are too small and are covered by the baseline in the spectrum. The amplitudes of the interaction components are functions of the off-diagonal Riemann matrix elements B_{ij}, $i\neq j$, as calculated by Eq. (2.44). The higher the difference between the wave numbers of the interacting cnoidal waves, the smaller are the interaction amplitudes. Finally, the free surface is composed of the basic cnoidal waves and their interactions. Therefore, the Fourier spectrum of the free surface $\eta(x)$ in Fig. 3.12e also can be regarded as to be composed by the spectra in a), b) and d).

Tab. 3.3: Table of the wave numbers of the cnoidal waves and their interactions for the nonlinear superposition of two Stokes2-like waves in Fig. 3.12 sorted by the resulting wave numbers.

k	components	k	components	k	Components
0.2	$k_{13\text{-}21}, k_{21\text{-}12}, k_{23\text{-}17}$	2.8	$k_{17}, k_{24\text{-}13}, k_{12+22}$	5.4	k_{11+25}, k_{16+23}
0.4	$k_{11}, k_{16-22}, k_{22-14}$	3.0	$k_{23}, k_{25-15}, k_{15+21}$	5.6	k_{14+24}
0.6	$k_{14-21}, k_{21-11}, k_{23-16}$	3.2	k_{24-12}, k_{13+22}	5.8	k_{12+25}, k_{17+23}
0.8	$k_{12}, k_{17-22}, k_{22-13}$	3.4	$k_{25-14}, k_{11+23}, k_{16+21}$	6.0	k_{15+24}
1.0	$k_{21}, k_{15-21}, k_{23-15}$	3.6	k_{24-11}, k_{14+22}	6.2	k_{13+25}
1.2	$k_{13}, k_{22-12}, k_{24-17}$	3.8	$k_{25-13}, k_{12+23}, k_{17+21}$	6.4	k_{16+24}
1.4	$k_{16-21}, k_{23-14}, k_{11+21}$	4.0	k_{24}, k_{15+22}	6.6	k_{14+25}
1.6	$k_{14}, k_{22-11}, k_{24-16}$	4.2	k_{25-12}, k_{13+23}	6.8	k_{17+24}
1.8	$k_{17-21}, k_{23-13}, k_{12+21}$	4.4	k_{11+24}, k_{16+22}	7.0	k_{15+25}
2.0	$k_{15}, k_{22}, k_{24-15}$	4.6	k_{25-11}, k_{14+23}	7.2	-
2.2	$k_{23-12}, k_{25-17}, k_{13+21}$	4.8	k_{12+24}, k_{17+22}	7.4	k_{16+25}
2.4	$k_{16}, k_{24-14}, k_{11+22}$	5.0	k_{25}, k_{15+23}	7.6	-
2.6	k_{23-11}, k_{14+21}	5.2	k_{13+24}	7.8	k_{17+25}

Fig. 3.13 shows a stacked plot of the Fourier amplitudes in Fig. 3.12e for $a>2.5\cdot10^{-4}$ that shows the origin of the amplitude components. The amplitudes that originate from the interactions are plotted in red, the amplitudes of the cnoidal waves in blue and green. This simple example shows the ability of the KdV-NLFT to distinguish the origin of FFT amplitudes, to identify bound and free harmonics and, furthermore, to provide their portions of each of the FFT amplitudes.

In a second example, the Riemann Θ-function approach is applied for the nonlinear superposition of two solitons (see Fig. 3.14). It is well-known in the literature (e.g. Brauer, 2004) and

many animations can be found in the internet showing that if two solitons with different wave height (and therefore different velocity) overtake each other, the resulting surface shape *during the collision* is strongly affected by nonlinear effects and does not look like the linear superposition of the two solitary waves. Instead, a reduction of the wave heights can be observed and the typical soliton shape is lost. *After the collision* the two solitons arise again with the same shape and velocity as before, but they are phase shifted (see Fig. 3.14). Analytical solutions of the KdV equation 2-soliton and 3-soliton case can be found in Brauer (2004).

Fig. 3.14 shows the overtaking process of two solitons at different time steps from the last to the first row. The solitons are travelling from left to right and the first solitons on the left side in the bottom row is going to overtake the smaller soliton on its right side. During the collision the amplitude is decreasing and finally the solitons is recovered after the overtaking process. Also the phase shift can be observed, exactly as known from the analytical solutions for the 2-soliton case. During the overtaking process and faster solitons merges with the smaller one from the left side, but evolves on the right side until it reached its initial shape and velocity (see Fig. 3.14). The only difference is that this faster solitons experienced a phase shift. This is visualized in Fig. 3.14 by means of two dashed lines, one for the larger soliton before the collision and one for the larger soliton after the collision. In case of a constant velocity without phase shift, the two dashed line would create one single instead of two parallel lines. The distance between them defines the phase shift between the incident and the evolved solitons.

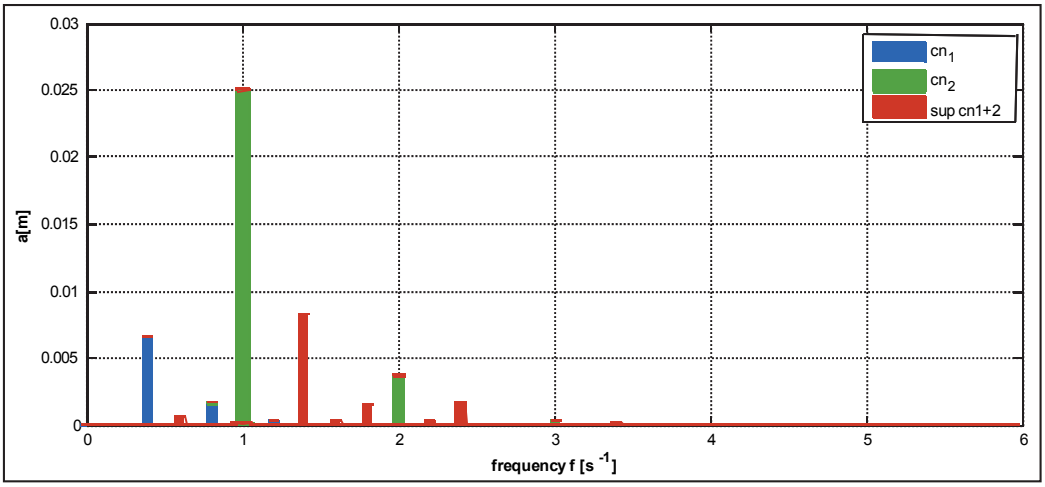

Fig. 3.13: Stacked Fourier amplitudes of the cnoidal waves and the interactions term from Fig. 3.12.

Note that the nonlinear superpositions in Fig. 3.12 and Fig. 3.14 are calculated with exactly the same numerical algorithm, the Riemann Θ-function approach. The only difference is the definition of the input parameters that define the two superposed cnoidal waves. In Fig. 3.12 relatively small values of the modulus m were used to generate and superpose Stokes-like waves, whereas in Fig. 3.14 high values of m were used to generate highly nonlinear solitary waves.

In this example, two solitons are superposed, but the algorithm is not restricted to a maximum number of waves, so that up to N solitons can be superposed as well as M oscillatory waves and N solitons. The limiting value is the required computation time, not the algorithm itself.

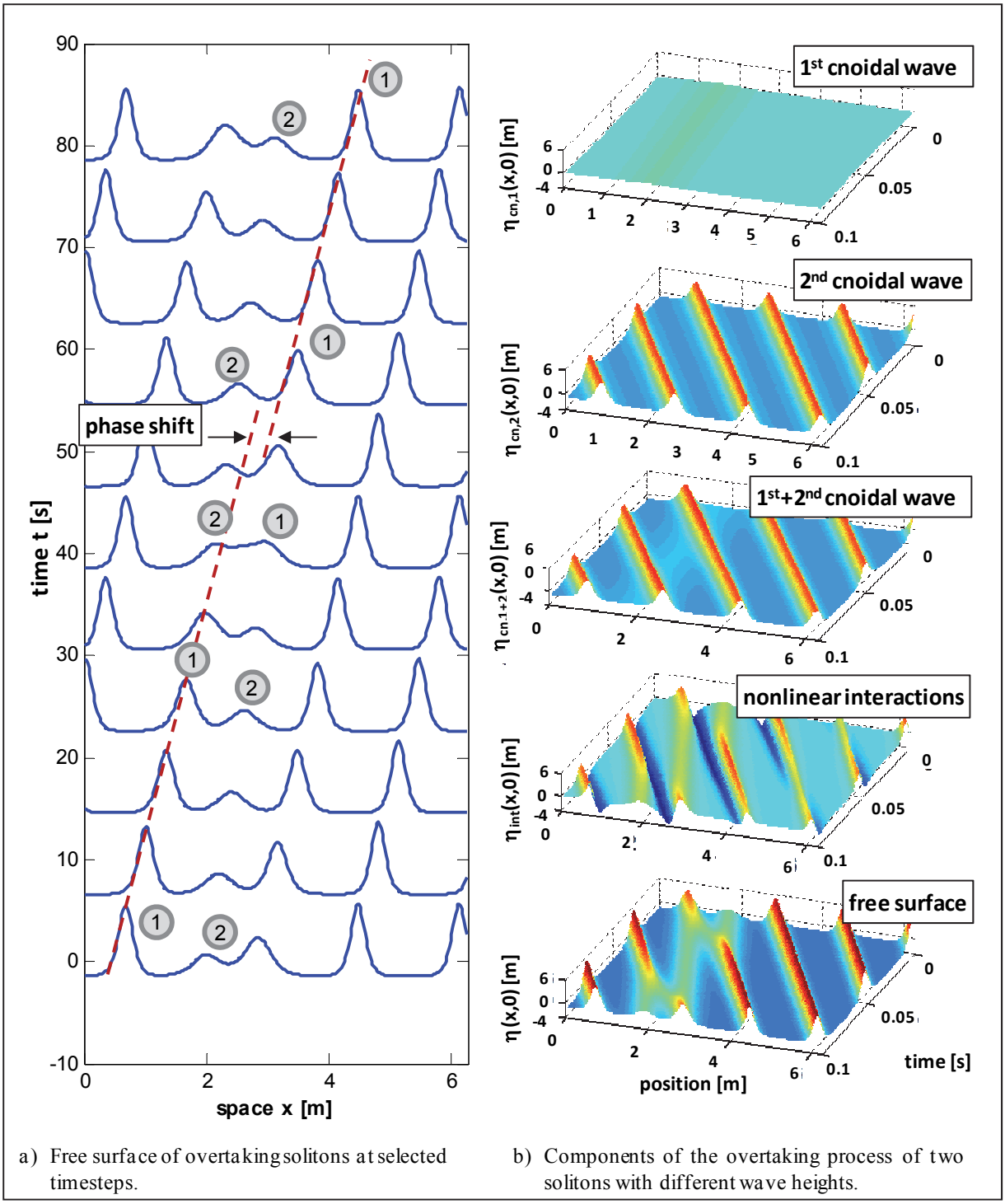

a) Free surface of overtaking solitons at selected timesteps.

b) Components of the overtaking process of two solitons with different wave heights.

Fig. 3.14: Overtaking process of two solitons with different wave heights.

3.2 Numerical implementation of the direct and inverse KdV-NLFT

The complete algorithm of the KdV-NLFT consists of two parts:

(i) the direct scattering transform (DST) that provides the nonlinear spectral decomposition of the free surface $\eta(x,t)$ into the basic cnoidal wave components $\eta_{cn,i}(x,t)$ (direct KdV-NLFT or dKdV-NLFT) either in μ- or θ-function representation (see sections 2.4.2, 2.4.5 and 2.5.3),

(ii) the inverse scattering transform (IST) as discussed in section 3.1 that returns the original data $\eta(x,t)$ by superposition of the cnoidal waves and their nonlinear interactions (inverse KdV-NLFT or iKdV-NLFT).

The results of the direct KdV-NLFT are presented in the nonlinear Fourier spectrum (for an examples see Fig. 3.16g and h) that contains the moduli m and amplitudes a (or A for solitons) as functions of wave numbers k (K) or frequencies f (F) of the cnoidal basic components in amplitude-frequency or energy-frequency pots (lower case characters for periodic waves, upper case for solitons). The phases φ (Φ) can be presented in an additional phase-frequency plot. This is analogous to the spectral decomposition and presentation of data within the conventional fast Fourier transform (FFT).

When the development and implementation of the KdV-NLFT was started by Osborne in the early 1980s (Osborne et al., 1982a; 1982b) the μ-function representation (see section 2.4.5) was used which also is a generalization of the conventional Fourier series approach. The application of the more powerful θ- and Θ-functions for the nonlinear Fourier transform was published the first time in Osborne (1995c), but in detail not until Osborne (2010). Due to several advantages that will be discussed in this section the implementation of the direct and inverse KdV-NLFT within this study focuses on the application of the Θ-function approach (see section 2.4.4). Nevertheless, the principles, the algorithms and most of the determined parameters for the μ- and Θ-function approaches in the direct KdV-NLFT are identical. Therefore, the descriptions given in the early publications on the μ-function approach are still valid, and updated descriptions of the direct KdV-NLFT with special respect to the Θ-functions are neither available nor necessary. Consequently, the following implementations and descriptions of the direct KdV-NLFT are given in terms of the hyperelliptic μ-functions.

3.2.1 Determination of the spectral parameters

The basic idea of the direct KdV-NLFT in terms of μ-functions is to decompose the original free surface $\eta(x,t)$ into N linearly superposed hyperelliptic functions $\mu_j(x;x_o,t)$, (with $1 \leq j \leq N$) (Osborne, 2010):

$$\lambda\eta(x,t) = -E_1 + \sum_{j=1}^{N}\Big[2\mu_j(x;x_o,t) - E_{2j} - E_{2j+1}\Big], \tag{2.47}$$

with λ as given in Eq. (2.3). The E_{2j}, E_{2j+1} are constant eigenvalues of the main spectrum of the periodic inverse scattering transform of the space-like KdV equation (2.2); x_o is referred to as an arbitrary base point in the periodic interval $0 \leq x_o \leq L_w$ (=the analysis window with length L_w). The μ_j are the nonlinear Fourier oscillation modes of the periodic KdV equation and they are thereby analogous to the sine waves in the linear Fourier analysis (Osborne, 1995a).

The main difference between μ- and θ-/Θ-functions is the way the nonlinear wave-wave interactions are considered. The θ-functions as introduced in section 2.4.2 represent the spectral nonlinear basic cnoidal-wave components of the decomposition. Note that one θ-function generates only one cnoidal wave and does not include any wave-wave interaction. As recently as the Θ-function approach is applied to the θ-functions, they are superposed nonlinearly by calculation of the explicitly arising nonlinear interactions. This *nonlinear superposition* con-

sists of the linear superposition of cnoidal basic components and the sum of their mutual nonlinear interactions (see section 2.4.4). In contrast, the μ-functions are not physical shallow-water wave as the cnoidal waves are in the θ-function approach. Instead, they are irregular oscillation modes that contain both, regular waves *and* interaction terms. Therefore, a distinct separation of nonlinear waves and their interactions is not possible with μ-functions.

Fig. 3.15 shows a typical spectral representation of a particular solution of the KdV equation in terms of μ-functions. The original example data $\eta(x,t)$ in (a) (broad line) is decomposed into six hyperelliptic functions (hyperelliptic oscillation modes) μ_1 to μ_6 which differ significantly from the regular cnoidal wave shape of the spectral basic components in the θ-function approach given in Fig. 2.10. Unlike the θ-functions the μ-functions represent the cnoidal basic components $\eta_{cn,j}(x,t)$ *and* their proportional nonlinear interaction modes $\eta_{int,j}(x,t)$ (= the modification of the free surface):

$$\mu_j(x,t) = \eta_{cn,j}(x,t) + \eta_{int,j}(x,t). \tag{3.7}$$

Note that the term $\eta_{int,j}(x,t)$ in Eq. (3.7) covers the summation of all proportional interactions of the $\eta_{cn,j}(x,t)$ with all other components $\eta_{cn,i\neq j}(x,t)$.

Osborne and Segre (1990) provide some important facts on μ-functions that help to better understand the nature of these hyperelliptic oscillation modes: The amplitudes of the μ-function are derived as the width of the so-called open bands in the Floquet discriminant $\Delta(E)$ shown in Fig. 3.15b. Details on this Floquet discriminant will be given later, but at this moment it is important to understand that the graph of the Floquet discriminant is adaptive and characteristic for the particular data that are analysed. Different wave trains provide different gradients of $\Delta(E)$, but for one given wave train the Floquet discriminant is independent of the phase of the data (exactly as in the conventional FFT). The gradient of $\Delta(E)$ is a function of $\eta(x,t)$ and contains all relevant spectral information that is required for the direct KdV-NLFT for both μ- and θ-function approaches. The amplitudes of the $\mu_j(x,t)$ are constant over space or time since the KdV-NLFT (as the conventional FFT) is a space or frequency domain analysis method even if the oscillation modes in Fig. 3.15, due to the influence of the nonlinear interactions, do not mirror these constant amplitudes. With decreasing wave nonlinearity, and thus decreasing nonlinear wave-wave interactions, the hyperelliptic functions $\mu_j(x,t)$ approximate the cnoidal waves $\eta_{cn,j}(x,t)$. In the absence of any nonlinear wave-wave interactions, e.g. a single cnoidal wave, applies $\mu_j(x,t) = \eta_{cn,j}(x,t)$.

Before starting the KdV-NLFT analysis, the initial data have to be pre-processed. The periodic inverse scattering transform (PIST) requires the conservation of mass in the considered analysis windows. Therefore, the water level has to be corrected to obtain the correct water depth for the soliton propagation. Let us consider a control volume of water without waves, then the still water level is the mean $\overline{\eta}(x,t)$. If inside this volume a soliton is generated in the middle of the considered box, then the conservation of mass implies that the water surface to the left and right of the wave crests will decrease (see Fig. 3.4d). The resulting depression level (*propagation* or *reference level*) represents the water depth on which the soliton propagates (see Fig. 3.15a). Since the shape of solitons (see Eq. (2.32)) and their celerity are functions of water depth, the knowledge of the reference level is significant (Osborne & Bergamasco, 1986).

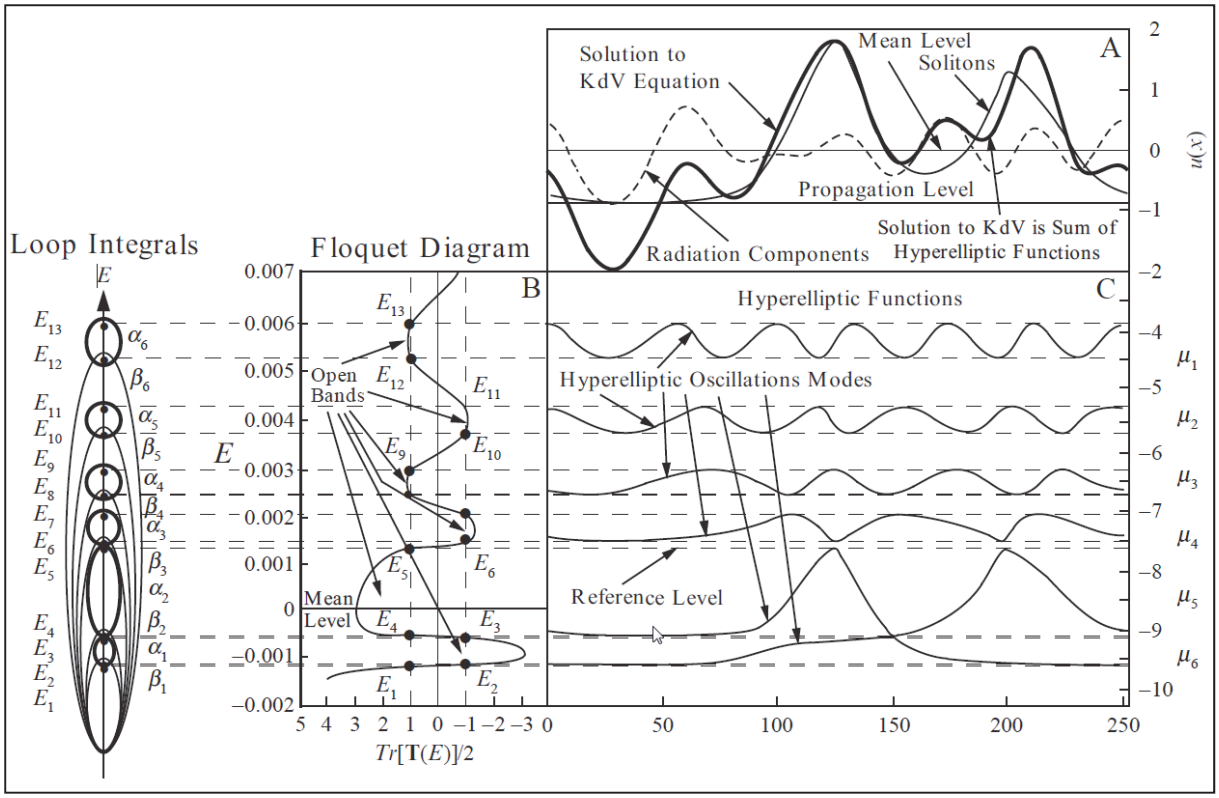

Fig. 3.15: Typical spectral representation of a particular solution of the KdV equation. Shown in (a) is a solution to KdV equation. In (b) the Floquet discriminant $\Delta(E)$ (the trace of the monodromy matrix as a function of $E=k^2$) is given that has exactly six open bands (degrees of freedom) in the spectrum. Shown in (c) are the six hyperelliptic function oscillation modes. The linear superposition of these six modes gives the exact solution to KdV equation shown in (a) (Osborne, 2010).

In Fig. 3.15c, the components μ_5 and μ_6 represent solitons, the components μ_1 to μ_4 are oscillatory waves, each including proportional nonlinear interactions. With increasing wave number, the number of oscillations within the hyperelliptic functions increases: The function μ_6 shows one oscillation, the function μ_5 two oscillations and so on. The nonlinear interactions can be of the same order of magnitude as the cnoidal wave itself (as already shown in section 3.1.4 and Fig. 3.14). Therefore, the nonlinear interaction terms can generally not be considered as negligible.

In the direct KdV-NLFT the direct spectral problem for the KdV equation, namely the Schroedinger eigenvalue problem, has to be solved for periodic boundary conditions $\eta_0(x,t) = \eta_0(x + L_{sp}, t)$ or $\eta_0(x,t) = \eta_0(x, t + T_{tf})$ with L_{sp} the spatial period (=the width of the analysis window) and T_{tf} the length of the analysed time frame. The Schroedinger eigenvalue problem is (Osborne & Bergamasco, 1986):

$$\psi_{xx} + \left[\lambda\eta(x) + k^2\right]\psi = 0, \quad (k^2 = E), \tag{2.53}$$

with $\eta(x) = \eta(x,0)$ the solution to the KdV equation (2.2) at arbitrary time $t=0$. The E_j are eigenvalues and $k_j = \sqrt{E_j}$ are the wave numbers of the basic components μ_i.

The solution of Eq. (2.53) for a measured space (or time) series provides all required information to calculate the parameters that are presented in the nonlinear Fourier spectrum. While

solving the Schroedinger eigenvalue problem, a monodromy matrix $\boldsymbol{M}$ is calculated and the trace of this matrix is called the Floquet discriminant $\Delta(E) = 1/2 \cdot Tr\ \mathbf{M}$. Fig. 3.15b shows the Floquet discriminant of the space series in Fig. 3.15a. The solutions of Eq. (2.53) from x to $x+L_{sp}$ are defined by the characteristics of the Floquet discriminant, especially by the positions where $\Delta(E)=\pm 1$. Two adjacent crossings of the eigenvalues at $+1$ or -1 define an open band (e.g. (E_2, E_3)) in Fig. 3.15b, or more general, (E_{2j}, E_{2j+1}) if between these points applies $|\Delta(E)|>1$. The oscillatory waves (which are denoted as *radiation components*) in the spectrum are defined by the open bands whose eigenvalues are larger that the reference level $(E_{2j}, E_{2j+1})>E_{ref}$. The difference between E_{2j} and E_{2j+1} (the width of an open band) defines the amplitude a_j of the corresponding hyperelliptic function $\mu_j(x,t)$ (Osborne et al., 1988):

$$a_j(k_j) = |\mu_j| = (E_{2j+1} - E_{2j})/(2\lambda) \qquad \text{for} \qquad (E_{2j}, E_{2j+1}) > E_{ref}\,. \tag{3.8}$$

This relation is illustrated in Fig. 3.15b and c (e.g. (E_6,E_7) for μ_4, (E_8,E_9) for μ_3, …). If $E_{2j}=E_{2j+1}$, for the Floquet discriminant applies $|\Delta(E)(E_{2j})|=1$ and therefore it is only touching but not crossing the ± 1-lines. In this case the band is denoted *degenerated* and the amplitude of the hyperelliptic mode is zero (see Eq. (3.8)). The eigenvalues (E_{2j} , E_{2j+1}) of the open or the degenerated bands define the wave numbers k_j and K_n of the oscillatory or solitary basic components (Osborne et al., 1988):

$$k_j = \sqrt{\overline{E}_j}, \quad K_n = \sqrt{\overline{E}_n} \tag{3.9}$$

with $\overline{E}_j$ the centre of the open bands or the contact point if the $a_j(k_j)=0$ (Osborne & Bergamasco, 1986):

$$\overline{E}_j = (E_{2j+1} - E_{2j})/2. \tag{3.10}$$

The amplitudes A_n of the solitons are calculated using the reference level E_{ref} and the eigenvalues determined from the Floquet discriminant that are smaller than E_{ref} (Osborne et al., 1988):

$$A_n = 2(E_{ref} - E_{2n})/\lambda \quad \text{for } E_{2n} < E_{ref}\,. \tag{3.11}$$

In Fig. 3.15b the soliton amplitude for μ_5 is calculated using E_{ref} and E_4, the amplitude for μ_6 with E_{ref} and E_2.

For the distinction between solitons (modulus $m_j>0.99$) and oscillatory waves ($0 \le m_j \le 0.99$) the modulus m_j is calculated (Osborne et al., 1988):

$$m_j = \frac{E_{2j+1} - E_{2j}}{E_{2j+1} - E_{2j-1}}. \tag{3.12}$$

The direct KdV-NLFT determines the amplitudes A_n and phases Φ_n of the solitons and the amplitudes a_j, wave numbers k_j and phases φ_j of the oscillatory waves, and the modulus m_j for each of the waves. These data are referred to as the main spectrum. The hyperelliptic functions that provided by the inverse scattering transform (IST) are called the auxiliary spectrum.

Further details for the theoretical background and the algorithms of the DST and IST, the solution of the eigenvalue problem and the numerical implementation can be found in Osborne

(1991b), Provenzale and Osborne (1991), Christov (2009) and Osborne et al. (1991) and especially in Osborne (2010). Detailed examples for the calculation of the soliton and oscillatory wave amplitudes from the Floquet discriminant $\Delta(E)$ are given in the next section.

3.2.2 Examples for the calculation of the spectral parameters from simulated space series

To better illustrate the benefit and the practical application of the KdV-NLFT, two example wave trains from numerical simulations for the analysis of soliton fission in chapter 4 are selected in Fig. 3.16. The two wave trains are recorded (i) over the reef with an infinite width (Fig. 3.16a) and (ii) behind a reef with finite width $b_r=10.0m$ (Fig. 3.16b). The wave train in Fig. 3.16a contains 8 clearly distinguishable solitons and three more peaks inside the bore that might later evolve as solitons. The water depth over the reef is $d_r=0.1m$ and therefore the relation between nonlinearity and dispersion over the reef from Eq. (2.3) is $\lambda=1500m^{-3}$. For the consideration of the propagation level the initial wave train (blue) is shifted in Fig. 3.16a by the mean of the data $\eta_{ref}=-0.0028m$ (red curve). The corrected water depth for the propagation of the solitons over the reef is $h_{ref}=0.10-0.0028=0.0972m$. Fig. 3.16b shows the Floquet discriminant $\Delta(E)$ of the data in Fig. 3.16a, and in Fig. 3.16c a detail of Fig. 3.16b is given. For better clearance, the vertical scale is logarithmic for $|\Delta(E)|>1$ and linear for $|\Delta(E)|\leq 1$. The reference level E_{ref} in Fig. 3.16c is at $E_{ref}=\lambda\cdot\eta_{ref}=1500\cdot0.0028=4.21m^{-2}$. In the figure, some ±1-crossings of the Floquet discriminant are denoted with their serial numbers E_1, E_2, … . The nonlinear spectrum in Fig. 3.16g shows 16 solitons in the original data. The soliton amplitudes are derived from Eq. (3.11). For the first soliton amplitude applies (for the numerical values see Fig. 3.16c):

$$A_1 = 2(E_{ref} - E_2)/\lambda = 2\cdot(4.21-(-17.687))/\lambda = 0.029m. \qquad (3.13)$$

The calculated amplitudes of the next solitons are $A_2=0.023m$, $A_3=0.022m$, $A_4=0.021m$, $A_5=0.0195m$ and $A_6=0.0179m$. For the determination of the soliton wave heights from the wave train the reference level has to be considered. The solitons are assumed to travel in a reduced water depth which has to be considered in the following way: The height of the first peaks in the wave train from visual observation is $A_1''=0.026m$ with respect to $\eta=0$ referring to water depth $h=0.10m$. Consideration of the lower propagation level provides a soliton amplitude of $A_1'=0.026+0.0028=0.0288m$. For the following five soliton amplitudes applies $A_2'=0.023m$, $A_3'=0.022m$, $A_4'=0.021m$, $A_5'=0.019m$ and $A_6'=0.018m$. The results show a very good agreement between the calculated and measured amplitudes.

Fig. 3.16e shows a detail of the Floquet discriminant with the open bands of the oscillatory wave on the left side of the reference level. According to Eq. (3.8), for the amplitude of the oscillatory basic component $j=21$ with (E_{42}, E_{43}) applies:

$$a_{21}(k_{21}) = (E_{43} - E_{42})/(2\cdot\lambda) = (4.8402 - 4.5885))/(2\cdot1500) = 8.49\cdot10^{-5}m. \qquad (3.14)$$

The range of the eigenvalues (here: $E_{min}=-20$ and $E_{max}=15$) has to be defined before the analysis. This corresponds to the filter definition before applying the conventional FFT. E_{max} defines the maximum determined wave number of the oscillatory waves and E_{min} has to be chosen with respect to the eigenvalue of the highest soliton. Fig. 3.16g shows the nonlinear Fourier spectrum that consists of the soliton spectrum with the determined 16 soliton ampli-

tudes (red bars) and the radiation spectrum with the amplitudes of the oscillatory waves (blue line). Furthermore, the modulus *m* is plotted (green dashed line) that defines the type of cnoidal wave. In this example, within the pre-defined range of eigenvalues a total number of 32 oscillatory waves ('radiation components') are determined. In the spectrum, the wave type (Airy-like, Stokes-like,...) of each of the basic elements can easily be determined by the value of the corresponding modulus m_j and the classification as given in Fig. 2.5.

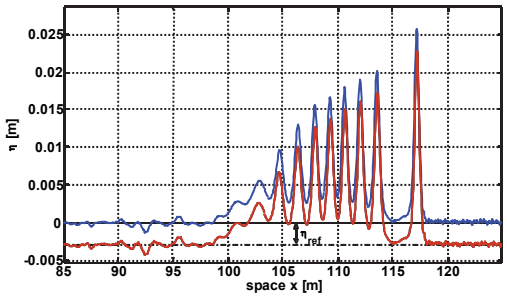

a) Data for KdV-NLFT analysis over reef with infinite width and water level correction by reference level at $t=80s$.

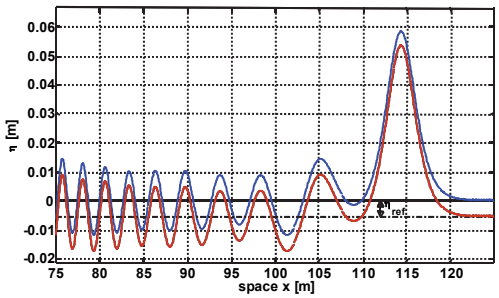

b) Data for KdV-NLFT analysis over reef with finite width ($b_r=10.0m$) and water level correction by reference level at $t=48s$.

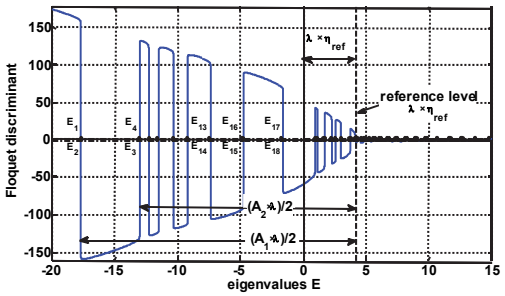

c) Floquet discriminant of the wave train in a).

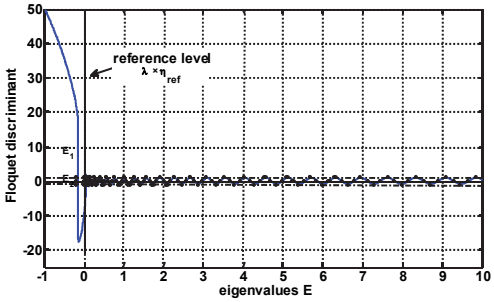

d) Floquet discriminant of the wave train in b).

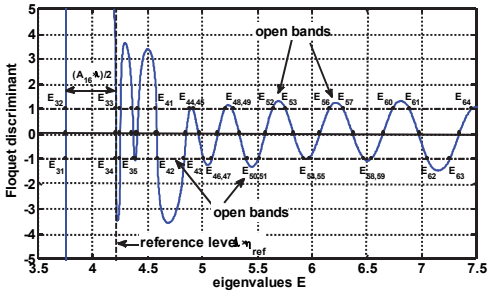

e) Detail of the Floquet discriminant in c).

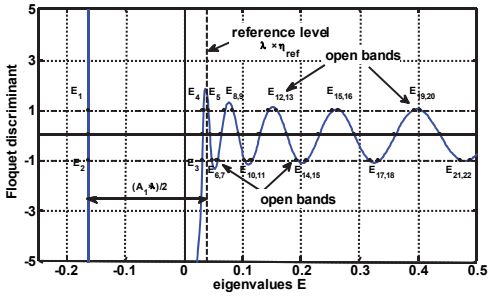

f) Detail of the Floquet discriminant in d).

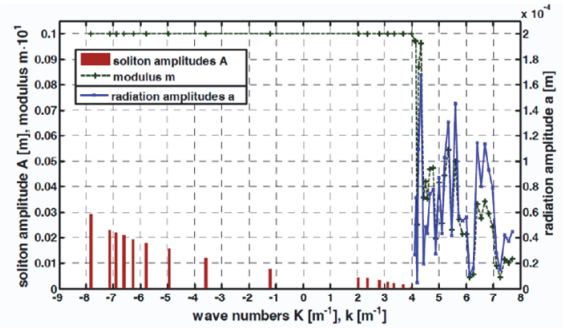

g) Nonlinear spectrum of the wave train in a).

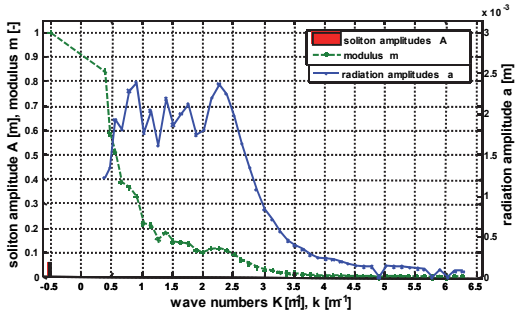

h) Nonlinear spectrum of the wave train in b).

Fig. 3.16: Example of the application of the KdV-NLFT to wave trains with solitons.

As an example for a signal with only one soliton, but more oscillatory waves with significant amplitudes, Fig. 3.16b shows the original data of the transmitted wave behind a reef with finite width. In this example applies $\lambda=6.944m^{-3}$ ($h=0.60m$). The reference level correction is $\eta_{ref}=-0.0054m$, and the water depth for the propagation of the solitons behind the reef is $h_{ref}=0.60-0.0054=0.5946m$. Fig. 3.16d shows the Floquet discriminant $\Delta(E)$ of the data in Fig. 3.16b. The reference level E_{ref} in the figure is at $E_{ref}=\lambda\eta_{ref}=6.944\cdot0.0054=0.037m^{-2}$ (see the detail in Fig. 3.16f). The Floquet discriminant shows only one soliton with amplitude

$$A_1 = 2(Eref - E_2)/\lambda = 2\cdot(0.037-(-0.163))/\lambda = 0.057m. \tag{3.15}$$

The height of the first peak in the wave train is $A_1''=0.0589m$. Consideration of the reference level correction provides $A_1'=0.0589+0.0054=0.0643m$. The measured and the calculated results agree quite well with a difference of $0.0073m$ (12.8% deviation from the calculated value A_1). The number of oscillatory waves in the Floquet discriminant is 49.

Until now, the explanation for the deviation between the KdV-NLFT results and the soliton amplitudes determined from visual observation cannot be given finally. Most probably, the reason is that the solitons are still within the bore and are subject to nonlinear interactions that reduce the visible height of the solitons at the free surface. This effect can be clearly seen in Fig. 3.14, where the nonlinear interactions significantly reduce the elevation of the free surface during the overtaking process. The overtaking solitons reaches its initial amplitude not until it completely stepped out of the overtaking process. In the undular bore in Fig. 3.16a, the solitons are still within in the bore, so that they have not yet recovered their initial height.

Fig. 3.16h shows the nonlinear Fourier spectrum of the wave train in Fig. 3.16b. As already mentioned, the soliton spectrum shows only one single soliton. This confirms the assumption from the visual observation of the wave train. The results of the NLFT and the nonlinear Fourier spectrum clearly show that the original data of the transmitted waves behind the reef with finite width consist of only one leading soliton and then trailing oscillatory waves. No trailing soliton is identified.

This example shows the capability of the NLFT for the analysis of shallow-water waves with high and low numbers of solitons. Furthermore, a more detailed analysis of the nonlinear spectrum shows the nonlinear character of the determined basic components: The higher the modulus m of an oscillatory wave, the higher is the nonlinearity of the wave and its corresponding nonlinear wave-wave interactions.

The most important implication for the further application of the KdV-NLFT is that this nonlinear analysis method is adaptive within the limits of the cnoidal wave equation. The specific type of the cnoidal wave (Airy-like, Stokes-like, cnoidal-like or solitary-like) and their number are *not predefined*. For each signal the individual required number of each of these wave types is determined. Furthermore, for each of the frequency components the nonlinear character is adaptive and strongly dependent on the original data. For example, the two cnoidal waves with $k=5.0m^{-1}$ in both spectra in Fig. 3.16 are examined. For the strongly nonlinear signal in Fig. 3.16a in the spectrum, the modulus is determined as $m=0.042$ (Stokes-like wave). For the reconstruction of the relatively weakly nonlinear data in Fig. 3.16b the component with $k=5.0m^{-1}$ requires a value of only $m=0.05$ and represents a nearly linear Airy-like wave. Furthermore, due to the influence of the water depth the minimum frequency or wave number of the oscillatory waves is adaptive. In the nonlinear spectrum in Fig. 3.16g the

minimum wave number of the oscillatory waves is $k>4.0m^{-1}$. All components with smaller values (and therefore larger wave lengths) are solitons. The reason is that due to the small water depth, oscillatory waves that are longer than those with the minimum value of k are not solutions to the KdV equation for these boundary conditions, but solitons are possible solutions. For larger water depths as for the data in Fig. 3.16b, longer oscillatory waves are possible solutions and therefore in the nonlinear spectrum in Fig. 3.16i the minimum wave number of oscillatory waves is $k=0.375m^{-1}$.

3.3 Comparative spectral analysis of the generated cnoidal waves using FFT and KdV-NLFT

In this section, sample waves from conventional wave theories and the cnoidal wave equation are comparatively analysed using the implemented KdV-NLFT and the conventional FFT. The purpose of the procedure is to show (i) that the cnoidal-equation waves also can be generated by application of the conventional wave theories, (ii) that the spectral properties in FFT are identical and (iii) that by application of the KdV-NLFT the problem of higher-harmonic waves is not existent.

In the previous sections, two basic approaches were reported for the generation of different types of shallow-water waves:

(i) the conventional approach with various *wave theories* and

(ii) the comprehensive method of using only one *cnoidal wave equation* in terms of Jacobi θ-functions for all types of waves in shallow water.

Both conventional wave theories and the cnoidal wave equation are now applied to generate waves. Based on the boundary conditions of the numerical simulations and the KdV-NLFT analyses in Brühl and Oumeraci (2011), Fig. 3.17 shows waves that are generated for a water depth of $h=0.6m$ (i) using conventional wave theories (Eqs. (2.15), (2.17), (2.18), (2.19), (2.24) and (2.32)) and (ii) as cnoidal waves in terms of theta functions (Eq. (2.35) and (2.36)). The left column contains the wave profiles, the corresponding linear Fourier spectra are given in the centre column and the right column shows the corresponding nonlinear spectra. Selected examples of the cnoidal-equation waves are already given in Fig. 2.8.

First, a linear wave is generated using Airy wave theory (see Fig. 3.17a, left plot). This wave is analysed by conventional Fourier transform (centre plot) and nonlinear Fourier analysis (right plot). The amplitude of the generated Airy wave is $a=0.01m$ and the wave number $k=5.240m^{-1}$ (see Tab. 3.4). The Airy-like wave is generated with the same amplitude and wave number by generating a cnoidal wave with a modulus of $m=0.01$ and the values given in Tab. 3.4. In the conventional Fourier spectrum, the results for Airy and Airy-like wave are the same. The same also applies for the results of the nonlinear Fourier transform. Furthermore, for these linear waves the KdV-NLFT provides exactly the same results as the FFT and confirms that for the case of linear waves the results of the KdV-NLFT reduce to those of the conventional FFT. This is, however, not the case for second-order Stokes waves (Stokes2, Fig. 3.17c and Fig. 3.17d) where the differences between the results of FFT and KdV-NLFT exist. In FFT, the higher-order waves are reconstructed by superposing an increasing number of higher-order harmonic wave components, exactly in the same way as the second-order and fifth-order waves are generated in Stokes wave theory (see Eqs. (2.17) and (2.18)). This pro-

cedure is necessary for the reconstruction of the nonlinear wave shape with higher crests and wider troughs in the conventional wave theories that use linear superpositions of sinusoidal waves. Tab. 3.4 shows the number of significant spectral components and the amplitudes and wave numbers of the first two spectral components. The same procedure is applied for waves from Stokes5 (Fig. 3.17e), cnoidal (Fig. 3.17g) and solitary wave theory (Fig. 3.17i). In contrast, Fig. 3.17f, Fig. 3.17h and Fig. 3.17j show the corresponding waves generated using the cnoidal wave equation in terms of θ-functions and the corresponding linear and nonlinear Fourier spectra.

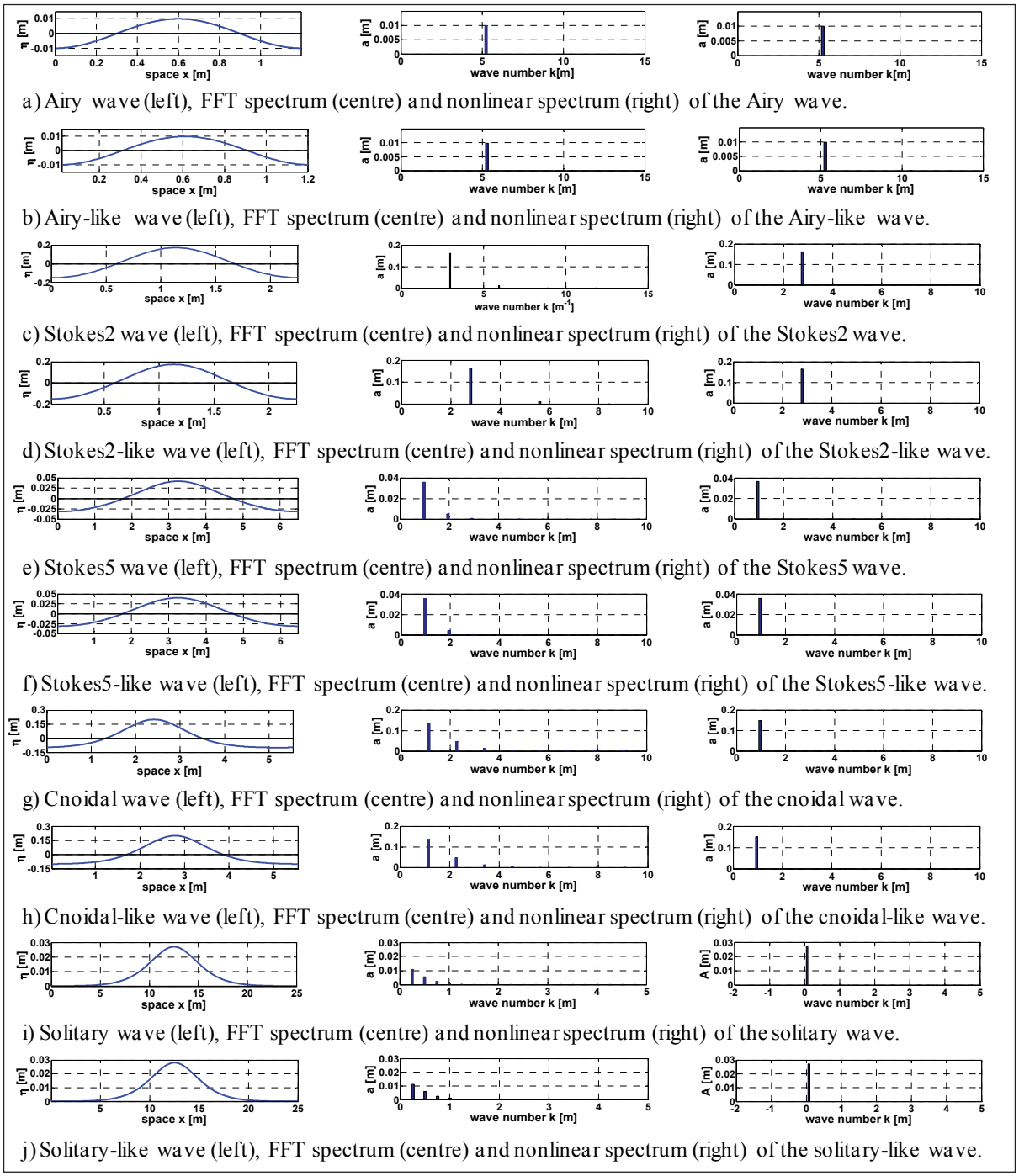

a) Airy wave (left), FFT spectrum (centre) and nonlinear spectrum (right) of the Airy wave.

b) Airy-like wave (left), FFT spectrum (centre) and nonlinear spectrum (right) of the Airy-like wave.

c) Stokes2 wave (left), FFT spectrum (centre) and nonlinear spectrum (right) of the Stokes2 wave.

d) Stokes2-like wave (left), FFT spectrum (centre) and nonlinear spectrum (right) of the Stokes2-like wave.

e) Stokes5 wave (left), FFT spectrum (centre) and nonlinear spectrum (right) of the Stokes5 wave.

f) Stokes5-like wave (left), FFT spectrum (centre) and nonlinear spectrum (right) of the Stokes5-like wave.

g) Cnoidal wave (left), FFT spectrum (centre) and nonlinear spectrum (right) of the cnoidal wave.

h) Cnoidal-like wave (left), FFT spectrum (centre) and nonlinear spectrum (right) of the cnoidal-like wave.

i) Solitary wave (left), FFT spectrum (centre) and nonlinear spectrum (right) of the solitary wave.

j) Solitary-like wave (left), FFT spectrum (centre) and nonlinear spectrum (right) of the solitary-like wave.

Fig. 3.17: Wave profiles, conventional FFT spectra and nonlinear KdV-NLFT spectra for different wave types generated from wave theories and the cnoidal wave equation in terms of θ-functions (water depth $h=0.6m$). For details see Tab. 3.4.

The direct comparison of the results between the waves from conventional wave theories and cnoidal wave equation in Fig. 3.17 and Tab. 3.4 shows that the generation of shallow water waves from conventional wave theories and from cnoidal wave equation are equivalent. Both approaches provide waves with the same shape and the same spectral properties in the FFT spectrum and the same spectral components in the nonlinear KdV-NLFT spectrum. In KdV-NLFT, every nonlinear wave that represents a solution of the cnoidal wave equation is a possible basic component in the spectral decomposition in the KdV-NLFT. This is the most important difference to the conventional Fourier transform which is limited to sinusoidal spectral components. The cnoidal wave equation can be used to generate waves with shapes equal to those described by conventional wave theories such as Airy, Stokes2, Stokes5, cnoidal or solitary wave theory. For the generation of waves in Stokes5 wave theory, up to five different cosine waves are linearly superposed. Consequently, the conventional FFT decomposes the Stokes5 wave into these five spectral components, which are the fundamental first-order component and four higher harmonic waves (see Fig. 3.17e and Fig. 3.17f). In KdV-NLFT, however, the Stokes5-like wave, which has the same properties as the Stokes5 wave, is considered as *only one spectral component* that solves the cnoidal wave equation. In this approach, the Stokes5 wave is regarded to represent *only one* real physical shallow water wave, and unlike in FFT, it is not decomposed into further spectral components. This is the reason why the nonlinear spectra of the Stokes5 and Stokes5-like waves show only one component and do not contain higher harmonic components as shown in the conventional linear Fourier spectrum. The same applies for Stokes2, cnoidal and solitary waves from the conventional wave theories (see Tab. 3.4). Therefore, the higher harmonics in the conventional FFT are identified as mathematical artefacts that are caused by the decomposition of *nonlinear* shallow water waves into *linear* sinusoidal spectral basic components. By application of the KdV-NLFT these mathematical artefacts are not required and the original data are decomposed into real nonlinear shallow-water waves without further decomposition into linear sinusoidal waves.

Tab. 3.4: Results of conventional FFT and nonlinear Fourier transform (KdV-NLFT) for the data in Fig. 3.17.

generated wave				results from FFT			results from KdV-NLFT			
wave type	a_{gen}	k_{gen}	m_{gen}	N_{FFT}	a_{FFT}	k_{FFt}	N_{NLFT}	a_{NLFT}	k_{NLFt}	m_{NLFT}
Airy	0.010	5.240	-	1	0.010	5.236	1	0.010	5.236	0.010
Airy-like	0.010	5.236	0.010	1	0.010	5.280	1	0.010	5.280	0.010
Stokes2	0.162	2.793	-	2	0.164, 0.011	2.805, 5.561	1	0.162	2.765	0.442
Stokes2-like	0.164	2.793	0.441	2	0.161, 0.010	2.978, 5.956	1	0.164	2.790	0.439
Stokes5	0.037	0.970	-	4	0.036, 0.005	0.968, 1.936	1	0.037	0.951	0.657
Stokes5-like	0.036	0.970	0.646	3	0.035, 0.005	0.973, 1.948	1	0.036	0.958	0.648
cnoidal	0.150	1.123	0.950	6	0.137, 0.047	1.132, 2.264	1	0.150	0.948	0.950
cnoidal-like	0.150	1.132	0.950	6	0.137, 0.047	1.134, 2.268	1	0.150	0.951	0.949
solitary	0.027	(0.251*)	-	5	0.011, 0.006	0.251, 0.502	1	0.027	(0.072**)	0.994
solitary-like	0.028	(0.251*)	0.993	6	0.011, 0.006	0.251, 0.503	1	0.027	(0.072**)	0.994

*: calculated wave length: $k_{gen}=2\pi$/length of generated solitary wave. **: real part of imaginary wave number K in KdV-NLFT

One of the conclusions of this comparison is that for the analysis of nonlinear waves in shallow-water, the FFT *does not consider* real physical shallow-water waves. It is rather an approximate solution that decomposes these nonlinear waves into basic sinusoidal waves and higher harmonic components ("mathematical artefacts"). In contrast, the KdV-NLFT is an exact solution that *does consider* these nonlinear waves as basic components, and therefore the nonlinear waves are identified as intrinsic nonlinear waves without further decomposition.

Finally, the comparative analyses of data from conventional wave theories and the cnoidal wave equation in θ-function representation have shown that:

(i) The θ-function representation for cnoidal waves provides exactly the same waves as the four conventional wave theories that are applied for the wave generation in coastal engineering (see Fig. 2.5). The conventional *four-theory* system can be replaced by the single cnoidal wave equation.

(ii) Both waves generated by conventional wave theories and from cnoidal wave equation are considered in the KdV-NLFT to be monochromatic waves, even if they are strongly nonlinear waves such as solitons. In contrast, the nonlinear waves are considered in the FFT to be a superposition of several harmonic cosine waves.

(iii) Due to their monochromatic properties the cnoidal waves propagate in time and space as *one* wave without changes in shape by simple variation of x and t. In contrast, the higher-harmonic components in the FFT spectrum have to be defined as phase-locked or bound to the first-order wave to avoid dispersion in the numerical wave propagation. This is not required for the cnoidal waves.

3.4 Summary and implications for further processing

Finally, a summary of the previous sections is given and the implications for the further processing are derived.

3.4.1 Summary

In this chapter, the direct scattering transform of the Korteweg-deVries (KdV) equation is introduced as a nonlinear Fourier transform (NLFT) for the analysis of nonlinear water waves in shallow water. The consideration of cnoidal waves as basic components allows us to consider 'real' shallow-water waves as spectral basic components, not just sinusoidal waves. A first approach of the theoretical background and of the underlying physical and the mathematical procedures is given. It was shown how the approach of the Jacobi θ-function and the superposition of these waves by application of the Riemann Θ-functions are applied to calculate the free surface and the nonlinear interactions between the underlying cnoidal waves.

The spectral properties of cnoidal waves are presented in terms of the conventional frequency domain FFT and the time-frequency domain HHT. It was shown that the cnoidal waves can be considered to be generated from N cosine waves, with N increasing with the nonlinearity of the wave. Furthermore, the number of the determined cosine waves in FFT is used as criterion to determine those moduli m_j that distinguish between Airy-like, Stokes-like, cnoidal-like and solitary-like waves. By application of the HHT could be shown, that a very strong correlation exists between the degree of nonlinearity as proposed by Huang et al. (2013) and the Riemann matrix element B_{11}. The Hilbert amplitudes and the instantaneous Hilbert wave number follow the cnoidal wave shapes and therefore are able to describe the intra-wave nonlinearity of the cnoidal waves. This provides a basis for possible future applications of a joint HHT/KdV-NLFT analysis

The KdV-NLFT is implemented as a Matlab code. This code for the direct and inverse KdV-NLFT is verified and validated by the comparative analysis of different data, such as single cnoidal waves, superpositions of oscillatory and solitary cnoidal waves and numerical simulation data that contain solitons. The results show that the implemented code is able to distinguish between oscillatory waves and solitons and provide the correct spectral characteristics of the identified spectral cnoidal basic components. This powerful analysis method is now available for first detailed nonlinear spectral analyses of coastal wave data.

The application of the inverse KdV-NLFT has shown that by application of the cnoidal wave equation the superposed nonlinear waves can easily be evolved in time and space without the need for the identification and distinction of bound and free harmonic wave components. This is a significant improvement compared to the conventional FFT.

Unfortunately, the required internal settings and parameters for the algorithms and procedures (such as filter settings, resolution of the eigenvalue vector, ...) had to be determined empirically during the ongoing analyses because these data and information are not sufficiently available in the literature. For verification, and also later for the practical application of the data, comparative analyses with different numerical and artificially generated data have been performed. Different settings for the resolutions of the wave numbers k and the resolution Δx of the data (the details are not given in this thesis) confirmed the sensitivity of the algorithm to these boundary conditions. Still, the application of KdV-NLFT to the wave-structure interaction is under development and many questions are not yet answered sufficiently. The references given in this thesis (especially Osborne, 2010) will guide the way for improving the insight into the spectral structure of the direct and inverse KdV-NLFT and the numerical implementation.

In this chapter, an attempt is made to extract some of the most important facts and aspects for coastal engineering applications and the understanding of the KdV-NLFT as a kind of generalised Fourier transform by using similar denotations as in the conventional approaches. Numerical examples for the determination of the soliton and radiation amplitudes from the Floquet discriminant are discussed and the nonlinear spectrum loses its mystery if it is considered as a Fourier spectrum that contains simple additional components such as the soliton amplitudes and the modulus.

3.4.2 Implications for further proceeding

In order to further investigate the potential of the KdV-NLFT, to improvement of the existing code and the find appropriate practical application, the following steps are proposed:

(i) In general, besides a further validation of the implemented algorithms, the KdV-NLFT has to be further verified, extended by additional modules and applied to different types of data in coastal and ocean engineering, especially those associated with different types of nonlinear wave-structure interactions, wave-wave interactions, wave-current interactions, wave-seabed-structure interactions, etc.

(ii) For first practical applications, the KdV-NLFT should be applied to existing data from numerical or experimental tests with nonlinear waves. If the nonlinear processes and the types of the data are known, then the results of the KdV-NLFT can be compared with those obtained from conventional methods. Thus, a first evaluation is obtained

that will show whether the KdV-NLFT will provide significant improvement for the understanding of the underlying nonlinear processes.

(iii) Since the KdV-NFLT explicitly considers solitary waves as spectral basic components, data should be analysed that contains these highly nonlinear waves. Therefore, the KdV-NLFT is first applied to experimental and numerical data from test on soliton fission over and behind submerged reefs with finite and infinite width in which a large number of solitons is contained. One of the main problems in the data analysis was the reliable determination of the solitons in the measured or simulated data. By application of the KdV-NLFT this problem should be solved, because the solitons are provided in the nonlinear spectra (see chapter 4).

(iv) The KdV-NLFT is valid for waves in shallow water. Therefore, the propagation of relatively long waves which is strongly affected by nonlinear processes will also be analysed using the KdV-NFLT. Since this method is able to distinguish between propagating cnoidal waves and local nonlinear wave-wave interactions, transient waves should be identified and the dispersion of these waves predicted. Furthermore, the problem of harmonic generation and free and bound harmonic wave components should be discussed in terms of nonlinear cnoidal waves (see chapter 5).

(v) Finally, the potential of the KdV-NLFT should be illustrated by means of further selected example applications. Therefore, the KdV-NFLT is applied for the spectral analysis of long cosine waves in shallow water and for the analysis of long-period primary ship waves from hydraulic model tests (see chapter 6). Based on these results, possible further applications should be named.

4 Comparative spectral analysis of soliton fission over and behind submerged reefs

In this chapter the implemented KdV-NLFT that considers solitons as possible spectral components for the nonlinear decomposition is applied for the reliable identification of solitons in incident and transmitted wave trains around submerged reefs with finite and infinite width. *First,* the problem of soliton fission over and behind submerged reefs is briefly introduced (section 4.1). *Second*, the theoretical background of soliton fission at submerged reefs is briefly discussed (see section 4.2). *Third*, the numerical set-up, the reef geometries and the test programme are presented (section 4.3). *Forth*, the problems of the decomposition of the soliton signal using conventional analysis methods in frequency and time-frequency domain are discussed (section 4.4). *Fifth*, the applicability of the KdV-NLFT for the spectral analysis of the soliton data is discussed (section 4.5). *Sixth*, the results of the KdV-NLFT analysis of the soliton data are presented (section 4.6). *Finally*, a summary is given (section 4.7).

Former versions of the sections 4.1 to 4.3, 4.5 and 4.6 have already been published completely or partially in Brühl and Oumeraci (2010) and Brühl and Oumeraci (2011).

4.1 Position of the problem

The processes of wave transformation over submerged reefs have been extensively studied for regular and irregular waves (e.g. Goda et al., 1999; Bleck & Oumeraci, 2002; Bleck, 2003) as well as for solitary waves (e.g. Strusinska & Oumeraci, 2008; Strusinska, 2011). These analyses are important for a proper assessment of the hydraulic performance of submerged wave damping structures. For solitary waves, only the propagation over submerged reefs with infinite width has been investigated systematically.

When a single solitary waves passes over a submerged reef with an infinite width, due to the wave-structure interaction at the sudden strong change of the water depth one part of the wave is reflected and the other part is transmitted over the reef front. This transmitted water body usually has a surface profile that differs (i) from the initial wave shape and (ii) from the shape of those waves that are stable in the given water depth. Therefore, the transmitted wave right behind the reef front has to be considered to be an instable wave package. If the water depth is small enough, the water body transforms into an undular bore that will disintegrate into a train of solitons with smaller wave heights (soliton fission), followed by a train of oscillatory waves. The shape of these transmitted solitary waves significantly differs from the shape of the incident solitary wave, due to the reduced water depth and, thus, the increasing nonlinearity.

In case of finite reef widths, different wave transformation processes are governing the transmission of solitary waves over the reef into the deeper area behind the reef. Strusinska and Oumeraci (2008) were among the first researchers to conduct systematic laboratory tests on the soliton fission of solitary waves passing over submerged reefs with finite widths, though only two reef widths were considered. These extensive and systematic small-scale model tests that have been performed at Leichtweiß-Institute (LWI) (Strusinska & Oumeraci, 2008; Strusinska, 2011) were the first of that kind. The objectives of these tests were to identify the number of transmitted solitons behind the reef, to measure their wave heights, and to deter-

mine a prediction formula that explicitly considers the narrow, finite reef width for the prediction of the expected number of solitons behind the reef.

One of the major problems encountered during the solitary wave analysis of the transmitted waves using conventional methods such as time-domain analysis and the frequency-domain FFT, especially for the case of breaking waves, was that an unambiguous distinction between solitons and trailing oscillatory waves from the wave gauge recordings behind the reef could not be achieved.

A further problem in the performed hydraulic model tests was that the variation of the reef width b_r with only two values b_r*=1.0m* and *2.0m* was too limited to get any sound relationship between the number of solitons N_{sol} behind the reef and the reef width b_r. Therefore, in this study it is necessary to increase the range of variations of the reef widths by the help of numerical simulations using validated numerical models. For this purpose, the RANS/VOF model *COBRAS-UC* (Lara, 2005; Losada et al., 2008) was verified and applied.

Therefore, the focus of this chapter is to analyse the feasibility and performance of the implemented KdV-NLFT for the unambiguous identification of the transmitted solitons in the original data, so that the number of solitons N_{sol} behind the reef can reliably be determined and a prediction formula can be developed. Moreover, FFT, HHT and KdV-NLFT are applied comparatively to selected experimental and numerical signals of incident waves in front of the reef and of transmitted waves over or behind the reef.

4.2 Theoretical background

In this section, a brief overview on the theoretical background of soliton fission over reefs with infinite and finite width will be given.

4.2.1 Soliton fission over reefs with infinite width $b_r=\infty$

As a very brief introduction into the processes related with soliton fission over reefs with *infinite* width, an example from a numerical simulation will be discussed (see Fig. 4.2). The incident solitary wave with wave height $H_{sol,i}$*=0.22m* propagates in a water depth of *h=0.6m* towards a submerged reef with height h_r*=0.50m*. The submergence depth over the reef is d_r*=0.10m* (d_r*/h=0.2)*. The numerical boundary conditions are fully reflective at the left boundary at the wave paddle and fully absorbing at the right boundary. At *t=10s* the undisturbed incident solitary wave in Fig. 4.1a is in front of the reef. At *t=20s* the wave passed the reef front and is transformed into a bore that propagates over the reef (Fig. 4.1b). At *t=20s* also the reflected wave (in this case also a soliton) is shown in front of the reef. It propagates towards the left boundary where it is re-reflected at *t=30s* at the left side which is defined as closed, reflective boundary (see Fig. 4.1c). This re-reflected solitary wave behaves in the same way as the incident soliton and finally becomes an undular bore over the reef (see *t=40s* to *60s* in Fig. 4.1d-f*)*.

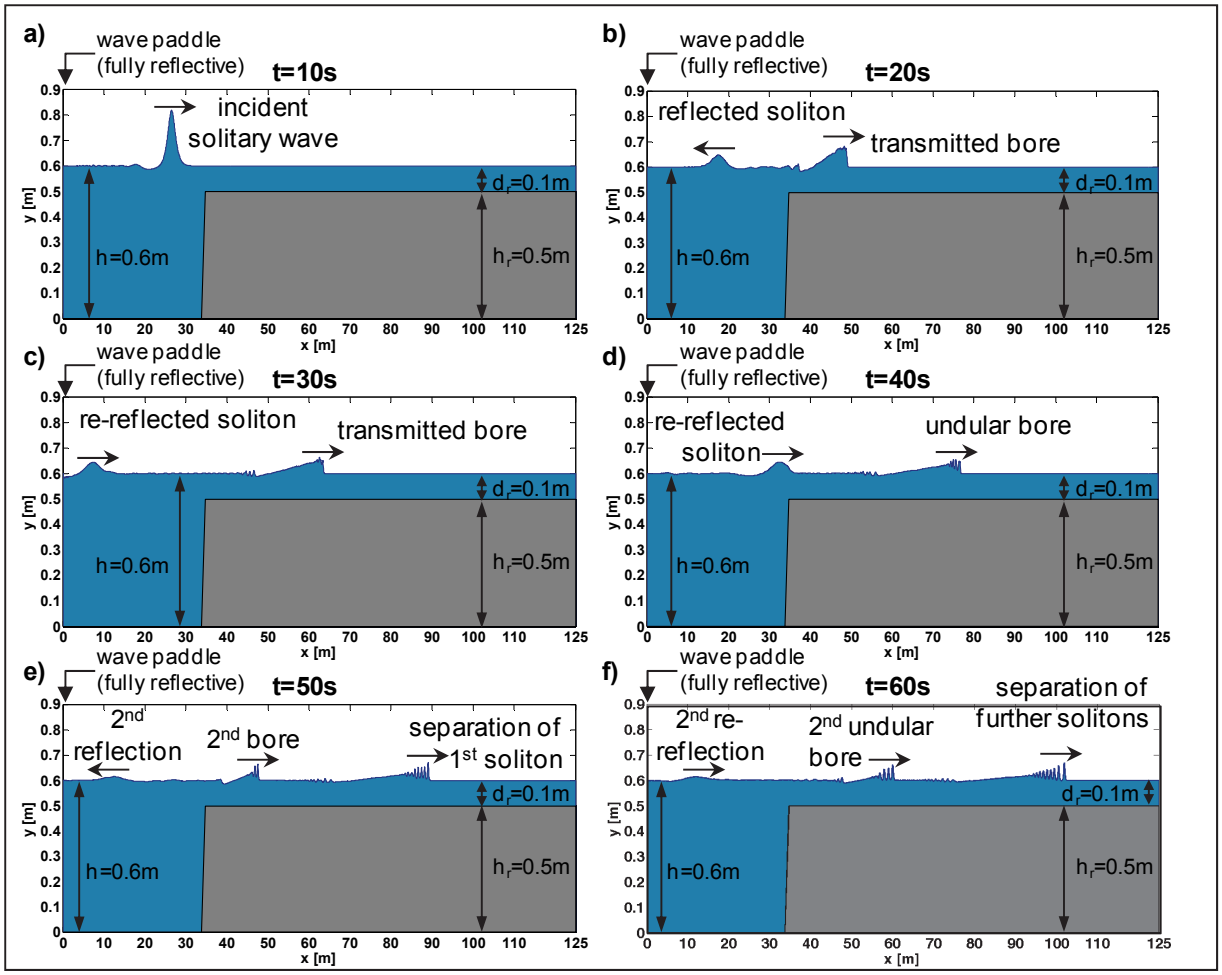

Fig. 4.1: Fission of a solitary wave with $H_{i,sol}=0.22m$ over a submerged reef ($h_r=0.5m$, $d_r=0.1m$) with infinite width, obtained from numerical simulation with *COBRAS-UC* (after Brühl & Oumeraci, 2010).

The front of the first transmitted bore over the reef at *t=20s* in Fig. 4.1b is highly turbulent. With increasing distance from the reef front, the fission process takes place and undular waves are generated at the front of the bore (see time steps *t=30s*, *40s* and *50s* in Fig. 4.1c-e). If the reef width is large enough, a wave train of isolated solitons will evolve from the undular bore (see Fig. 4.1f at *t=60s*). Fig. 4.2 shows the detailed water surface elevation of the transmitted wave train at the end of the simulation area ($d_r=0.1m$, *x=100-125m*, *t=77.0s*). For the interpretation of the data, a soliton is assumed to be completely separated from the undular bore if the water surface elevation behind the soliton returns to still water level. Considering that SWL is at *y=0.6m* (see Fig. 4.1) it is seen that at least two solitons (no. 1 and no.2, and maybe also no. 3) have already completely separated from the undular bore in Fig. 4.2. Further 11 (maybe up to 14) local peaks can be found in the remaining undular bore which might represent more or less evolved but not yet completely separated solitons. The longer the evolution time, the more solitons will evolve from the undular bore in this example. But we have to keep in mind that the space series in Fig. 4.2 represents the state of soliton fission at a selected time step (*t=77.0s*) and that this process is not yet completed. Therefore, the final number of solitons that are contained in the bore cannot be determined from the figures.

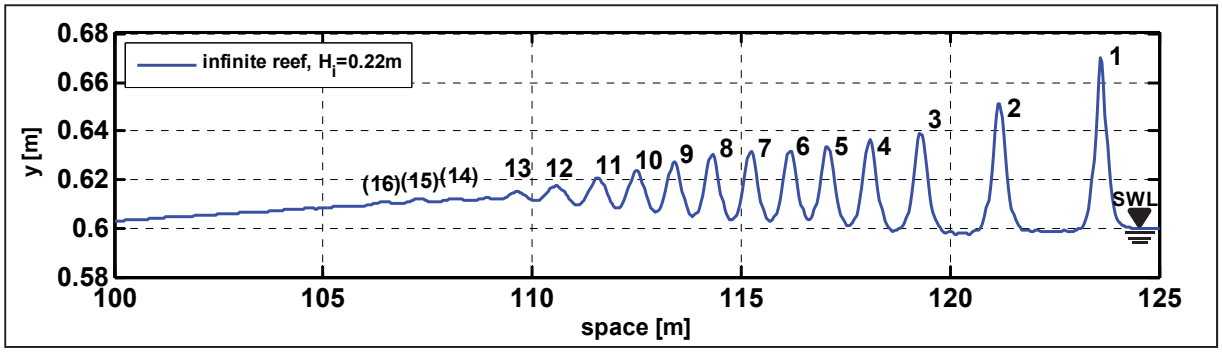

Fig. 4.2: Water surface elevation over the reef in Fig. 4.1(h_r=*0.5m*, d_r=*0.1m*) with infinite width at location *x=100-125* and time *t=77s*. The still water level (SWL) is at *y=0.6m* (Brühl & Oumeraci, 2010).

The first soliton is called *leading soliton*, the others are denoted as *trailing solitons*. Depending on the wave properties, the water depth and the structure geometry, the bore and the evolving solitons can be followed by a *train of oscillatory waves*.

The interactions between solitary waves and obstacles with infinite width such as long slopes (e.g. by Madsen & Mei, 1969) or coastal shelves (as in Fig. 4.1) have been described (e.g. by Losada et al. (1989) and Seabra-Santos et al. (1987). The expected number of solitons N_{sol} over a reef with *infinite width* b_r=∞ can be predicted by the following formulae proposed by

Tappert and Zabusky (1971):
$$\frac{d_r}{h} = \left[0.5 \cdot N_{sol}\left(N_{sol} - 1\right)\right]^{-4/9} \tag{4.1}$$

Johnson (1972):
$$\frac{d_r}{h} = \left[0.5 \cdot N_{sol}\left(N_{sol} + 1\right)\right]^{-4/9} \tag{4.2}$$

Germain (1984) and Kabbaj (1985):
$$M = 0.5\left\{\left[1 + \frac{16\left(h/d_r\right)^{5/2}}{1 + \left(h/d_r\right)^{1/2}}\right]^{1/2} - 1\right\}, \quad \text{with } N_{sol} = \left|M\right| \text{ the largest integer } N_{sol} \le M \tag{4.3}$$

According to these equations the expected number of solitons for the example in Fig. 4.1 is between 10 and 12, followed by small oscillatory waves. The equations assume the ratio d_r/h (with d_r the submergence depth over the reef and h the water depth in front of the obstacle, see Fig. 4.1) to be the only governing parameter for the prediction of the number N_{sol} of transmitted solitons over the obstacle with infinite width. They do not consider the incident wave height $H_{i,sol}$ or the reef width b_r as influencing parameters for N_{sol}. Since only the two geometrical parameters d_r and h are used in these equations, this approach can be applied without further information or analysis of the real hydrodynamic processes around the reef such as the bore evolution, wave reflection or the type of wave breaking over the reef front.

Numerical studies by Lin (2004) compared energy coefficients for reflection, transmission and energy dissipation of rectangular obstacles with finite and infinite widths. Detailed analyses for the influence of the reef width on the number of transmitted solitons over submerged reefs are not available.

4.2.2 Soliton fission behind narrow reefs

The physical processes of wave transmission behind narrow submerged reefs with $b_r=1.0m$ and $2.0m$ as tested by Strusinska (2011) differs significantly from the processes over submerged reefs with infinite width ($b_r=\infty$). The transmission of the same incident soliton with $H_{sol,i}=0.22m$ that has already been discussed in Fig. 4.1 over an infinitely wide reef with $h_r=0.5m$, $d_r=0.1m$ ($d_r/h=0.2$) is now shown in Fig. 4.3 for a reef with finite width $b_r=2.0m$. At $t=10s$ the incident solitons in Fig. 4.1a and Fig. 4.3a are the same since the wave-structure interaction has not started yet and the incident waves are still undisturbed. At $t=18s$ the soliton Fig. 4.3b has passed the reef and a soliton-like wave with reduced amplitude can be observed behind the structure, followed by an additional wave train. In front of the reef the reflected soliton propagates back to the left boundary. As already shown in Fig. 4.1, this wave will be re-reflected and act as a new incident wave. The evolution of the transmitted wave behind the reef at $t=18s$, $25s$ and $35s$ (Fig. 4.3b-d) clearly shows that no bore or undular bore is generated under these boundary conditions. The transmitted wave seems to become a stable soliton again very soon after passing over the reef and propagates without further fission, disregarding the generation of the following train of trailing oscillatory waves.

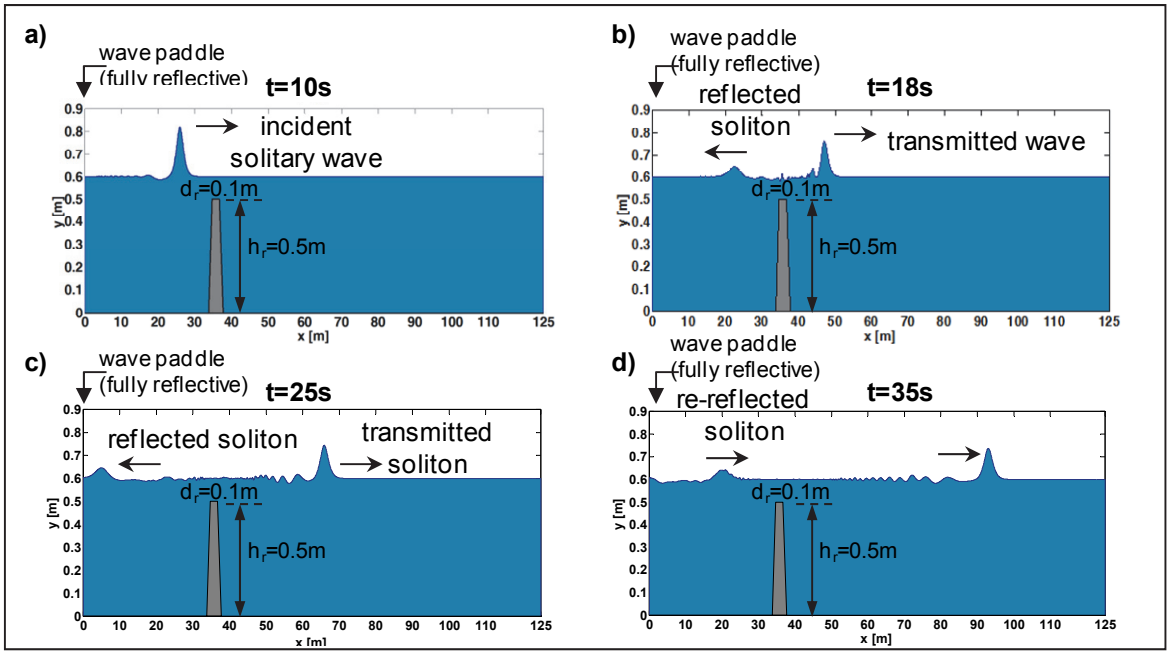

Fig. 4.3: Fission of a solitary wave with $H_{i,sol}=0.22m$ over a submerged reef ($h_r=0.5m$, $d_r=0.1m$) with finite width $b_r=2.0m$ (after Brühl & Oumeraci, 2010).

This simple example already shows the fundamental difference between transmitted solitons that propagate in very shallow waters over the reef with finite width (as discussed in Fig. 4.1) and those that propagate in deeper water behind the reef with finite width as shown in Fig. 4.3. Therefore, the prediction formulae given in Eqs. (4.1) to (4.3) cannot be applied for the latter case. To date, prediction formulae for the number of solitons behind submerged reefs with finite width are not available. Therefore, the objectives of the numerical simulations and analyses that are described in the following sections are to apply the implemented KdV-NLFT to the transmitted wave trains over and behind the submerged reefs to evaluate the performance of this method for a proper identification of the transmitted solitons.

4.3 Experimental and numerical set-up, reef geometries and test program

Small-scale model tests with solitary waves were performed in 2007 and 2008 by Strusinska and Oumeraci (2008) in the 90m long small wave flume at LWI with finite reef widths b_r=*1.0m* and *2.0m*. In 2010, for the analysis within this thesis, a total number of 18 different numerical geometry set-ups have been considered (see Fig. 4.4) by variation of the reef width (b_r=*2.0m*, *10.0m*, *30.0m*, *50.0m*, *70.0m* and *90.0m*) and the reef height (h_r=*0.30m*, *0.40m* and *0.50m*). The set-ups included those tested by Strusinska and Oumeraci (2008) for the reef width b_r=*2.0m*. In both, model tests and simulations the waves are generated at *x=0* and the seaward reef top is located at *x=34.75m*. The simulated total flume length is 125 m. The reef with b_r=*90.0m* represents the 'infinite' reef width because it lasts until the end of the simulation area at *x=125m*. Due to the variations of reef height h_r and the constant water depth *h=0.60m* for the submergence depth applies d_r=*0.10m*, *0.20m* and *0.30m*. Fig. 4.4 shows the set-up with three reef heights h_r (and therefore three submergence depths d_r) and six different reef widths b_r.

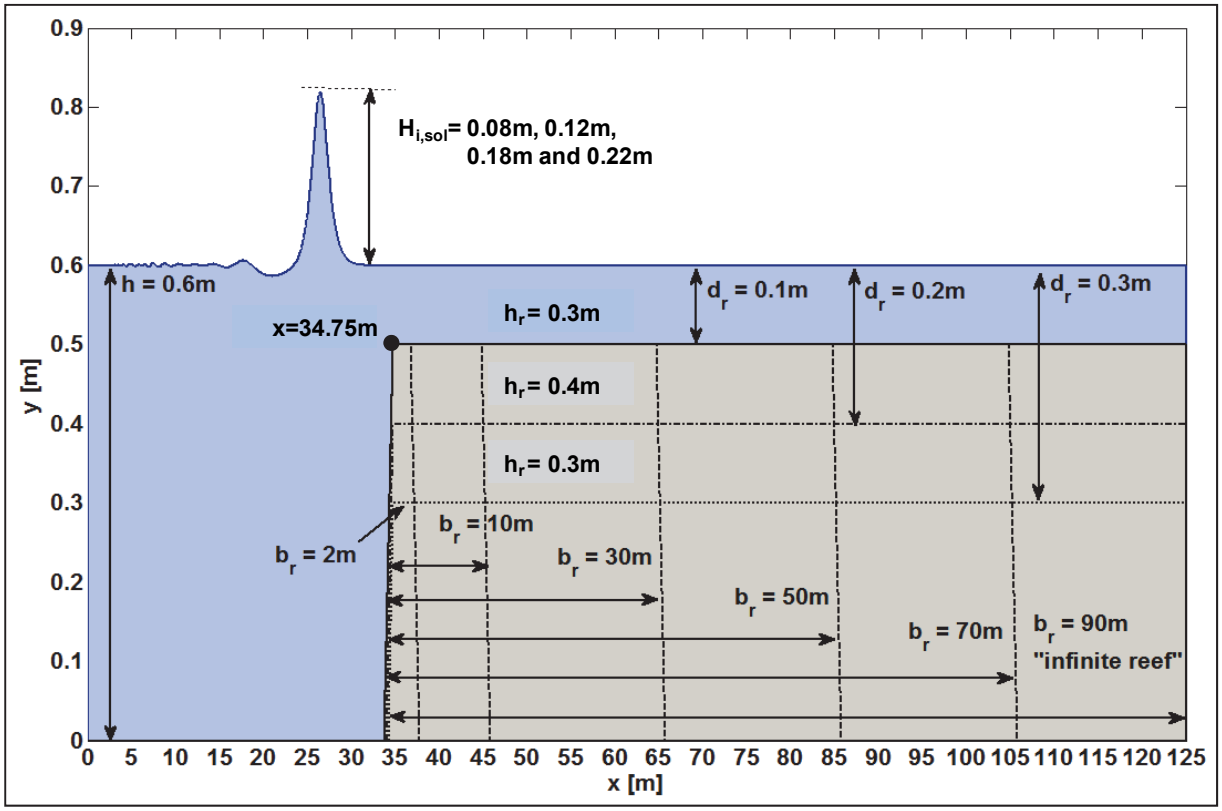

Fig. 4.4: Numerical set-up for COBRAS-UC simulations with solitary waves over submerged reefs with finite width (Brühl & Oumeraci, 2010).

The numerical simulations have been performed with the RANS/VOF (Reynolds-averaged Navier-Stokes/volume-of-fluid) model *COBRAS-UC*. The simulations were run with incident solitary wave heights $H_{i,sol}$=*0.08m*, *0.12m*, *0.18m* and *0.22m*. The total number of simulations with 18 set-ups and four wave heights is 72.

The RANS/VOF model provides detailed information on the wave dynamics (e.g. pressure field, horizontal and vertical velocity field) around the reefs that are required for the analyses of the processes during the wave-structure interaction and for the verification of the KDV-

NLFT analysis results. The simulations are run with a rectangular mesh with a constant resolution of $\Delta x=0.04m$ and $\Delta y=0.015m$. The numerical simulations provide the detailed space series that are required for the data analyses using conventional data analysis methods in section 4.4 and for the KdV-NLFT analyses in section 4.5

4.4 Spectral analysis of soliton fission using conventional analysis methods

In the following sections different conventional analysis methods will be applied to the experimental and numerical test data on soliton fission. *First*, a time-domain analysis is performed. *Second*, the conventional FFT is applied. And *finally*, the results of the time-frequency domain analysis using the HHT are presented.

4.4.1 Time-domain analysis of soliton fission

Madsen and Mei (1969) show that in both, numerical and experimental tests, the solitons that propagate over uneven bottoms into shallower water depth over a slope or onto a shelf are scattered into a train of solitons and subsequent oscillatory waves. In Fig. 4.5 the evolution of the incident solitary wave over a horizontal bottom (from $x/h=0$ to 6 in Fig. 4.5a), then over a slope with $1:m=1:20$ (from $x/h=6$ to 16) *in* Fig. 4.5a) and then over a shelf with constant depth (starting from $x/h=16$ until ~ 71 in Fig. 4.5a-c is presented. The initial incident-amplitude-to-depth ratio is $\eta/h=0.12$. The amplitudes η/h and the position x/h in the figure are given as relative values with respect to the water depth h_0 in front of the slope. The water depth over the shelf is $d_r=0.5 \cdot h$. The plots of the transmitted wave at different time steps in Fig. 4.5 show that due to the solitary wave transformation the wave profile becomes more peaked as the maximum amplitude increases (see Fig. 4.5a). The red line in Fig. 4.5a and b denotes the evolution of the highest peak. Furthermore, a hump of smaller wave height appears at the rear side of the wave around $x/h=20$ in Fig. 4.5a. This hump evolves into a second, trailing soliton between $x/h=25$ and 35 in Fig. 4.5b.

In Fig. 4.5a, first the peak height increases due to shoaling over the slope. But after entering the constant depth over the reef, the peak increases further while the first soliton separates and the first hump is generated. The peak height of the first soliton remains constant (starting from about $x/h \approx 40$) only after it has separated completely. At this stage, the transformation of this leading soliton and its adaption to the new, reduced water depth d_r are completed. Similarly to the 'birth' of the second soliton from the leading soliton by the first hump, a second hump appears behind the second soliton (which has not been completely separated yet) around $x/h=22$ (see Fig. 4.5b). This hump later evolves into a third soliton (see Fig. 4.5c). In this example given by Madsen and Mei (1969) the third soliton is followed by at least one trailing wave oscillation. Results from other numerical simulations for different boundary conditions within this thesis have also provided a higher number of separated solitons (see Fig. 4.1 and section 4.5).

As a result of the descriptions given by Madsen and Mei (1969) it can be concluded that the 'birth' of solitons is announced by the generation of humps at the back side of the separation solitons. These humps evolve into the peaks of the new solitons. During the separation process the emerging solitons increase their amplitudes until they have completely separated from

the remaining wave package and propagate in front of the remaining waves with their own (higher) soliton celerity.

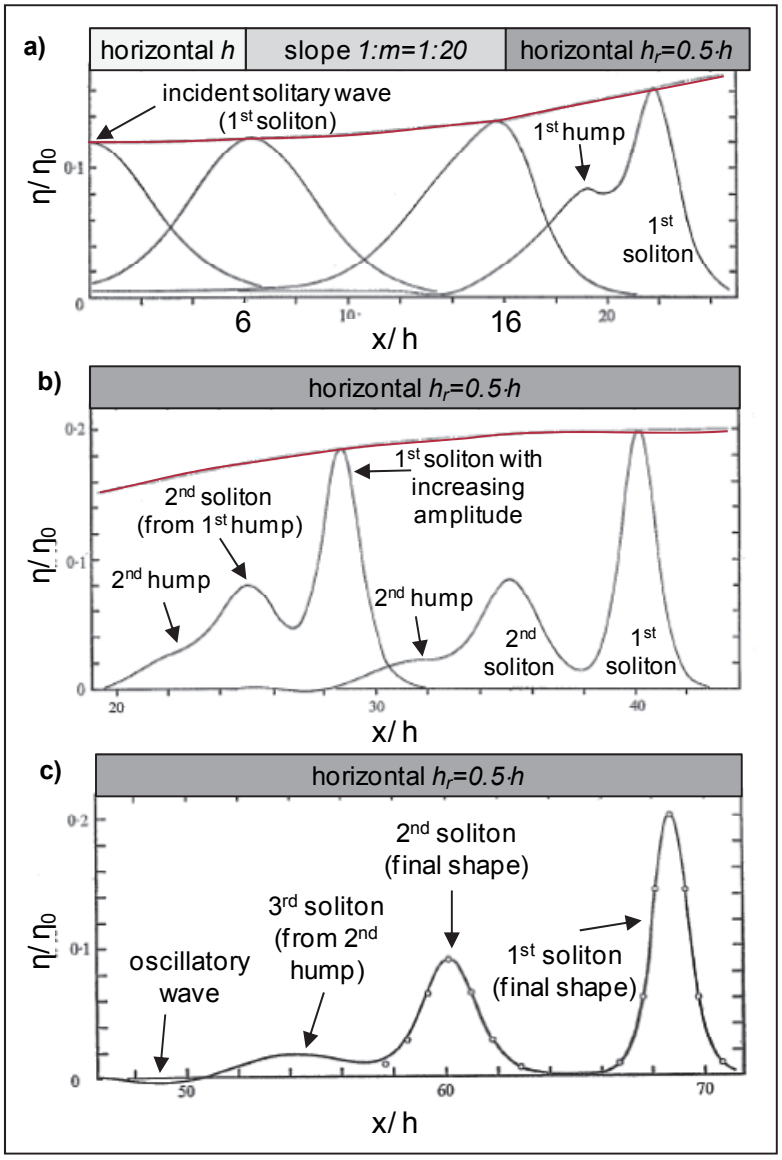

Fig. 4.5: Transformation of a solitary wave propagating over a slope onto a shelf of smaller depth (after Madsen & Mei, 1969).

For a better overview on the spatial and temporal evolution of the reflected and transmitted solitary waves at a reef with infinite width the results from a numerical simulation with incident solitary wave height $H_{i,sol}=0.08m$, reef width $b_r=02.0m$, and reef height $h_r=0.5m$ (submergence depth $d_r=0.1m$) are plotted in Fig. 4.6.

The figure shows, on the x axis, the free surface space series $\eta(x,t)$ in z direction as colour contour for different time steps from $t=0$ to $t=100s$ (on the y axis). In point (1) the soliton is generated and propagates towards the reef (in x direction). When the soliton arrives at the reef in (2) then a part of the soliton is transmitted onto the reef and another, in this case a smaller part, is reflected at the 1:2 slope of the reef. In this example, the transmitted wave is breaking over the reef and then a set of solitons is generated over the reef by soliton fission (3). The higher the soliton amplitude, the higher is the wave celerity. As an effect of wave transforma-

tion, first an undular bore is generated from the wave that is transmitted over the reef. The solitons evolve from the front of that bore and finally propagate as single, free solitons with different celebrities. This can be observed in right part of the figure.

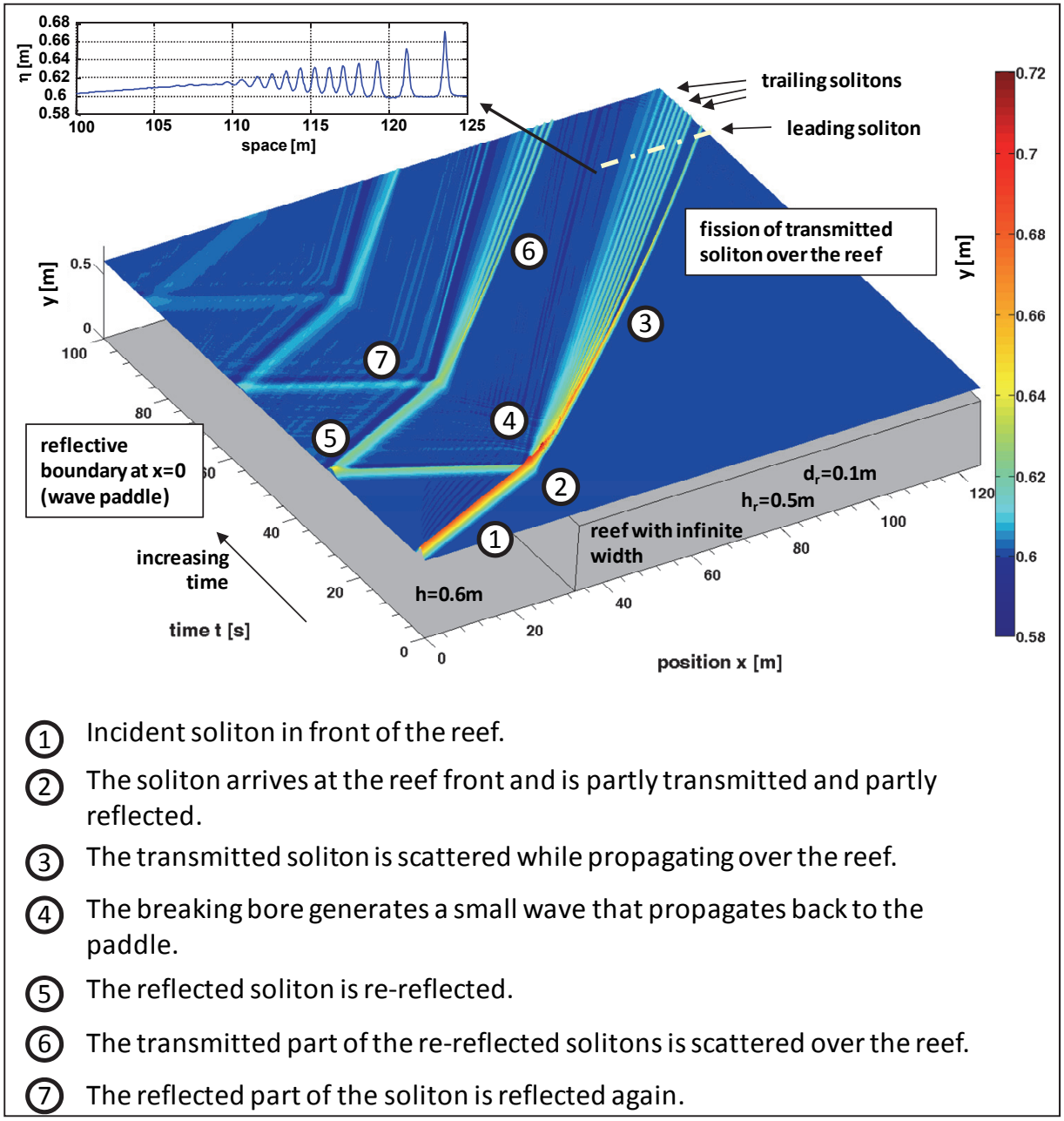

Fig. 4.6: Transmission and fission of a solitary wave over a reef with infinite width ($H_{i,sol}=0.08m$, $b_r=\infty$, $h_r=0.5m$ and $d_r=0.1m$).

As an effect of the wave breaking close behind the reef front, additional upstream surge waves are generated at position (4) that propagate back to the wave paddle, as shown in this example. In the numerical simulation, the right boundary was defined as fully reflective in order to simulate the same conditions as in the wave flume tests with the paddle. Therefore, in (5) the reflected part of the soliton is re-reflected at the right end of the flume and afterwards travels towards the reef. Then the same processes start again: this reflected soliton acts as a new incident wave, but with smaller amplitude. The transmitted part is scattered into several solitons over the reef (6) and the reflected part is re-reflected at the right boundary (7) and the

processes will repeat again and again until the wave energy and the mass of this 'bouncing' wave are completely transmitted over the reef or dissipated in the reflection and transformation processes.

In the tests by Strusinska and Oumeraci (2008) narrow reefs with finite width $b_r=1.0m$ and $b_r=2.0m$ have been tested. By plotting the results of a numerical situation of this case, it can be shown that the physical processes at reefs with limited width with $b_r=2.0m$ (see Fig. 4.7) are significantly different from the solitary wave propagation over reefs with infinite width as shown in Fig. 4.6.

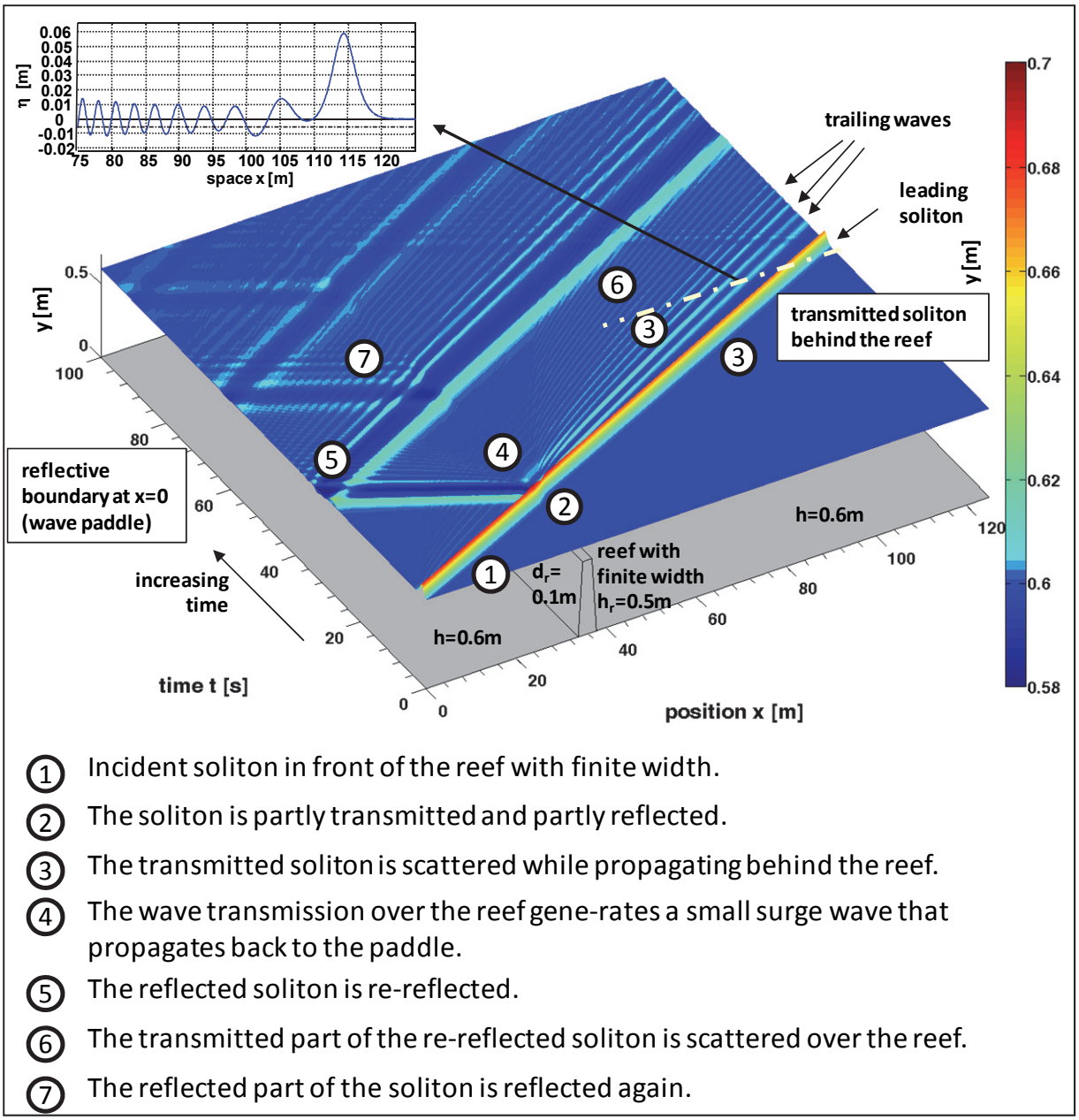

Fig. 4.7: Transmission and fission of a solitary wave over a reef with finite width ($H_{i,sol}=0.08m$, $b_r=2.0m$, $h_r=0.5m$ and $d_r=0.1m$).

First, like in Fig. 4.6, the incident soliton (1) is partly transmitted and partly reflected at the reef front (2). The transmitted part propagates behind the reef (now without generation of a bore) and shows wave dispersion (3) that leads to the generation of one clearly visible soliton

that is followed by waves that obviously strongly differ from the typical soliton-like wave shape that has been observed over the reef with infinite width. Similar like in Fig. 4.6, the transmitted wave generates additional surge waves (4) that propagate back towards the paddle. And again, the reflected part of the incident soliton is re-reflected at the paddle (5) and the processes of wave transmission, wave fission (6) and reflection between the reef front and the right boundary (7) are repeated again and again. The main difference between Fig. 4.7 and Fig. 4.6 is the physical behaviour of the transmitted waves, especially the generation and propagation of the bore: over the reef with infinite width, first, a bore is generated, and then this bore develops into a train of solitons, while behind the reef with finite width the transmitted wave propagates without generation of a bore and without generation of a train of rank-ordered solitons.

For the determination of the number of transmitted solitons N_{sol} behind submerged reefs with finite width, the method of counting the humps on the back side of the transmitted wave (see Fig. 4.5) as described by Madsen and Mei (1969) was adopted by Strusinska and Oumeraci (2008). Examples on for application of this method are given in Fig. 4.8.

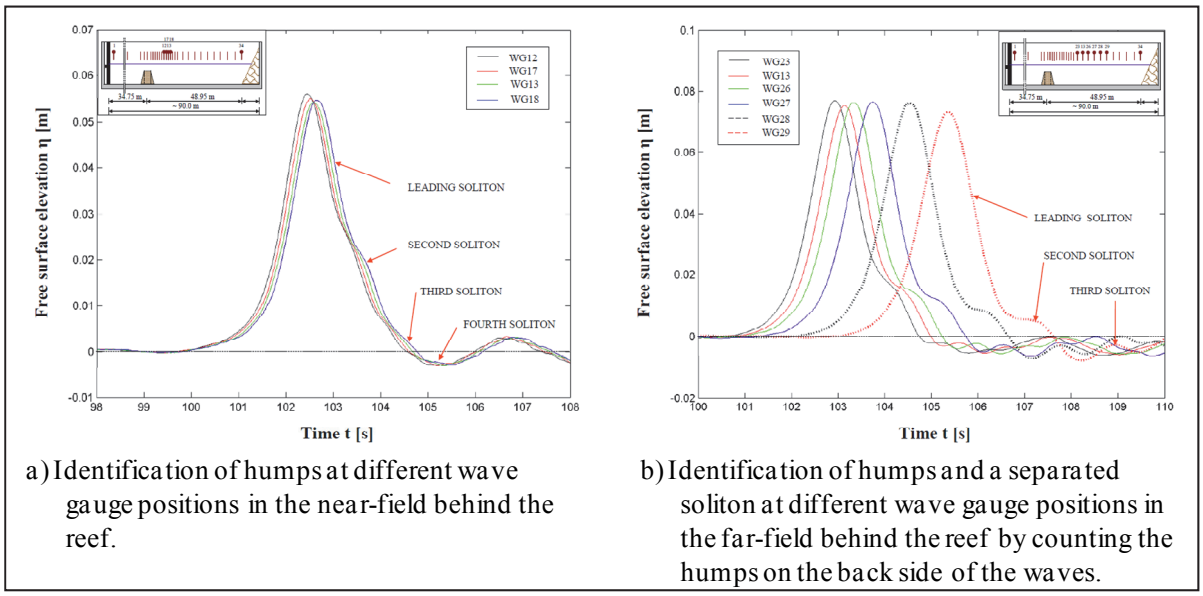

a) Identification of humps at different wave gauge positions in the near-field behind the reef.

b) Identification of humps and a separated soliton at different wave gauge positions in the far-field behind the reef by counting the humps on the back side of the waves.

Fig. 4.8: Example for the determination of the number of transmitted solitons N_{sol} behind the reef with finite width in Strusinska (2011).

The two selected examples in Fig. 4.8 clarify the problems that arise if the number of transmitted solitons is determined from wave gauge time series in the near-field of the reef. In Fig. 4.8a the value $N_{sol}=4$ is obtained from counting the number of humps at the backside of the solitons. Especially the forth hump in the wave trough behind the reef represents the difficulty to reliably distinguish between humps that are in the back side of the wave package and will evolve into new solitons, and those that are possibly caused by trailing oscillatory or surge waves and therefore will *not* result in new solitons. In Fig. 4.8b the value $N_{sol}=3$ is obtained from the leading soliton, one hump at its back side and a wave component that has already been separated from the wave package. In this case, especially for the wave denoted as third soliton the classification as a soliton has to be questioned mainly because of three reasons:

(i) According to Madsen and Mei (1969) the separation of the solitons occurs subsequently in the order of the soliton amplitudes, because of dispersion effects. The

higher solitons are faster (see Eq. (2.33)) and therefore evolve first from the wave package. In the example in Fig. 4.8b, the third soliton has already separated completely although it is the smallest and slowest of the three. This is not in agreement with the process of soliton fission as discussed before.

(ii) As already stated in Strusinska (2011) for the results of the analyses of her experimental data, 'only the leading solitons tends to resemble a solitary wave, while the successively emerged solitons resemble rather oscillatory waves'. Since the shape, properties and behaviour of solitary and oscillatory waves are clearly defined by the available conventional wave theories, these 'successively emerged solitons' should, in accordance with these theories, rather be assumed to be oscillatory waves instead of solitons if they look and behave like oscillatory waves.

(iii) As will be shown in Fig. 4.9, the upstream surge waves that are generated during the wave transmission into deeper water behind the reef also evolve from humps in the back side of the leading wave. Therefore, the existence of humps is not a sufficient proof for soliton birth from the leading soliton, but might also be caused by other effects during the transmission of an incident solitary wave over a reef with finite width.

Generally, the problem of the reliable distinction of the number of solitons arises with the finite reef width. For infinite reefs the procedure of the soliton fission is well described by Madsen and Mei (1969) as discussed above. In case of reefs with finite width additional physical processes (see Fig. 4.6) have to be taken into account such as the insufficient reef width for the evolution of solitons out of the bore and the generation of surge waves when the wave package is re-entering the deeper water behind the reef.

According to the results by Madsen and Mei (1969), the first hump is generated after a propagation length of the wave crest on the slope of at least $x/h=15$ (at $x/h\approx21$ the hump is already separated). In the example in Fig. 4.6 with $h=0.6m$ in front of the reef a minimum propagation length of about $10m$ would be necessary for the separation of the second soliton (if we assume $d_r=h/2$, which is not given here, because here applies $d_r=h/6$). So the general assumption can be drawn that a minimum propagation length over the reef is required to obtain a second soliton. If the incident soliton enters the reduced water depth over the reef, then its shape changes (i) due to the reflection of parts of the wave at the front of the reef and (ii) due to the reduced water depth over the reef. Therefore, at the beginning of the reef, the transmitted water body propagates as a bore that has to adapt to the new water depth conditions by reshaping during the propagation. The soliton fission is a result of this reformation process over the reef that is assumed to need a minimum time and propagation length before the solitons can evolve from the front of this wave package. The influence of the reef width b_r on the number of transmitted solitons N_{sol} is discussed in section 4.6.3.

If the approach by Madsen and Mei (1969) is applied to wave fission over reefs with finite widths, then other effects have also to be considered that lead to the generation of surge waves (see Fig. 4.9). Therefore, when a solitary wave passes the reef, not only waves in direction of the incident solitary wave are generated, but also waves that propagate back over the reef towards the wave maker.

In Fig. 4.9*a*, different time series $\eta(t)$ at several positions x are plotted in different colours. First, the incident wave is shown (in front of the reef at $x=33.96m$). The reef top is located

from *x=34.75m* to *x=36.79m*. The following waves are measured over (*x=35.96m*) and behind the reef (*x=36.79m*). These waves show humps on the back side and, finally, with increasing distance from the reef wave trains with several crests and troughs can be determined.

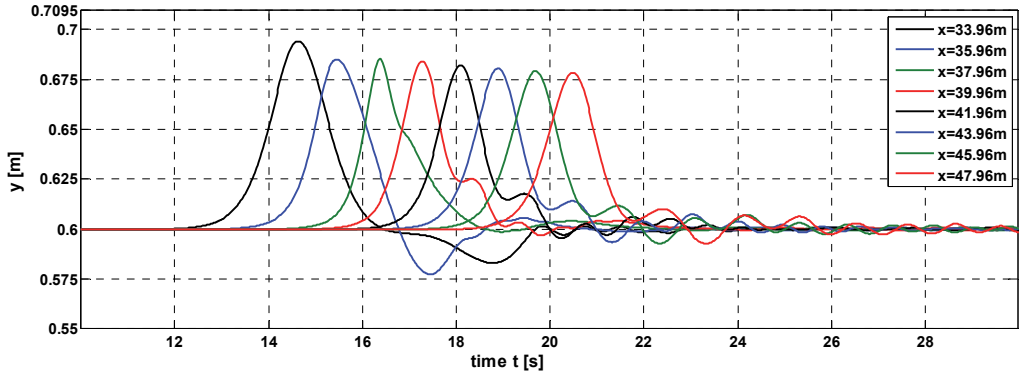

a) Time series at different wave gauge positions showing the transmitted wave and the 'humps' on the back side of the leading wave.

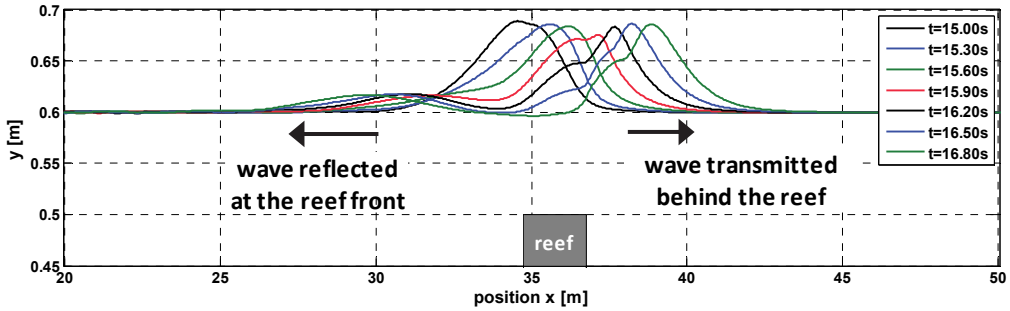

b) Space series at different time steps *t=15.0s* to *t=16.8s* showing the separation of the incident wave into a transmitted and a reflected part at the reef front.

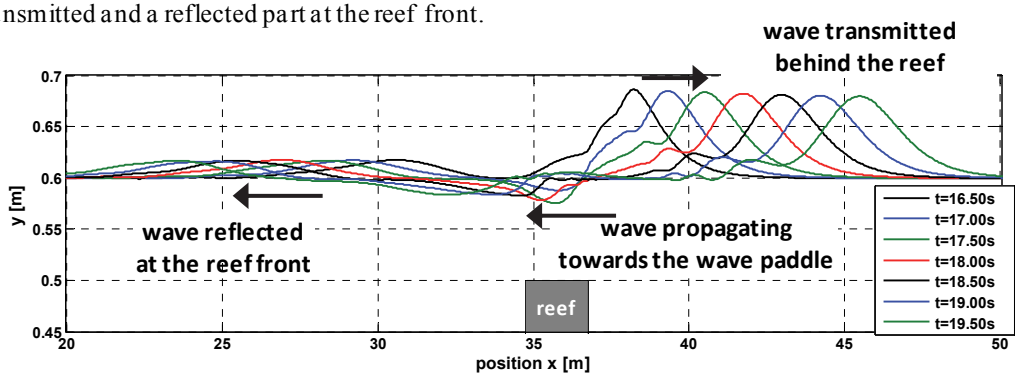

c) Space series at different time steps *t=16.8s* to *t=19.5s* showing that after the separation of the reflection part some of the 'humps' in the transmitted leading soliton evolve into waves that propagate back towards the wave paddle.

Fig. 4.9: Time and space series from a numerical simulation of the transmission of a solitary wave over a reef with finite width ($H_{i,sol}$=*0.08m*, b_r=*2.0m*, h_r=*0.5m* and d_r=*0.1m*). The reef top is located at *x=34.75-36.79m* (see the grey box indicating the reef position).

In Fig. 4.9*b*, different space series at different time steps are plotted in different colours in order to show also the direction of the wave propagation due to the wave reflection at the reef. The signals show the separation of the incident wave at the reef front into a transmitted part that propagates to the right and a reflected part that propagates to the left.

In Fig. 4.9*c*, further space series of the transmitted waves behind the reef are given. After the generation of the reflected wave at the reef front, additional wave components are generated behind the reef by the transmitted wave that also propagate back over the reef towards the wave paddle. These additional waves evolve from some of the humps at the back side of the transmitted wave (the leading soliton). These humps will *not* develop into trailing solitons. This example shows that in case of narrow reefs the number of these humps does neither represent the number of waves that propagate in the correct direction nor do they represent the number of transmitted solitons that will evolve from that transmitted wave in the far-field behind the reef.

A possible explanation for the generation of the additional waves that propagate toward the wave paddle can be found by a detailed step-by-step analysis of the evolution of the free surface within the numerical simulations: If the wave package that propagated over the reef with finite width re-enters the deeper water behind the reef, then the motion of the surface resemble a mass of water falling into a tank. This re-entering water mass causes a drop of the water surface, followed by an oscillation of the free surface that generates surge waves which propagate in both directions (upstream and downstream) from the source. Since the dropped water has an initial velocity in direction of wave propagation when it passes the reef, most of the momentum is passed to the leading soliton. The processes related to this surge generation have not been further studied in detail within this thesis. Nevertheless, the analyses show that additional effects must be taken into account, if the transformation processes are to be analysed and the number of transmitted solitons is to be determined from time-domain data analysis of near-field wave gauge data.

Finally, the presented time-domain analyses clearly show that by simply analysis of wave gauge time series and counting the number of humps on the back side the number of transmitted solitons cannot be determined or predicted correctly. Furthermore, in the near-field of the reef front and the reef back of narrow reefs transformation processes occur that generate waves that are travelling in both directions, upstream and downstream, and that the upstream waves are not necessarily solitons. Unfortunately, the direction of the waves cannot reliably be determined from the wave gauge time series and the waves with reverse direction also generate humps. For further processing and the determination of N_{sol} in the following sections time and space series from numerical simulations in the *far-field* behind the reef are analysed to avoid the problems of these near-field upstream waves. The objective of the following sections is to demonstrate the ability of the KdV-NLFT for the determination of the correct number of transmitted solitons (section 4.5). A detailed analysis of the physical processes of solitons transmission in the near-field of the submerged reefs is not the subject of this thesis.

But before the KdV-NLFT is applied, first, in the next sections the conventional analysis methods Fourier (FFT) and Hilbert-Huang transform (HHT) are applied to the numerically generated data to examine their ability to reliably determine the number of solitons resulting from the fission of a solitary wave over submerged reefs with finite and infinite width (sections 4.4.2 and 4.4.3).

4.4.2 Spectral analysis of soliton fission using the conventional fast Fourier transform (FFT)

The conventional fast Fourier transform (FFT) as described in section 2.6.1 was developed for the analysis of linear stationary signals. Unfortunately, solitary waves are nonlinear and non-stationary waves that can be regarded to be a linear superposition of a large number of cosine waves $\eta_{cos,i}(x,t)$ with harmonic frequencies $f_{cos,i}$ and phases $\varphi_{cos,i}=0$. In analogy to the generation of Stokes wave as described in section 2.3.1, solitary waves can be regarded as Stokes waves of order $N=\infty$. Examples for the spectral decomposition of solitary waves using the FFT are given in section 3.1.2.1. For a first overview on the spectral behaviour of the transmitted waves over and behind submerged reefs, the temporal evolutions of these waves and their FFT amplitude spectra are presented in Fig. 4.10 and Fig. 4.11. To exclude disturbing waves and wave components from the FFT analysis, a moving space frame of length $L_{sp}=30.0m$ is applied. Within the moving frame the maximum peak amplitude of the wave is located constantly at $x=10.0m$ from the beginning of the window. So the frame is moving with the velocity of the highest wave crest.

The temporal evolution of transmitted waves over the reef with an infinite width is plotted in Fig. 4.10a. For each of the space series with length $L_{sp}=30m$ the FFT spectrum is determined and plotted in Fig. 4.10b for the corresponding time with the Fourier amplitudes as colour contour. The figures show the fission of the incident solitary wave after it passed the reef at $t\sim15s$. The yellow signal that runs from ($t=15s$, $x=12m$) to ($t=20s$, $x=30m$) is the part of the initial soliton that is reflected at the reef front and propagates back downstream. Therefore, the distance between its crest and the crest of the transmitted wave is increasing. If the difference is larger than 20m, then the wave crest of the reflected wave is not shown in the figure any longer (this happens around $t=20s$).

Starting from $t\sim20s$ the soliton fission can be observed in the transmitted wave. The FFT spectrum in Fig. 4.10b shows that the frequency distribution and the amplitudes are functions of propagation time and therefore of the propagation length. The incident soliton is represented by a large number of low-frequency components with decreasing amplitudes, exactly as discussed in section 3.1.2.1. The area of wave breaking between $t=15s$ and $t=22s$ is characterised by a wide range of high- and low-frequency components. During the soliton fission and the separation of the solitons, the frequency range reduces to lower frequencies and at the same time several harmonic peak frequencies can be observed that change their frequencies from higher to lower values with time. The results show clearly that the characteristics of the conventional Fourier spectrum vary with time and the progress of the soliton fission as the wave train propagates over the reef. Nevertheless, before the number of the transmitted solitons can be determined by visual observation of the time or space series, they have to be evolved completely from the transmitted wave package. From the obtained results as presented in Fig. 4.10b, the FFT it is not possible to determine the correct number of transmitted solitons from the amplitude or energy spectra, neither from the far-field nor from the near-field data.

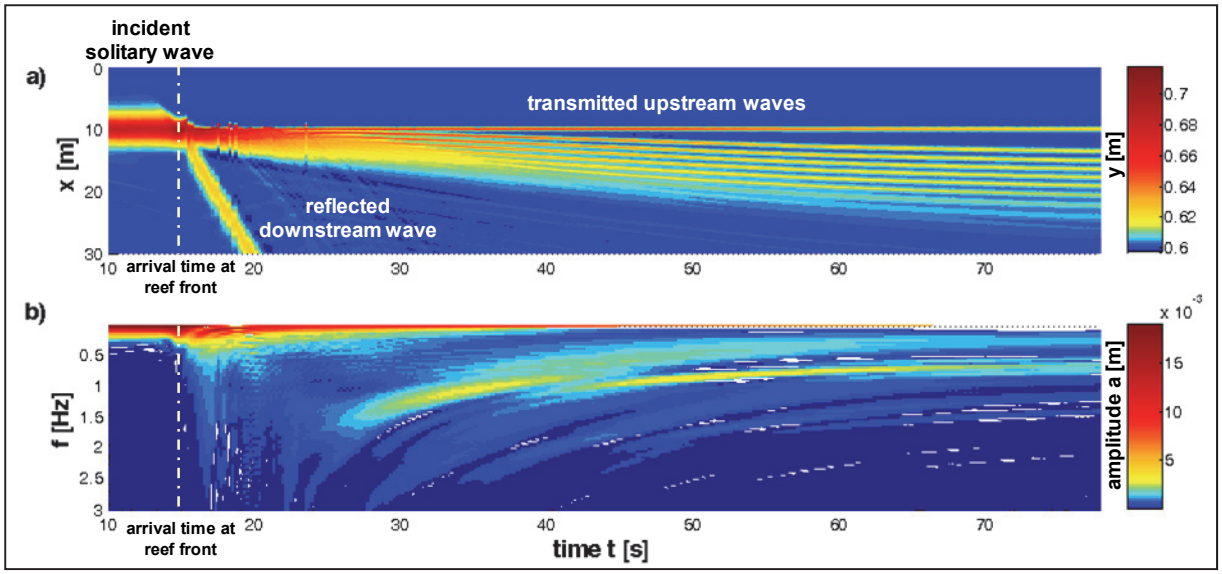

Fig. 4.10: a) Temporal evolution of the transmitted wave over the reef with *infinite width* using a running window of length $l=30.0m$ with the maximum elevation constant at $x=10.0m$ ($H_{sol,i}=0.08m$, $b_r=\infty$, $h_r=0.5m$ and $d_r=0.1m$). b) Temporal evolution of the conventional fast Fourier amplitude spectra of the space series in a).

The temporal evolution of the transmitted waves behind a reef with finite width $b_r=2.0m$ is shown in Fig. 4.11. The difference to the fission process over the reef with infinite width is obvious. In both plots in Fig. 4.11, the free surface in Fig. 4.11a and the Fourier amplitudes in Fig. 4.11b, it seems that the incident soliton passes the reef without significant changes in width or spectral properties. Only the wave height seems to be a little reduced. The additional waves that arise from wave fission here are wider than the obvious very narrow solitons in Fig. 4.10a and they do not provide those additional peaks in the Fourier spectrum as observed in Fig. 4.10b. Furthermore, the scale of the free surface in Fig. 4.10a does not show any wave troughs with values smaller than $y=0.6m$ (the SWL value). In Fig. 4.11a the additional waves do show wave troughs with $y<0.6m$. Therefore, these waves have to be assumed to be oscillatory waves, not solitons as above the reef with infinite width. Again, as concluded for Fig. 4.10b from the spectra of the transmitted waves the number of solitons cannot be determined correctly.

Solitons are represented in the conventional Fourier spectrum by a large number of harmonic wave components (which are 'in phase') with decreasing amplitudes. The results in Fig. 4.10 and Fig. 4.11 show that the spectral properties of the analysed signals vary with time and distance from the reef front. In addition, for a reliable identification of solitons from a Fourier spectrum it might be necessary to determine the different frequency components from the different solitons as well as their spectral amplitudes. Since the focus of this thesis is the implementation and application of the KdV-NLFT, no further detailed analyses using the FFT are performed here. The KdV-NLFT is expected to provide much better results because the solitons are possible basic components and their interactions are considered explicitly during the spectral decomposition.

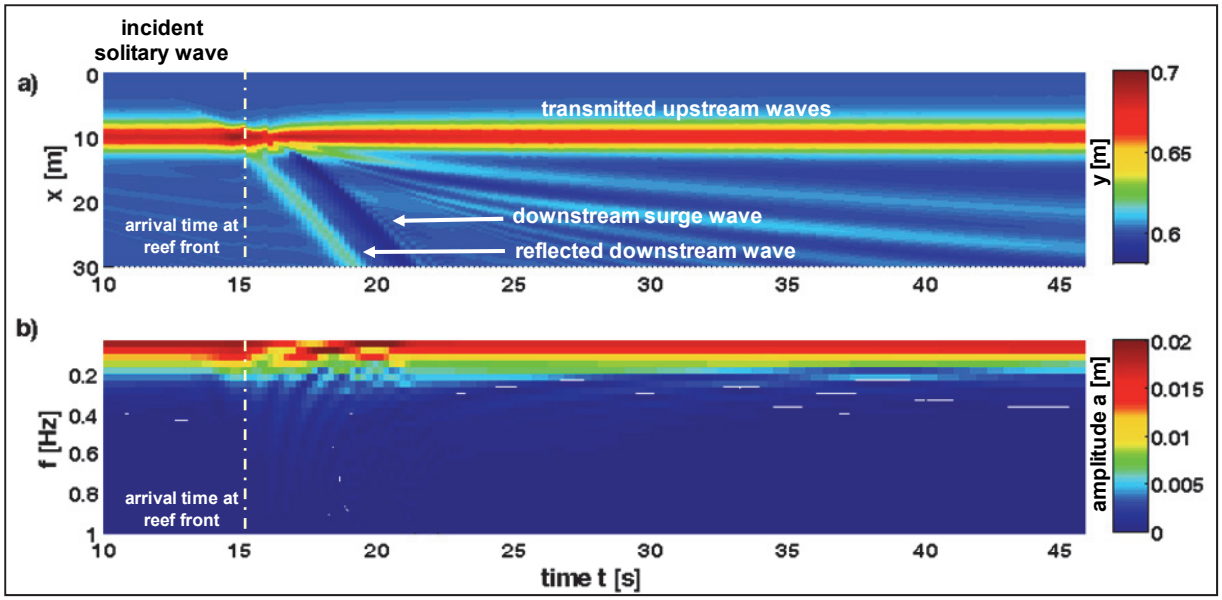

Fig. 4.11: a) Temporal evolution of the transmitted wave behind the reef with *finite width* using a running window of length $L_{sp}=30.0m$ with the maximum elevation constant at $x=10.0m$ ($H_{i,sol}=0.08m$, $b_r=2.0m$, $h_r=0.5m$ and $d_r=0.1m$). b) Temporal evolution of the conventional fast Fourier spectra of the space series in a).

4.4.3 Spectral analysis of soliton fission using the Hilbert-Huang transform (HHT)

The Hilbert-Huang transform (HHT) which is a combination of the decomposition of the original data by the (ensemble) empirical mode decomposition (EEMD, EMD) into intrinsic mode functions (IMFs) and the Hilbert transform (HT) as the time-frequency analysis of the determined IMF (see section 2.6.2) is applied to the soliton data obtained from numerical simulations. *First*, the decomposition of the data by application of the EMD and the EEMD is discussed. *Second*, the HT is applied to the determined IMFs. *Finally*, a summary and conclusions are given.

With the empirical and the ensemble empirical mode decomposition (EMD and EEMD) which are introduced in section 2.6.2, two different methods for the decomposition of the original data are available that seem to differ only slightly by the addition of white noise before the decomposition. But if applied numerically to soliton data from solitary wave theory, the two methods show significantly different results (see Fig. 4.12):

(i) *Application of EMD*: Fig. 4.12a shows the IMFs that are determined from the application of the EMD to a solitary wave generated from solitary wave theory. The solitary wave information is contained completely in the first IMF, but unfortunately large boundary effects occur that strongly influence the whole signal. During the sifting process cubic spline functions are constructed as upper and lower envelope by using the local minima and maxima within the signal as supporting points. In case of this numerical solitary wave only very few extrema are available as supporting points for the spline construction and therefore the end effects are dominating the whole data. As balance for the large deviations at the beginning and end of the 1st IMF the residual contains the counterpart of these end effects. The other IMFs (2nd to 7th) do not contain any significant signal information. The linear superposition of the seven IMFs and the residual returns the original solitary wave data. This example shows that the EMD is

not a proper decomposition method for the further analysis of single solitons that are generated from common wave theories. These artificial data do not contain any background noise that would provide a sufficient number of additional supporting points for the spline construction.

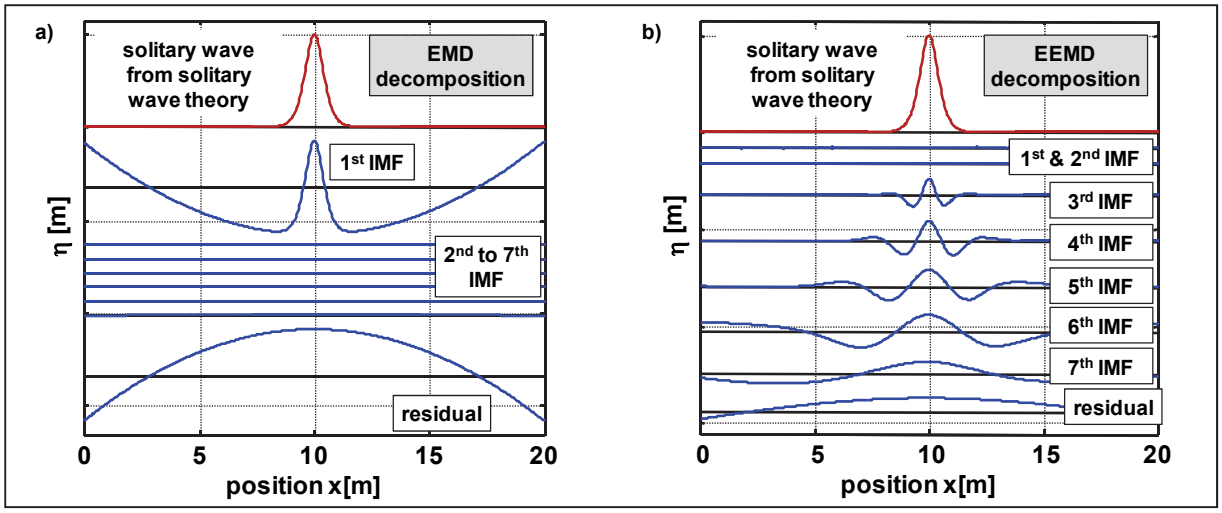

Fig. 4.12: Decomposition of a solitary wave that is generated from solitary wave theory using a) the empirical mode decomposition (EMD) and b) the ensemble empirical mode decomposition (EEMD).

(ii) *Application of EEMD:* To overcome the problem of the insufficient number of local extrema, an arbitrary white noise signal is generated numerically and added to the original signal. In Fig. 4.12b the results of the application of EEMD on the same solitary wave as in Fig. 4.12a are given. Due to the added white noise, the original solitary wave now is 'contaminated' with sufficient local extrema that provide sufficient local supporting points for the spline generation. Therefore, the soliton is decomposed into several wavelet-like oscillations with decreasing wave number. This example shows how the white noise provides an external scale for the decomposition (as already mentioned in section 2.6.2). By applying the EEMD, the initial *physical* solitary wave is decomposed into several *mathematical* wavelet-like oscillation modes that are mathematically in accordance with the procedure of the EEMD, but not necessarily in accordance with real physics.

This problem occurs in both results in Fig. 4.12 and is similar to that of the FFT decomposition: A given signal is decomposed using an algorithm that does not explicitly consider the real physical nonlinear properties of the original data. The result is a representation of the original data in terms of the selected basic constituents (pre-defined physical cosine waves in FFT, adaptive mathematical oscillation modes in the EEMD). The linear superposition of the basic components returns the original data and therefore the decomposition is mathematically correct, but the determined components are not necessarily in accordance with the underlying physics. Especially for shallow-water waves this limitation is obvious: Waves in shallow-water are functions of the water depth, but neither FFT nor EEMD consider the water depth as a governing variable for a physical correct decomposition of the data. Therefore, to proceed further, the original solitons have to be reconstructed manually from the EEMD analysis results. This means, the different IMFs that contain portions of the solitary-wave information have to be identified and these IMFs have to be superposed in order to obtain an IMF

with the correct properties of the original soliton instead of a number of wavelet-like oscillation modes. This latter analysis and superposition procedure has to be executed either manually or automatically (if appropriate analysis routines and identification criteria are available).

If the original solitary wave is generated by a wave theory then it does not contain any noise and therefore the IMFs obtained from EMD are strongly different from those determined from EEMD. If a soliton signal from physical model tests is analysed (see Fig. 4.13) then the results of the two methods are very similar, but not identical. The two plots show the same measured time series (blue line) from a laboratory test. The application of both EMD (Fig. 4.13a) and EEMD (Fig. 4.13b) decomposes the signal in seven IMFs and the residual (plotted in different colours). The noisy experimental data already contains various local extreme so that even the EMD decomposes the data into several wavelet-like oscillation modes as does the EEMD. Therefore, for the analysis of noisy laboratory test soliton data, the EMD is applicable and provides similar results as the EEMD.

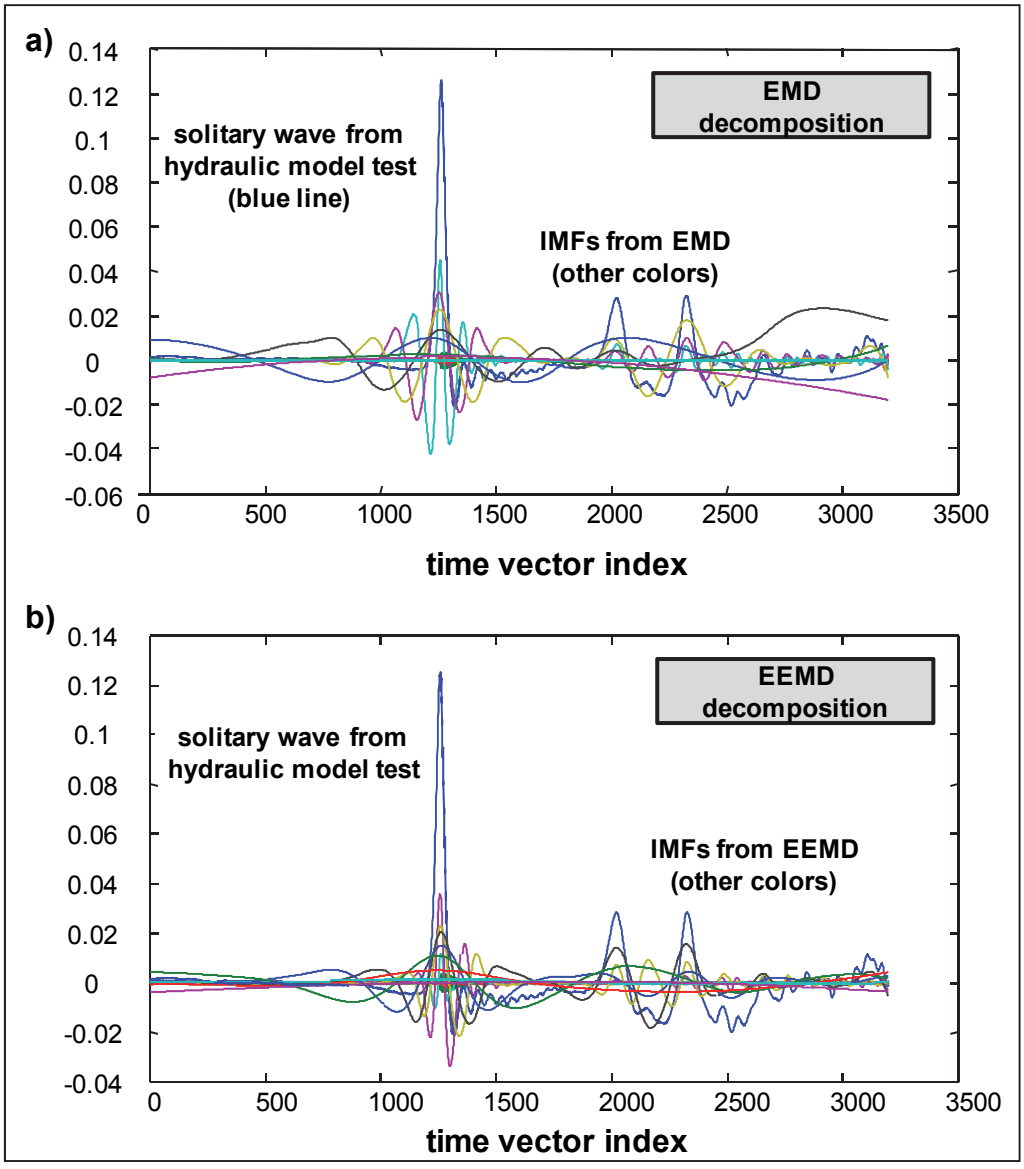

Fig. 4.13: Decomposition of a noisy solitary wave measured in hydraulic model tests using a) the empirical mode decomposition (EMD) and b) the ensemble empirical mode decomposition (EEMD).

Once the original signal is decomposed into the IMFs, the Hilbert transform (HT) is applied to each of these oscillation modes and the instantaneous frequencies f_{inst} or wave number k_{inst} (see section 2.6.2) are determined for each of these IMFs. Note that like the FFT, the HHT can be applied to time and space series without any problems. For time series, the results are provided in terms of instantaneous frequencies f_{inst}, for space series in terms of instantaneous wave numbers k_{inst}.

In the Hilbert spectrum in Fig. 4.14 the values of k_{inst} are plotted in the Hilbert spectrum for IMF3 to IMF7 and the residual *Res* as functions of space. IMF1 and IMF2 do not contain significant wave number information, they represent the noise. For the generation of the Hilbert spectrum, the amplitudes for these wave numbers are plotted as colour contours versus space or position x. High amplitudes are displayed by red colours, small amplitudes as blue. If a certain frequency is contained in more than one IMF, then the different amplitudes for this frequency are superposed before the frequency is displayed in the Hilbert time-frequency spectrum.

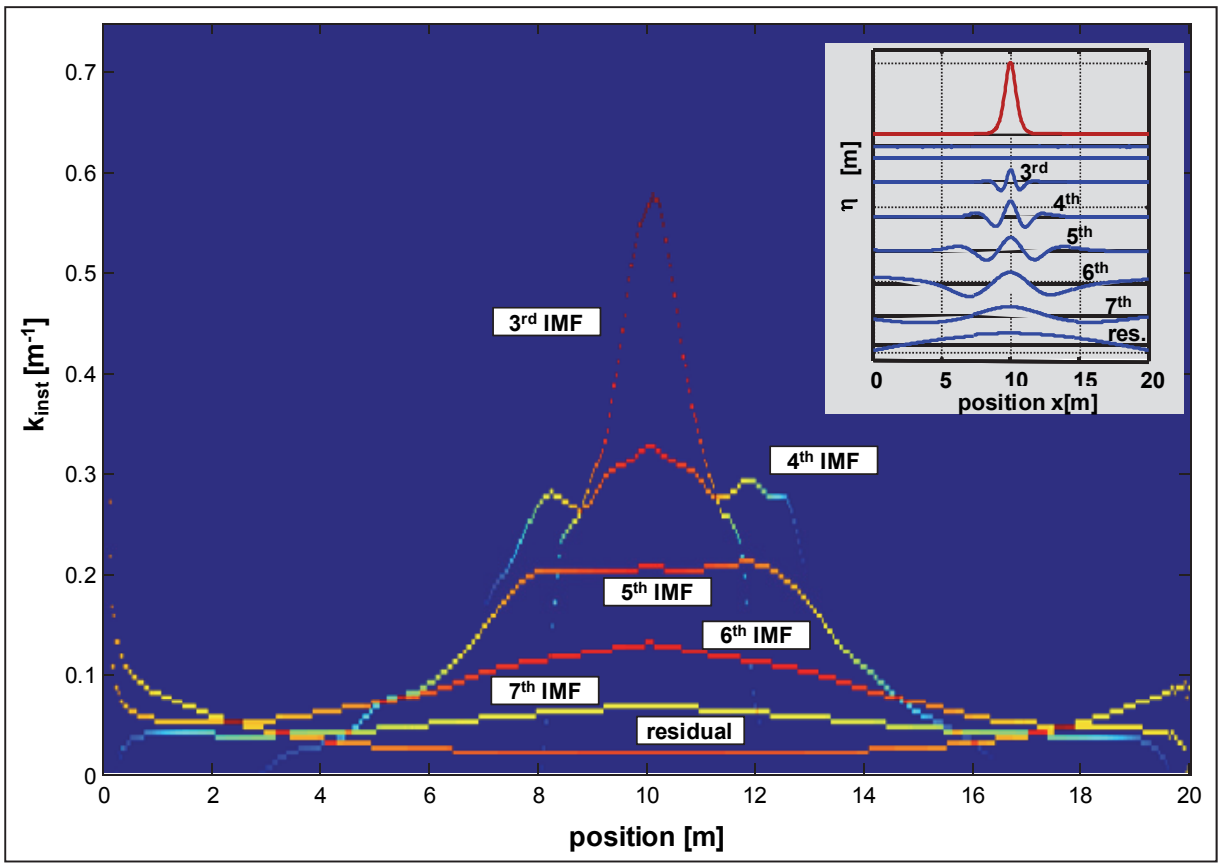

Fig. 4.14: Hilbert spectrum with the instantaneous wave numbers k_{inst} of the IMFs from Fig. 4.12b.

The wave number scheme in Fig. 4.14 is characteristic for a solitary wave that is analysed using the EEMD. The wavelet-like components in Fig. 4.12b are separated in the EEMD by decreasing order of wave number and therefore the Hilbert wave numbers of these IMFs show decreasing peak wave numbers. Since the HT provides a space-wave number analysis, the width of the wave number distribution depends on the width of the analysed signal. The first IMF has a short wavelength and therefore a narrow width and a high wave number. Each of the Hilbert frequencies of the following IMF provides entries at lower wave numbers since the wave lengths increase and therefore the wave numbers decrease. A characteristic property

of all these IMFs and the corresponding Hilbert wave numbers is that the peaks are located at the same value of x (they are 'in phase'). At this point the assumption is made that the Hilbert spectrum in Fig. 4.14 is typical for single solitons that are analysed using the EEMD.

The objective of the EEMD is to decompose a wide-banded signal into narrow-banded modes for the application of the HT. In principle, a solitary wave generated by application of the solitary wave theory already represents an IMF and does not need to be pre-processed with the EEMD. Since the objective of this thesis is the determination of the number of transmitted solitons in noisy data from hydraulic model tests and numerical simulations, the EEMD is always applied to the original data original data in the following analyses. A manual and visual or automatic time-domain pre-processing of the data in order to identify those solitons that do not require an EEMD is in opposite to the idea of the approach within this thesis. The solitons shall be determined automatically by application of an appropriate frequency or time-frequency domain analysis method.

After the application of the HHT to single-soliton data, this method is now applied to numerical data of an incident wave and of transmitted waves behind the reef with finite width and over the reef with infinite width.

In Fig. 4.15, the incident solitary wave with $H_{i,sol}=0.08m$ in front of the reef from a numerical simulation is presented. The upper blue curve shows the original data, the other curves the IMFs as determined by the EEMD with $A_n=0.1$ the amplitude of the added white noise, and $N_{wn}=100$ the number of cycles of white noise addition. Finally, the Hilbert spectrum of the IMFs is plotted. As expected, this incident solitary wave shows the same characteristic Hilbert spectrum properties as already determined in Fig. 4.14 for the wave from solitary wave theory: The solitary wave is decomposed into several wavelet-like components with their peaks at the same position.

In Fig. 4.16, the transmitted solitary wave behind a reef with $b_r=2.0m$ is decomposed with the EEMD and the HT spectrum is determined. The leading soliton is decomposed qualitatively in the same way as the incident soliton in Fig. 4.15. Based on these results, it might be possible to identify single solitary waves by these characteristic properties in the Hilbert spectrum. Unfortunately, the analysed signal contains only one obvious, free soliton that can easily be identified just by visual observation. Therefore, further analyses with more free and hidden solitons are required to validate the HHT as an appropriate method for the identification of solitons in test data.

But not only solitons are present in the sample data in Fig. 4.16. The leading soliton is trailed by oscillatory waves with decreasing wave length (due to frequency dispersion effects). In the space-wave number representation of the Hilbert spectrum these trailing oscillatory waves are given as typical nonlinear waves with non-stationary frequencies that vary over the wave length (compare with Fig. 2.14 for the properties of the non-stationary frequency of a nonlinear wave). Since the wave lengths of these trailing waves are decreasing with increasing distance to the leading soliton, the instantaneous wave numbers increase as indicated in the figure.

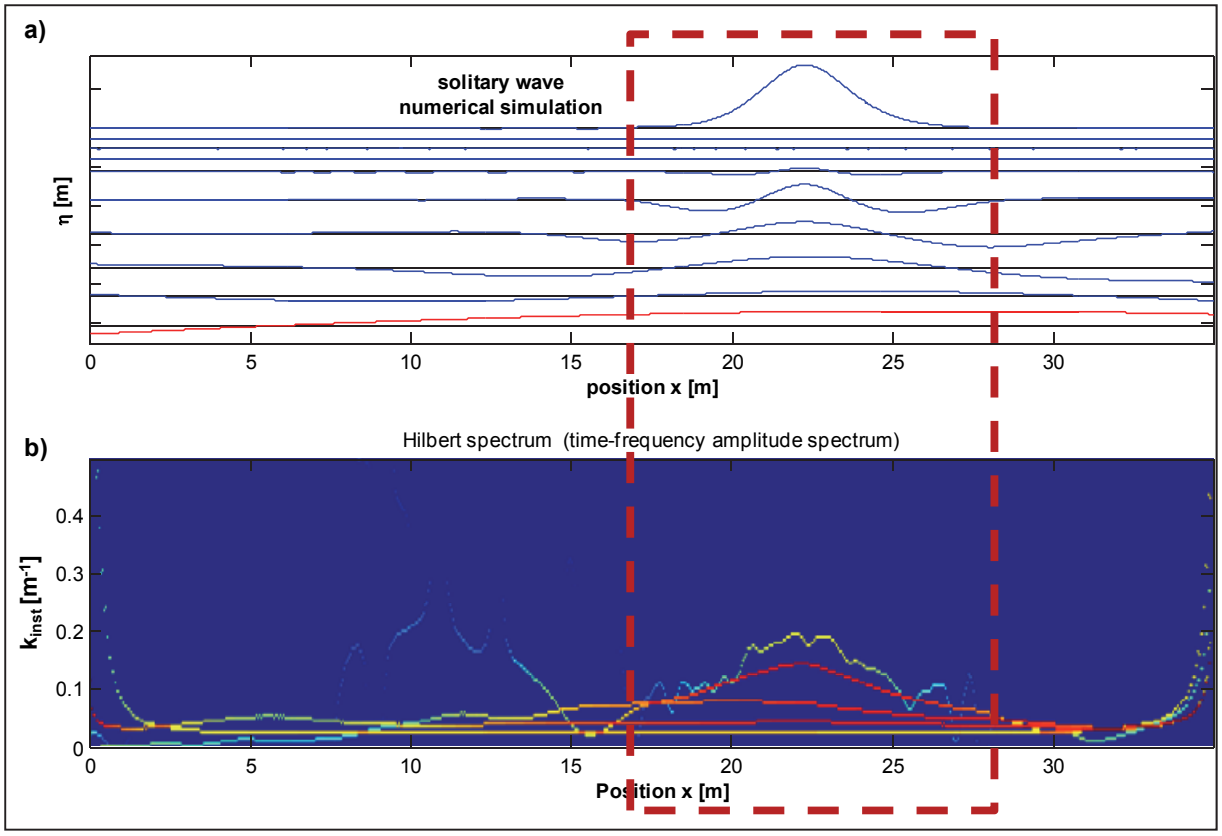

Fig. 4.15: a) Undisturbed incident solitary wave with $H_{i,sol}$ =0.08m in front of a reef with b_r=2.0m, the determined IMFs from EEMD and b) the corresponding Hilbert spectrum.

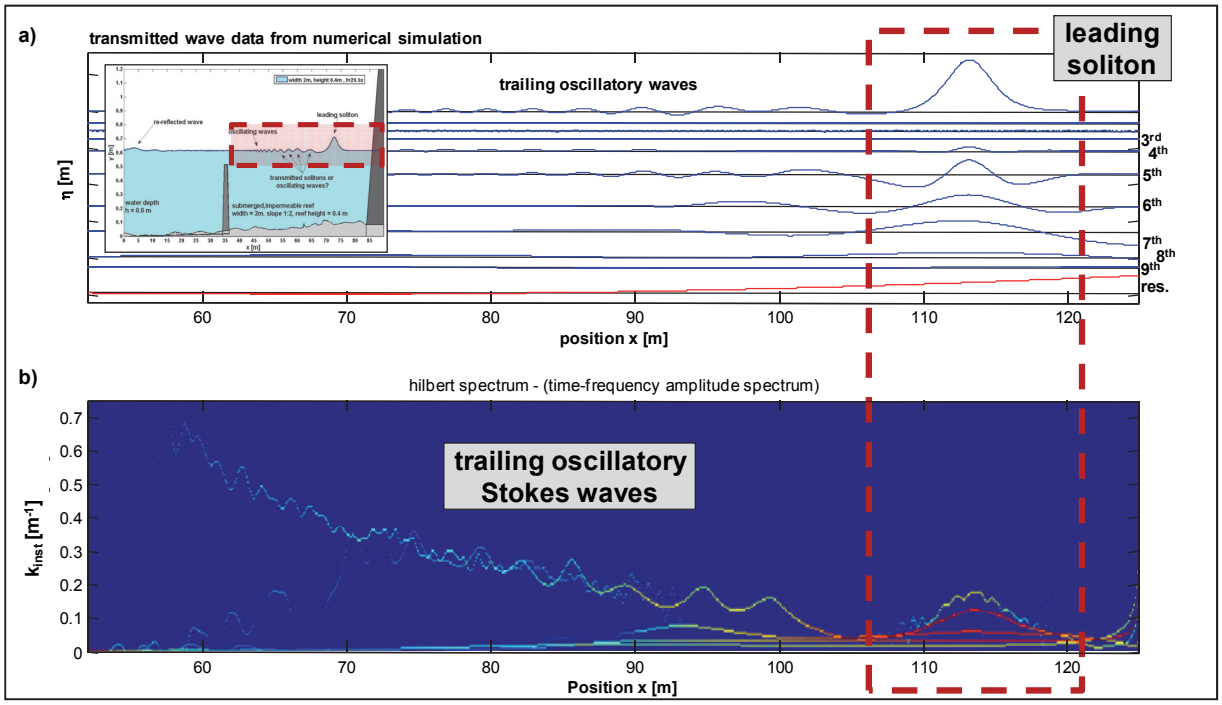

Fig. 4.16: Transmitted solitary wave with $H_{i,sol}$ =0.08m behind a *finite width* reef with b_r=2.0m, the determined IMFs from EEMD and the corresponding Hilbert spectrum.

In Fig. 4.17, the HHT is applied to a signal of transmitted waves over a reef with an infinite width that contains several already separated and therefore obvious solitons. As in the previ-

ous examples, the solitons are decomposed into wavelet-like components and the spectral representation of the solitons in the spectrum is similar to that in Fig. 4.14 to Fig. 4.16. Again, these solitons are obvious and can easily be obtained from the signal by visual observation because they have already separated from the bore and are travelling as independent free solitons. Behind the three solitons, the instantaneous wave numbers in the Hilbert spectrum do neither show the characteristic properties of further solitons nor the oscillations of nonlinear Stokes or of cnoidal-theory waves, as shown in Fig. 4.16 for the trailing oscillatory waves. Visual observations of the original signal show two more possible solitons with peaks at *x=98m* and *x=95m*. The soliton at *x=95.5m* might be represented in the Hilbert spectrum with a peak, but the solitons at *x=98m* is missing. It can be concluded, that the EEMD and the HHT seem to be able to determine the free solitons, but they do not provide sufficient information to reliably categorize the trailing peaks behind the free soliton either as soliton or oscillatory waves.

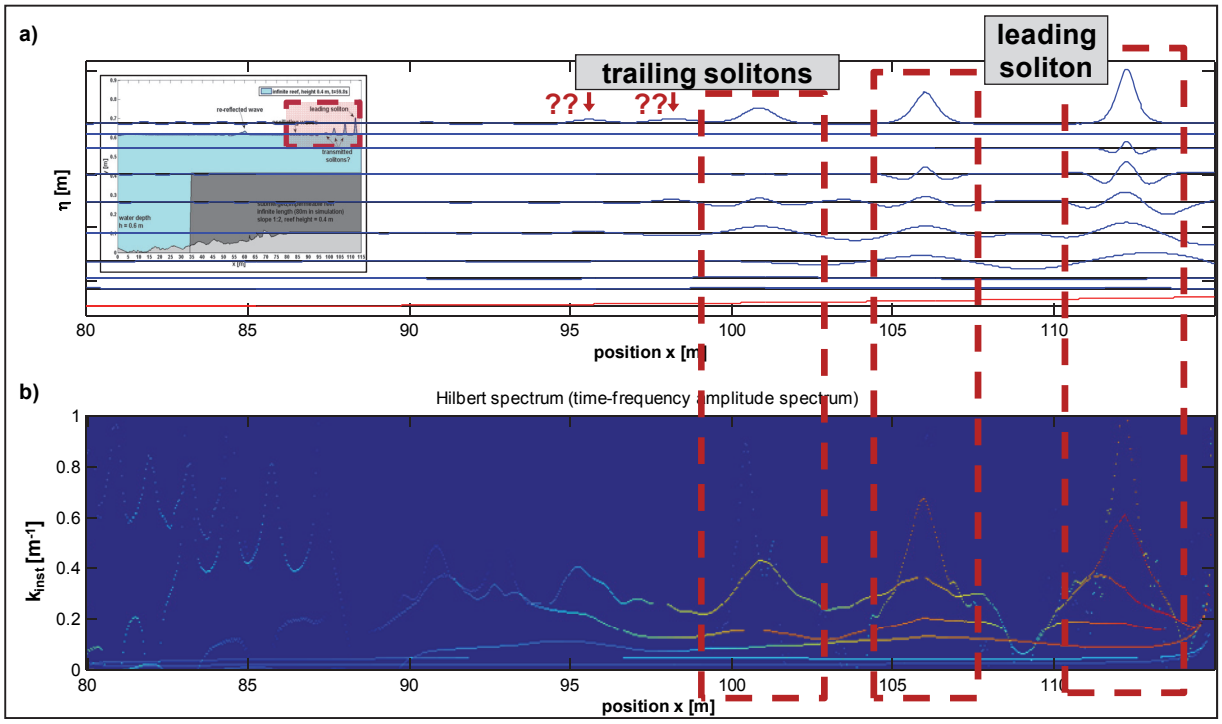

Fig. 4.17: Transmitted wave train of a solitary wave with $H_{i,sol}$ *=0.08m* over an reef with an *infinite width*, the determined IMFs from EEMD and the corresponding Hilbert spectrum.

In Fig. 4.18, the EEMD is also applied to another signal of an undular bore over a reef with infinite width. In this signal, only one soliton has already completely separated from the bore, but up to 10 more less obvious peaks can be found still inside this undular bore. After a sufficient long propagation length they will evolve as free solitons. In the IMFs in Fig. 4.18, the leading soliton again shows the characteristic properties of the wavelet-like curves in the Hilbert spectrum as already observed in Fig. 4.12b. However, the trailing waves that will evolve as solitons later, but have not separated from the bore yet, are not identified as solitons in this EEMD result. Their spectral properties in the Hilbert spectrum are those of nonlinear oscillatory waves (see IMF2 and IMF3), because the instantaneous frequency oscillates within one wave length. This example clearly shows that the identification of solitons in the HHT is limited to those free solitons that have already separated from the bore and are thus obvious by visual observation in Fig. 4.18. In the KdV-NLFT that was applied to the data in parallel to

the HHT analyses these trailing, not yet separated solitons can be clearly identified as solitons (see section 4.5 and Fig. 4.25). Therefore, the KdV-NFLT has proved to be much more powerful for the identification of solitons, especially for those solitons that are still hidden within the bore. The results are presented in section 4.5. Since the results of the KdV-NLFT are very convincing, no further detailed investigations on the application of the EEMD and the HHT were conducted within this thesis. The HHT turned out to be unable to reliably determine the number of transmitted (hidden) solitons and for further analyses the KdV-NLFT was applied (see section 4.5).

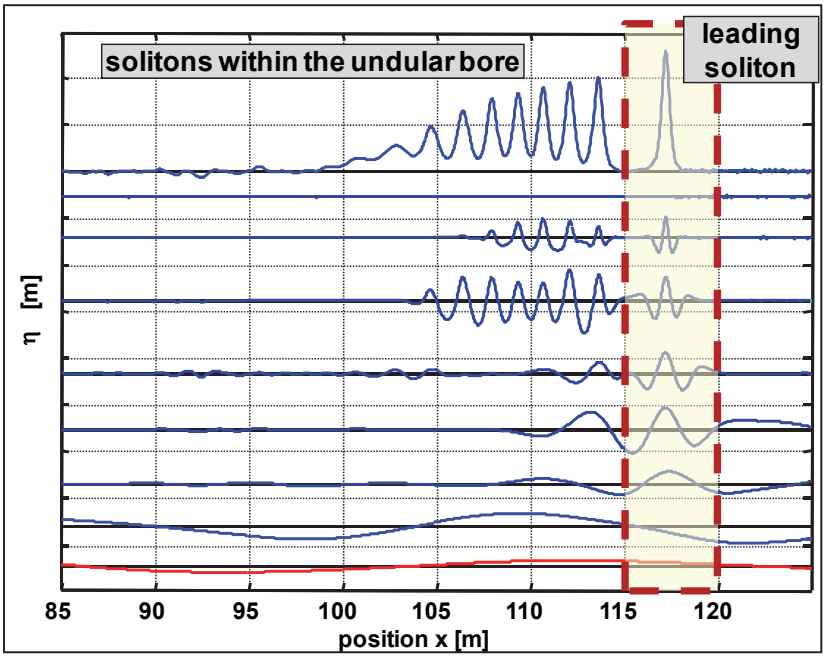

Fig. 4.18: Decomposition of an undular bore caused by the propagation of a solitary wave over a reef with an *infinite width* and the determined IMFs from EEMD.

4.5 Spectral analysis of soliton fission using the KdV-NLFT

This section primarily aims at examining the performance of the KdV-NLFT for the unambiguous determination of the total number of transmitted solitons N_{sol} over and behind submerged reefs, including both "hidden" and already separated solitons. *First*, an introduction into the application of the KdV-NLFT to soliton data is given. *Second*, the validation of the KdV-NLFT analysis results by means of numerical simulation data is presented. *Finally*, in section 4.6 the implemented and verified KdV-NLFT analysis is applied to various soliton data with different wave heights, relative submergence depths and reef widths, including reefs with finite and infinite width.

In the following sections, the data of wave transmission over and behind submerged reef are analysed as used in the previous sections. Where necessary, additional numerical data are analysed that have been determined for the same model set-ups, but with different reef width and therefore different propagation lengths over the reef.

4.5.1 Application of the direct KdV-NLFT to soliton data

For the reliable identification of transmitted solitons, an appropriate analysis method should have the capability to reliably determine the 'hidden' solitons that are still contained within the bore as well as those 'free' solitons that are already separated from the bore. Complete separation of *all* solitons requires a very long propagation reef width, and therefore will usually not be observed in experimental tests or real prototype situations. Finally, if all solitons would be completely separated, they could easily be determined visually and no advanced analysis method would be required. As a consequence, the required analysis method must be able to analyse the available data of (undular) bores and then predict the number of solitons that are still hidden within that bore and that will evolve from that bore in the future. As will be shown in the following examples, the KdV-NLFT fully meets these requirements.

To illustrate the benefit of KdV-NLFT the example wave train from Fig. 4.17 is selected at the end of the simulation area of a reef with an infinite width in Fig. 4.19. The corresponding nonlinear Fourier spectrum of this signal is shown in Fig. 4.20.

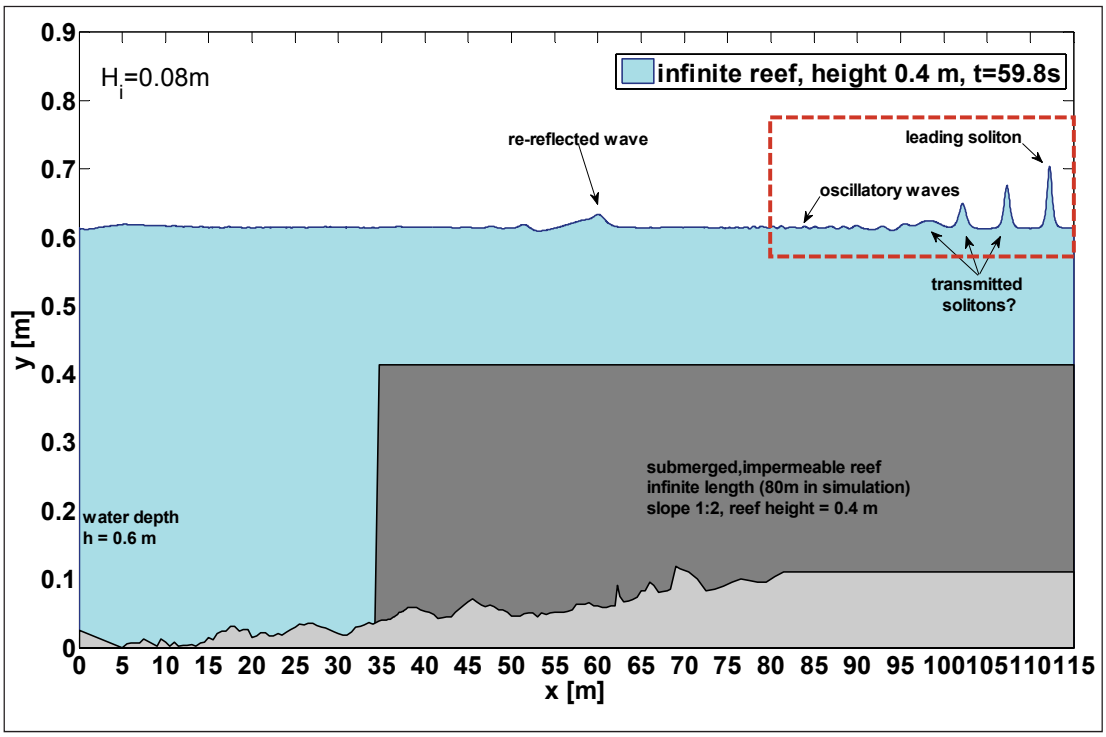

Fig. 4.19: Selection of an example wave train with leading soliton, trailing solitons and oscillatory waves over a reef with ($d_r/h=0.33$) an infinite width for the KdV-NLFT analysis (Brühl & Oumeraci, 2010).

The results in the nonlinear spectrum in Fig. 4.20 show that the solitons are considered as basic spectral components in the nonlinear analysis algorithms and that they are properly identified and represented in the nonlinear Fourier spectrum. The KdV-NLFT spectrum consists of the *soliton spectrum* with the soliton amplitudes A_j (red bars) and the *radiation spectrum* (green line) which contains the amplitudes a_j of the oscillatory waves (with shapes corresponding to Airy, Stokes and cnoidal-theory waves) depending on the value of the modulus m. The modulus m_j (blue dashed line, also denoted as soliton index I_j) represents the nonlinearity of the determined basic cnoidal components. For $m_j>0.99$ the cnoidal waves are solitary-like, for the limit $m_j=0$ the waves are linear. For $0<m_j<0.99$ the nonlinearity of the cnoi-

dal waves increases with m_j and the wave shape changes from Airy ($0<m_j<0.5$) over Stokes ($0.5<m_j<0.95$) to cnoidal-theory waves ($0.95<m_j<0.99$) and finally up to solitons ($m_j>0.99$) (see Fig. 4.5 and section 3.1.2). The underlying theories of the KdV-NLFT and the spectral cnoidal basic components are presented in chapter 2. Details of the numerical implementation of the KdV-NLFT are given in chapter 3.

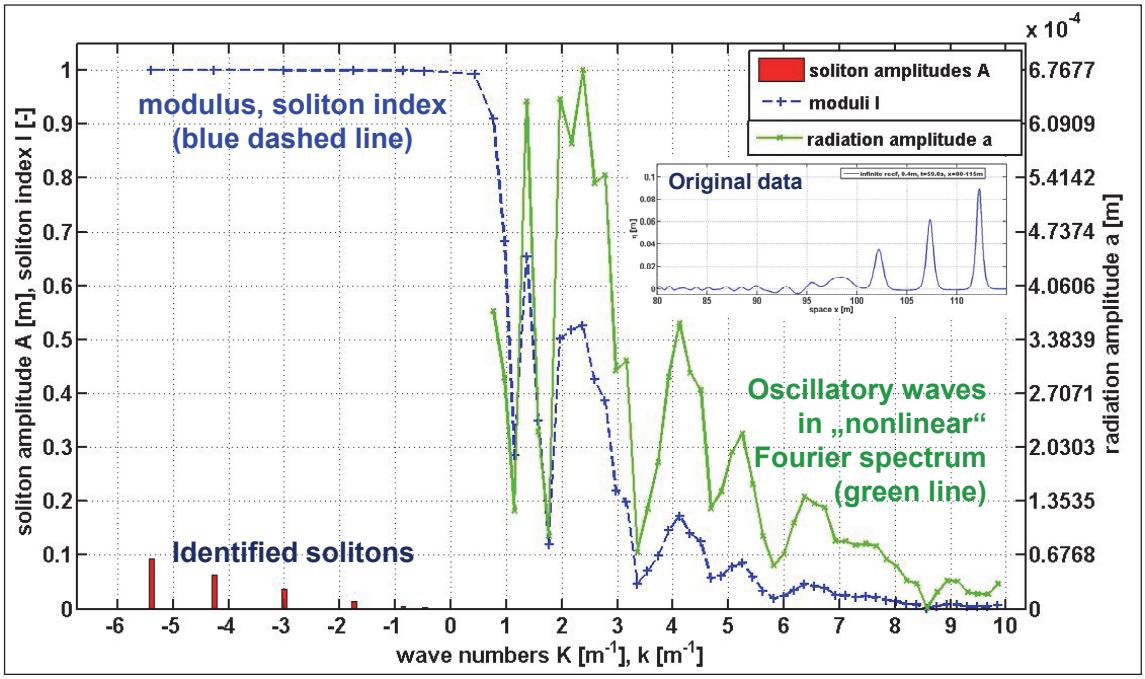

Fig. 4.20: Nonlinear Fourier spectrum of the example wave train in Fig. 4.19 (Brühl & Oumeraci, 2010).

The analysed space series from Fig. 4.19 contains three free solitons, a bore-shaped water package as trailing wave and a number of oscillatory waves. In the HHT analysis in Fig. 4.17 the three leading solitons were identified, but the signal section with the bore and the trailing oscillatory waves could not be analysed sufficiently. In the KdV-NLFT, the nonlinear spectrum shows a total of seven solitons, indicated by the large values of $m_j>0.99$ (blue plus signs) and plotted with their amplitudes as red bars. The first six soliton amplitudes can be seen in the spectrum whereas the seventh amplitude is too small. The first three bars give the correct soliton amplitudes of the free solitons. The other four solitons cannot be identified from the signal by visual observation. The bore shows two local maxima that might indicate two further solitons, but this is not sure. Furthermore, the nonlinear spectrum contains a number of oscillatory waves in the right part of the spectrum. Their amplitudes are very small, but this also corresponds to the small amplitudes of the trailing oscillatory waves in the data.

For the validation of the proper identification of hidden solitons, the soliton signal from Fig. 4.18 is re-analysed with the KdV-NLFT in Fig. 4.25b. The details will be discussed below, but at this point the main result can already be given: The KdV-NLFT is able to identify those solitons within the undular bore that have not completely separated yet. These waves have been represented in the HHT as oscillatory waves, but the KdV-NLFT gives the correct interpretation as solitons.

These very simple examples from Fig. 4.19 and Fig. 4.20 shows that the KdV-NLFT, unlike FFT and HHT, is able

(i) to identify free solitons as basic components with their correct amplitudes,

(ii) to identify the solitons that are sill hidden within the bore, and

(iii) to identify the oscillatory waves with their amplitudes and wave numbers or frequencies.

Furthermore, the application of the KdV-NLFT to wave-structure interaction in shallow water and the analysis of this kind of numerical test data are unique in the sense that this is the only method that directly identifies free and hidden solitons from experimental and numerical test dat. Reference data for numerical boundary conditions or program settings were not available and had to be determined empirically during the ongoing analyses. Comparative analyses with different numerically and analytically generated data have been performed with different settings for the resolutions of the wave numbers k, the pre-defined range of the Eigenvalue vector and the resolution Δx of the data. Still, the application of KdV-NLFT to the wave-structure interaction is under development and many details still have to be investigated in the future.

4.5.2 Validation of the results from KdV-NLFT using numerical simulation data

The nonlinear analysis method KdV-NLFT was implemented within this thesis and for the first time this method is applied for the analysis of transmitted solitons over submerged reefs. Therefore, in the following section an example is given on how the results obtained from the KdV-NLFT have been verified using numerical RANS/VOF simulation data. It will be shown that by analysis of the flow fields under the free surface the results from KdV-NLFT and especially the distinction between transmitted solitons and trailing oscillatory waves can be proved. The flow fields under translatory solitary wave and oscillatory travelling waves are completely different and therefore the different wave types can easily be distinguished if the flow under the waves is know. In the following examples the numerical simulations provide detailed information on the time-dependent flow fields under the incident and transmitted waves over and behind reefs with finite and infinite width.

Under a translatory solitary wave the horizontal orbital velocities are *always* directed in direction of the wave propagation (see Fig. 4.21a). No oscillatory flow components with reverse direction $-x$ can be observed under a solitary wave. In contrast, the flow field under an oscillatory wave consists of flow components in wave direction under the wave crest and of flow components in opposite direction under the wave trough (see Fig. 4.21b). For the distinction between solitary and oscillatory waves the flow fields under different waves and wave trains from numerical simulation are analysed.

For a first validation of this approach, the flow field under the incident solitary wave is analysed (see Fig. 4.22). This wave can easily be identified as a solitary wave by visual observation. Furthermore, the incident waves in front of the reef will be identified as solitary waves in the KdV-NLFT spectra as shown in Fig. 4.24. The flow field in Fig. 4.22 shows that the water is at rest in front of and behind the solitary waves. Under the wave, the flow is directed only in wave direction. No reverse flow can be observed. Comparison with the schematic particle paths of a solitary wave in Fig. 4.21 shows that the flow field under the incident solitary wave is a typical solitary flow field. Hence, the flow field analysis proves to be appropriate to identify solitary waves.

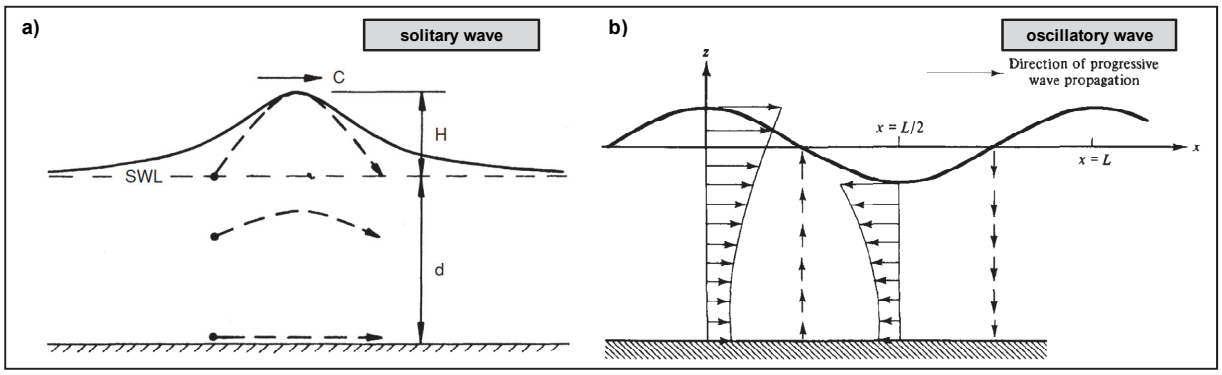

Fig. 4.21: a) Surface profile and particle paths for a solitary wave (Sorensen, 2006). b) Water particle velocities in a progressive oscillatory waves (Dean & Dalrymple, 1991).

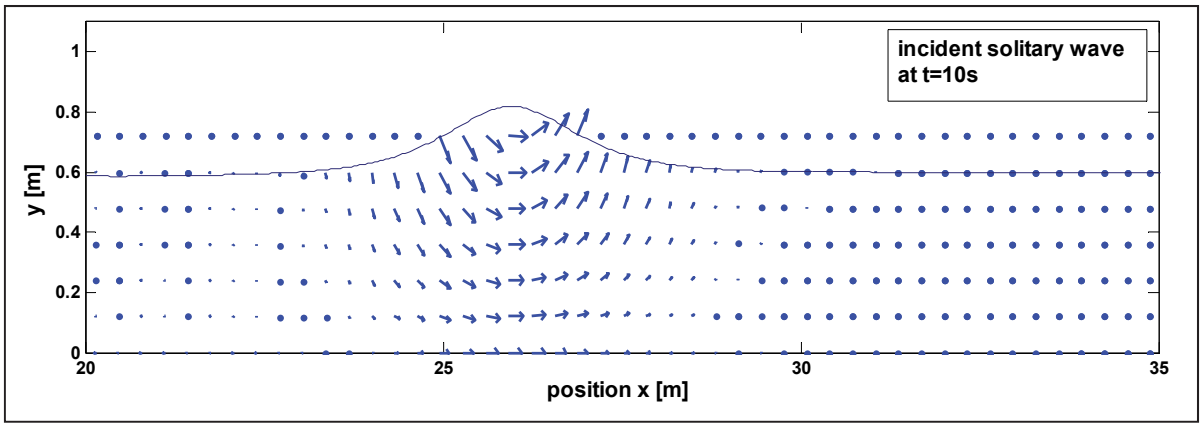

Fig. 4.22: Flow field under the incident solitary wave with $H_{i,sol}=0.22m$ in water depth $h=0.6m$ from numerical simulations with COBRAS-UC.

In the next step, an example of the flow field under the transmitted wave train behind a submerged reef with finite width $b_r=2.0m$ is given in Fig. 4.23. The first plot in Fig. 4.23a shows the flow field under the leading soliton for the range $x=65.0$-$85.0s$. The flow direction is indicated by the blue arrows and is always in direction of the wave propagation. The example in the figure is given for $t=29.6s$, but the characteristic solitary-wave flow field with unidirectional flow under the leading wave is obtained for each time step. The flow velocity in front of this leading wave is zero, the flow velocity behind the wave is much smaller, but shows reverse flow directions. The very large flow velocities also are characteristic for a solitary wave, since the oscillatory waves show much smaller velocities. The second plot in Fig. 4.23b shows the detail of the flow field of the trailing oscillatory waves for the range $x=60.0$-$77.0s$ with increased scale for the flow vectors in order to better visualize the flow. Nevertheless, the vectors within the flow field are to scale, so that the flow under the back side if the soliton (starting from $x=75s$) is represented by longer arrows than in Fig. 4.23a. Behind the soliton, the flow direction between $x=70.5m$ and $75m$ is in opposite direction to the wave direction, followed by flow in wave direction between $x=68m$ to $70.5m$. Further to the left, the flow directions change again and again, as typical for propagating oscillatory waves. Therefore, the trailing waves are clearly identified as oscillatory waves and can be distinguished from the leading soliton without any doubt.

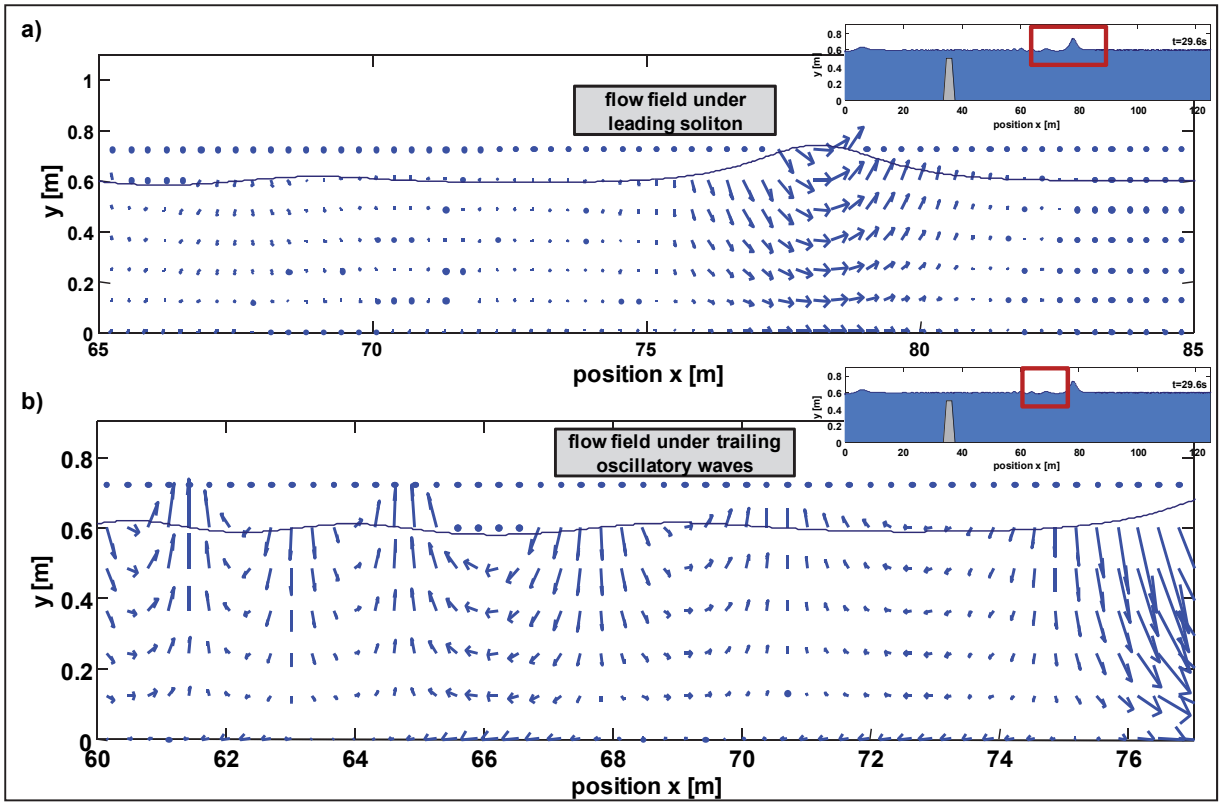

Fig. 4.23: Flow field under the transmitted waves behind a submerged reef with finite width $b_r=2.0m$ and incident solitary wave with $H_{i,sol}=0.22m$ in water depth $h=0.6m$ from numerical simulations with COBRAS-UC: a) flow field under the leading solitons and b) flow field under the trailing oscillatory waves. Note that the lengths of the flow field vectors in the two plots have different scales.

The flow field analysis as presented in the selected examples allows validating the KdV-NLFT analysis results for the wave transmission behind submerged reefs with finite widths. The existing prediction formulae in Eqs. (4.1) to (4.3) are valid for reefs with infinite width, but are not applicable to reefs with finite width, so that no comparison with data from literature is available to validate the KdV-NLFT analysis results. Furthermore, the determined results from KdV-NLFT differ from those in Strusinska (2011), so that a reliable validation of the results from the nonlinear spectra is required in order to judge which results are correct. Thus, the flow field analysis was applied to validate the KdV-NLFT results which are presented in the following section and proved, that in the simulations with reefs with finite width a maximum number of $N_{sol}=2$ transmitted solitons was not exceeded (see Tab. 4.4). Finally, the examples given here show that the observation of the flow field data provides more reliable results than only the visual observation of the free surface, and therefore this method is used to validate the results obtained from both visual observation and KdV-NLFT.

4.6 Determination of the influence of different parameters on the number of transmitted solitons using the KdV-NLFT

A first visual analysis of numerical simulations of wave-structure interactions between solitons and submerged reefs confirmed clearly that the processes of soliton fission (e.g. the locations at which the solitons separate from the undular bores or the total number of transmitted solitons N_{sol}) depend on both the incident soliton wave height $H_{i,sol}$ and the relative submergence depth d_r/h. But in the prediction formulae for the expected number of transmitted soli-

tons over submerged reefs with infinite width, only the relative submergence depth is considered (see section 4.2.1). Therefore, in the first two steps, the effect of the incident solitary wave height $H_{i,sol}$ on the development of solitons over the reef (section 4.6.1) and the influence of the submergence depth d_r over the reef (section 4.6.2) are analysed. Then the effect of the reef width b_r on the number of solitons is determined (section 4.6.3). Finally, the results of the application of NLFT for the analysis of transmitted solitons N_{sol} behind the submerged reefs with finite width are summarized and an outlook is given (section 4.6.4).

4.6.1 Effect of incident solitary wave height $H_{i,sol}$ on the development of solitons over reefs with infinite width

First, the incident solitary waves are analysed as reference waves for the following wave transformation processes. Fig. 4.24a shows the incident solitary waves with different wave heights $H_{i,sol}$=*0.08m, 0.12m, 0.18m* and *0.22m* in front of the reef at simulation time *t=10.0s* in water depth *h=0.6m* and in b) their theoretical absolute and relative 95% wave lengths after Dean and Dalrymple (1991). In Fig. 4.24c the nonlinear Fourier spectrum of the solitary wave with $H_{i,sol}$=*0.22m* is given as an example for the nonlinear analysis of the incident waves. The red bar in the lower left corner represents the only soliton that is determined from the simulation data. The wave height is correctly calculated with *H=0.22m*. Similar spectra are available for the other incident waves. Due to the small waves that follow the solitons, a small number of oscillatory waves with wave amplitudes $a<5\cdot10^{-3}m$ are determined in the KdV-NLFT analysis.

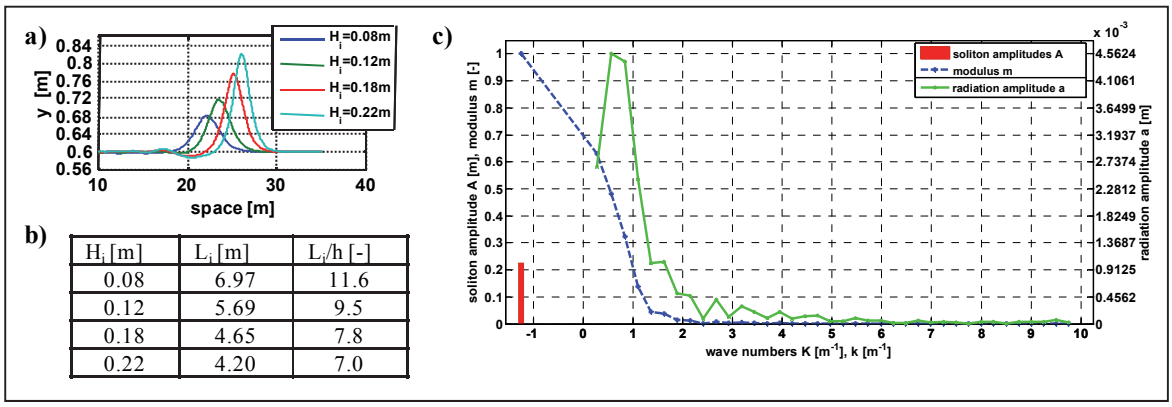

H_i [m]	L_i [m]	L_i/h [-]
0.08	6.97	11.6
0.12	5.69	9.5
0.18	4.65	7.8
0.22	4.20	7.0

Fig. 4.24: a) Undisturbed incident solitary waves in *h=0.6m* in front of the reef: Wave heights $H_{i,sol}$ = *0.08 m* (dark blue line); *0.12 m* (green); *0.18 m* (red); *0.22 m* (cyan). b) Absolute and relative solitary 95% wave lengths of incident solitary waves shown in the figure above. c) Nonlinear Fourier spectrum of the incident solitary wave with $H_{i,sol}$ = *0.22 m*.

For the analysis of the influence of the wave height $H_{i,sol}$ of the incident soliton on the wave transmission, the transmitted wave trains at the end of the reef with an 'infinite' width at *x=100-125m* are shown in Fig. 4.25a. In contrast to Fig. 4.20, now a transmitted solitary wave with $H_{i.sol}$=*0.22m* is analysed over a reef with d_r/h=*0.17* (instead of $H_{i,sol}$=*0.08m* and the lower reef with d_r/h=*0.33*).

The space series clearly show that the analysed wave trains differ in the number of clearly isolated solitons, in the shapes of the remaining bores, in the number of the waves that have not separated yet and in the wave heights of the solitons. Due to the limited reef width of the

'infinite' reef in the numerical simulations, the possible total number of solitons cannot be determined exactly. Unfortunately, with the selected numerical model longer reefs could not be simulated with the required grid resolution. Nevertheless, the space series are analysed using the KdV-NLFT and the results are compared. Fig. 4.25b shows the nonlinear Fourier spectrum of the undular bore for $H_{i,sol}=0.22m$ which shows a total of 26 solitons. This spectrum is determined from the signal in Fig. 4.25a for $H_{i,sol}=0.22m$. In the data, only two solitons have already clearly separated, but eleven further peaks are found in the bore, followed by at least four further oscillations that might evolve into future solitons. In the KdV-NLFT the bore is considered to be a superposition of physical nonlinear shallow-water waves and their nonlinear interaction. As this packet of dispersive waves propagates, the different wave components separate and the solitons evolve from the bore. In this respect, the most important feature of the KdV-NLFT is that each surface elevation is reconstructed by physical cnoidal waves that are stable in the given water depth *and* their mutual nonlinear wave-wave interactions. Therefore, the KdV-NLFT is able to predict the dispersion of waves in shallow water. The incident soliton is stable in the larger water depth in front of the reef. If this wave enters the shallow-water region over the reef, it is not a stable wave anymore, because the shape of the solitons in this shallow depth is completely different. So suddenly, the incident solitons becomes a dispersive wave package. Since the water depth is explicitly considered in the KdV-NLFT as governing input parameter, the number and the spectral properties of these new waves can be predicted.

Overall, the application of the KdV-NLFT on different space series of incident and transmitted waves showed that the nonlinear Fourier spectra are plausible and meet the following expectations (see Fig. 4.19):

(i) the obvious (already) separated solitons (transmitted and reflected) are identified with correct amplitudes,

(ii) the amplitudes of the oscillatory waves are small compared to the soliton amplitudes and

(iii) the higher the wave number (i.e. shorter waves) the smaller the modulus m and thus the nonlinearity of the oscillatory waves in a given water depth.

The results clearly show that the NLFT is able to determine a large number of solitons from the undular bore, even if the solitons have not yet completely separated from the bore. In this example, a total of 26 solitons is determined in the nonlinear spectrum. From visual observation (by counting the total number of soliton-shaped peaks in the signal), up to 18 peaks can be found (1 leading solitons, 10 peaks at the front of the undular bore and additional 7 peaks within the bore) and most probably, further solitons might still be hidden within the bore. Tab. 4.1 comparatively shows the number of solitons determined by (i) visual analysis of the space series, (ii) application of NLFT and (iii) calculated from Eqs. (4.1) to (4.3).

Furthermore, the number of visible undular waves in the bore is given in Tab. 4.1. The total number of solitons and undular waves observed in the data for $H_{i,sol}=0.08m$ corresponds very well to the number of solitons predicted by Eqs. (4.1) to (4.3). This confirms the assumption that this undular waves will disperse into separated solitons if the reef is long enough. For the higher waves, the visual analysis of the undular bore provides more peaks than predicted by the equations. Since the determined values are still smaller than N_{sol} from KdV-NLFT, it can

be concluded that not all solitons that are contained in the bore generate significant peaks at the surface of the undular bore.

Tab. 4.1: Number of solitons N_{sol} from visual observation of the time series plot, NLFT analysis and theoretical formulae (h_r=*0.5m*, h=*0.6m*) (after Brühl & Oumeraci, 2010).

wave height H_i [m]	N_{sol} from visual observation*	undular waves at front of bore	N_{sol} from KdV-NLFT analysis	N_{sol} by Tappert and Zabusky (1972) (Eq. (4.1))	N_{sol} by Johnson (1972) (Eq. (4.2))	N_{sol} by Germain (1984) and Kabbaj (1984) (Eq. (4.3))
0.08	1	9	16	12	11	10
0.12	1	12	21			
0.18	1	14	22			
0.22	2	16	26			

*visual observation: Here, the number of *completely separated* solitons is determined by visual analysis of the data.

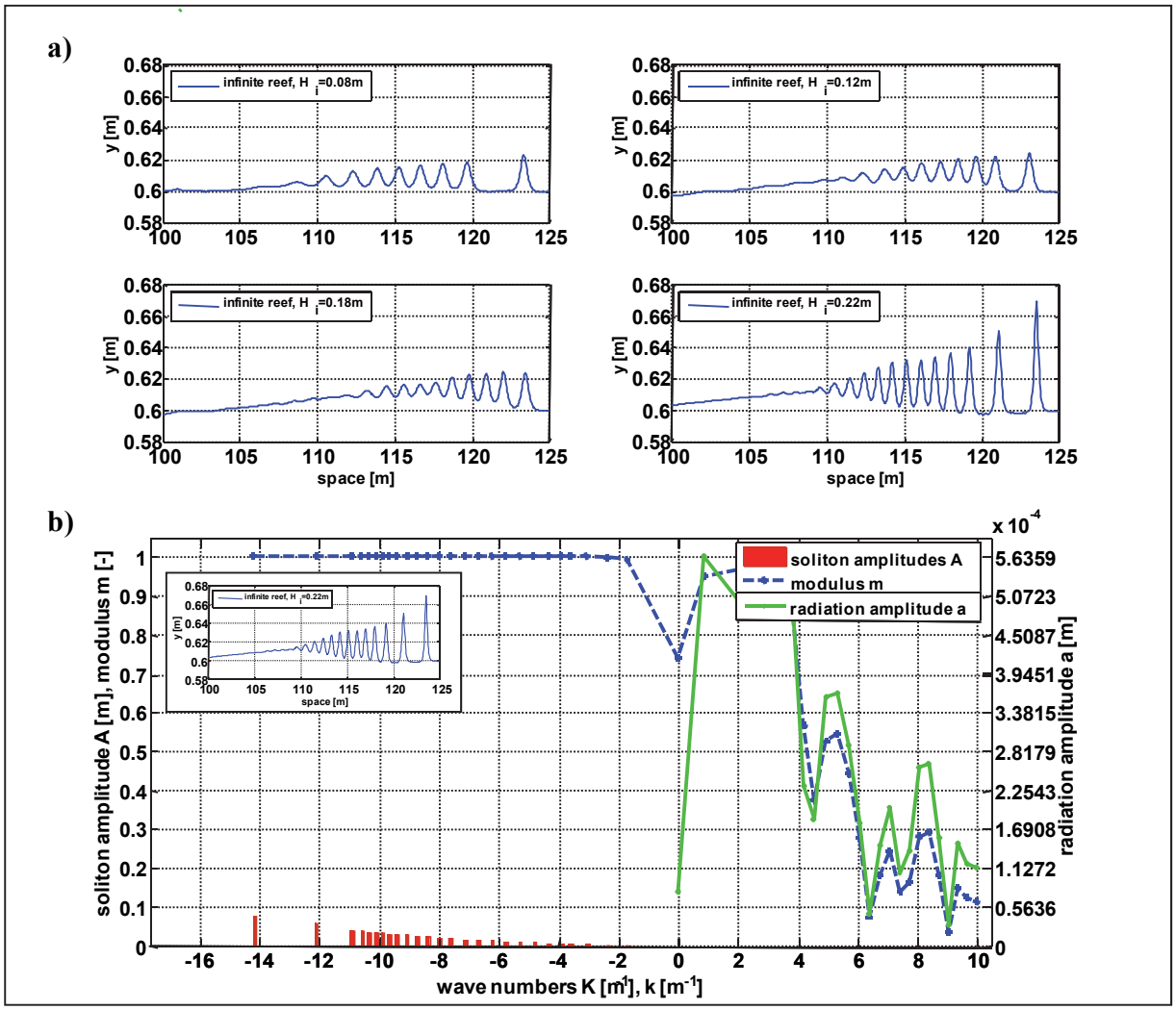

Fig. 4.25: a) Transmitted wave trains at the end of the simulation area. b) Nonlinear spectrum of the wave train for the example shown in Fig. 4.18 and this Fig. 4.25a (right lower corner) which was generated by an incident solitary wave with $H_{i,sol}$ = *0.22 m* as shown in Fig. 4.24.

In contrast to the visual observations, the available prediction formulae for the expected number of solitons does not consider the incident wave height $H_{i,sol}$, although the observed solitons and the number of undular waves clearly show the influence of incident solitary wave height $H_{i,sol}$ on the number N_{sol} and amplitude A of the transmitted solitons. For $H_{i,sol}$=*0.08m*

the amplitude values of the 9 highest solitons that are obtained from KdV-NLFT are *A=0.026m*, *0.022m*, *0.021m*, *0.020m*, *0.018m*, *0.017m*, *0.015m*, *0.012m* and *0.008m*. For $H_{i,sol}=0.22m$, a total of 12 solitons are obtained with from KdV-NLFT with amplitudes *A=0.077m*, *0.056m*, *0.041m*, *0.037m*, *0.035m*, *0.034m*, *0.033m*, *0.031m*, *0.030m*, *0.028m*, *0.026m* and *0.024m*. The analysis of undular bores and soliton wave trains with NLFT showed that the number of determined solitons is always significantly larger than the number of solitons that can be observed in the data.

For $H_{i,sol}=0.08m$ the visual observation of the data provides soliton amplitudes *A=0.023m*, *0.019m*, *0.018m*, *0.017m*, *0.016m*, *0.015m*, *0.013m*, *0.009m* and *0.005m*. The determined solitary wave amplitudes A_j from NLFT and their relations correspond with the observed separated soliton and the undular waves, especially the small jumps in the wave height between solitons 1 and 2, solitons 7 and 8 as well as between solitons 8 and 9. The wave height is overestimated in the KdV-NLFT analysis by about $0.035 \cdot H_{i,sol}$. For $H_{i,sol}=0.22m$ the analysed values are *A=0.070m*, *0.051m*, *0.039m*, *0.037m*, *0.034m*, *0.032m*, *0.032m*, *0.030m*, *0.027m*, *0.024m*, *0.021m* and *0.017m*. In this case, the soliton amplitude is overestimated by about $0.032 \cdot H_{i,sol}$. This comparison shows that the KdV-NLFT does not distinguish between the solitons that have already separated from the undular bore and the waves inside the bore. The undular waves are regarded as solitons. Due to the close distance between them, they interact nonlinearly and the resulting wave heights in the signal are smaller than they would be if the solitons would have already separated. The nonlinear interaction terms reduce the visible wave height. The higher the waves, the stronger the nonlinear properties and the larger are the interactions. Therefore, the overestimation at $H_{i,sol}=0.08m$ is smaller than in the test with higher solitons.

The comparison of simulation data with different incident soliton wave heights $H_{i,sol}$ over a reef with finite width shows that the number of separated solitons at this location (*x=65-90m* behind the reef front, i.e. 13 to 21 times the incident wave length) cannot be determined correctly from observation and by application of the available theoretical formulae which do not consider $H_{i,sol}$ as a governing factor for N_{sol}. The KdV-NLFT determines the separated solitons, the clearly visible waves in the undular bore and an additional number of solitons that represent the rest of the bore. The analysis results obtained from KdV-NLFT proof, that the number of solitons (observed and determined from the nonlinear spectra) as well as the number of the waves in the undular bore depends on the incident wave height. These results are in contrast to the available prediction formulae as given in the literature.

The results with the conventional FFT and the HHT in section 4.4 show that neither from FFT nor from HHT analysis results the number of transmitted solitons can be reliably determined. Therefore, the KdV-NLFT is the only analysis method that is capable to provide the required analysis results and show the influence of $H_{i,sol}$ on the number of transmitted solitons N_{sol}.

As shown in this section, N_{sol} is a function of $H_{i,sol}$. In systematic future analyses the influence of the relations $H_{i,sol}/h$ and/or $H_{i,sol}/d_r$ should be analysed, since the relation *wave height / water depth* is a known nonlinearity parameter, and therefore might provide further information that finally lead to an improved prediction formula for N_{sol} that does not only consider the water depths h and d_r but also the wave height $H_{i,sol}$ of the incident solitary wave.

4.6.2 Effect of relative submergence depth d_r/h over the reef on the development of solitons over reefs with infinite width

The relative submergence depth d_r/h is the governing variable for the calculation of the number of expected solitons over reefs with infinite width in Eqs. (4.1) to (4.3). Fig. 4.26 shows transmitted wave trains over reefs with infinite width for all four incident wave heights $H_{i,sol}$ and all reef heights h_r. Within the signals for one wave height $H_{i,sol}$, the number of solitons increases with decreasing relative submergence depth d_r/h (and increasing reef height h_r). Note that the curve for $d_r/h=0.33$ in Fig. 4.26a shows the selected free surface from Fig. 4.19 and Fig. 4.20, and the curve for $d_r/h=0.17$ in Fig. 4.26d shows the analysed signal from Fig. 4.25b.

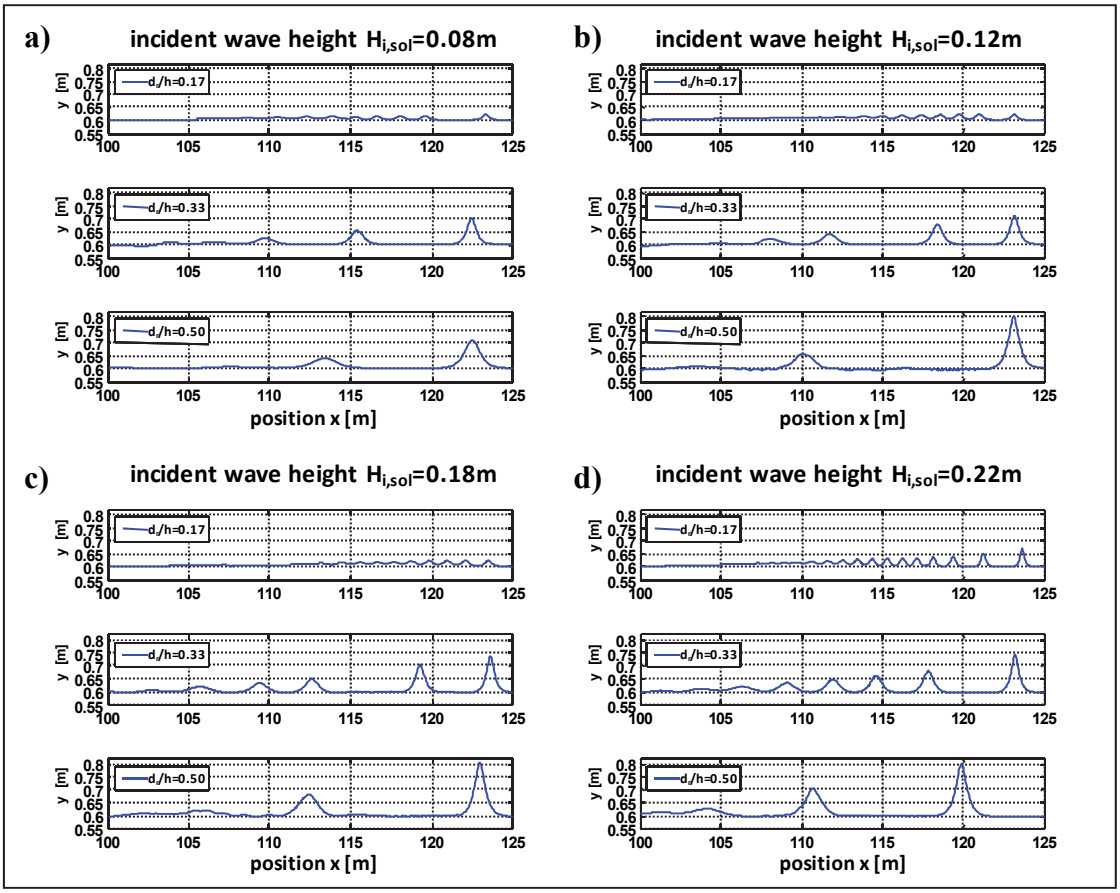

Fig. 4.26: Transmitted wave trains at the end of the reefs with infinite width for all incident wave heights $H_{i,sol}$ and all reef heights h_r.

For the determination of the number of transmitted solitons N_{sol} in the curves from Fig. 4.26 three different approaches are used: (i) calculation of N_{sol} from the prediction formulae in Eqs. (4.1) to (4.3), (ii) visual observation of the time series and counting of the total number of free solitons and those that are still within the undular bore, and (iii) application of the KdV-NLFT and counting of the solitons in the determined nonlinear spectra. Tab. 4.2 shows the number solitons from the three methods.

For reefs with $h_r=0.40m$ ($d_r/h=0.33$) and $0.30m$ ($d_r/h=0.5$) no undular bore can be identified in the data, because at the end of the simulation area ($x=100$-$125m$) the solitons have already

separated from the bore or because no bore was generated at all. Therefore, the values of N_{sol} from visual observation that are given in the table represent the number of free solitons.

Tab. 4.2: N_{sol} from prediction formulae, visual observation and KdV-NLFT analysis at *x=100*-125m for all $H_{i,sol}$ and d_r/h from Fig. 4.26 (after Brühl & Oumeraci, 2010).

h_r [m]	d_r/h [-]	predicted N_{sol} from Eqs. (4.1), (4.2), (4.3)	$H_{i,sol}$ = 0.08 m		$H_{i,sol}$ = 0.12 m		$H_{i,sol}$ = 0.18 m		$H_{i,sol}$ = 0.22 m	
			visual observation	KdV-NLFT	visual observation	KdV-NLFT	visual observation	KdV-NLFT	visual observation	KdV-NLFT
0.5	0.17	*12, 11, 10*	*8*	*16*	*9*	*21*	*10*	*22*	*12*	*26*
0.4	0.33	*6, 5, 4*	*5*	*7*	*5*	*7*	*6*	*8*	*7*	*8*
0.3	0.50	*4, 3, 3*	*2*	*2*	*3*	*3*	*3*	*4*	*3*	*4*

For reef height h_r*=0.50m* (d_r/h*=0.17*), the number of solitons and undular waves within the bore increases from 8 (from visual observation) and 16 (from KdV-NLFT) for $H_{i,sol}$*=0.08m* over 9 (21) and 10 (22) to 12 (26) for $H_{i,sol}$*=0.22m*. The prediction formulae provide expected values of N_{sol}*=12*, *11* and *10*. These three different values are obtained from three different equations (Eqs. (4.1) to (4.3)), do not consider the wave height as governing parameter and therefore provide the same values of N_{sol} for all wave heights $H_{i,sol}$. For d_r/h*=0.33* the results for visual observation and KdV-NLFT analysis show 5 (7), 5 (7), 6 (8) and 7 (8) solitons. The prediction formulae provide N_{sol}*=6*, 5 and *4*. For d_r/h*=0.5* and $H_{i,sol}$*=0.08m* in visual observation and KdV-NLFT analysis only 2 (2) clear solitons are found, followed by a third one for $H_{i,sol}$*=0.12m* (3 solitons in KdV-NLFT), *0.18m* (3) and *0.22m* (3). For this case, the prediction formulae provide N_{sol}*=4*, 3 and *3*.

The curves in Fig. 4.26 and the results for N_{sol} in Tab. 4.2 clearly show the influence of the incident wave height $H_{i,sol}$ on the generation of a (undular) bore and therefore on the number of transmitted solitons, although the prediction formulae do not contain $H_{i,sol}$. Over the reefs with d_r/h*=0.33* and *0.5* no bores are observed in the selected analysis windows at the end of the simulation area and N_{sol} from KdV-NLFT nearly corresponds to the free solitons observed in the data. Since no bore is contained in the surface data, all solitons have already evolved and no more solitons are hidden within a bore. Therefore, all solitons propagate as free solitons and can easily be observed in the data by visual observation. Furthermore, the number of determined solitons from visual observation and KdV-NLFT is very similar to those obtained from the prediction formulae.

In case of higher reefs and therefore decreased relative submergence depth d_r/h*=0.17* a distinct undular is observed for all wave heights. This means that the propagation length of the bore over the reef is too short for the separation of all solitons. Therefore, the number of visually observed solitons is smaller than the number determined by KdV-NLFT, because many solitons are still hidden and cannot be determined as free solitons or peak within the undular bore. For high incident solitary waves, the values of N_{sol} from prediction formulae and visual observation are very similar. For smaller waves, the number of observed solitons is significantly smaller than those from the prediction formulae. Furthermore, as expected the number of transmitted solitons from KdV-NLFT more than double the values of visual observation.

The observations and analyses confirm the strong influence of both d_r/h and $H_{i,\mathrm{sol}}$ on the number of transmitted solitons. The results clearly show, that the physical processes over the reef and the process of bore generation change between d_r/h*=0.17* (distinct undular bore for all $H_{i,sol}$) and *0.33* (no bore observed at all). For relative depth d_r/h*=0.33* and $H_{i,sol}$*=0.22m* the

process of undular bore generation and separation of the solitons is much faster than observed over the higher reef with d_r/h. At $x=100\text{-}125m$ all solitons have already evolved and the bore has disappeared. For $d_r/h=0.33$ and $H_{i,sol}=0.08m$ no undular bore is generated at all and the incident soliton disintegrates into several solitons directly at the beginning of the reef without forming a turbulent bore shape. The same applies for $d_r/h=0.5$.

Finally, the data of transmitted waves and the analysis results presented in this section confirm, that the relative submergence depth d_r/h significantly affects not only the number of transmitted solitons N_{sol}, but even the process of bore generation and propagation. Therefore, the number of free and hidden solitons at a selected position behind the reef is not only a function of x and $H_{i,sol}$, but also strongly depending on d_r/h. Although the relation d_r/h is contained in the prediction formulae in Eqs. (4.1) to (4.3), the results presented here for different combinations of d_r/h and $H_{i,sol}$ clearly show that the formulae are not covering all influence parameters that are governing the KdV-NLFT results. Therefore, in further analyses missing most important parameters should be determined and the prediction formulae should be modified and extended. In further numerical simulations with longer reef width the final number of free solitons should be determined and compared with the prediction formulae results. Note that the solitons amplitude in the nonlinear spectrum in Fig. 4.25 decrease from left to right, so that maybe the smaller solitons become too small to be detected by visual observation. This might explain the smaller values of N_{sol} from the prediction formulae.

4.6.3 Effect of relative reef width b_r/L_i on the number of transmitted solitons N_{sol} behind reefs with finite width

The analysis of the influence of the wave height $H_{i,sol}$ and the relative submergence depth d_r/h showed that for high reefs, a turbulent bore is generated at the beginning of the reef (see Fig. 4.1) that propagates over the reef. Then, undular waves are generated at the front of the bore that will, if the reef width b_r is long enough, evolve into a train of separated solitons. Tab. 4.3 shows the approximate propagation length over the reef with infinite width until (i) at least three undular waves are generated within the bore and until (ii) the first soliton is completely separated from the bore. In the analysed simulations, generally a reef width of at least 30 m is necessary for the *first soliton* to separate from the bore. Considering the incident solitary wave lengths $L_i=6.97m$ to $4.20m$ (see Fig. 4.24) for $H_{i,sol}=0.08m$ *to* $0.22m$ and the required propagation widths of 30m to 70 (see Tab. 4.3) for $H_{i,sol}=0.22m$, then for the required relative reef widths applies $b_r/L_i=4.3$ to 16.7. This means that for the generation of the first soliton and depending on $H_{i,sol}$, the reef width b_r has to be at least more than four times the incident soliton wave length for the lowest wave and more than 16 times for the highest waves in the simulations.

To obtain the number of transmitted solitons behind reefs with finite widths the wave trains behind reefs with $b_r=2.0m$ ($b_r/L_i=0.3$ to 4.3), $10.0m$ ($b_r/L_i=0.4$ to 5.3) and $30.0m$ ($b_r/L_i=0.5$ to 7.1) are analysed at the end of the simulation area ($x=100m\text{-}125m$ for $b_r=2.0m$ and $x=70m\text{-}125m$ for $b_r=10.0m$ and $30.0m$). The numbers of solitons N_{sol} from KdV-NLFT analysis are given in Tab. 4.4. In all analysed tests, only one or two transmitted solitons were found by the implemented KdV-NLFT algorithm. Behind the reef with $b_r=2.0m$ no more than one soliton was detected. This small reef width does not allow any bore generation or soliton fission. The

incident solitary wave just passes over the reef and generates a surge wave behind the reef that continues to propagate as a solitary wave.

Tab. 4.3: Approximate relative propagation length b_r/L_i [-] over the reef with infinite width (i) before at least three undular waves are generated and (ii) before the first soliton is completely separated from the bore (after Brühl & Oumeraci, 2010).

d_r/h [-]	$H_{i,sol}$ = 0.08 m				$H_{i,sol}$ = 0.12 m				$H_{i,sol}$ = 0.18 m				$H_{i,sol}$ = 0.22 m			
	3rd undular wave		1st soliton		3rd undular wave		1st soliton		3rd undular wave		1st soliton		3rd undular wave		1st soliton	
	b_r [m]	b_r/L_i [-]	b_r [m]	b_r/L_i [-]	b_r [m]	b_r/L_i [-]	b_r [m]	b_r/L_i [-]	b_r [m]	b_r/L_i [-]	b_r [m]	b_r/L_i [-]	b_r [m]	b_r/L_i [-]	b_r [m]	b_r/L_i [-]
0.17	20	2.9	30	4.3	30	5.3	45	7.9	40	8.6	60	12.9	50	11.9	70	16.7
0.33	-	-	25	3.6	-	-	30	5.3	-	-	50	10.8	35	8.3	50	11.9
0.50	-	-	30	4.3	-	-	30	5.3	-	-	30	6.5	-	-	30	7.1
Entry '-' means that no bore is generated.																

The higher $H_{i,sol}$ the more solitons are generated, but a value of $N_{sol}=2$ was not exceeded in the analysed tests. The analysis of samples with $b_r=50.0m$ gave the same result: one soliton for $H_{i,sol}=0.08m$ and two solitons for the higher waves.

Tab. 4.4: Number of solitons N_{sol} from KdV-NLFT analysis of wave trains behind reefs with $b_r=2.0m$, $10.0m$ and $30.0m$ (after Brühl & Oumeraci, 2010).

	$H_{i,sol}$ = 0.08 m			$H_{i,sol}$ = 0.12 m			$H_{i,sol}$ = 0.18 m			$H_{i,sol}$ = 0.22 m		
	b_r [-] (b_r/L_i [-])			b_r [-] (b_r/L_i [-])			b_r [-] (b_r/L_i [-])			b_r [-] (b_r/L_i [-])		
d_r/h [m]	2.0 (0.3)	10.0 (1.4)	30.0 (4.3)	2.0 (0.4)	10.0 (1.8)	30.0 (5.3)	2.0 (0.4)	10.0 (2.2)	30.0 (6.5)	2.0 (0.5)	10.0 (2.4)	30.0 (7.1)
0.17	1	1	1	1	2	2	1	2	2	1	2	2
0.33	1	1	2	1	1	2	1	2	2	1	2	2
0.50	1	1	2	1	1	2	1	2	2	1	2	2

The analysis of the influence of the reef width b_r has shown that very narrow reefs do not allow any bore generation or soliton fission. In the simulations, the minimum reef width at which a second soliton is generated for higher incident soliton wave heights $H_{i,sol}\geq0.12m$ is $b_r=10.0m$ ($b_r/L_i=1.8$). Increasing the reef width to $b_r=30.0m$ or $50.0m$ does not increase the maximum number of solitons in the analysed test data of transmitted waves behind the reef. For smaller waves with $H_{i,sol}<0.12m$ a minimum relative reef width of $b_r/L_i=2.2$ is required in order to obtain a second transmitted soliton.

The results show that for very narrow reefs with $b_r/L_i\leq1.4$ no second transmitted solitons is observed at all. For higher waves and $b_r/L_i\geq1.8$ or for small waves and $b_r/L_i\geq4.3$ a second soliton is determined behind the reef. But a value of $N_{sol}=2$ is not exceeded in all tests. Note that the difference to the results in Tab. 4.3 is that now the transmitted solitons are not determined *above* the reef, but *behind* the reef after the transmitted wave entered the area with higher water depth. Therefore, the results are not comparable, even for longer reef widths.

The analyses of the KdV-NLFT results as well as the observations of the numerical simulation results shows that the physical processes of wave transmission over reefs with infinite and finite widths are completely different. Over long reefs the transmitted waves propagate in

relatively small water depth and develop into bores, undular bores and finally, if the reef is wide enough, into free solitons. In this case, the number of solitons is a function of the propagation length above the reef. In case of narrow reefs, the transmitted wave passes of the reef and enters the deeper water before a bore or an undular bore is generated. Therefore, the transmitted wave generates surge waves that form the transmitted soliton. In case of higher incident wave height, the transmitted wave trains contain two solitons. Finally, a clear influence of the reef width cannot be determined with the small number of available tests. Future research might provide more systematic results that allow including the reef width in prediction formulae for the number of transmitted solitons N_{sol}.

4.6.4 Summary and concluding remarks

Systematic numerical model tests of solitary waves passing over submerged reefs with infinite and finite width have been analysed by visual observations and by application of the KdV-based nonlinear Fourier transform (KdV-NLFT). The results have been compared with the expected number of transmitted solitons N_{sol} from prediction formulae from the literature. The objective was to investigate the effect of the solitary wave height $H_{i.sol}$, the relative submergence depth d_r/h and the relative reef width b_r/L_i on the development of solitons over reefs with infinite width and behind reefs with finite width.

First, the analysis results obtained within this thesis show clearly that the number of transmitted waves N_{sol} is depending on the incident solitary wave height $H_{i,sol}$. However, this variable is not considered as governing factor for N_{sol} in the existing prediction formulae from the literature. The results show that for a given relative submergence depth d_r/h the values of N_{sol} are increasing with increasing wave height $H_{i,sol}$. For very small submergence depth, the transmitted solitary wave transforms into an undular bore and the KdV-NFLT analysis results provide a large number of transmitted solitons. Compared to the results of the prediction formulae the value of N_{sol} is more than doubled. Nevertheless, this high number of transmitted solitons cannot be observed in the undular bore because only up to two solitons have already separated from the bore. Further solitons can be identified by their soliton-shaped peaks within the undular bore, but half of the waves determined by KdV-NLFT cannot be found in the time series by visual observation. Hence, the KdV-NLFT does not only identify those solitons that have already completely separated from the bore or that appear in the peaks of the undular bore. The KdV-NLFT also identifies those solitons that are still completely hidden within the bore, that cannot be determined by visual observation and that will evolve from the bore in the future. The reason is that the KdV-NLFT is able to identify the transient character of the undular bores and to determine the underlying nonlinear spectral wave components, which are solitons in this case of very shallow water depth $d_r/h=0.17$. In systematic future analyses the influence of the relations $H_{i,sol}/h$ and/or $H_{i,sol}/d_r$ should be analysed, since the relation *wave height / water depth* is a known nonlinearity parameter, and therefore might provide further information that finally lead to an improved prediction formula for N_{sol} that does not only consider the water depths h and d_r but also the wave height $H_{i,sol}$ of the incident solitary wave.

Second, the observations and analyses for the relative submergence depth d_r/h confirm the strong influence of d_r/h on the number of transmitted solitons. The results clearly show that the physical processes over the reef and the process of bore generation change if the reef

height falls below a certain value. For lower reefs with $d_r/h \geq 0.33$, no undular bore is generated and the incident soliton disintegrates into several solitons directly at the beginning of the reef without forming a turbulent bore. For higher reefs with $d_r/h=0.17$ the transmitted solitary wave transforms into a bore, the process of solitons fission starts and the number of transmitted solitons is significantly increased.

Third, the analysis of the influence of the relative reef width b_r/L_i has clearly shown that very narrow reefs with $b_r=2.0m$ ($b_r/L_i=0.3$ to 0.5) do not cause any bore generation or soliton fission. The maximum number of solitons behind the reef in this case is one. In the simulations, the minimum reef width at which a second transmitted soliton is observed behind the reef is $b_r=10.0m$ ($H_{i,sol}=0.22m$, $b_r/L_i=1.4$ to 2.4). Increasing the reef width to $b_r=30.0m$ or $50.0m$ ($b_r/L_i=4.3$ to 7.1) does not increase the maximum number of solitons: The maximum number of transmitted solitons N_{sol} behind the reef in the analysed tests did not exceed $N_{sol}=2$. Madsen et al. (2008) stated that solitons 'may steepen and disintegrate into an undular bore' when they approach the coast. But they have seen 'no evidence that this can develop into a leading soliton'. The analyses show that in the examples given in this section the bores have to propagate at least 4.3 to 7.1 times the incident solitary wave length before the first soliton will be fully dispersed from the bore. Considering the prototype length of a real tsunami in the ocean that first propagates as a solitary wave before entering the shallow regions above the continental shelf, this means that soliton fission is 'not relevant for geophysical tsunamis' (Madsen et al., 2008), because the continental shelves are not at all wide enough to allow soliton fission before the tsunami reaches the coastline. Therefore, bores and undular bores represent the coast line wave forms resulting from soliton-shaped tsunami waves in the ocean.

The analysis of soliton fission within the previous sections well illustrates the capability of KdV-NLFT for the analysis of nonlinear waves and especially solitary waves. This method explicitly considers cnoidal waves (that include solitons) as basic components for the analysis. The KdV-NLFT reliably identifies solitons in undular bores from data of incident solitary waves and transmitted wave trains, even if the solitons have not yet fully dispersed from the bore or still are completely hidden inside it.

In the analyses presented here, the local processes at the beginning of the reef, such as the type of wave breaking, is not considered in the analyses because only test with non-breaking wave are analysed.

4.7 Summary

The KdV-NLFT approach considers a given surface elevation in shallow water as a transient wave package that is generated by the nonlinear superposition of nonlinear shallow water waves. This means that the shape of the free surface can be determined by the linear superposition of nonlinear cnoidal waves *and* their mutual nonlinear wave-wave interactions. Therefore, the KdV-NLFT is able to predict the dispersion of the bore and to determine the expected number of solitons even if they are not fully dispersed from the bore or are still fully hidden within it. The most important fact is that this spectral decomposition is not empirical but based on the Korteweg-deVries equation and the cnoidal wave equation, and therefore is in accordance with shallow water physics.

The KdV-NLFT analyses are performed for numerically generated data from the RANS/VOF model *COBRAS-UC* that was validated with laboratory test data. The application of the numerical model has made possible (i) the simulation of additional reef widths than those tested in the flume (including the reef with infinite width for comparison with available formulae), (ii) the generation of space series for the application of the implemented KdV-NLFT for the space-like KdV which are difficult to obtain in the required resolution in the laboratory, and (iii) the description of the detailed flow field under the waves which is important to validate the capability of KdV-NLFT to reliably distinguish between solitons and oscillatory waves in the transmitted wave trains behind submerged reefs.

The results of the KdV-NLFT analysis show that the wave height $H_{i,sol}$ as well as the relative reef width b_r/L_i (with b_r the reef width and L_i the incident soliton wave length) have a significant influence on the number of transmitted solitons N_{sol}. The higher the waves, the more solitons evolve from the undular bore. It is important to underline that the experimental and numerical data are derived from small scale model tests and simulations with sufficient relative propagation width $b_r/L_i>4.3$. At prototype scale the conditions might differ, so that the bore or the solitons might reach the shore before the soliton fission is completed or before it has even been started. Nevertheless, it is shown that the analysis of soliton fission well illustrates the capability of KdV-NLFT for the analysis of nonlinear solitary waves. The analysis results have been confirmed by available formulae for infinitely wide reefs and by visual observation of the analysed wave trains. The KdV-NLFT is able to identify solitons from undular bores even if the solitons have not yet fully dispersed from the bore or still are completely hidden inside it. The KdV-NLFT has proved to be a powerful advanced analysis method for the analysis of nonlinear waves.

5 Harmonic generation and wave transformation at, over and behind submerged reefs

Within two research projects at Leichtweiß-Institute for Hydraulic Engineering and Water Resources (LWI), TU Braunschweig, hydraulic model tests in the twin-wave flume with submerged rectangular reefs were analysed using the conventional fast Fourier transform (FFT). The primary objectives of the model tests were to analyse the wave transformation in front of, over and behind the artificial reefs. While performing the nonlinear Fourier transforms based on the Korteweg-deVries equation (KdV-NLFT) on the measured data, another problem of wave generation in shallow-water flumes came to the centre of attention: *the harmonic generation*. This latter phenomenon of nonlinear shallow-water wave propagation means the generation of higher-order harmonic wave components when a relatively long incident wave propagates in or into shallow water. Since the harmonic generation, clearly visible as an energy shift in the FFT spectra of incident and transmitted waves, also occurs when incident waves pass over submerged reefs, the theoretical background of harmonic generation in shallow-water flumes and basin is *first* discussed for such a case. *Second*, the FFT and the KdV-NLFT are applied to selected data from hydraulic model tests to identify the effects of harmonic generation in both linear and nonlinear approaches. *Finally*, a summary is given and the implications for further analyses are drawn.

5.1 Global and local effects at, over and behind submerged reefs

When water waves pass over submerged reefs with finite or infinite width, global and local effects occur that significantly change the shape of the free surface over and behind the reef. As a result of different effects such as wave reflection, energy dissipation and the generation of additional higher-order harmonic wave components, the wave amplitudes behind reefs with finite width are smaller than those of the incident waves. A schematic representation of global effects (such as energy losses and energy transfer in the FFT spectrum from low- to high-frequency components) and local effects (such as wave breaking and vortex generation) are shown in Fig. 5.1. In general, not all effects at submerged reefs have been yet sufficiently investigated. The remaining uncertainties or unknown processes are usually subsumed as *nonlinear effects*. The FFT spectra in Fig. 5.1 from incident waves in front of the reef and transmitted waves behind the reef show the effects of energy transfer or harmonic generation at the reef: As the waves pass over the reef, higher-order wave components are ‘generated’ in the transmitted spectrum that have not been determined in the incident spectrum.

In order to determine the hydraulic efficiency of submerged reefs from model test and to predict the impact of planned reefs, the energy balance of incident and transformed waves is considered based on the energies

$$E_t + E_r + E_d = E_i \tag{5.1}$$

or the energy coefficients

$$C_t^2 + C_r^2 + C_d^2 = 1 \tag{5.2}$$

$$C_t = \frac{H_t}{H_i} = \sqrt{\frac{E_t}{E_i}}, \qquad C_r = \frac{H_r}{H_i} = \sqrt{\frac{E_r}{E_i}}, \qquad C_d = \frac{H_d}{H_i} = \sqrt{\frac{E_d}{E_i}}, \tag{5.3}$$

where E_t, E_r, E_d and E_i are the transmitted, reflected, dissipated and incident energies, C_t, C_r and C_d are the transmission, reflection and dissipation coefficients and H_t, H_r, H_d and H_i are the wave heights of transmitted, reflected, dissipated and incident waves. The *dissipated wave height* H_d represents the wave height of a theoretical cosine wave with the dissipated energy E_d. The underlying idea of Eqs. (5.1) and (5.2) is that the sum of the energies E_t and E_r of the transmitted and the reflected waves plus the dissipated energy E_d has to return the energy E_i of the incident wave to fulfill the law of conservation of energy. The wave energies E (and therefore the transformation coefficients C) are functions of the wave height H:

$$E = \frac{1}{8}\rho g H^2 . \tag{5.4}$$

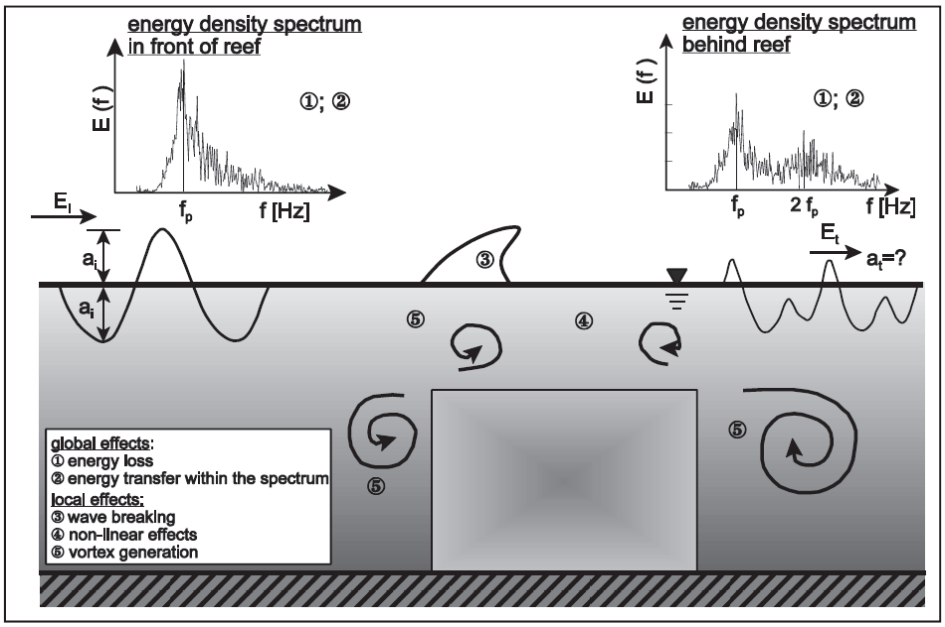

Fig. 5.1: Schematic representation of global and local effects at submerged reef with finite width (Bleck & Oumeraci, 2002).

If the wave height is determined from FFT then usually the spectral wave height H_{m0} is used:

$$H_{m0} = 4\sqrt{m_0} , \tag{5.5}$$

with m_0 the spectral moment of order Zero, calculated with the spectral density $S(f)$ from conventional Fourier spectrum

$$m_0 = \int S(f)\, df . \tag{5.6}$$

From Eqs. (5.3) and (5.5) follows that the coefficients C are calculated from the FFT spectra as $C_{m0,t}$, $C_{m0,r}$ and $C_{m0,d}$.

One of the drawbacks of this approach is that the dissipated energy E_d cannot be determined completely by measurements because only parts of it such as some of the vortex energies

might be partly measured. Other sources of energy losses such as friction losses or the acoustic energy of the typical sound of breaking waves are not measured. Hence, the dissipation energy E_d is the residual after subtracting the reflected and transmitted energies E_r and E_r from the incident wave energy E_i. Therefore, the different energy parts of the conservation law, unfortunately, cannot be calibrated. All errors and uncertainties that occur in measurements and/or the determination of E_i, E_t and E_r would be added up in Eqs. (5.1) and (5.2) as parts of E_d.

Different formulae for the prediction of the reflection, transmission and dissipation coefficients can be found in the literature, e.g. in Bleck (2003), Losada et al. (1997) and Van der Meer and D'Angremond (1991). A detailed list of relevant studies of wave transformation at artificial reefs is given in Bleck (2003).

5.2 Harmonic generation in shallow-water flumes and basins

In this section, *first* a short overview on the problem of harmonic generation in flumes and basins is given. *Second*, hydraulic model test data are analysed using the KdV-NLFT and the results are presented and discussed. *Third*, the problem of harmonic generation over sloping bottoms is analysed. *Finally*, a summary and conclusions are given.

5.2.1 Position of the problem

The 'harmonic generation' that occurs when relatively long waves propagate in shallow water is a well-known phenomenon that can be observed in field observations as well as in laboratory experiments and numerical simulations in wave flumes and basins. *Harmonic generation* means, in brief words, the generation of secondary wave crests in the troughs of the initial longer-period initial waves or the occurrence of higher-order components in FFT spectra of data at position B that have not been detected in other spectra of data from another position A located in front of B. In the time domain, these secondary higher-harmonic waves can be observed when waves propagate from deep water onto the continental shelf (Massel, 1983; Stoker, 1957) or in laboratory tests when waves with long periods are generated in shallow-water flumes or basins.

An example for harmonic generation in a wave flume is given in Fig. 5.2. The calculated initial cosine wave with $H=0.1m$ and $T=6.0s$ that is generated in a water depth of $h=0.56m$ is given in Fig. 5.2a. The conventional Fourier amplitude-frequency spectrum of this initial signal is plotted in Fig. 5.2b. Since this signal is a cosine wave, the FFT spectrum shows only one significant frequency component at $f=0.167Hz$. The signal in Fig. 5.2c was recorded in the far-field and shows two additional wave crests, one in front of the main peaks and a smaller one (a hump) behind it. The fast FFT spectrum in Fig. 5.2d now contains several additional peaks at higher-harmonic frequencies. These wave components have not been determined in the spectrum of the initial signal in Fig. 5.2a. Therefore, these harmonic frequency components are assumed to be generated during the propagation of the initial cosine wave to the position of the wave gauge in the far-field (*harmonic generation*). The smaller the relative water depth h/L the higher are the amplitudes of the harmonic components.

In the selected example, the generation and propagation of a linear cosine wave is selected to show the maximum effect of harmonic generation. For the generation of waves in flumes the

generated waves in daily practice usually are much better adapted to the water depth by application of nonlinear wave theories or numerical stream function theory, so that the effect of harmonic generation is reduced. But nevertheless, harmonic generation is a well-known phenomenon and can be observed in many test data.

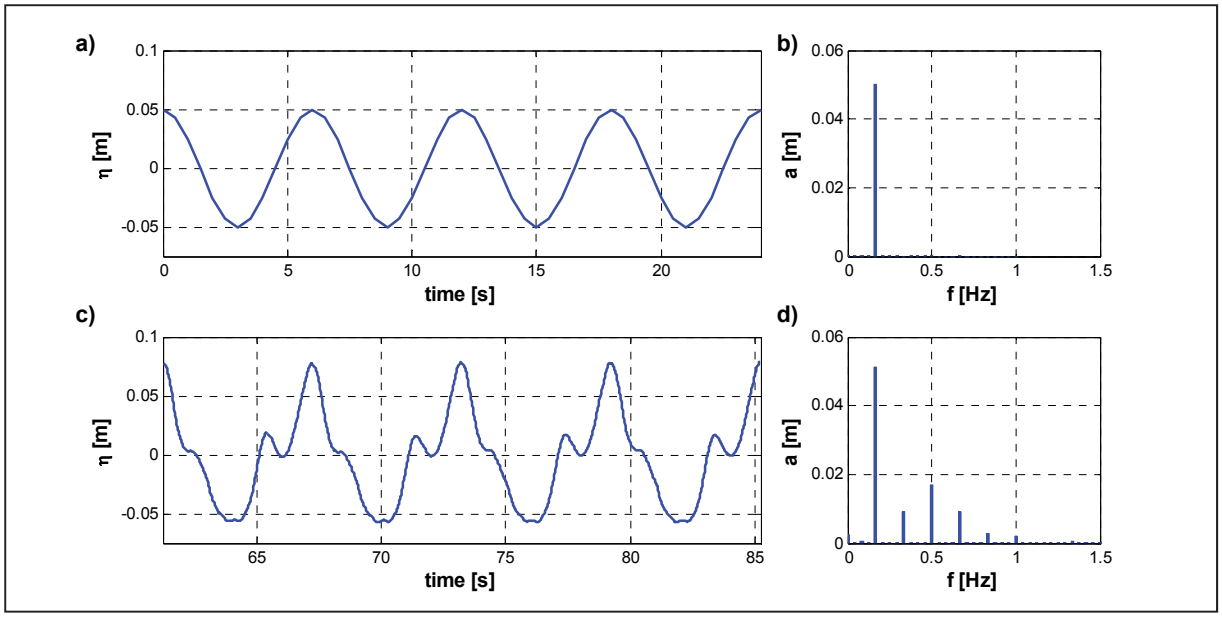

Fig. 5.2: Examples of harmonic generation in measured data in the wave flume at Aalborg University with a) the calculated target cosine signal for the wave generation (*H=0.1m*, *T=6.0s*, *h=0.56m*), b) the conventional Fourier spectrum of the target signal, c) the measured signal in the far-field and d) the conventional Fourier spectrum of the measured signal.

The signals from at least two different locations are required to detect harmonic generation. If the comparison of the two determined FFT amplitude-frequency or energy-frequency spectra show some spectral components only in the data of the rear gauge, then harmonic generation occurs for the given boundary conditions. The process of harmonic generation proceeds gradually while the waves are propagating and - as will be shown later - can be explained simply by the dispersion of underlying spectral cnoidal wave components. For the illustration of harmonic generation, a numerical simulation of an initial cosine wave with *H=0.1m* and *T=6.0s* in a water depth of *h=0.56m* (the same wave conditions and the same depth as in Fig. 5.2) is performed. The length of the simulation area was 50m and a total of 50 numerical wave gauges were arranged with distances of 1m. The recorded time series of these gauges are plotted in Fig. 5.3a starting with the gauge at *x=1.0m* in the lowermost row. The figure clearly shows how the initial cosine wave slowly changes its shape into a more complex shape with one or two observable additional secondary wave crests. For better illustration, the evolution of one selected oscillation in each signal is plotted in red. First, the wave profile becomes asymmetric with a steeper front and then dispersion effects (or harmonic generation) lead to the generation of secondary wave crests. Note that the number and the heights of these observable secondary crests can change as function of propagation length. In Fig. 5.3b, the conventional Fourier amplitude-frequency spectra of each of the red-plotted oscillation are presented as colour contour plot in order to determine the effect of harmonic generation in the data. Starting at gauge position *x=1m* only one spectral component at *f=0.167Hz* with amplitude *a=0.05m* is determined. This is the spectral representation of the initial cosine wave with *H=0.1m* and *T=6s*. With increasing propagation distance additional higher-harmonic wave

components appear in the Fourier spectra. The figure shows maximum of five components - the basic frequency *f=0.167Hz* and four higher harmonics at *2f*, *3f*, *4f* *5f*. Note that the amplitudes of these higher-harmonic components are neither constant nor monotonically increasing but a function of the propagation length while the amplitude of the basic frequency component is monotonically decreasing. The spectrum contours shows that the amplitude of the third harmonic wave with *f=0.501Hz* has its maximum around *x=33m* while the amplitude of the second-order component at *f=0.334Hz* is still increasing at *x=50m*.

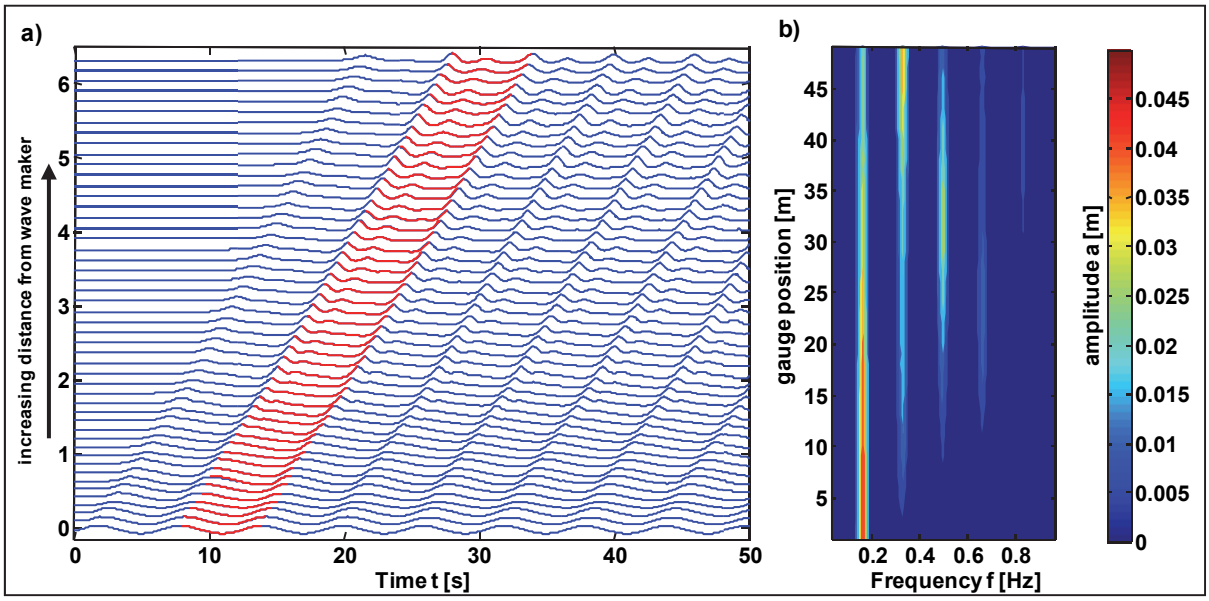

Fig. 5.3: Numerical simulation of an initial cosine wave (lowermost curve) with *H=0.1m* and *T=6.0s* in a water depth of *h=0.56m*. a) Time series measured at numerical wave gauges from *x=1m* (lowermost curve) to *x=50m* (uppermost curve). b) Colour contour plot of the conventional FFT amplitude-frequency spectra of the data in a). The colour bar legend shows the FFT amplitudes.

Hence, the implication of this figure is that the initial cosine wave turns into a more complex wave shape with additional secondary wave crests while propagating in the flume. This additional wave crests lead to additional higher-harmonic wave components in the conventional Fourier spectrum. Therefore the effect is called *harmonic generation*. Furthermore, the spectrum plot shows that the number of harmonic components as well as the amplitude distribution among these waves is not constant but is a function of gauge position *x*.

Osborne (2010) gives another example for the harmonic generation by means of the numerical simulation of the KdV equation (see Fig. 5.4) that provides similar results as the example in Fig. 5.3 for both modification of the wave shape and the changes in the conventional Fourier spectra. Note that the numerical simulation of the KdV equation as performed by Osborne (2010) in order to generate the free surface in Fig. 5.4 is *not* the same as the application of the inverse KdV-NLFT for the reconstruction of the surface data.

The initial wave profile A in Fig. 5.4a is a cosine wave with amplitude *a=0.01m* and wave length *L=2.56m* in a water depth of *h=0.15m*. With increasing propagation time the free surface changes as shown in profiles B to E. In Fig. 5.4b-f, the conventional Fourier spectra of the wave profiles A to E are shown. The spectrum for the initial in A shows only the expected cosine spectrum without any higher-order harmonics. With increasing time, additional harmonic frequencies are found with relatively high amplitudes (up to 58% in Fig. 5.4c) com-

pared with the initial cosine wave amplitude. In this example, the phenomenon of harmonic generation in the conventional Fourier spectra can be observed, exactly as is in the flume test data in Fig. 5.2 and the RANS/VOF simulations in Fig. 5.3.

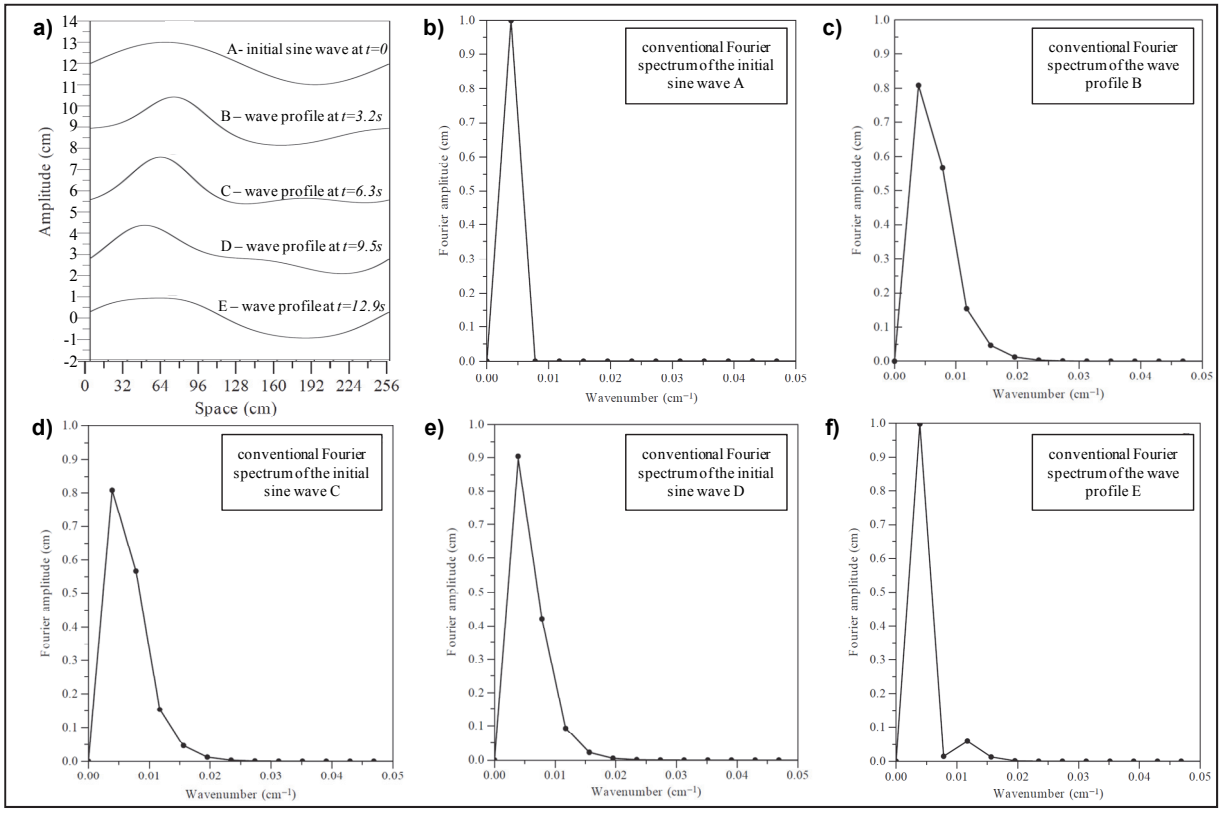

Fig. 5.4: Example for the harmonic generation by means of the numeric solution of the KdV equation for an initial sine wave with $a=0.01m$, $L=2.56m$ in $h=0.15$m. a) The initial sine wave A at $t=0$ and further wave profiles for $t=3.2s$ (B), $t=6.3s$ (C), $t=9.5s$ (D) and $t=12.9s$ (E). (b) to (f) the conventional Fourier spectra of the five space series in (a) (after Osborne, 2010).

In a next step, Osborne (2010) applied the KdV-NLFT to each of the signals A to E in Fig. 5.4a to determine their nonlinear spectra. Then he plotted the obtained spectral cnoidal basic components, calculated their interactions and superposed them linearly. The details are shown in Fig. 5.5a-e. The result of this procedure is very impressive and clear: For all five different wave profiles A to E the nonlinear spectral basic components of the signals A to E from Fig. 5.4a are identical and differ only in their phases. Therefore, the same cnoidal spectral basic components are determined for each of the different signals A to E.

The conclusions are clear as Osborne (2010 stated: 'Analytical, numerical, and experimental results demonstrate that the nonlinear dynamics of the KdV equation have no resonances in the Θ-function formulation.' The term *resonance* refers to the shift of energy from lower to higher harmonic components. The effect of harmonic generation (or resonance) cannot be observed in the nonlinear KdV-NLFT spectra. All spectral basic components that cause the generation of the secondary crests in the wave profiles are already contained in the initial regular cosine wave, because no additional wave components appear in the nonlinear spectra obtained a different locations. Hence, in the KdV-NLFT representation the initial cosine wave profile A is not a single mono-component wave, but a transient wave composed by five cnoidal waves and their nonlinear interactions. The first three wave components are (i) one highly

nonlinear Stokes-like wave with modulus *m=0.932*, (ii) two Airy-like waves with *m=0.219* and *m=0.011* and (iii) the next two waves have even smaller moduli and very small amplitudes and also are Airy-like waves. The linear superposition of these five cnoidal waves for each original signal A to E is given in Fig. 5.5 in row six ('sum of cnoidal waves'). The comparison with the original data in row shows that these curves are not identical yet and differ from the free surface in Fig. 5.4a.

When nonlinear cnoidal waves are superposed, phase-depending nonlinear wave-wave interactions occur that can significantly influence the shape of the free surface. The sum of the nonlinear interactions among the five cnoidal waves is plotted, too (see row seven, 'nonlinear interactions'). In each case the linear superposition of the five identical cnoidal waves (but with different phases) and the phase-dependent interactions returns back the original data (as plotted in row eight, 'reconstructed numerical wave train').

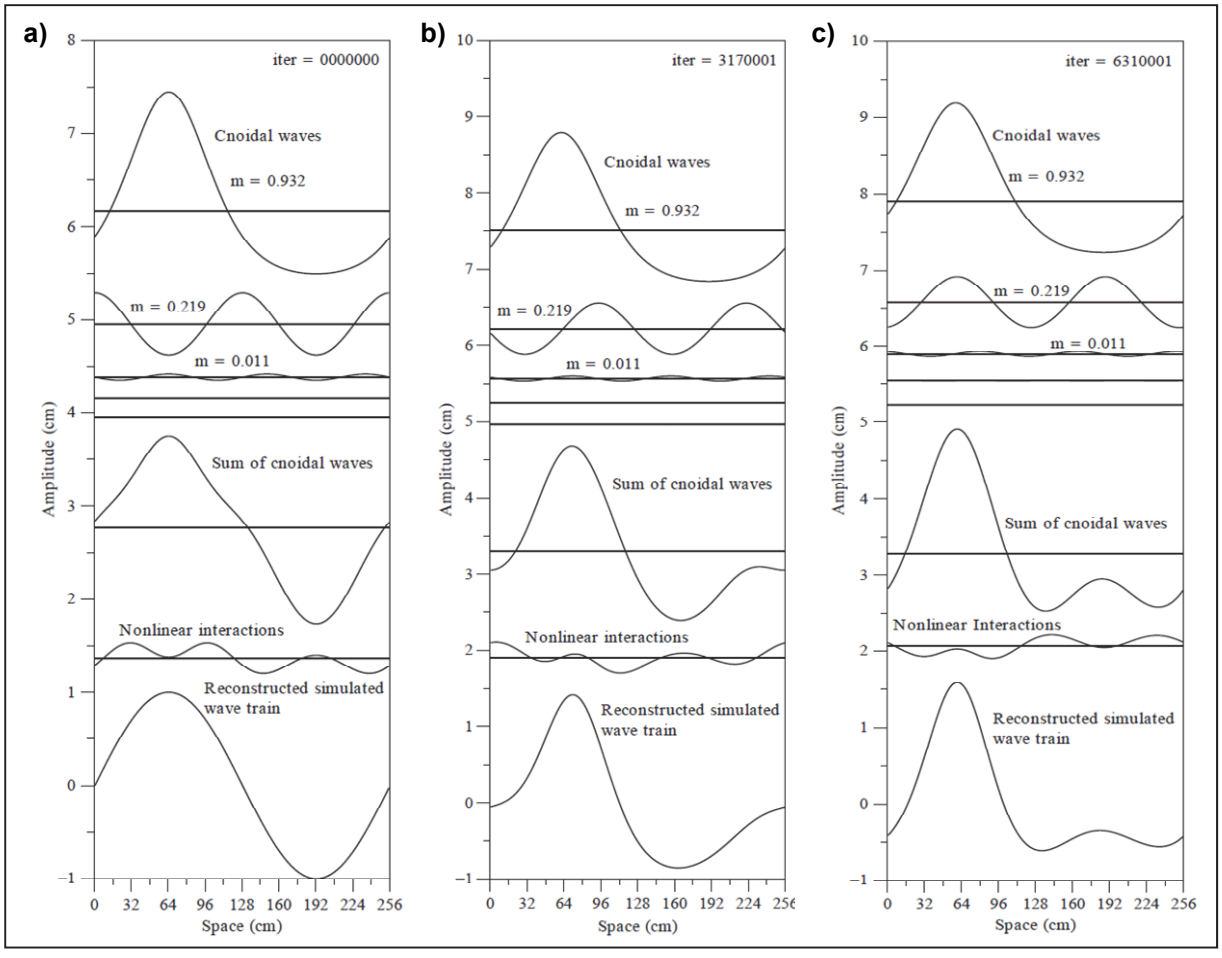

Fig. 5.5: Decomposition of the free surfaces A to C from Fig. 5.4a into the underlying cnoidal basic components and their nonlinear interactions. The basic components and the nonlinear interactions are summed up separately, and finally the superposition provides the free surfaces as shown in Fig. 5.4a (after Osborne, 2010).

The implication of this results leads to a 'new insight and perspective about the nonlinear dynamics of shallow-water wave trains' (Osborne, 2010). The conclusion of the results of the KdV-NLFT analysis in Fig. 5.5 is that in the KdV-NLFT each of the five analysed free surfaces (including the initial cosine wave) are regarded to be superpositions of *the same identi-*

cal(but phase-shifted) nonlinear cnoidal basic components *and* their phase-depended nonlinear wave-wave interactions. This implies

(i) that harmonic generation does not occur in the KdV-NLFT analysis of wave propagation in constant water depth,

(ii) that the different free surfaces A to E are transient waves that are generated by exactly the same cnoidal basic waves that differ only in their phases and their phase-dependent nonlinear interaction terms and

(iii) that harmonic generation is not a physical effect but rather a consequence of the inability of the conventional Fourier transform to identify the nonlinear character of the shallow-water basic components and to determine the nonlinear wave-wave interactions.

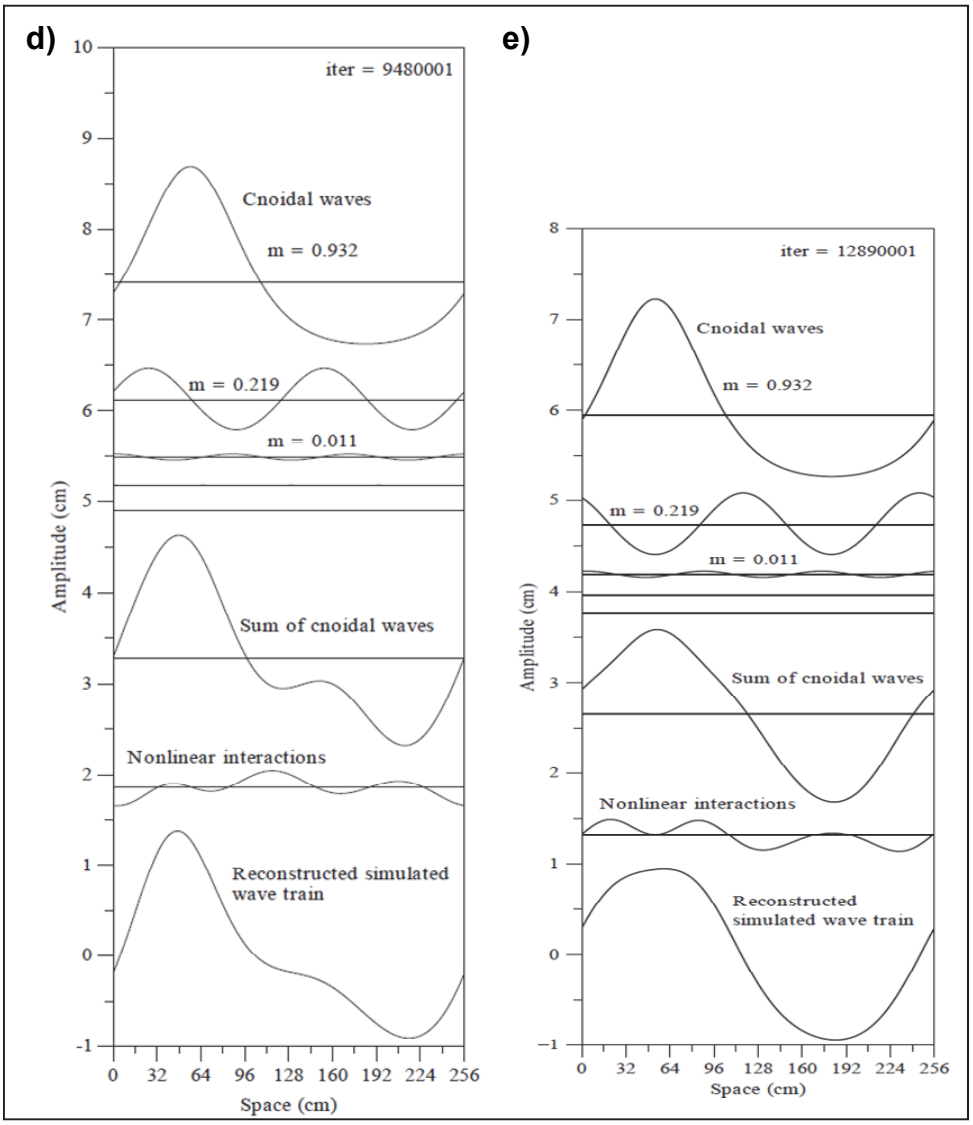

Fig. 5.6: Decomposition of the free surfaces D and E from Fig. 5.4a into the underlying cnoidal basic components and their nonlinear interactions. The basic components and the nonlinear interactions are summed up separately, and finally the superposition provides the free surfaces as shown in Fig. 5.4a (after Osborne, 2010).

To better understand why harmonic generation does only occur in the conventional FFT analysis (and not in the KdV-NLFT), we have to recall that in section 3.1.3 was shown that in the KdV-NLFT representation each of the nonlinear cnoidal spectral basic components is considered to be *one* wave, even if each of these cnoidal waves are decomposed into *several* linear harmonic components in the FFT (see section 3.1.3). Therefore, the definition of *phase-locked* or *bound harmonics* is not necessary in the nonlinear KdV-NLFT approach to describe the spectral properties of nonlinear waves. Based on the principles of the KdV-NLFT, already the initial cosine wave A in Fig. 5.4a can be decomposed into cnoidal waves and their nonlinear interactions. When this initial cosine wave would be assumed to be a solution to the KdV equation in the given water depth, then this cosine wave would propagate as a stable wave without harmonic generation and the KdV-NLFT would determine only one cnoidal basic component; and this would be the initial cosine wave. But the wave does not propagate as a stable cosine wave, and therefore this wave is too long for the given water depth and it cannot be a solution to the KdV equation.

If the initial wave is not a solution to the KdV equation, as in this example, then it is regarded to be a dispersive transient shallow-water wave that is composed by different (at least two) cnoidal waves that *are* solutions to the KdV equation for the given water depth. These cnoidal basic components that are determined in the data which are measured at the first gauge evolve in constant water depth in space and time without transformation. Therefore, these cnoidal waves are determined at the following gauges, too, without having changed their shapes. Note that the nonlinear character of a wave oscillation might not be easily observed by visual observation if the higher-harmonic wave amplitudes still are too small. The linear superposition of these cnoidal waves and their nonlinear wave-wave interactions returns the original free surface. The different surface profiles are caused (i) by different phases of the cnoidal waves at each gauge and, in addition, (ii) therefore by nonlinear interaction terms. As a special case, the nonlinear interactions completely cover the contained short-period cnoidal waves and the surface profile looks like a linear cosine waves. With increasing phase shifts this ‘cosine wave’ disperses and the underlying cnoidal waves with higher frequencies become visible (see signals B to E in Fig. 5.4). For a more detailed explanation on the transient nature of long-period waves in very shallow water see section 6.1.

Now the simulation data from Fig. 5.3 are analysed using the nonlinear KdV-NLFT. In Fig. 5.7a these data are given, again one period is plotted in red for better visualization. The determined KdV-NLFT amplitude-frequency spectrum of the red-plotted data is shown in Fig. 5.7b. The constant peak plotted at the negative frequency $f=-0.18Hz$ represents a soliton. Originally, the solitons frequencies are determined in the analysis algorithm as complex numbers, which do not have any physical relevance. The real part of these complex numbers is used to plot the soliton amplitudes in the spectrum to separate the soliton spectrum on the left part of the plot from the radiation spectrum with the oscillatory waves on the right side. Note that the KdV-NLFT is performed for periodic boundary conditions and therefore solitons are periodic, too. This means that a soliton is solitary only within the analysis time frame, but is repeated to the right and left of this time frame as the latter is assumed to be periodic. In this example three oscillatory waves with significant amplitudes $a=0.026m$, $0.01m$ and $0.001m$ are determined with $f=0.053Hz$, $0.068Hz$ and $0.083Hz$. The last component cannot be observed in the contour plot due its small amplitude.

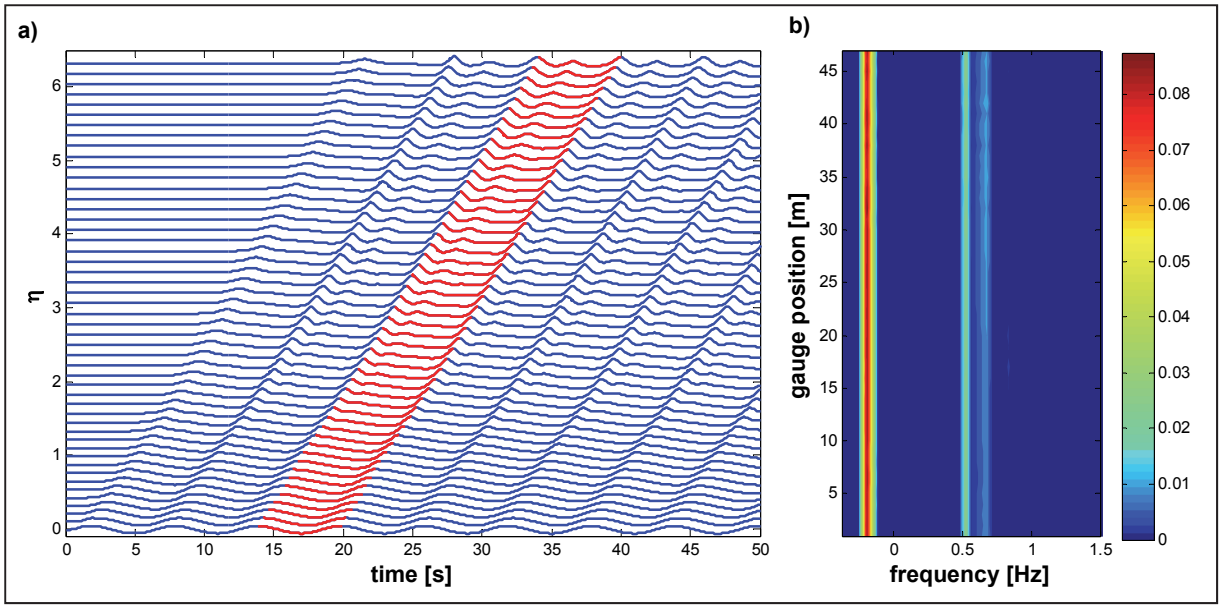

Fig. 5.7: Numerical simulation of an initial cosine wave (lowermost curve) with *H=0.1m* and *T=6.0s* in a water depth of *h=0.56m*. a) Time series measured numerical wave gauges from *x=1m* (lowermost curve) to *x=50m* (uppermost curve). b) Colour contour plot of the nonlinear KdV-NLFT amplitude-frequency spectra of the data in a). The colour bar legend shows the KdV-NLFT amplitudes.

The results of the KdV-NLFT in Fig. 5.7 show, as expected, that the number of spectral components as well as their amplitudes and frequencies do not change with space. Thus, no harmonic generation can be observed in the KdV-NLFT representation. The approach of harmonic generation only occurs if the nonlinear propagation of shallow-water waves is analysed using the conventional linear Fourier transform. Thus, harmonic generation cannot be regarded as a physical phenomenon, but can easily be explained as an effect that occurs if the linear conventional Fourier transform is applied for the analysis of nonlinear effects in shallow water. The FFT is not able to determine the true nonlinear cnoidal shallow-water wave components that generate the observed transient surface shape. As soon as these waves disperse due to their different frequencies and celerities, three effects occur:

(i) the formerly hidden nonlinear cnoidal wave at the basic frequency disperses and its original asymmetric wave shape becomes visible,
(ii) additional secondary wave crests appear when the formerly hidden higher-harmonic wave components disperse from the initial cosine wave and
(iii) the short-period crests and troughs of the nonlinear interactions are not longer balanced by the nonlinear superposition of the cnoidal waves.

In the FFT, the asymmetric and additional crests can only be reproduced by introducing additional higher-order harmonic wave components. Furthermore, the results of the FFT in Fig. 5.4 show that the harmonic generation in the FFT is not necessarily straightforward, but the higher-order amplitudes can increase and decrease as a function of the gauge position. In the KdV-NLFT, these harmonic components are not required, because already in the first signal the underlying cnoidal waves are determined correctly. No additional wave components are required to explain the observed shapes of the free surface at the other wave gauges.

Finally, the application of the KdV-NLFT for the analysis of harmonic generation clearly shows that the generation and modification of higher-order wave amplitudes in the FFT is not

a real physical phenomenon but rather an effect of the insufficiency of the conventional Fourier transform to identify the transient character of shallow-water waves and to determine the real underlying nonlinear cnoidal wave components. By application of the KdV-NLFT to the same data in constant water depth no harmonic generation occurs. For further details on the transient character of long-period waves in shallow-water see section 6.1.

5.2.2 Analysis of harmonic generation based on measured wave flume data

After the position of the problem of harmonic generation in wave flumes and the presentation of the theoretical background in section 5.2, now the KdV-NLFT analysis of the experimental wave flume data from Fig. 5.2 is performed. In this example a cosine wave with $H=0.1m$ and $T=6s$ was generated in a constant water depth of $h=0.56m$. The calculated initial cosine wave is shown in Fig. 5.8a. Due to the small relative water depth, this wave is not stable but a dispersive transient shallow-water wave. The result of the KdV-NFLT analysis of the initial wave is given in Fig. 5.8b. The amplitude spectrum shows four significant peaks at harmonic frequencies $f=0.16Hz$, $0.33Hz$, $0.5Hz$ and $0.67Hz$. Due to the values of the moduli in the modulus-frequency spectrum these components can be categorised as cnoidal-like ($f=0.16Hz$), Stokes-like ($f=0.33Hz$) and two Airy-like cnoidal waves ($f=0.5Hz$ and $0.67Hz$). The time series of the spectral components waves are plotted in Fig. 5.8c. According to the results of the nonlinear spectrum in Fig. 5.8b, these four cnoidal waves are already physically contained in the initial cosine wave in Fig. 5.8a and the linear superposition of these waves *and* the nonlinear interactions return the original cosine wave. Since the spectral cnoidal waves are *not* bound or phase-locked they propagate as free waves with their individual wave celerities. Therefore, dispersion occurs, the phases between the basic components change, and additional secondary wave crest can be observed at the free surface. Furthermore, the nonlinear interactions between the four waves are functions of the phase differences of the cnoidal waves. Therefore, with advancing wave dispersion the nonlinear interaction modes also change. Finally, in the far-field at a specific gauge position the time series in Fig. 5.8d can be determined. This signal is composed by the four cnoidal waves in Fig. 5.8c that already provided the initial cosine wave in Fig. 5.8a, but with different phases and therefore different local nonlinear interactions.

After the spectral decomposition of the initial cosine wave in Fig. 5.8, some details on the reconstruction of the original data and the spectral properties of the far-field data are presented in Fig. 5.9. The measured far-field data is plotted in Fig. 5.9a. For illustration, the four cnoidal waves are given directly under the signal in Fig. 5.9c. For better clarity, they are potted phase-shifted. The first cnoidal wave represent the basic oscillation with a period of $T=6.0s$ in the upper plot. Two successive wave crests are marked with two red arrows in both, the measured data in Fig. 5.9a and the plotted cnoidal waves in Fig. 5.9c. The second plot in Fig. 5.9c shows the first higher-harmonic component with $T=3.0s$. Instead of only one oscillation the data shows two oscillations and three crests (marked with three green arrows) within the basic period of $T=6.0s$. In the third component with $T=2.0s$ three oscillations and four crests are marked with blue arrows. Due to the phase shift in Fig. 5.9c most of the wave crests can easily be identified in both the original data and the cnoidal waves. The coloured arrows help to find the peaks. Due to the small amplitude ($a<10^{-3}\ m$) the crests of the fourth wave component cannot be observed in the original data. Note that the nonlinear interactions have

to be added to the cnoidal waves Fig. 5.9c to obtain the original data Fig. 5.9a, and that therefore the assignment of the crests in the original data is not completely perfect.

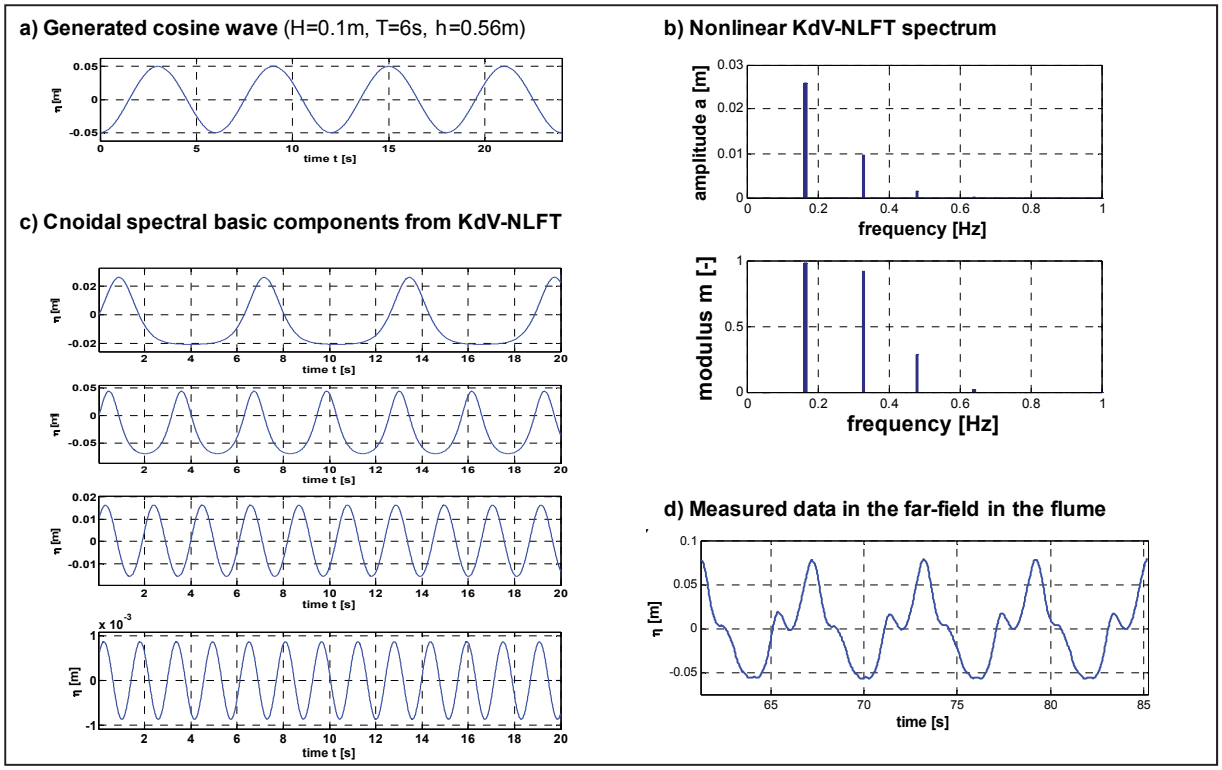

Fig. 5.8: KdV-NLFT analysis of a laboratory test signal: a) the calculated initial cosine wave, b) the nonlinear KdV-NLFT spectrum of the original data in a), c) the determined cnoidal basic components and d) the measured free surface in the far-field.

The comparison between the nonlinear KdV-NLFT amplitude-frequency spectrum of the initial cosine wave in Fig. 5.8b and the linear FFT spectrum of the same data in Fig. 5.2b clearly shows the advantages of the KdV-NLFT. As already stated, the approach of phase-locked or bound harmonics is not necessary in the nonlinear analysis. The first plot of the FFT spectra of the four cnoidal basic components in Fig. 5.9d shows the FFT amplitude-frequency spectrum of the basic cnoidal wave with $T=6.0s$. The cnoidal wave has nonlinear asymmetries such as the higher, narrow crest and the shallower, wider trough. This first nonlinear wave component is decomposed in the FFT in Fig. 5.9d into a basic cosine wave (with $f=0.17Hz$) and at least three higher-harmonic wave components (with $f=0.33Hz$, $0.5Hz$ and $0.67Hz$). For the temporal and spatial evolution of this cnoidal wave, the higher-harmonics have to be bound to the basic frequency. In this spectrum only the harmonic components of one cnoidal wave are contained, so that this phase-locking can easily be done.

The FFT spectra of the next cnoidal waves also are plotted in Fig. 5.9d (rows two to four). Since the nonlinearity of the cnoidal waves is decreasing from cnoidal-theory over Stokes-like to Airy-like waves, the number of higher-harmonic waves in the FFT spectra is also decreasing. Note that the representation in Fig. 5.9d is limited to a frequency range of $0 \le f \le 1.0Hz$, so that harmonics with $f > 1.0Hz$ are not shown. But due to the small amplitudes, no significant components are found four higher frequencies. A comparison of the spectrum in Fig. 5.9b and the spectra in Fig. 5.9d shows that the spectrum of the original data can be obtained with good agreement by linear superposition of the four cnoidal-wave spectra. Unfortunately,

from Fig. 5.9b cannot be determined which portions of the higher-order amplitudes have to be treated as phase-locked and which free components are. For this distinction, further extensive analyses are required, whereas the KdV-NLFT decomposition easily provides this information. Furthermore, the linear analysis does not allow the calculation of the nonlinear interactions between the spectral basic components.

Since the water depth is a governing parameter in the KdV-NLFT analysis, the initial cosine-shaped wave is identified to be a transient wave that is composed by four cnoidal waves. Therefore, the KdV-NLFT spectrum of the initial transient cosine-shaped wave and that of the far-field measurement are identical. Furthermore, the comparison of the nonlinear spectrum in Fig. 5.8b and the linear FFT spectrum of the far-field data in Fig. 5.9b shows the implication of KdV-NLFT application for the identification of bound and free harmonics in the FFT spectra.

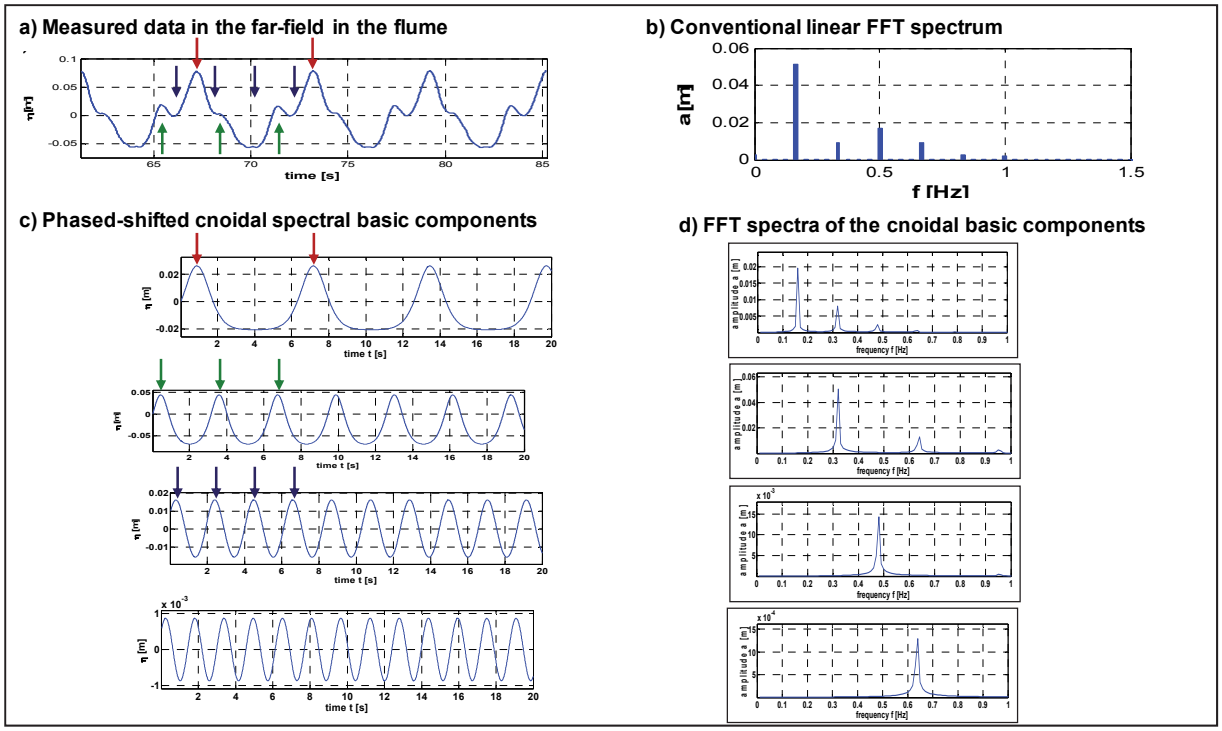

Fig. 5.9: Reconstruction and spectral FFT properties of the measured far-field data: a) the measured data in the far-field of the wave flume, b) the conventional linear FFT spectrum of the far-field data in a), c) the phase-shifted cnoidal basic components and d) the conventional linear FFT spectra of the four cnoidal basic components in c).

5.2.3 Harmonic generation over sloping bottoms

The analyses in sections 5.2.1 and 5.2.2 have shown that harmonic generation in constant water depth can only be observed in conventional the FFT spectra. The nonlinear KdV-NLFT spectra do not show any harmonic generation. In case of harmonic generation over and behind submerged reefs the water depths are not constant but change, usually to smaller water depth when the wave propagates onto the reef, and to higher water depths again when the waves enter the deeper water behind reef with finite width. The wave propagation of solitary waves over reefs with infinite and finite width and constant water depth above the reef is analysed in

more detail in chapter 4. In this section, the focus in on the development of the waves over a sloping bottom.

To obtain wave data over a sloping bottom the simulation from Fig. 5.3 was repeated with sloping bottom with constantly decreasing water depths from *h=0.56m* at *x=0* to *h/2=0.28m* at *x=50m*. The determined surface waves are plotted in Fig. 5.10a. Again, one oscillation is plotted in red in all the curves. The conventional FFT spectra of these waves are given in Fig. 5.10b as colour contour plot. Compared to the FFT plot in Fig. 5.3b for constant depth the waves over this sloping bottom show a significantly increased number of higher-order components. And again, the amplitudes of the different harmonic components are neither constant nor constantly increasing, but they vary with gauge position *x*.

For the nonlinear spectra in Fig. 5.11b that are obtained from the KdV-NLFT analysis of the data in Fig. 5.11a (which are identical to the curves in Fig. 5.10) again different results are determined. *First*, the frequency of the soliton changes towards smaller values. The frequency of the first oscillatory wave is decreasing from *f=0.37Hz* at *x=1m* to *f=0.31Hz* at *x=50m* while the frequency of the second oscillatory wave is increasing from *f=0.53Hz* to *f=0.69Hz*. The analysis show eight further components with very small amplitudes that cannot be observed in the colour plot in Fig. 5.11b. For each of these waves the frequencies are increasing with increasing propagation length on the slope.

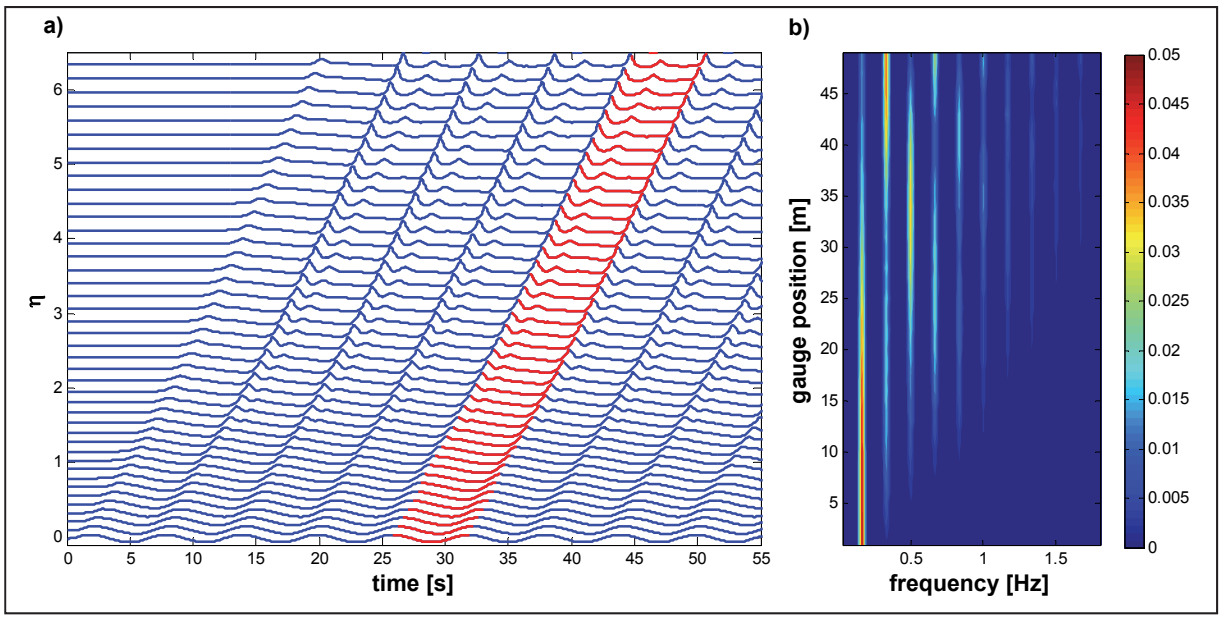

Fig. 5.10: Numerical simulation of an initial cosine wave (lowermost curve) with *H=0.1m* and *T=6.0s* in a constantly changing water depth of *h=0.56m* at *x=0* to *h/2=0.28m* at *x=50m*. a) Time series measured at numerical wave gauges from *x=1m* (lowermost curve) to *x=50m* (uppermost curve). b) Colour contour plot of the conventional FFT amplitude-frequency spectra of the data in a). The colour bar legend shows the FFT amplitudes.

Second, the amplitudes of the solitary wave and the first oscillatory are increasing with gauge position *x*. The amplitude of the second oscillatory component is increasing until *x=22m* and then decreasing again. Some of the amplitudes of the other eight components are constantly increasing; some are first increasing and then decreasing, similarly to the higher-order components in the FFT plot in Fig. 5.3.

Third, the moduli of the KdV-NLFT components are showing different behaviour. The nonlinearity of the first two components is constantly increasing with *x*. Some of the other higher-order components show constantly increasing moduli, too, and some have maximum values and then the moduli are decreasing again, just as observed for the amplitudes.

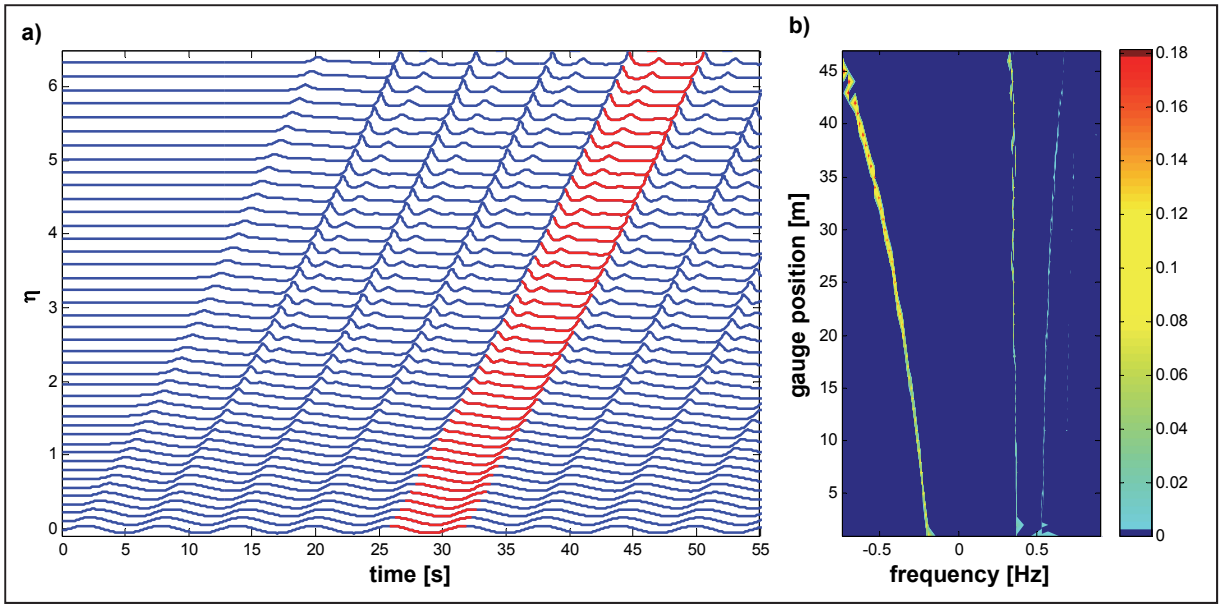

Fig. 5.11: Numerical simulation of an initial cosine wave (lowermost curve) with *H=0.1m* and *T=6.0s* in a constantly changing water depth of *h=0.56m* at *x=0* to *h/2=0.28m* at *x=50m*.a) Time series measured t numerical wave gauges from *x=1m* (lowermost curve) to *x=50m* (uppermost curve). b) Colour contour plot of the nonlinear KdV-NLFT amplitude-frequency spectra of the data in a). The colour bar legend shows the KdV-NLFT amplitudes.

5.2.4 Summary and conclusion

In the previous section, wave signals over horizontal and sloping bottoms have been analyzed comparatively using the conventional linear FFT and the nonlinear KdV-NLFT. The results have shown that the phenomena of harmonic generation over flat bottoms only can be determined in the FFT spectra. The KdV-NLFT spectra of waves at different gauge position do *not* show harmonic generation.

Harmonic generation occurs (i) if waves are generated in flumes and basins in a water depth in which they are not solutions to the KdV equation, and in which they, therefore, cannot propagate as stable waves, or (ii) if stable long waves enter shallower water depths where they now are no longer stable waves. In both cases the initial relatively long wave is now, suddenly, a transient wave that is composed from shorter waves that are stable KdV solutions for the given water depth. These underlying waves propagate as free and independent waves with different celerities. Due to simple dispersion effects the initial cosine-shaped transient wave changes its shape and the peaks of the different waves appear. At the same time, the nonlinear interactions change with the wave's phases. Instead of a generation of harmonic components as indicated by the FFT results, the generation of the secondary peaks can easily be explained by simple wave dispersion effects since the KdV-NLFT is able to identify the underlying cnoidal wave components. Therefore, harmonic generation over flat bottoms is not a physical effect, but an artefact from the linear FFT that is insufficient to correctly analyse nonlinear wave propagation processes.

For sloping bottoms, harmonic generation is also observed in the KdV-NLFT spectra. The analysis of wave data over sloping bottoms have shown that the harmonic generation in the FFT spectra is significantly increased. In the KdV-NLFT, the varying water depth causes changes in the cnoidal wave frequencies of the wave components and the frequencies or wave numbers are not constant any longer. This effect cannot be observed in the FFT spectra. Furthermore, in the KdV-NLFT spectra the amplitudes are now functions of the gauge position on the sloping bottom, too. For constant water depth, this could be observed only in the FFT spectra, *but over sloping bottoms harmonic generation can be observed in the KdV-NLFT representation*, too. The explanation can be given by the concept of transient waves, too. A stable long wave that enters the sloping bottom area has to transform to components that fit the new water depth. With decreasing water depth the wave will first slightly change its shape, but at one point over the slope, a wave is dispersed into two waves in order to fit the new boundary conditions. First, the former stable wave becomes a transient wave of $N \geq 2$ new dispersive components. Therefore, as a result of the new water depth, this wave now is represented in the KdV-NLFT spectrum as at least two cnoidal waves instead of one as in front of the slope. For each of these two or more waves the process starts from the beginning again when they enter shallower depths, and they will disperse into even shorter waves. Finally, the number of cnoidal wave components in the nonlinear spectrum will be increasing with decreasing water depth.

5.3 Total wave energy obtained from conventional FFT and nonlinear KdV-NLFT spectra

The analyses in section 5.2.2 have shown that in the FFT spectra, as a consequence of harmonic generation, the amplitude values of the different frequency components are changing. Therefore, in Fig. 5.12 the FFT energy density $S(f)$ from Eq. (2.73) of the data in Fig. 5.3 is discussed in more detail. In Fig. 5.3a, the spatial variation of the energy densities of the first six spectral components is plotted. The curves in Fig. 5.3a clearly show that the energy of the first-order component with $f=0.17Hz$ is decreasing while the energies of the higher-order components with $f > 0.17Hz$ are increasing first. Later some of the higher-order amplitudes are decreasing again. The same can be observed in the plot in Fig. 5.12a. At the end of the simulations area the third-order component with $f=0.500Hz$ shows the highest energy density. The plots in Fig. 5.12b-d show the spectral densities at the position $x=1m$ 25m and $49m$. Note that the total energy density of all components with $f \leq 1.000Hz$ (red curve) is nearly constant and is not a function of the gauge position x. Therefore, the observed harmonic generation seems not to be relevant for discussions of the total wave energy for horizontal bottoms.

But for qualitative and quantitative analyses of energy distribution and energy transfer in incident, reflected and transmitted wave spectra as shown in Fig. 5.1 the initial distribution of the energy to the spectral components is relevant. Let us assume the initial cosine wave in Fig. 5.3 to be the incident wave that will later propagate over or onto a submerged reef. In this case the FFT spectrum of this incident wave as given in Fig. 5.12b will be reference spectrum for the analysis of energy transfer effects over or behind the reef. If the incident wave is not measured at $x=1m$, but at $x=25m$ or $49m$, then the spectra in Fig. 5.12b or c would be the reference spectra for the wave transformation analysis. But comparison of the FFT energy density plots in Fig. 5.12b-d clearly shows that due to harmonic generation already the comparison of these three incident spectra provides strong energy transfer effects. If we select the

spectrum in Fig. 5.12b as the incident spectrum, then *all* energy transfer to higher-harmonic components would be identified as caused by the wave transformation at the reef. But if the spectrum in Fig. 5.12d would be treated as the initial spectrum, then only a reduced energy transfer rate would be caused by wave transmission effects because in this example the incident spectrum already contains wave energy at higher-harmonic frequencies.

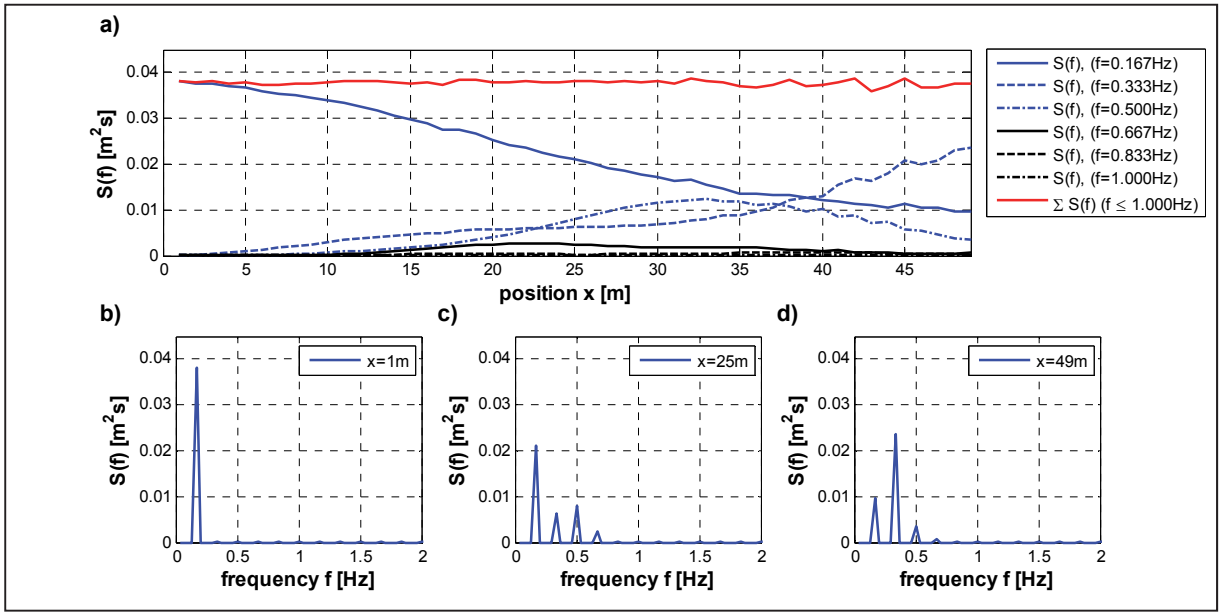

Fig. 5.12: Energy density *S(f)* determined for the data from Fig. 5.3 by applying Fourier transform. a) *S(f)* of the first six spectral components and the total sum of *S(f)* as function of gauge positions *x*. b) *S(f)* at *x=1m*. c) *S(f)* at *x=25m*. d) *S(f)* at *x=49m*.

For a closer look on the energy distribution in the determined FFT and KdV-NLFT spectra, the total wave energies of the linear and nonlinear spectral basic components are calculated by application of Eqs. (2.21) to (2.23) for linear cosine waves from the FFT spectra and by Eqs. (2.29) to (2.31) for the cnoidal waves from the nonlinear spectra. As stated by Dean & Dalrymple (1991) for linear waves the energy $E/H^2=1/8[J/m^2]$ is constant and not a function of water depth. For cnoidal waves, the water depth is a governing factor for (i) the nonlinear wave shape (and therefore potential energy E_{pot}) and (ii) nonlinear wave celerity (and therefore the kinematic energy E_{kin}). The conclusion that has to be drawn is that the spectral energy density *S(f)*, which is only a function of the wave amplitude *a*, is only appropriate to represent the energy of linear waves. Therefore, in the following sections the calculated total wave energies E_{tot} are calculated and compared instead of the spectral density *S(f)*.

In Fig. 5.13, the calculated total wave energies of the waves measured at three different positions at the beginning (*x=1m*), the middle (*x=25m*) and the end (*x=49m*) of the simulation area (see Fig. 5.3). First, in Fig. 5.13a-c the total wave energies E_{tot} of the first five spectral components of the FFT spectra in Fig. 5.12b to d are calculated. The energies of the remaining higher-order wave components are negligible.

The energy density *S(f)* and the total energy E_{tot} are just different representations of the wave energies and therefore the spectra in Fig. 5.12b-d and Fig. 5.13a-c only differ in the scale on the left axis. Since the sum of the energy density is nearly constant for all FFT spectra (see Fig. 5.12a), the sum of the calculated total wave energies also has to be constant over the

gauge position x (see the values given in Fig. 5.13a-c). But exactly as in Fig. 5.12 the total energy fractions of the different spectral components changes due to harmonic generation.

The total energies $E_{tot,cn}$ of the cnoidal waves from the KdV-NLFT spectra at different gauge positions are given in Fig. 5.13d to f. These spectra show the same results that were already obtained from Fig. 5.7b: The amplitudes and therefore the energies of the cnoidal waves are constant over x and no harmonic generation is observed. Furthermore, the sum of the total energies (see the values given in Fig. 5.13d-f) is nearly constant, too. Direct comparison between the spectra in Fig. 5.13 shows that the sum of total energies derived from FFT is $E_{tot}=12.4J/m^2$ (as the mean value of the three determined values) while the KdV-NLFT spectrum provides a total energy mean of the cnoidal waves of $E_{tot,cn}=8.5J/m^2$.

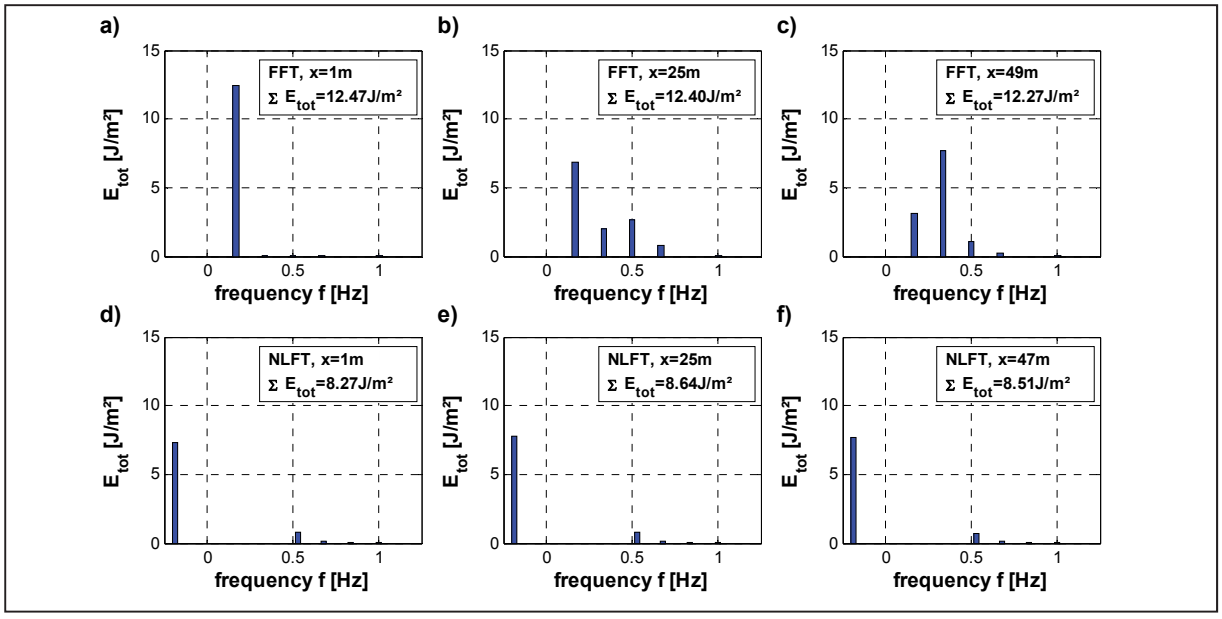

Fig. 5.13: Total wave energy E_{tot} $[J/m^2]$ of the spectral components from the numerical simulation in Fig. 5.3. In a) to c) the total energies of the FFT cosine waves at positions $x=1m$, $25m$ and $49m$ given, in d) to e) the total energies of the NLFT spectral cnoidal wave components at positions $x=1m$, $25m$ and $47m$ are plotted.

Possible explanations for the determined differences in E_{tot} and $E_{tot,cn}$ are:

(i) The different approaches and results in the FFT and KdV-NLFT just provide different spectral representation for the same original data with different energy scales. Dingemans (1997a) stated that nonlinear cnoidal waves always show lower energy values than linear Airy waves. But a closer view on Fig. 2.4 shows that these lower energies cannot explain the observed energy losses of 32% in the KdV-NLFT spectrum.

(ii) The conventional FFT spectrum represents the complete original data and therefore does not only contain the energies of the underlying cnoidal basic components but also implicitly contains the nonlinear wave-wave interactions. These interactions are not provided in the nonlinear KdV-NLFT spectrum, and therefore in Fig. 5.13d-f only the energies of the cnoidal waves are considered. The energy parts of the nonlinear interactions are missing in this KdV-NLFT representation.

In order to determine the reason for the energy differences between the FFT and KdV-NLFT representation, for the first four cnoidal wave components from Fig. 5.13d the following procedure is applied: *First*, the cnoidal waves are constructed by applying the amplitudes and moduli from the KdV-NLFT spectrum. *Second*, the conventional FFT is applied to each of the four cnoidal waves (denoted as cn_1 to cn_4). The results (frequencies and amplitudes) for each of the four cnoidal waves are given in Tab. 5.1. *Third*, for each of linear spectral FFT components the total wave energy E_{tot} is calculated. *Forth*, the wave portions are summed up to obtain the total wave energy for each of the four cnoidal waves. *Finally*, the wave energies obtained from FFT and those calculated from the KdV-NLFT results and the energy equations for cnoidal waves in Eqs. (2.29) to (2.31) are compared. The details of the energy calculation are given in Tab. 5.1.

The values in Tab. 5.1 are the energies of the first four cnoidal waves in the KdV-NLFT spectrum without the energies of the nonlinear interaction terms. The sum of the cnoidal wave energies provides a values of $E_{tot,cn}=8.267 J/m^2$. This is exactly the energy of the cnoidal waves as obtained in Fig. 5.13d.

Tab. 5.1: Results of the conventional FFT of each of the first four cnoidal waves (denoted as cn_1 to cn_4) from Fig. 5.12d. In the table the determined frequencies f, amplitudes a and calculated total energies E_{tot} of the first eight spectral cosine waves are given. For comparison the total wave energies of the cnoidal waves from Fig. 5.12d are also given.

$a(cn_1)$ [m]	$E_{tot}(cn_1)$ [J/m²]	$a(cn_2)$ [m]	$E_{tot}(cn_2)$ [J/m²]	$a(cn_3)$ [m]	$E_{tot}(cn_3)$ [J/m²]	$a(cn_4)$ [m]	$E_{tot}(cn_4)$ [J/m²]
0.03170	4.92899	0.01230	0.7420775	0.0048300	0.11442825	0.0007500	0.00275906
0.01880	1.73362	0.00381	0.0712015	0.0003410	0.00057036	0.0000038	0.00000007
0.00912	0.40797	0.00091	0.0040440	0.0000015	0.00000001	0.0000008	0.00000000
0.00398	0.07770	0.00019	0.0001771	0.0000020	0.00000002	0.0000006	0.00000000
0.00163	0.01303	0.00004	0.0000071	0.0000021	0.00000002	0.0000000	0.00000000
0.00064	0.00203	0.00001	0.0000004	0.0000000	0.00000000	0.0000000	0.00000000
0.00025	0.00029	0.00000	0.0000000	0.0000000	0.00000000	0.0000000	0.00000000
0.00009	0.00004	0.00000	0.0000000	0.0000000	0.00000000	0.0000000	0.00000000
Σ	**7.16367**	**Σ**	**0.81751**	**Σ**	**0.11500**	**Σ**	**0.00276**
$E_{tot,cn}$:	**7.34303**		**0.80835**		**0.11303**		**0.00266**

The comparison shows, that the calculated cnoidal wave energy of the four cnoidal waves is returned very well in the conventional FFT representation. Therefore, the observed energy differences between the FFT and the KdV-NLFT spectra cannot be caused by the different cosine and cnoidal wave representation. These representations of the cnoidal wave energy are equivalent and the following conclusions can be drawn:

(i) The results from Fig. 5.13 for the KdV-NLFT have shown that the total cnoidal wave energy $E_{tot,cn}$ is constant and that the energy $E_{tot,cn}$ is significantly smaller than E_{tot} that is obtained from FFT for the original data.

(ii) The original data is considered in the KdV-NLFT to be generated by the superposition of cnoidal waves *and* their nonlinear interactions. The cnoidal waves are provided in the nonlinear spectrum and their total wave energy $E_{tot,cn}$ can be calculated. The interactions are however *not included* in the spectrum and therefore *their energy is not considered*. Therefore, the energy $E_{tot,cn}$ does not represent the energy E_{tot} of the original signal ($E_{tot,cn} \neq E_{tot}$).

(iii) It has been shown in this section that the cnoidal wave energy $E_{tot,cn}$ can be obtained correctly from both FFT and KdV-NLFT energies. Therefore, the differences in the wave energies E_{tot} and $E_{tot,cn}$ in Fig. 5.13 cannot be explained by the different approaches and representations in FFT and KdV-NLFT.

(iv) Therefore, the missing energy must be contained in the nonlinear interactions. The total energy of both original wave ($E_{tot}=12.47J/m^2$) and cnoidal wave components ($E_{tot,cn}=8.27J/m^2$) is obtained by FFT. Therefore, the missing energy has to be caused by the nonlinear interactions. Furthermore, since both total and cnoidal wave energies are constant over x, the total energy of the interaction term also has to be constant, even if the shapes of the interactions change.

(v) Finally, the total wave energy $E_{tot,int}$ of the nonlinear interactions can be simply determined by the combination of FFT and KdV-NLFT: (i) The total wave energy E_{tot} of the original data can be obtained from FFT. (ii) The total wave energies $E_{tot,cn}$ of the cnoidal spectral basic components can be obtained from KdV-NLFT. (iii) The total wave energy $E_{tot,int}$ of the sum of the nonlinear interactions can be obtained by simple subtraction

$$E_{tot,\mathrm{int}} = E_{tot} - \sum E_{tot,cn} \,. \tag{5.7}$$

In this example applies $E_{tot,int}=E_{tot}-E_{tot,cn}=12.47-8.27=4.20J/m^2$ from Fig. 5.13a and for $x=1m$. For both positions $x=25$ and $x=47/49m$ a value of $E_{tot,int}=3.76J/m^2$ is determined.

5.4 Example for the comparative analysis of wave transmission over submerged reefs with finite width using FFT and KdV-NLFT

As shown in section 5.1 the analysis of the hydraulic efficiency of submerged reefs is based on the analysis of the energies of the incident, reflected, transmitted and dissipated energies. Usually the wave energies are obtained from conventional FFT spectra. Then, in section 5.2 the phenomenon of harmonic generation is discussed and it could be shown that already the position of the gauges for the measurement of the incident waves might influence the energy distribution and therefore the analysis results. Furthermore, in section 5.3 some examples are shown how to determine the total wave energies from nonlinear KdV-NLFT spectra and how to combine FFT and KdV-NLFT for energy analyses. Hence, in this section an example is given for a comparative analysis using FFT and KdV-NLFT of experimental transmission test data on submerged reefs with finite width.

The experimental set-up in the twin-wave flume at Leichtweiß-Institute, TU Braunschweig, is given in Fig. 5.14. The waves are generated as cosine waves at the piston-type wave maker at $x=0m$. The nominal wave parameters are $H_{nom}=0.16m$, $T_{nom}=6.0s$ and the water depth is $h=0.70m$. The waves propagate along the flume and pass over a submerged reef at $x=34.75m$ with width $b_r=1.04m$. The reef height is $h_r=0.60m$, the submergence depth $d_r=0.10m$ and the reef front and back are sloped with 1:2. The incident waves are measured at gauge group GG3 (starting at $x=30.39m$) directly in front of the reef, the transmitted waves are determined at gauge group GG7 (starting at $x=35.75m$) directly behind the reef. For both, GG3 and GG7 the reflection analysis with the FFT-based method by Mansard and Funke (1980) was applied to

separate incident and reflected waves. Finally, the method provided the incident and reflected waves at GG3 and the transmitted wave at GG7 (as the incident wave at this gauge group) as given in Fig. 5.15a to c.

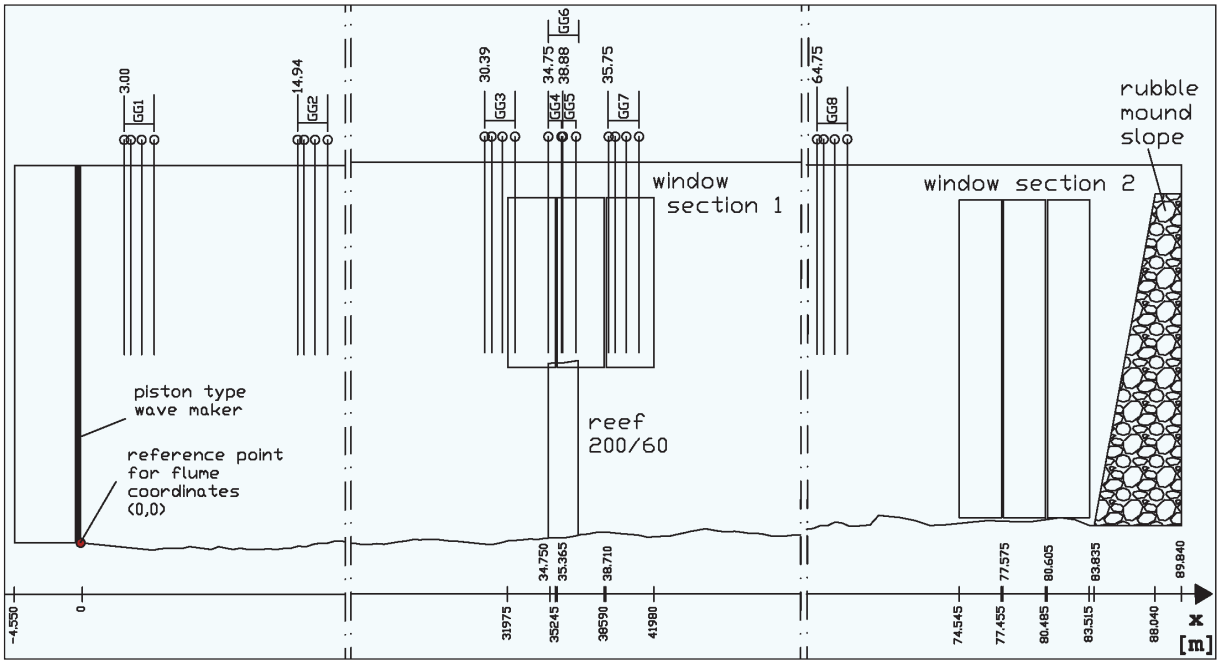

Fig. 5.14: Experimental set-up in the LWI twin-wave flume. Incident waves are measured at gauge group GG3 (*x=30.39*), transmitted waves are measures at gauge group GG7 (*x=35.75m*). The 1m reef is located at *x=34.75m-35.79m*.

For the comparative analysis using FFT and KdV-NLFT the waves in Fig. 5.15a-c are selected. For each wave the conventional FFT (Fig. 5.15d-f) and the nonlinear KdV-NLFT (Fig. 5.15g-i) is applied and the total energies from FFT and KdV-NLFT are calculated. As can be seen in Fig. 5.15a due to harmonic generation the initial cosine wave already shows secondary wave crest at the gauge position at *x=30.39m* and the FFT total energy spectrum in Fig. 5.15d shows a total of three significant peaks instead of the one of the cosine wave. Since the generated cosine wave is not stable in the given water depth, as can be seen from the fact that harmonic generation occurs in the FFT spectrum. Hence, the KdV-NLFT spectrum in Fig. 5.15g shows two significant peaks. The same applies for the reflected and the transmitted waves. They show secondary crests and are represented in both linear and nonlinear spectra by at least two components. As expected, the elevations of the reflected and transmitted waves are much smaller than those of the incident wave.

In the spectra in Fig. 5.15, the sum of the total wave energies for each spectrum is given and a detailed analysis is given in Tab. 5.2. The incident wave energy from FFT is $E_{tot,i}$*=15.05J/m² (100%)*, the reflected energy is $E_{tot,r}$*=2,76J/m² (18.3%)* and the transmitted energy is $E_{tot,t}$*=4,19J/m² (27.8%)*. The dissipated total energy has to be $E_{tot,d}$*=15.05-2.76-4.19=8,10J/m² (53.8%)*. For the results of the KdV-NLFT applies $E_{tot,cn,i}$*=6.42J/m² (42,7%)*, the reflected energy is $E_{tot,cn,r}$*=0.68/m² (10.6%)* and the transmitted energy is $E_{tot,cn,t}$*=0.98/m² (15.3%)*. In this case the dissipated total energy has to be $E_{tot,cn,d}$*=6,42-0,68-0,98=4.76J/m² (74.1%)*. The percent values of the FFT results describe the energy portions of the reflected, transmitted and dissipated waves. They add up to 100%, which is the total energy E_{tot} of the incident wave. The percent values of the KdV-NLFT results are with respect to the values of the FFT. For

example, the energy of the incident wave consists of 42.7% cnoidal wave energy and 57.3% interaction energy. The transmitted energy from FFT is composed from 23.4% cnoidal wave energy and 76.6% interaction energy.

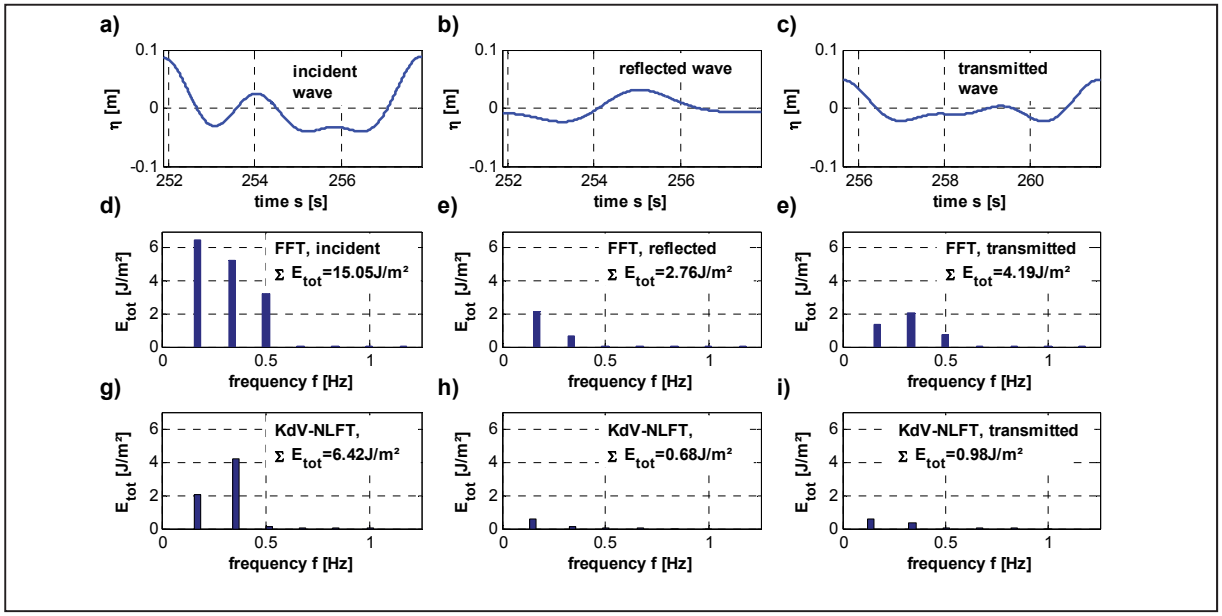

Fig. 5.15: Example for conventional FFT and nonlinear KdV-NLFT analysis of wave transformation at submerged reefs. a-c: incident, reflected and transmitted waves; d-f: conventional FFT total energy spectra of the waves in a-c; g-i: nonlinear KdV-NLFT total energy spectra of the waves in a-c.

According to Eq. (5.7) the total wave energy $E_{tot,int}$ of the interactions can be determined by subtraction of the total cnoidal wave energy $E_{tot,cn}$ from the total FFT energy E_{tot}. The obtained values are given in Tab. 5.2. Note that the term *"dissipated wave"* refers to a theoretical wave that would have exactly the energy that is determined as dissipated energy E_d.

A closer look on the values in Tab. 5.2 shows that the incident wave energy consists of 42.7% cnoidal wave energy and 57.3% interaction energy. In the reflected and transmitted waves, this relation has changed to approx. 24% cnoidal wave and 76% interaction energy. The "dissipated" wave energy consists of 59% cnoidal wave and 41% interaction wave energy. Since this example shows the analysis of only one model test, no conclusion can be drawn that are universally valid for all tested wave parameters, water depths and reef geometries. Nevertheless, this example provides new details for the discussion of wave transformation and hydraulic efficiency which are based on a deeper understanding of the nonlinear nature of the measured free surface waves. The KdV-NLFT identifies the underlying cnoidal spectral basic components and allows the separation of these cnoidal waves from their nonlinear interactions. Based on this analysis, the wave energy of the measured waves can be decomposed into the energy of the cnoidal basic components and the energy portion of the nonlinear interactions. In future research projects, a closer and systematic analysis of these energy components and the energy transfer between these components could provide an improved understanding of the nonlinear processes involved in the wave transformation around submerged reefs.

Tab. 5.2: Total wave energies from comparative analysis of wave transformation at submerged reefs for incident, reflected, transmitted and dissipated wave. All energies in [J/m²], all percentage values are relating to the FFT total energy of each wave type.

		incident wave	reflected wave	transmitted wave	dissipated wave
FFT	E_{tot} [J/m²]	15.05	2.76	4.19	8.10
	E_{tot} [%]	100.0	18.3	27.8	53.8
KdV-NLFT	$E_{tot,cn}$ [J/m²]	6.42	0.68	0.98	4.76
	$E_{tot,cn}$ [%]	42.7	24.6	23.4	58.8
	$E_{tot,int}$ [J/m²]	8.63	2.08	3.21	3.34
	$E_{tot,int}$ [%]	57.3	75.4	76.6	41.2

5.5 Summary and implications for further analysis

The transformation of incident waves induced by submerged reef is well-analysed in the literature (Mei & Ünlüata, 1972; Massel, 1983; Bleck & Oumeraci, 2002; Bleck, 2003). In this chapter, the focus is laid on the interpretation of the harmonic generation as a shallow-water effect, the existence and generation of transient waves and the explanation of the generation of higher-harmonic wave components using the KdV-NLFT. Furthermore, wave energy is calculated comparatively from both conventional FFT and nonlinear KdV-NLFT spectra. Finally, an example is given how the nonlinear wave energy could be applied for the analysis of the hydraulic efficiency of submerged reefs. For more details on the harmonic generation or dispersion of long-period waves in shallow water see chapter 4 that describes the propagation of solitary waves over submerged reefs and section 6.1 that presents the KdV-NFLT analysis of long-period sinusoidal shallow-water waves.

Based on the results of the chapter, including those in section 6.1, the following tentative conclusions may be drawn for the wave propagation in shallow water (see Fig. 5.16):

(i) All surface waves that *are solutions* of the KdV equation are stable waves in shallow waters and propagate in constant water depth *without dispersion effects and therefore without harmonic generation*.

(ii) All surface waves that *are not solutions* of the KdV equation *are transient waves* that are generated by the superposition of solutions of the KdV equation (spectral basic components) and their nonlinear interactions. They show *dispersion effects* (see Fig. 5.16) *and therefore harmonic generation occurs in the conventional FFT spectra, but not in the nonlinear KdV-NLFT spectra*.

(iii) The spectral cnoidal basic components (KdV solutions) of these transient waves (non-KdV solutions) propagate as free waves. The approach using *bound* or *phase-locked waves* which is developed in the conventional FFT representation is *not necessary* in the nonlinear KdV-NLFT approach. The different shapes of the free surface are functions of the phase shift between the spectral components and the result of the phase-dependent nonlinear interactions.

(iv) Solutions of the KdV equation are stable, non-dispersive surface waves only for the given boundary conditions (and especially the given water depth). If the boundary conditions change, e.g. due to changes in water depth, then the formerly stable waves might not be solutions of the KdV equation for the modified boundary conditions and therefore the waves may become transient waves starting from that location of changed water depth (see Fig. 5.16).

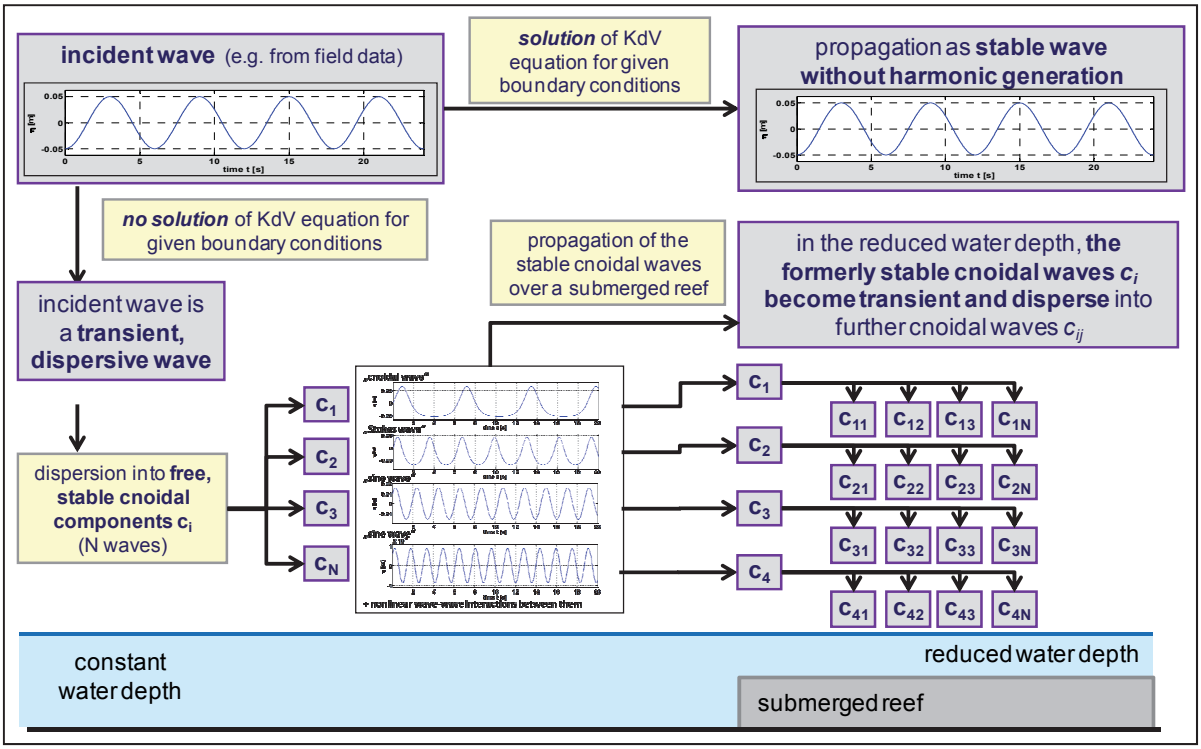

Fig. 5.16: Schematic representation of the concept of long-wave propagation in shallow water and wave adaption to water depth as the waves propagates over the front of a submerged reef with infinite width.

For the interpretation of harmonic generation over and behind submerged reefs the last point (iv) is most important. As noted by Stoker (1957), harmonic generation can often be observed when waves enter from deep water onto the continental shelf. The stable long incident waves in deeper water that are entering in shallower water depth suddenly become transient waves which are composed by new underlying cnoidal ($c_1, c_2, c_3,...$) waves and their interactions (see Fig. 5.16). Due to the reduced water depth, the longer incident waves will disperse into several waves with shorter periods and wave lengths that are the new solutions of the KdV equation for the new boundary conditions. Each of these new spectral components travels as a free wave with its own characteristic nonlinear celerity and secondary wave crests will appear. As long as the water depth is constant, the nonlinear KdV-NLFT spectrum of these waves in the new water depth does not change. As soon as the water depth changes again, each of the new basic components is subject to the described changes in shape, transient character and dispersion again ($c_1 \rightarrow c_{11},c_{12},c_{13},...$ $c_2 \rightarrow c_{21},c_{22},c_{23},...,...$). If the step is finite, like a submerged reef with finite width, the newly generated shallow-water waves propagate over the reef as free waves until they pass the step and enter deeper water again. Now each of the spectral basic components might become a transient wave again.

For the analysis of the hydraulic efficiency of submerged reefs, the energy balance of incident, reflected, transmitted and dissipated waves is analysed. Due to harmonic generation, the

energy distribution in the conventional FFT spectrum might change with gauge position while the total energy remains constant. Therefore, the selection of the gauge position for measuring the incident wave might affect the results of the analysis of the energy transfer from incident to transmitted waves. In the KdV-NLFT no harmonic generation occurs for wave propagation over flat bottoms, and therefore the energy distribution is constant and independent of the gauge position.

The KdV-NLFT determines the underlying cnoidal waves and the nonlinear spectrum does not contain the wave-wave interactions. Therefore, in case of nonlinear interactions the total wave energy $E_{tot,cn}$ of the cnoidal waves in the KdV-NLFT spectrum is smaller than the total wave energy E_{tot} obtained from conventional FFT. The energy difference between the FFT and the KdV-NLFT spectra provides the energy content $E_{tot,int}$ of the nonlinear interactions. If just one cnoidal wave is analysed, then no nonlinear interactions occur and both FFT and KdV-NLFT provide the same results.

Many processes around submerged reefs are not completely understood and simply subsumed as nonlinear effects. With the KdV-NLFT the decomposition of the total wave energies of incident, reflected, transmitted and dissipated waves into the portions of both cnoidal waves and nonlinear wave-wave interactions has become possible. Future analysis with more systematic decomposition of the wave energy into cnoidal wave energy and interaction energy will reveal whether this new approach will have important implications for practical applications and for the research of the underlying nonlinear processes.

6 Application of KdV-NLFT to other coastal and shallow water wave problems

In the previous chapters, the theoretical background (chapter 2) and the numerical implementation (chapter 3) of the inverse scattering transform of the Korteweg-deVries equation (KdV-NLFT) were introduced and described. In chapters 4 and 5, this powerful spectral analysis method for nonlinear waves in shallow water was applied for the reliable identification of solitary waves behind an artificial submerged reef and the analysis of regular waves in front of and behind submerged structures. So far, in the given examples the method has clearly shown its advantages for the nonlinear analysis of shallow-water waves compared to the conventional analysis method fast Fourier (FFT) and Hilbert-Huang transform (HHT). Since the KdV-NLFT provides a completely new view on shallow-water waves as a nonlinear superposition of nonlinear cnoidal basic components and their nonlinear wave-wave interactions, this method can also provide an improved understanding for many other coastal and shallow water wave problems as presented by means of selected examples in the following sections.

The purpose of the selected example applications is only to further illustrate the potential of the KdV-NLFT. The focus will therefore be laid neither on the systematic analyses of these example problems nor on detailed results and discussions. Each of these examples might be considered as an indication and motivation for future research.

First, the KdV-NFLT is applied for the spectral analysis of long cosine waves in shallow water. The analyses will show that the nonlinear interaction phenomena among propagating solitary waves that are observed by Zabusky and Kruskal (1965) in numerical solutions of the KdV equation can also be observed in hydraulic model tests in the wave flume. Furthermore, the application of the implemented KdV-NLFT can predict and explain the observed phenomena by regarding the initial long sine wave as a transient wave composed by solitons, periodic cnoidal waves and their nonlinear interactions (section 6.1).

Second, the application of the implemented KdV-NLFT to long-period primary ship waves from hydraulic model tests shows that this analysis method regards these waves to be composed of a large number of solitons and some oscillatory cnoidal waves (section 6.2). Since primary ship waves do not look like solitons at all, this interpretation of primary waves as a transient wave composed of solitons and their nonlinear wave-wave interactions is completely new. Regarding the results of the propagation of long sine waves in shallow-water (section 6.1), this interpretation is the logical next step toward the general interpretation that all long-period waves in shallow-water that are not solutions of the Korteweg-deVries equation have to be regarded to be dispersive transient waves.

Finally, a summary is given that also mentions some more coastal and shallow-water wave problems that might be possible future applications for the KdV-NLFT (section 6.3).

6.1 Analysis and prediction of long-period cosine wave transformation in shallow water using the KdV-NLFT

Hydraulic model tests and numerical simulations show that long cosine waves that are generated in shallow-water are not stable, but show modifications of the free surface as a function

of propagation in time and space. With increasing distance from the wave maker, the wave becomes asymmetric and develops into a bore-shaped wave. With further increasing distance, more additional wave crests emerge progressively from the front of the bore. The number of additional wave crests increases with shallower water. In extremely shallow water, the periodic cosine waves completely disintegrate into periodic trains of solitons. The nonlinear KdV-based nonlinear Fourier transform (KdV-NLFT) provides an explanation for this nonlinear phenomenon and allows the prediction of the propagation and dispersion of these long cosine waves in shallower water.

In the following sections, *first*, a short introduction to the theoretical background is given. *Second*, the hydraulic model test data on long-period cosine waves in shallow water are analysed using the KdV-NLFT method. *Third*, numerical simulations of the model tests are analysed, too. *Forth*, the data are comparatively analysed with the KdV-NLFT as well as with the conventional Fourier transform (FFT) and the Hilbert-Huang transform (HHT). *Finally*, a summary and implications for further analyses are given.

6.1.1 Theoretical background

Zabusky and Kruskal (1965) computed the propagation of solitons and small, but finite-amplitude shallow-water waves in nonlinear dispersive media. Within the numerical results they observed 'unusual nonlinear interactions among 'solitary-wave pulses''. They found that these phenomena could be categorized into three different states (presented in Fig. 6.1 as graphs A, B and C) with *u(x)* being the current wave form (indicated by the green, blue and red curves) in each of the states (Zabusky & Kruskal, 1965):

> (curve A): 'Initially, the first [three] terms of [the KdV equation (2.2)] dominate and the classical overtaking phenomenon occurs; that is, *u(x)* steepens in regions where it has a negative slope.'
> (curve B): 'Second, after *u(x)* has steepened sufficiently, the [forth] term becomes important and serves to prevent the formation of a discontinuity. Instead, oscillations of small wavelength […] develop on the left of the front. The amplitudes of the oscillations grow and finally each oscillation achieves an almost steady amplitude (which increases linearly from left to right) and has a shape almost identical to that of an individual solitary-wave solution of [the KdV equation (2.2)].'
> (curve C): 'Finally, each such '*solitary-wave pulse'* or '*soliton'* begins to move uniformly at a rate (relative to the background value of *u(x)* from which the pulse rises) which is linearly proportional to its amplitude. Thus, the solitons spread apart. Because of the periodicity, two or more solitons eventually overlap spatially and interact nonlinearly. Shortly after the interaction, they reappear virtually unaffected in size or shape. In other words, solitons '*pass through*' one another without losing their identity. Here we have a nonlinear physical process in which interacting localized pulses do not scatter irreversibly.'

The consequence of these descriptions is clear: The initial wave form *u(x)* changes its shape from a cosine wave (curve A in Fig. 6.1) towards a (undular) bore-shaped wave (curve B) and finally the solitons evolve from the front of the bore and the initial cosine wave becomes a train of independent solitons (curve C). The free solitons are 'almost identical' (Zabusky & Kruskal, 1965) to the solitary-wave solution of the KdV equation and the initial sinusoidal wave shape is the result of the nonlinear interactions of these solitons. The solitons pass

through each other without changing their shape, but the superposition of these solitons and their nonlinear wave-wave interactions, which are functions of the phase differences between the interacting solitons, provide the different shape of the free surface in Fig. 6.1: (curve A) cosine-shaped if all solitons are in phase and strongly interacting, (curve B) bore-shaped wave profile if the solitons start to disperse and (curve C) a set of solitons when the solitons are completely dispersed from the initial condition.

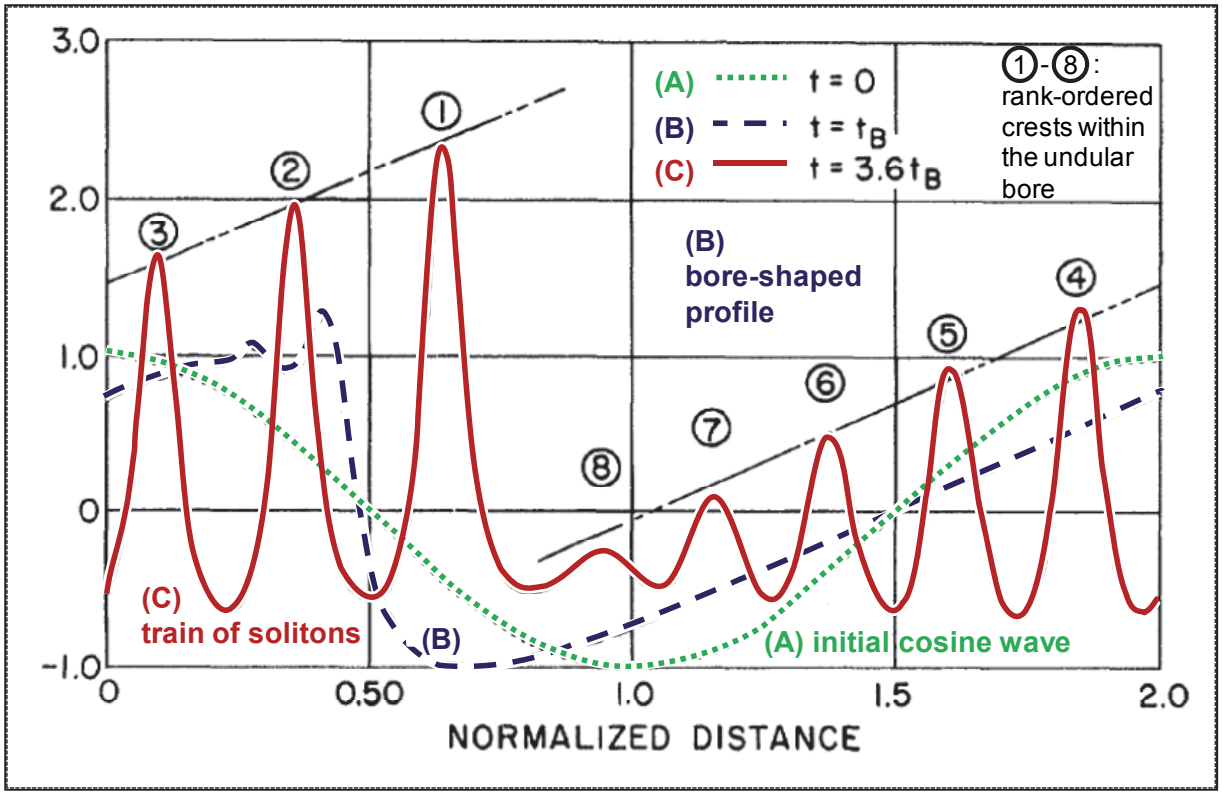

Fig. 6.1: The temporal development of the initial cosine wave form (curve A at $t=0$) at different time steps $t=t_B$ (curve B) and $t=0.3t_B$ (curve C). The number indicate the rank-ordered crests within the undular bore (after Zabusky & Kruskal, 1965).

Osborne and Bergamasco (1986) and Osborne (2010) applied the periodic direct scattering transform (PDST) on the initial cosine wave (wave form A in Fig. 6.1 and Fig. 6.2a that was used by Zabusky and Kruskal (1965) as a sine wave in Fig. 6.2a. In Fig. 6.2, the temporal evolution of the initial sine ($t=0$) wave is shown for different time steps ($t=330s$, $580s$ and $850s$). In Fig. 6.2c, the initial sine wave has disintegrated into a train of rank-ordered solitons at $t=580s$. Note that both the initial sine wave and this specific soliton solution only occur at a specific time step and therefore represent transient waves. At other time steps, the solitons have other phases and, therefore, the free surface has a complex structure that is composed by the solitons at different phases and the phase-dependent nonlinear soliton interactions. Furthermore, even if the signal is dominated by solitons, some additional oscillatory cnoidal waves and their nonlinear interactions might be involved, too. The soliton amplitudes that are provided by the DST are compared by Osborne and Bergamasco (1986) with those obtained by Zabusky and Kruskal (1965) from Fig. 6.1 and with values given in a table in Zabusky and Kruskal (1965) (see Fig. 6.3). The results show that the numerical solution of the KdV equation after propagation in space and the application of the KdV-NLFT directly to the initial sinusoidal wave form provide the same soliton amplitudes. Therefore, the KdV-NLFT is able

to predict the correct solitons that will evolve from the initial cosine wave directly from the initial free cosine-shaped surface without the need to calculate the cosine wave propagation in time or space or to conduct physical model tests.

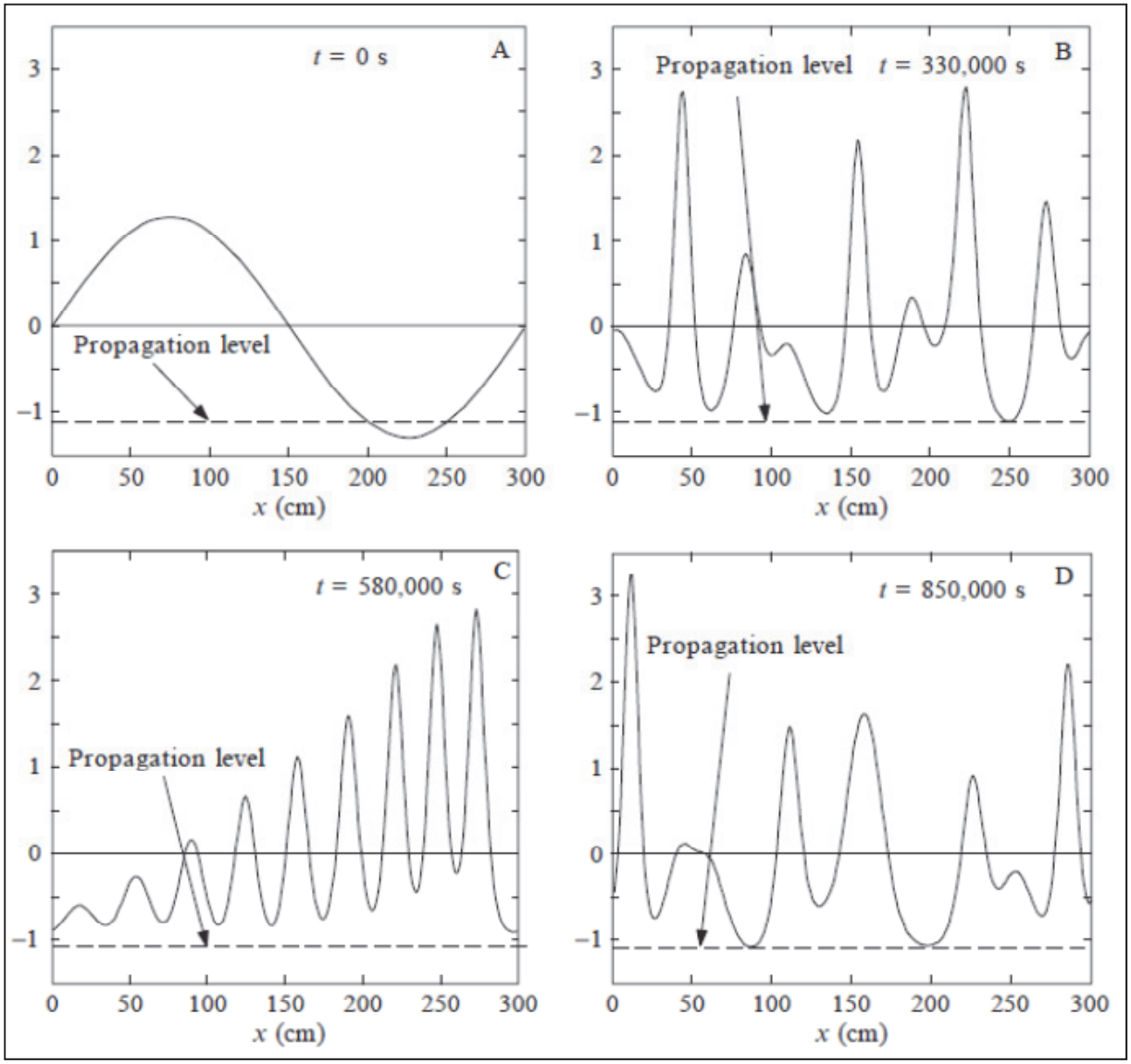

Fig. 6.2: Illustration of the discovery of the soliton by Zabusky and Kruskal (1965). The KdV equation is integrated numerically with periodic boundary conditions, which are appropriate for some simple kinds of internal soliton dynamics on the continental shelf. Four time values are shown in the numerical solutions for a sine wave (internal tide) initial condition (A). At a later time, one observes that solitons emerge from the sine wave and undergo quite complex interactions (B). At a particular instant of time the nine solitons are well delineated, indeed rank ordered as in the infinite-line case (C). The soliton complex interaction structure is again seen at later times (D) (Osborne, 2010).

6.1.2 KdV-NLFT analysis of hydraulic model test data

The analyses by Zabusky and Kruskal (1965), Osborne and Bergamasco (1986) and Osborne (2010) presented in section 6.1.1 were performed on numerically generated data. Hammack and Segur (1974) showed that the same phenomenon of the disintegration of an initial wave into solitons can also be observed in hydraulic model tests, too. They used a vertical piston that was displaced e.g. either *0.05m* up or down to generate initial waves with an approximate

square shape in a water depth of *h=0.05m* that develop into trains of solitons and trailing oscillatory waves. This confirms the results by Gardner et al. (1967) that found that for the exact solution of the KdV equation for infinite line (not periodic!) boundary conditions any initial wave form develops into a train of rank-ordered solitons and trailing oscillatory waves. For specific initial wave forms no solitons or no oscillatory waves occur, but in general the arbitrary initial shallow-water signal is composed by solitons and oscillatory waves.

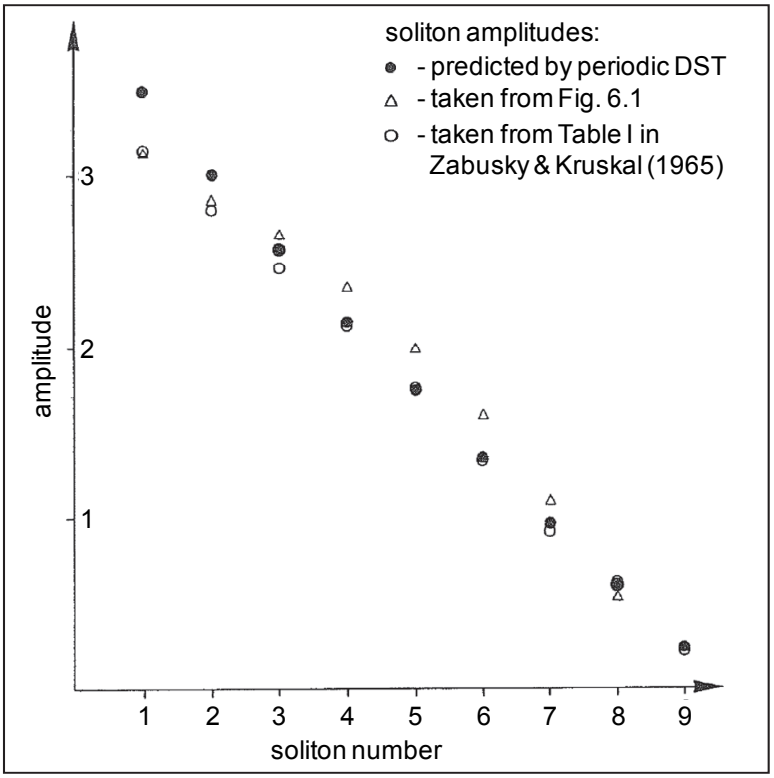

Fig. 6.3: Comparison of soliton amplitudes (i) predicted by the periodic DST (black dots), (ii) taken from Fig. 6.1 in Zabusky and Kruskal (1965) (open circles), and (iii) taken from Table I in Zabusky and Kruskal (1965) (triangles) (after Osborne & Bergamasco, 1986).

In this section, measured data from hydraulic model tests in the 2m section of the LWI twin-wave flume will be analysed using the KdV-NLFT. The waves were generated as periodic sinusoidal waves with a piston-type wave maker in a water depth of *h=0.21m*. The initial nominal wave height is *H=0.05m* and the period is *T=16.67s*. The measured free surface at *x=1.05m* close to the paddle and at *x=41.26m* in the far field are shown in Fig. 6.4. Note that this figure is a modification of Fig. 1.2 in the introduction.

After the ramping-up phase in Fig. 6.4a, starting at *t=20s*, the measured wave at *x=1.05m* very close to the wave generation can clearly be identified as a cosine-shaped wave. After having travelled about 40m (1.7 times the initial wave length *L=23.92m*) the periodic cosine wave has disintegrated into periodic trains of solitons (see Fig. 6.4b). The leading soliton has separated almost completely from the following wave packet. The complete separation of all the solitons could not be observed clearly as a rank-ordered train of solitons due to (i) the limited length of the wave flume, (ii) the reflection of the first waves at the end of the flume that interfere with the incident waves (starting from the forth incident wave period) and (iii) the fact that before complete separation, the first solitons of a wave package already overtook the last solitons and the trailing waves of the previous wave packet and additional interactions

occurs. Nevertheless, it can be shown that in this very shallow water depth (*h/L=0.009*) the initial periodic long-period cosine wave disintegrates into periodic trains of solitons and the results of Zabusky and Kruskal (1965) could in principle be reproduced.

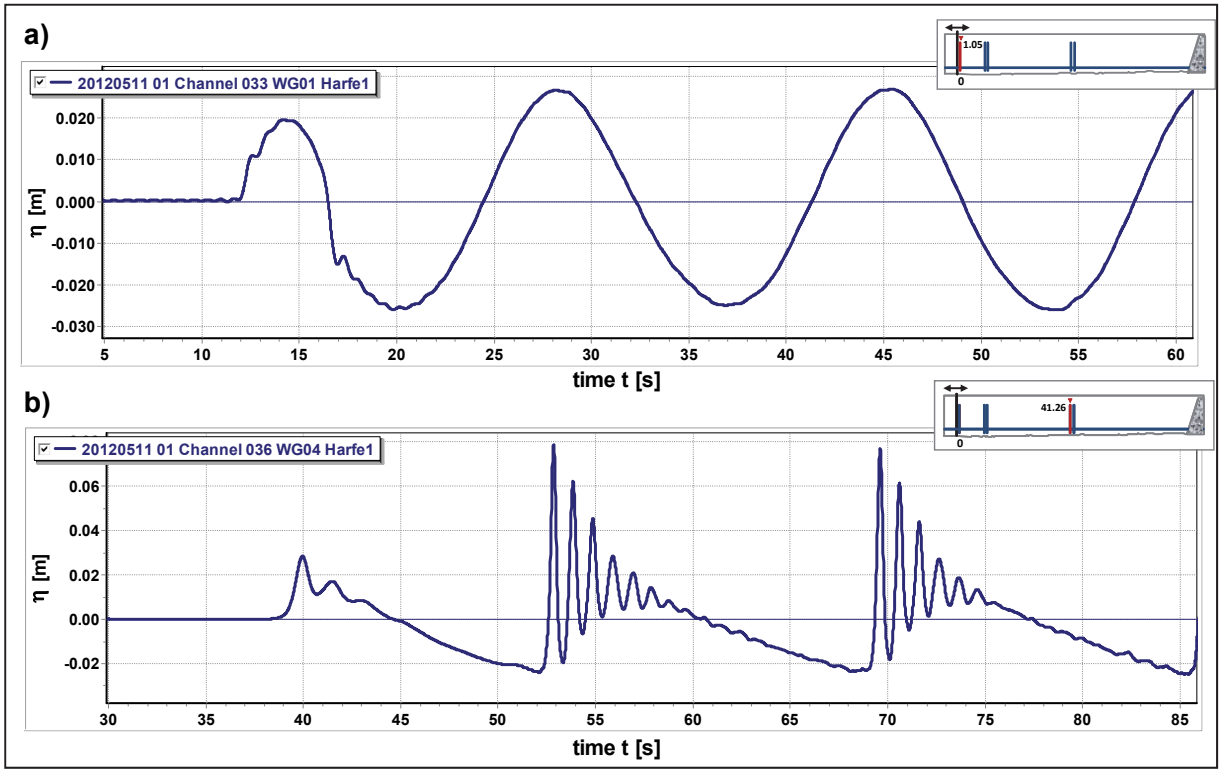

Fig. 6.4: Measurements of long cosine waves generated in the wave flume at LWI with *h=0.21m*, *h/L=0.009*, *H=0.05m* and *T=16.67s*. a) Generated cosine wave profile measured at *x=1.05m* from the wave paddle. b) Measured data at *x=41.26m* in the far-field: The incident periodic sinusoidal wave is decomposed into periodic trains of solitons.

The application of the KdV-NLFT to the initial cosine wave in Fig. 6.4a provides the nonlinear spectrum shown in Fig. 6.5a. In Fig. 6.5b, the nonlinear spectrum of the train of solitons from Fig. 6.4b is shown. For the determination of the spectra from each time series, a single period was selected. In both spectra, the soliton spectra on the left side clearly show that this initial signal is dominated by eleven solitons, followed by nonlinear oscillatory waves with insignificant amplitudes. The nonlinearity of these latter waves is decreasing with increasing frequency. These results correspond to the measured data in Fig. 6.4b that show already at least seven developing solitons as peaks in the undular bore. As already shown by Osborne and Bergamasco (1986) and Osborne (2010) for numerical data, here is shown that the KdV-NLFT analysis also predicts correctly the disintegration of a measured long-period shallow-water cosine wave in the wave flume. Furthermore, the applications of the KdV-NFLT to the measured incident signal at *x=1.05m* shows the same spectrum. The few frequency shifts in the solitons are not relevant since these frequencies have no relevance for the solitons and are used only for plotting reasons. The result is clear: The cosine-shaped initial wave in Fig. 6.4a and the periodic train of solitons in Fig. 6.4b are decomposed in the KdV-NLFT into identical spectral components. As will be shown in section 6.1.3 the initial cosine wave and the train of solitons can be constructed by nonlinear superposition of the same cnoidal basic components. The results in Fig. 6.5 show that the implemented KdV-NLFT is able to reliably identify these identical spectral basic components independent of the current phase shift of the underlying

cnoidal waves and independent of the shape of the free surface. The spectral soliton structure can be determined directly from the incident signal without the need for numerical simulations of the wave propagation or hydraulic model tests.

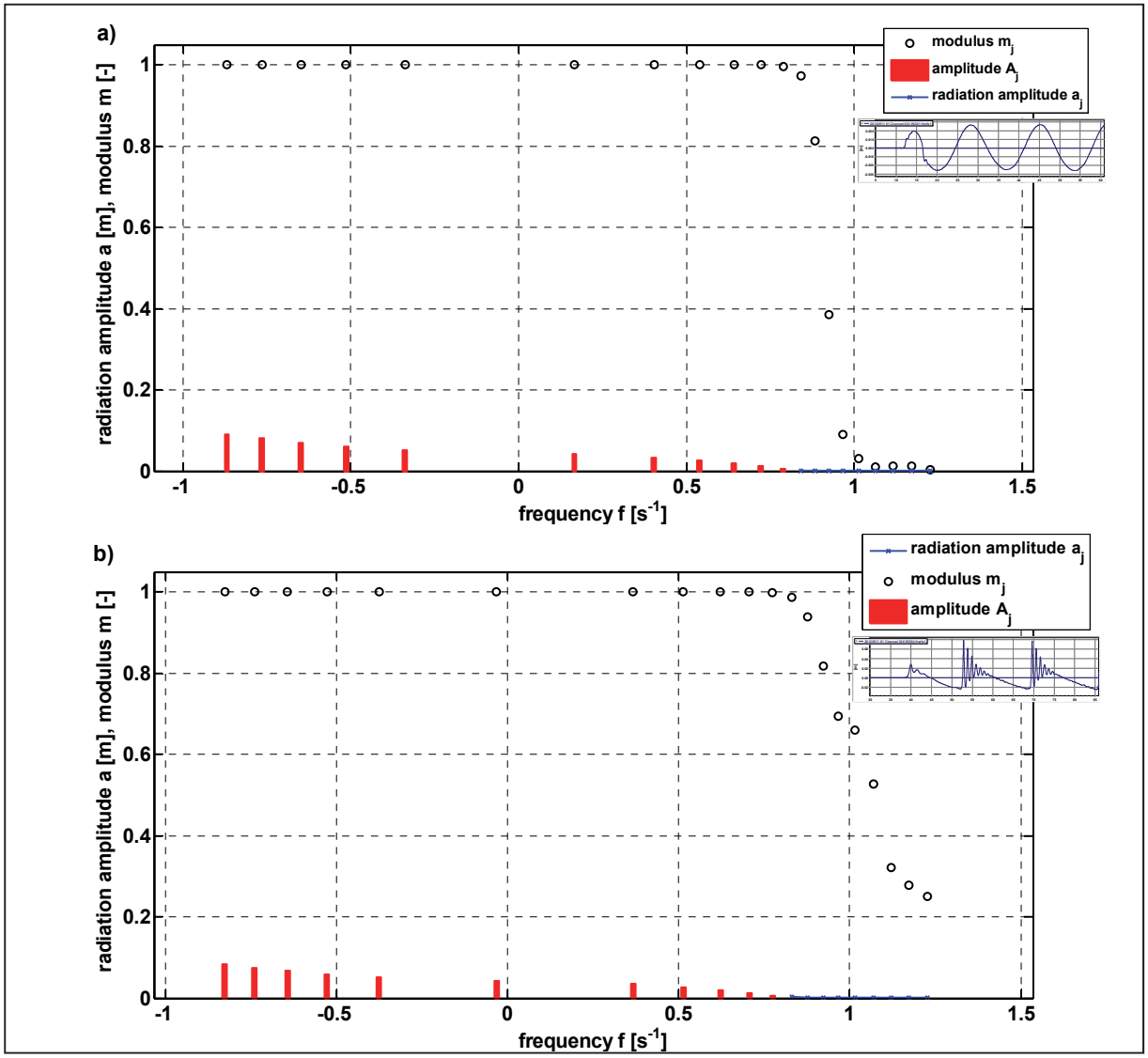

Fig. 6.5: Nonlinear spectrum of selected wave periods of the measured signals from Fig. 6.4 in water depth *h=0.21m* with *h/L=0.009*: a) section *t=20.2 - 36.87s* of the initial cosine wave from Fig. 6.4a and b) section *t=52.16 - 68.83s* of the train of solitons from Fig. 6.4b.

The most important governing parameter for the nonlinear wave analysis with the KdV-NLFT is the water depth *h*. In fast Fourier (FFT), wavelet (WT) or Hilbert-Huang transform (HHT) the analysis procedure and thus the results are completely independent of the water depth since this variable is not considered in the algorithms at all. In contrast to those conventional analysis methods, in KdV-NLFT the results change significantly with changing water depth. The results in Fig. 6.5 are obtained for the correct water depth *h=0.21m* in which the measured initial wave actually was generated. Now the assumption is made (just theoretically) that the signal in Fig. 6.4a has been generated and measured in a water depth *h=10.0m* instead of *h=0.21m*. The same measured cosine-shaped data and the new water depth information is provided to the KdV-NLFT as input values. As can be seen in Fig. 6.6, now the nonlinear spectrum does not show any soliton at all, but, similar as would have been expected from the

conventional FFT, a peak in the radiation spectrum with correct amplitude *a=0.0257m* at the correct frequency of *f=0.06Hz*. The small modulus of *m=0.10* and the absence of significant higher-harmonic components in the spectrum indicates that this main components is a nearly linear Airy-like wave. In this latter analysis, the initial cosine wave is regarded to be a nearly linear cosine wave, not a superposition of a large number of solitons, even if the relative water depth is only *h/L=0.06* and, hence, just outside shallow-water conditions in the intermediate region. These different results for the same signal, but different water depths, highlight the importance of the water depth as input variable and the sensitivity of the KdV-NLFT to changes of the water depth.

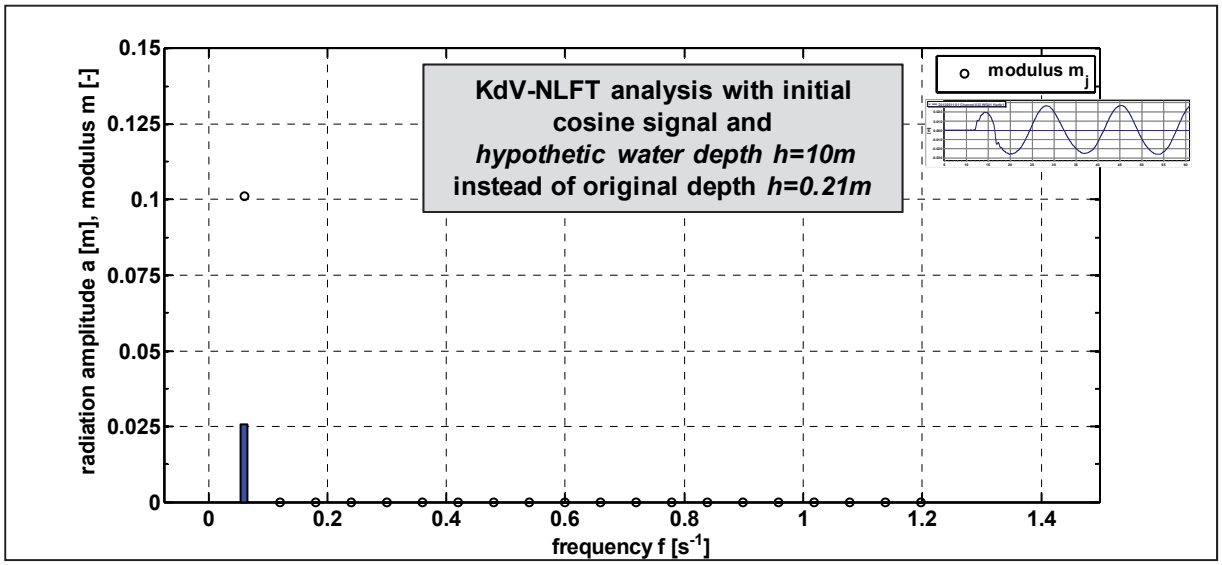

Fig. 6.6: Nonlinear spectrum of the same initial cosine-shaped wave (Fig. 6.4a) as in Fig. 6.5 but with modified water depth *h=10.0m* with *h/L=0.06*: The initial wave is considered to be a (slightly nonlinear) Airy-like wave with wave amplitude *a=0.257m*, frequency *f=0.06Hz* and modulus *m=0.10*.

In order to find out the reason for these completely different results with different relative water depths (still in shallow water: *h/L=0.009* and *h/L=0.06*), we have to recall that in the KdV-NFLT the initial data is regarded to be composed of nonlinear basic components that are solutions of the KdV equation and their nonlinear wave-wave interactions. The shape and character of the solutions of the KdV equation strongly depend on the relative water depth. For very shallow waters (e.g. the case *h/L=0.009*) the KdV equation can be solved by solitons. In this case, solitons are available for the reconstruction of the initial data in shallow water as well as very short-period oscillatory waves. If the water becomes deeper even still under shallow water conditions (e.g. the case *h/L=0.06*), solitons are not longer solutions to the KdV equation, but cnoidal-like, Stokes-like and Airy-like waves with longer periods and higher amplitudes. So the 'toolbox' of available cnoidal basic components that can be used for the reconstruction of the data in the given water depth completely changes. In different water depths, the same signal has to be reconstructed by completely different wave types and their interactions. If we reach deeper water (not deep-water yet), then the original cosine wave from Fig. 6.4a can be a stable solution to the KdV equation and no further components or interactions are required for the reconstruction. In this case, the result of the KdV-NLFT in Fig. 6.6 is the same as that of the conventional FFT. In very shallow water, this long-period cosine wave is not available as a spectral basic component for the decomposition since it is not a solution to the KdV equation and therefore, under these boundary conditions the cosine-

shaped original signal has to be composed by very shallow water waves such as solitons. This result can only be obtained if the nonlinear spectral structure is determined as a function of the water depth, as happens in the KdV-NLFT.

6.1.3 Numerical simulation of the propagation of long cosine waves in shallow-water

In the two previous sections, the decomposition of periodic long cosine waves into periodic trains of solitons is shown numerically in the literature by solving the KdV equation (section 6.1.1) and in hydraulic model tests performed in the frame of this doctoral thesis at LWI (section 6.1.2). In this section, numerical simulations will be used to show that this phenomenon also occurs in the RANS-VOF simulations of the hydraulic model tests. Furthermore, the proof is made that the long cosine-shaped waves in shallow-water *are* transient wave that are composed by solitons and their nonlinear wave-wave interactions.

In a first step, the same boundary conditions as in the hydraulic model test from Fig. 6.4 are used in numerical RANS-VOF simulations with *COBRAS-UC*. The initial periodic cosine waves with $H=0.05m$, $T=16.67s$ and $h=0.20m$ ($h/L=0.09$) are generated at the right boundary. In Fig. 6.7 the numerical measurements of wave gauges at different positions are plotted. The gauges are located at $x=0.015m$, $0.045m$ and $0.075m$ close to the wave generation boundary, followed by 10 gauges from $x=1.0m$ to $10m$ with 1m distance between the gauges, 5 gauges from $x=12m$ to $20m$ with 2m distance and finally 15 gauges from $x=25m$ to $90m$ with 5m distance. The measured time series at these numerical gauges are plotted in Fig. 6.7, with increasing distance from the wave generation from bottom to top. Close to the wave generation, the free surface still is a cosine-shaped wave. With increasing distance, the wave shape changes first into a bore, then an undular bore and finally the first solitons separate from the front of the bore. This is the same nonlinear behavior as described by Zabusky and Kruskal (1965) in Fig. 6.1. Since the numerical wave flume is long enough to allow the transmitted bore to evolve into a train of solitons, and since no reflection occurs at the end of the flume, the separation of several solitons can be observed until the first solitons of each train overtake the last solitons of the previous train. Once the first wave period has passed a gauge, starting from the second period the behaviour of the free surface is identical to all following periodic waves and wave trains. The results from Zabusky and Kruskal (1965), Osborne and Bergamasco (1986) and Osborne (2010) and the results of the KdV-NLFT from the nonlinear spectra in Fig. 6.5 can be confirmed by the results of the numerical simulation in Fig. 6.9: In shallow-water, the initial periodic long cosine wave disintegrates into periodic trains of solitons.

The graphs in Fig. 6.7 show that the initial cosine wave disintegrates into solitons. However, the underlying problem is still unsolved: Where are the solitons coming from? Are they generated newly during the wave propagation or were they already contained in the initial long cosine wave right from the beginning as assumed from the KdV-NLFT results? In the latter case, the initial cosine-shaped wave would be a transient wave that is generated from solitons that mutually interact at specific phases, so that the solitons and their nonlinear wave-wave interactions would form the transient long-period cosine wave. After the formation of this transient wave, the solitons propagate with their own amplitude-dependent celerity, so that the phase differences and therefore the nonlinear interactions change. As a result, the shape of the wave changes into a bore and finally into free solitons.

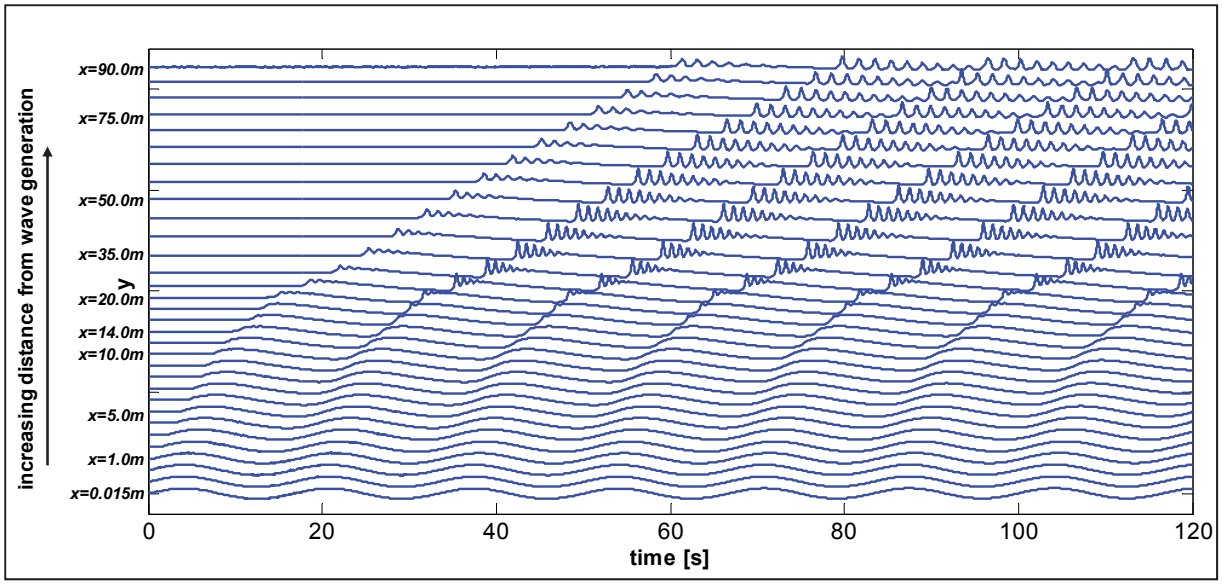

Fig. 6.7: Time series at different locations of the numerical simulation of the propagation of periodic long initial sine waves with *H=0.05m* and *T=16.67s* in a water depth of *h=0.20m* (*h/L=0.009*) (with increasing distance from wave generation from bottom to top).

In order to verify this assumption of the transient character of the initial cosine-shaped wave, a procedure for the generation of transient periodic cosine waves in the numerical model is applied in three steps (see Fig. 6.8):

(i) One of the periodic trains of solitons from the numerical simulation at *x=41.16m* is selected (step 1).

(ii) The sample is mirrored to obtain solitons that are travelling in the opposite direction, so that the faster solitons can overtake the slower ones. Then this sample of length *T=16.67s* is repeated several times (step 2).

(iii) This generated data is used as input for the wave generation in *COBRAS-UC* (step 3).

The results of the numerical simulation with reverse trains of solitons are shown in Fig. 6.9.

In the lowest graph in Fig. 6.9, the free surface directly at the wave generation boundary is shown. Note that in this plot of time series the waves propagate from right to left. With increasing distance from the source of wave generation, the higher solitons slowly overtake the smaller and therefore slower solitons. Due to the nonlinear wave-wave interaction the free surface becomes first a bore, than an undular bore and finally a nearly cosine-shaped wave form (red curve in Fig. 6.9). This cosine-like wave is not stable, because with further increasing distance, the wave profile changes into a bore and an undular bore again, and finally the initial solitons evolve from that undular bore. As Zabusky and Kruskal (1965) already stated, the solitons pass through each other without losing their identity. This can also be observed in collision and overtaking processes of two or three solitons (see section 3.1.4). This example here shows the effect of this phenomenon for a couple of solitons. If two solitons overtake each other (see Fig. 3.14), then the nonlinear interactions cause a depression of the free surface so that the observed wave form is completely different from a simple linear superposition of the two overtaking solitons. The same interaction effect causes the modifications of the free surface in Fig. 6.9 from the train of solitons into a bore, and finally a transient cosine wave while the fast solitons are overtaking the slower ones. The cosine shape defines the

point of the maximum interaction when the highest soliton is overtaking the slowest soliton. With further propagation, the fast solitons come out at the other side and start to move away from the (now trailing) slower soliton. Consequently, the cosine wave transforms back into a bore that has the steep front at the other side than before the formation of the cosine wave. Finally, the solitons evolve from that bore and come out with their initial shape, undisturbed in shape.

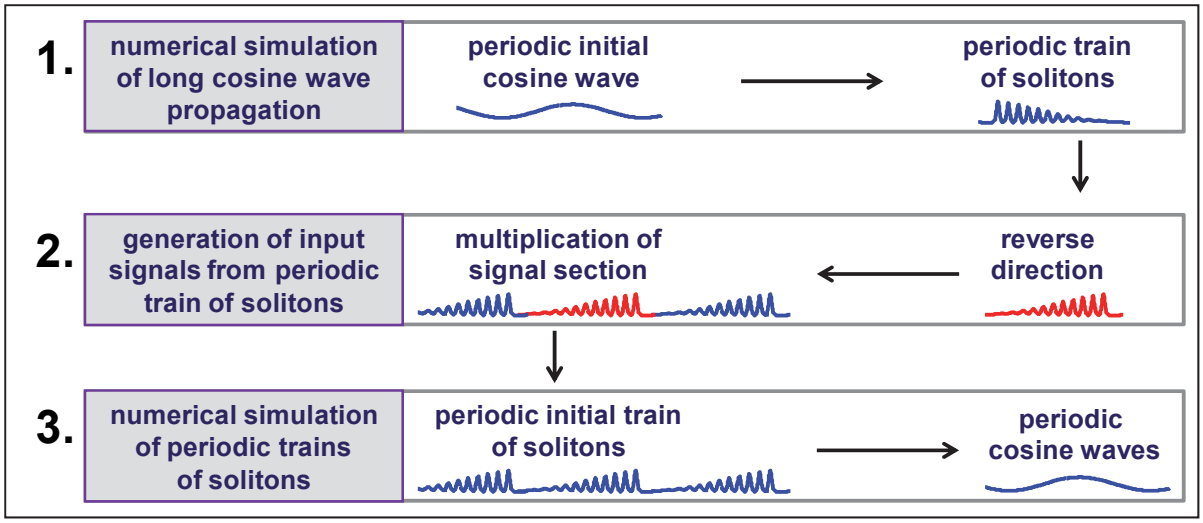

Fig. 6.8: Procedure for the generation of transient periodic cosine waves in the numerical model.

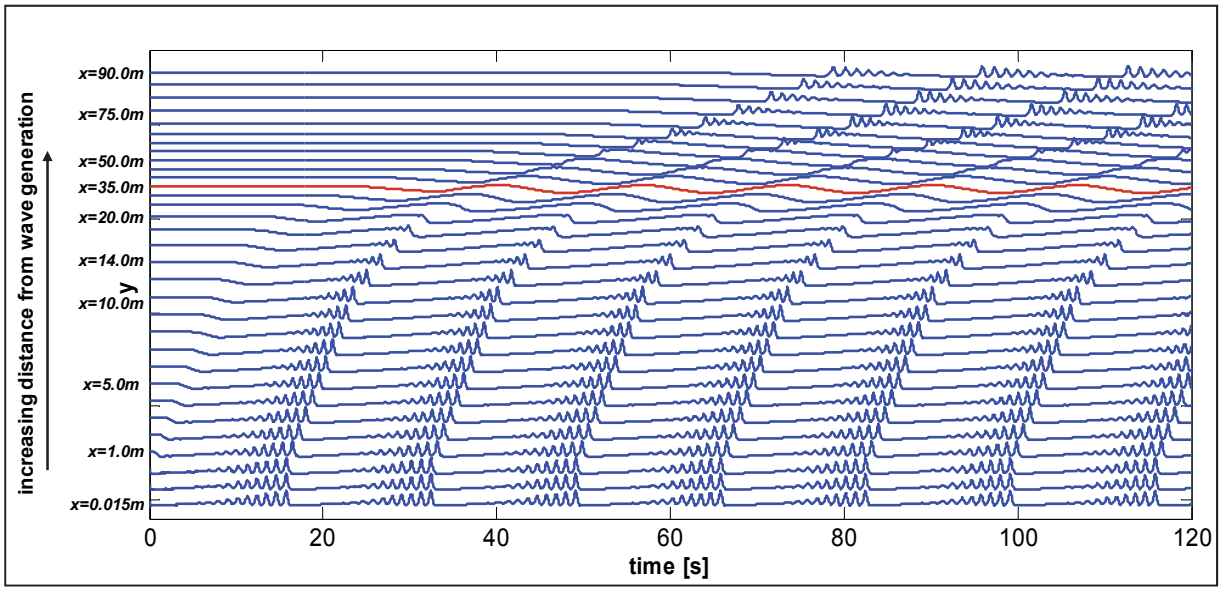

Fig. 6.9: Time series at different locations of the numerical simulation of the propagation of periodic initial trains of solitons. The solitons are taken from Fig. 6.7 and travel now in the opposite direction in a water depth of $h=0.20m$. The red cosine-shaped curve shows the signal measured at $x=35.0m$ where the maximum interactions occur.

The process of the solitons overtaking each other and coming out again without changes in shape can also be observed in the space series representation in Fig. 6.10. The generation of the bore-shaped free surface with opposite locations of the steep front and opposite sequence of the order of soliton amplitudes can easily be seen. As an approach for a better understanding, the free surface of the left side of the black dashed lines can be regarded to the mirrored

to the right side. Fig. 6.11 shows a time series that is recorded at *x=37.08m* (the position of the black dashed line in Fig. 6.10). In fact, the signal is not exactly cosine shaped, most probably due to uncertainties in the pre-processing of the input signal and the numerical simulation. Nevertheless, the comparison with the red dashed cosine function shows that it is very close to a cosine wave. Therefore, the results of the numerical simulations clearly confirm that in fact the periodic train of overtaking solitons generates transient periodic cosine waves. Furthermore, in shallow-water the long-period cosine waves already contain these solitons right from the beginning because the linear long-period shallow-water cosine wave is generated by solitons and their nonlinear wave-wave interactions. For better understanding, one might assume the wave maker from Fig. 6.4 to be located at the position of the black-dashed line in Fig. 6.10. The generated cosine-shaped long-period wave is a transient wave right from the moment when it was generated.

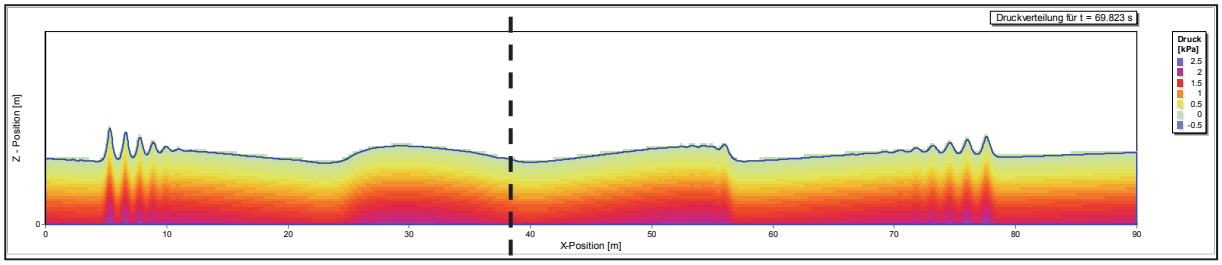

Fig. 6.10: Space series of the free surface and pressure distribution under the propagating initial train of solitons from Fig. 6.9 at *t=69*.8s. The black line denotes the position of the numerical wage gauge at *x=37.08m* (see details in Fig. 6.11).

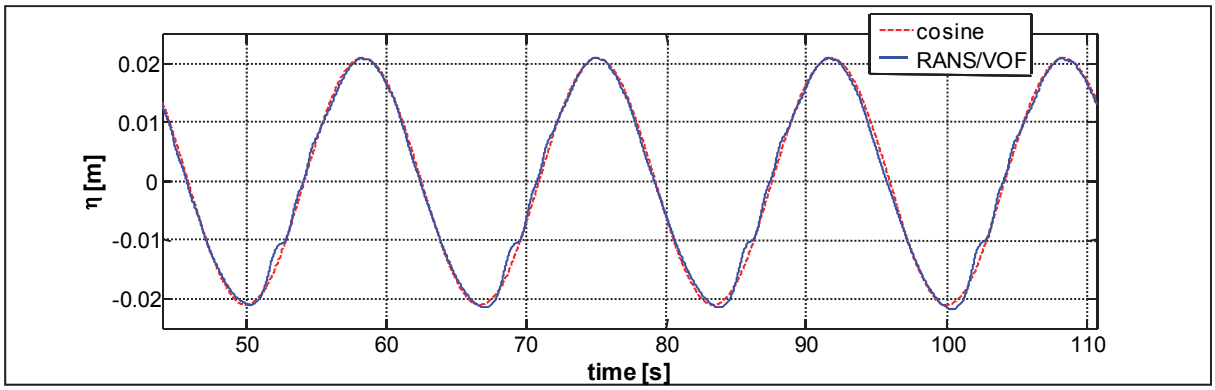

Fig. 6.11: Time series (blue curve) recorded at a numerical gauge at *x=37.08m* (black dashed line in Fig. 6.10) in the simulation of the propagation of the periodic initial train of solitons (see Fig. 6.9), and a cosine function from Airy theory which is calculated with the incident wave parameters (red dashed curve).

6.1.4 Comparative analysis of long-period cosine waves in shallow-water using different analysis methods

The approximately cosine-shaped data (see Fig. 6.11) from the numerical simulations in Fig. 6.9 and Fig. 6.10 is analysed using the conventional Fourier transform (FFT), the wavelet transform (WT) and the Hilbert-Huang transform (HHT). The FFT, WT and HHT analysis results are given in Fig. 6.12.

The main difference between the conventional analysis methods FFT, WT and HHT and the nonlinear KdV-NLFT is that the water depth is only considered in the algorithm of the latter

method. The comparison of the nonlinear spectra in Fig. 6.5a and Fig. 6.6 which show the results of the KdV-NLFT for exactly the same data, but different water depths outlines the considerable influence of the water depth on the analysis result. FFT, WT and HHT do not consider the water depth and therefore cannot identify nonlinear shallow-water wave or related processes within the analysed data. The results of the application of the conventional analysis methods to the numerical transient long-period cosine-shaped wave (blue curve) from Fig. 6.11 are plotted in Fig. 6.12.

The first plot in Fig. 6.12a shows the conventional FFT frequency-amplitude spectrum. The main peak is correctly determined at $f=0.06Hz$ with $a=0.021m$. Significant amplitudes at higher-harmonic frequencies are not observed. The highest higher-order amplitude is determined for $f=0.18Hz$ with a very small amplitude of only $a=0.0006m$. Therefore, the FFT identifies the analysed data as an Airy wave with $H=0.042m$ and $T=16.67s$.

The plot in Fig. 6.12b presents the time-frequency spectrum of the WT with the wavelet coefficients plotted as colour contours. The plot shows the main frequency at $f=0.06Hz$ and a second component around $f=0.18Hz$, but with very small coefficients. Like the FFT, the wavelet spectrogram provides the characteristics of a linear wave with $T=16.67s$ and small higher-harmonic disturbance.

The plot in Fig. 6.12c shows the HHT time-frequency spectrum with the amplitudes as colour contour. This spectrum shows frequency components around $f=0.06Hz$ and additional components at lower frequencies, but no higher-order waves. Therefore, this HHT result confirms the results obtained from FFT and WT.

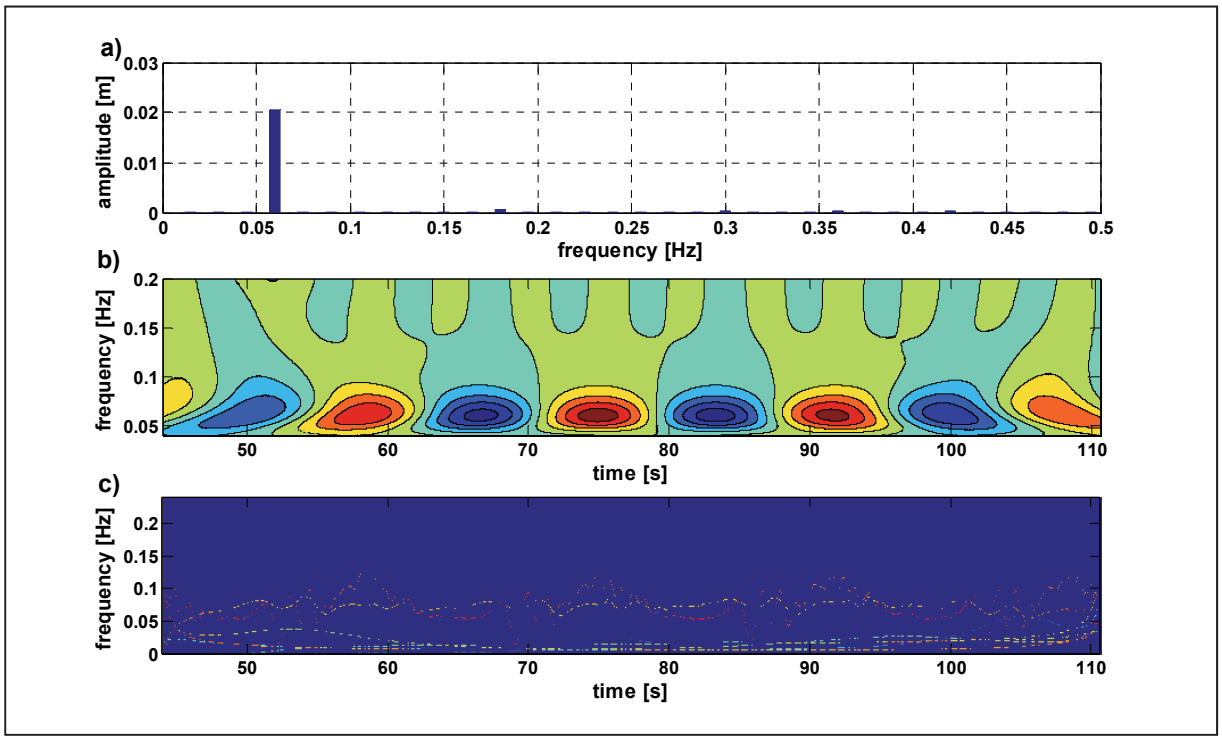

Fig. 6.12: Results of the application of the conventional analysis methods to the time series in Fig. 6.11; a) the FFT amplitude-frequency spectrum, b) the WT time-frequency spectrogram with the wavelet coefficients as colour contour and c) the HHT time-frequency spectrum with the amplitudes as colour contour.

The results from FFT, WT and HHT indicate that the analysed signal is a nearly linear cosine wave. Neither FFT, WT nor HHT provide any hint on the cosine wave's transient character or the underlying solitons that created the cosine-shaped free surface. However, the results of the numerical simulations in Fig. 6.9 show that this wave in fact is generated from solitons, and that it is a transient wave that can only be observed at a specific location in the flume for a specific combination of the soliton phases in the centre of the soliton overtaking process.

To provide a final proof for the reliability of the KdV-NLFT, the result of the nonlinear KdV-NLFT analysis of the blue curve in Fig. 6.11 is given in Fig. 6.13. Again, the nonlinear spectrum is soliton-dominated and contains eleven solitons and only insignificant oscillatory wave amplitudes, exactly as in the results of the experimental initial cosine-shaped wave in Fig. 6.5a. The results clearly confirm that the generated long-period cosine wave in Fig. 6.4a, the train of solitons in Fig. 6.4b and the transient cosine-shaped wave in Fig. 6.11 are regarded by the KdV-NFLT to be composed *by the same* soliton basic components. This result was already shown by the numerical simulations in Fig. 6.7 and Fig. 6.9, but now the reliability of the KdV-NLFT and the explanation of transient long-period shallow-water waves are proved.

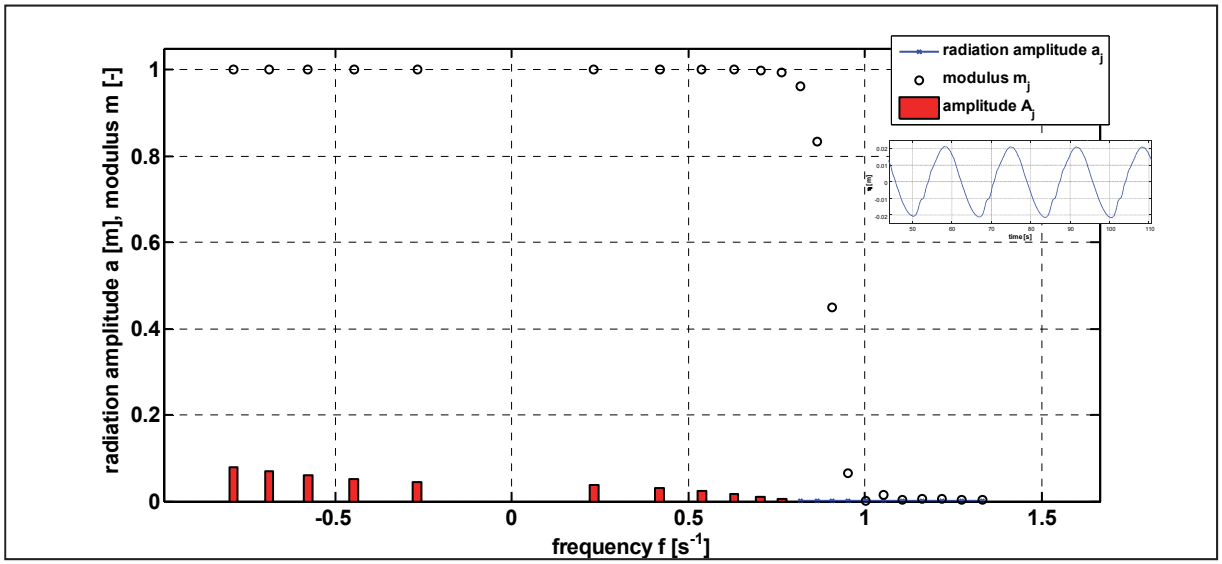

Fig. 6.13: Nonlinear amplitude-frequency spectrum from the KdV-NFLT analysis of the numerical time series (blue curve) in Fig. 6.11.

6.1.5 Summary and implications for future analyses

The analyses in the previous sections have shown that long-period cosine waves in very shallow water have to be regarded as transient waves that are composed by solitons. In numerical simulations with a couple of overtaking solitons it could be shown, that periodic trains of solitons can indeed generate periodic transient long-period cosine waves. At least for two reasons, the conventional analysis methods FFT, WT and HHT are not able to determine this transient character and the underlying nonlinear spectral basic components: (i) they are not based on shallow-water wave theories and (ii) they do not consider the water depth during the analysis algorithms and therefore cannot use adaptive wave components for the decomposition of the signal. In contrast, the KdV-NLFT is based on the Korteweg-deVries equation that describes the propagation of waves in shallow water. Therefore, the spectral basic components always are physical shallow-water waves. Furthermore, the spectral cnoidal basic com-

ponents are adaptive with respect to the actual water depth and the nonlinear wave-wave interactions between the nonlinear wave components are considered in the analysis algorithm.

The implication of these results is that each wave form in shallow-water which is not a solution of the KdV equation for the given boundary conditions is a transient wave that will disintegrate into two or more waves that are solutions of the KdV equation. As shown in the long-period cosine wave example, depending on the nonlinear character of the underlying basic components and due to the nonlinear interactions the shape of the free surface can change significantly (e.g. from a cosine wave to a bore-like very steep wave and finally to a train of solitons).

Wave forms that are not solutions of the KdV equation can be observed when (i) waves are generated in shallow water or (ii) the water depth changes. When waves are generated in shallow water that are not solutions of the KdV equation, e.g. by paddles in flumes or by swell and surge effects, then the initial wave form will change its shape after it started propagation. The underlying cnoidal waves propagate as stable waves and in the far-field the basic cnoidal components are revealed. Note that due to nonlinear wave-wave interaction these cnoidal waves might not be easily observed in the data. If these stable cnoidal waves enter areas with different water depth, then the boundary conditions change. Then these former stable waves are not longer solutions to the KdV equation in the new water depth and therefore they are not stable anymore, they become dispersive and disintegrate into new solutions of the KdV equation for the new water depth. This means at each change in the water depth a former stable wave becomes transient and disintegrates into two or more new waves. For both cases, waves that are generated in improper water depths and waves that enter shallow water depths, applies that the higher the discrepancy between the initial shape and a stable solution to the KdV equation the higher the number of these new waves.

If the example of the transient long-period cosine waves is transferred to other waves in shallow water, then we can assume that it should be possible to generate *any non-breaking wave in shallow water* as a transient wave at any arbitrary position by the nonlinear superposition of cnoidal waves. The implication for practical application is that by application of the KdV-NLFT the generation of target waves in flumes and basins can be simplified. This means not the simplification of the mathematical approach that is required to calculate the required waves. In fact, by application of the KdV-NLFT the required wave at the wave generator can be determined which, after propagation and nonlinear dispersion provides the target wave at the desired position in the flume or the basin. Therefore, systematic future simulations, hydraulic model tests and nonlinear KdV-NLFT analyses should be executed in order to better understand the process of nonlinear disintegration and generation of the transient waves.

6.2 Analysis of long-period primary ship waves using the KdV-NLFT

In a research project at Leichtweiß-Institute for Hydraulic Engineering and Water Resources (LWI), Department of Hydromechanics and Coastal Engineering, on behalf of the Federal Waterways Engineering and Research Institute (Bundesanstalt für Wasserbau, BAW, Hamburg) ship wave data from hydraulic model tests and field measurements in rivers and estuaries were analysed to determine characteristics of long-period primary waves and short-period secondary waves. The analyses at LWI were performed with the conventional Fourier transform (FFT) and the Hilbert-Huang transform (HHT). Since the primary ship waves in rivers

and estuaries are shallow-water waves, selected data were analysed within this thesis for test purposes using the nonlinear KdV-NLFT. The results presented here are promising. Moreover, they present another impressive example of how the application of the KdV-NLFT to shallow-water wave problems can lead to a new understanding of the nature and propagation of waves.

6.2.1 Theoretical background

A ship causes disturbances and flows when moving through the free water surface within a channel or a river. The water in front of the ship is displaced and moves around the ship to fill the gap behind the body of the ship. The generated ship wake field is three-dimensional and is composed by different wave components.

In Fig. 6.14, a two-dimensional cut through a typical schematic wave field caused by a ship in a river passage is shown. In narrow channels and estuaries ('canal conditions') a solitary wave (not shown in the figure) can occur in front of the actual wave field. Right in front of the ship the bow wave is caused by the displacement of water directly at the bow of the ship. Due to Bernoulli effects around the ship in a narrow channel or river, a long-period water level depression (drawdown) occurs besides the ship. Directly behind the ship the stern wave occurs. Short-period secondary waves are riding on this latter (primary) wave. The long-period primary wave system consists of the bow wave, the depression and the stern wave (which is also denoted as primary wave). The height of the primary wave is defined as the vertical distance between the deepest point of the drawdown and the crest of the stern wave. The primary wave system is bound to the ship and travels with the ship's speed in direction of the ship. The wave components of the primary wave system do not propagate as free waves. In contrast, secondary waves are free waves as soon as they detach from the shoulders and curvatures of the ship hull. They travel with an angle of 19.47° with respect to the heading (Kelvin angle). For practical purposes such as the pre-processing and filtering of measured data the primary wave fields are assumed within the following analyses to consist of wave components with $f \leq 0.067Hz$ (filter period $T=15.0s$).

Due to their long periods and the small water depths in rivers and estuaries, primary ship waves are shallow-water waves. Unlike to normal free waves they are bound to the ship and propagate with ship speed. Nevertheless, since they are shallow-water waves they are within the limit of validity of the KdV equation and therefore can be analysed using the KdV-NLFT.

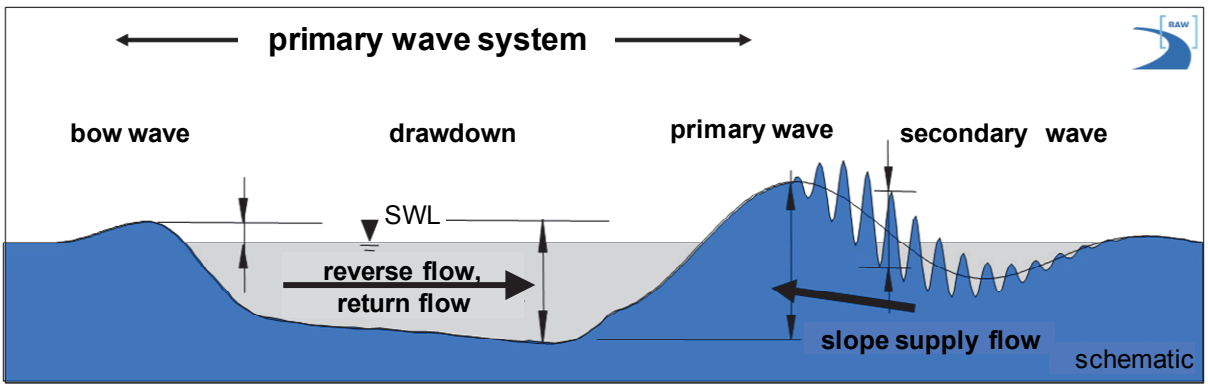

Fig. 6.14: Schematic representation of ship-induced wave and flow characteristics in river passages (after BAW, 2012).

6.2.2 KdV-NLFT analysis of long-period primary ship waves

Within the framework of this thesis and the research project mentioned above, the KdV-NLFT was, for test purposes, applied to selected ship wave signals. Later Sopper (2012confirmed in a feasibility study these first results that are presented here.

As a typical example of a ship wave pattern, the ship wave in Fig. 6.15 is selected. The data were measured in hydraulic model tests with a ship moving independently through a channel. The curve in Fig. 6.15 shows the bow wave around $t=360s$, the drawdown from $t=370s$ to $t=410s$, the stern wave around $t=415s$ and the short-period secondary waves from $t=420s$ to $t=440s$. The water depth in the test is $h=18.0m$ and the ship speed is $v_s=15.4kn$. All values are given in prototype scale, although the model tests were performed with a scale 1:40.

The nonlinear KdV-NLFT spectrum of the ship wave in Fig. 6.15 is presented in Fig. 6.16. Similar to the nonlinear spectra in section 6.1 the large number of soliton amplitudes (red bars) in the soliton spectrum on the left side of the nonlinear spectrum shows that this long-period shallow-water primary ship wave is soliton-dominated. The soliton spectrum shows a characteristic curvature in the development of the rank-ordered soliton amplitudes that seems to be typical for the analysed primary waves. Without the previous results of the nonlinear analysis of the long-period cosine waves in section 6.1, these results might be surprising. As stated in section 6.1.5, long-period waves (such as the primary ship wave) in shallow-water are not solutions to the KdV equations and therefore disperse into waves that are solutions to the KdV equation. Since the ship wave period is very long compared with the small water depth ($T\approx100s$, $h=16m$, $L\approx1250m$, $h/L\approx0.013$), solitons evidently seem to be the suitable basic components for the nonlinear decomposition in the KdV-NLFT. In contrast to the transient cosine-shaped waves in the previous section, the primary ship waves do *not* propagate as free waves. Therefore, future analyses have to show the implication of this fact on the propagation of this type of waves. Most probably, an approach of phase-locked solitons and oscillatory cnoidal waves has to be established for the calculation of the propagation of the ship-locked primary wave field, similarly to the approach of phase-locked harmonics in the FFT analysis of nonlinear waves.

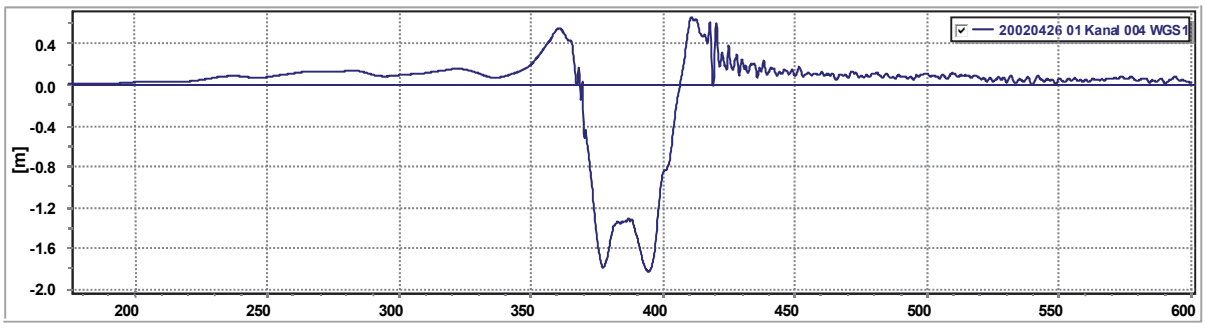

Fig. 6.15: Ship wave from hydraulic model test at BAW, Hamburg, at $x=39m$ (prototype scale).

The spectrum in Fig. 6.16 does not only show solitons, but also cnoidal-like, Stokes-like and Airy-like wave components. Since the original wave form is more complex than the simple cosine wave and also contains short-period secondary waves, it cannot be reproduced just by solitons and their interactions. Additional oscillatory waves with different frequencies, ampli-

tudes and nonlinearities as well as their nonlinear interactions are necessary to return the original data from Fig. 6.15.

For the reconstruction of the data and the propagation of the basic components in time and space, the limits of the validity of the KdV equation have to be considered. The waves with $kh<1.36$ are within these limits and therefore can be computed using the KdV equation. For those components with shorter periods, higher wave numbers and shorter wave lengths ($kh>1.36$) the given relative water depth is intermediate or deep water. They do not obey the KdV equation, but have to be computed using the nonlinear Schroedinger (NLS) equation (see section 2.2.3).

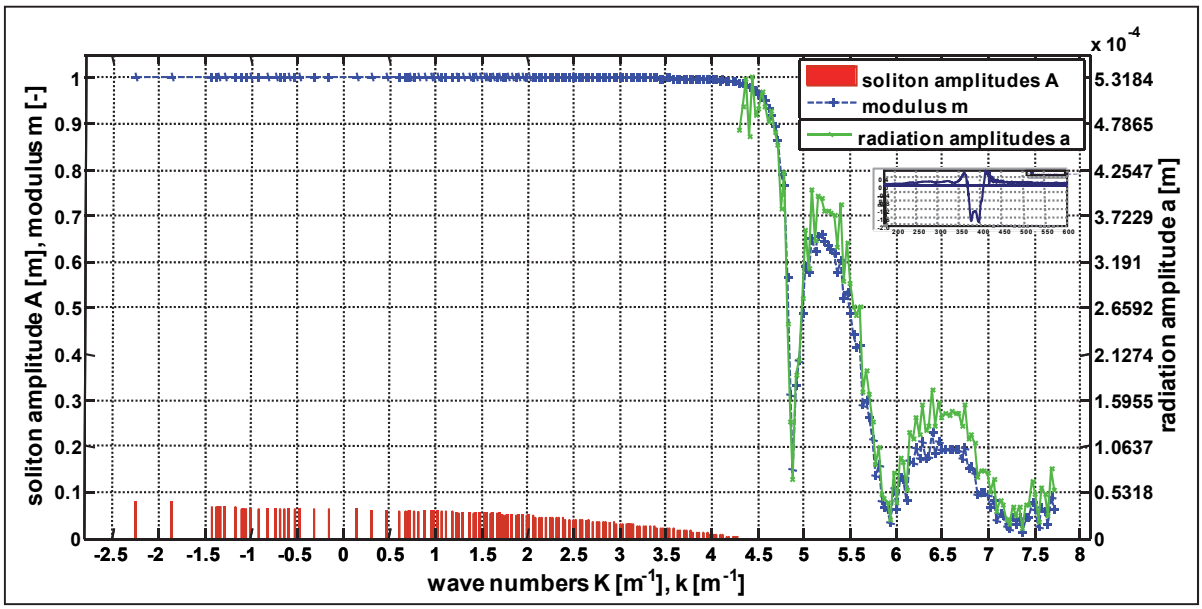

Fig. 6.16: Nonlinear spectrum of the ship wave in Fig. 6.15.

6.2.3 Summary and implications for future analyses

Primary ship waves in channels or rivers which are long-period shallow-water waves and which are, therefore, within the limit of the KdV equation ($kh<1.36$) can be analysed using the KdV-NLFT. The nonlinear spectrum of selected ship waves shows that the primary wave is soliton dominated. This approach leads to a completely new understanding of the transient structure of primary ship wave fields in shallow-water. Although surprising on the first view, these results correspond to the results and conclusions of the KdV-NLFT analysis of long-period cosine waves in shallow-water drawn in section 6.1.5. The long-period primary ship waves are regarded to be dispersive transient waves composed by solitons, oscillatory cnoidal waves and their nonlinear wave-wave interactions.

In contrast to free long cosine waves, the primary ship waves are bound to the ship and cannot propagate freely. Therefore, further systematic studies are required to analyse the effect of this boundary condition on the propagation, dispersion and transformation of the primary ship wake field as well as the implications for the KdV-NLFT analyses and the interpretations of the results. Most probably an approach of phase-locked solitons and oscillatory waves has to be developed to allow the temporal and spatial evolution of the primary wave without dispersion effects that do not occur in the real world. Furthermore, the interactions between the

KdV-governed long waves and solitons from KdV-NLFT and the NLS-governed short waves from NLS-NLFT and their influence on the wake field should be investigated in detail. The results will show if separate calculations for the KdV and NLS components are possible or if a joint analysis and simulation approach has be developed, implemented and applied. Furthermore, ship waves form complex three-dimensional wake fields that cannot be exactly described by two-dimensional analysis methods. The application of the Kadomtsev-Petviashvili (KP) for shallow water (KP-NLFT) and the Davey-Stewartson (DS) equation for deep water (DS-NLFT) (see section 2.2) might present possible approaches to this problem.

6.3 Summary and possible further applications

In the previous sections, two selected examples for shallow-water water and coastal wave problems are given in which the application of the KdV-NLFT clearly proved its superiority over the conventional analysis methods Fourier, wavelet and Hilbert-Huang transform. In shallow-water, the waves become strongly nonlinear so that the influence of the nonlinear wave-wave interactions is increasing with decreasing water depth. Consequently, in the examples the shape of the free surface in shallow-water is dominated by the nonlinear interactions. The conventional analysis methods cannot consider these interactions and they cannot identify or adapt the spectral physical basic components to the actual water depth in order to provide physical correct basic components. In the implemented KdV-NLFT the water depth is explicitly considered and the cnoidal waves for the decomposition are adapted to the water depth. Furthermore, the KdV-NLFT is able to consider the nonlinear wave-wave interactions and allows a new insight into the inner spectral structure of transient long-period waves in shallow waters.

The most important results of the presented analyses are that the KdV-NLFT is able to identify the underlying cnoidal waves even if they are completely hidden and that the KdV-NLFT is able to predict the dispersion of these transient initial waves without the need for numerical simulations or experimental model tests. The implication of the propagation of long-period cosine waves into trains of solitons is that each wave form in shallow water that is not a solution of the KdV equation has to be considered to be a transient, instable wave that disperses into stable KdV solutions. As can be seen in the long-period cosine wave example, the shape of the free surface can be strongly depending on the phases of the cnoidal wave, e.g. the cosine wave that disintegrates into a train of solitons. Waves which are not solutions of the KdV equations occur when waves are generated by external forces like wind, dropping objects, moving bottoms, swell and surge effects. While evolving in time and space, the underlying nonlinear cnoidal waves propagate as free waves with their own celebrities and nonlinear wave dispersion occurs. If these stable cnoidal waves enter areas with different water depth, they become transient waves themselves that show further dispersion.

Possible practical future applications for the KdV-NLFT are:

(i) The calculation of nonlinear wave propagation from one position to another by identifying the cnoidal basic components at position and/or time A, evolution of each of the cnoidal waves in time and space until position and/or time B and then superposing the evolved cnoidal waves nonlinearly by calculation of the nonlinear interactions. This provides the free surface at positions B, including all the nonlinear components and interactions.

(ii) The generation of non-dispersive waves in hydraulic model tests in flumes and basins by application of the KdV equation. If the generated waves are solutions to the KdV equation, then no dispersion occurs.

(iii) Generation of specific nonlinear wave types in hydraulic shallow-water models like long-period primary ship waves, focussed waves or long-period waves at specified positions in flumes or basins. If the desired nonlinear waves cannot be obtained at the specified position by linear methods, then the spectral nonlinear components can be generated and evolved with different phases so that the nonlinear superposition in the inverse KdV-NLFT provides the desired transient nonlinear waves at the specified position.

This list of possible applications is not final but helps to give few first indications of the enormous potential of the application of the KdV-NLFT to shallow water problems in coastal engineering.

7 Summary, conclusions, recommendations and outlook

In coastal engineering, the conventional linear fast Fourier transform (FFT) has been established as the standard method for data analysis in the frequency domain. This technique was originally developed for the analysis of original linear and stationary data that is composed of linear sinusoidal wave components. Nevertheless, in daily practice this method is applied to all kind of data from field measurements, hydraulic model tests or numerical simulations. For many applications, the results are within engineering accuracy. For other applications we have learned how to interpret the results of the linear FFT correctly, e.g. in case of higher harmonics in the linear spectrum of nonlinear Stoked waves. Furthermore, approaches have been developed in order to deal with "contradictions" that arose from the results of the conventional FFT. A descriptive example is the assumption of phase-locked or bound higher-harmonic waves to dissolve the contradiction between the physical non-dispersive propagation of Stokes waves in flumes and their (free) higher-harmonic wave components in the linear spectrum. Finally, there are some shallow-water problems that are caused by highly nonlinear processes that cannot be determined or explained by the conventional FFT. Therefore, special method are required that explicitly consider these nonlinear properties of wave propagation processes in shallow water.

In this study, the non-conventional nonlinear Fourier transform based on the Korteweg-deVries equation (KdV-NLFT) is introduced into coastal engineering as a new analysis method for shallow-water wave problems. The KdV-NLFT was already applied in mathematics and physics as an *inverse scattering transform (IST)* for the solutions of the partial differential KdV equations. Unfortunately, the publications of the description of the method and its applications includes too much complicated mathematics, and are thus generally hardly understandable for coastal engineers. Therefore, one of the most important and time-consuming tasks was to 'translate' the concept of the KdV-NLFT in the terminology of coastal engineers. Mathematicians and physicians may feel uncomfortable with some of the descriptions and explanations given in this thesis or may find them trivial. The author's experience in the coastal engineering community has shown that, in fact, they are neither trivial nor unnecessary for civil and coastal engineers.

Once having translated the underlying mathematical theory of the IST, the thesis focused on the following issues: (i) the numerical implementation and validation of the KdV-based nonlinear Fourier transform (KdV-NLFT) as a non-conventional analysis method for coastal engineering problems, (ii) the practical application of the KdV-NLFT exemplarily to some selected shallow-water wave problems, (iii) a comparative analysis using the KdV-NLFT and the conventional frequency and time-frequency analysis methods fast Fourier Transform (FFT) and Hilbert-Huang transform (HHT).

Based on the results of the implementation and validation of the KdV-NLFT, those of the practical applications and the comparative analyses, recommendations are given for the practical application of the KdV-NFLT and the conventional methods FFT and HHT. Therefore, in the following sections, the main results are *first* summarized and conclusions are drawn. *Second*, comments and remarks on the applicability and the limitations of the implemented

KdV-NLFT are given. *Finally*, recommendations for the most important tasks for future research are given.

7.1 Summary of main results and conclusions

7.1.1 Numerical implementation and validation of the KdV-based nonlinear Fourier transform (KdV-NLFT)

In this study, the direct and inverse scattering transforms (DST and IST) is implemented numerically in a MATLAB code. Since DST and IST can be regarded as generalized direct and inverse Fourier transforms and since the IST is applied for solving the partial differential Korteweg-deVries (KdV) equation, the implemented analysis is denoted as KdV-NLFT.

The KdV equation describes the propagation of waves in shallow water with $kh<1.36$. The KdV-NLFT can be regarded as an extension of the conventional fast Fourier transform (FFT) in a cnoidal basis. Instead of linear cosine waves, the KdV-NLFT uses nonlinear cnoidal waves for the nonlinear decomposition of the original data. In coastal engineering, cnoidal waves typically are used only within the so-called cnoidal wave theory for the description of highly nonlinear waves. The complete range of linear and nonlinear waves in coastal engineering can be covered by successive application (with increasing nonlinearity of the wave) of the Airy, the Stokes, the cnoidal and finally the solitary wave theory. Appropriate diagrams are available that give the best-fit wave theories as functions of water depth, wave height and wave period or wave length. In the KdV-NLFT, a more generalized definition of cnoidal waves is applied. In mathematics and physics, the cnoidal wave equation, which is an exact solution of the KdV equation, is applied to generate these four different types of waves in shallow water by applying just one equation. Cnoidal waves are defined by wave height, wave period or wave length, water depth and a nonlinearity parameter called modulus m. For the modulus being zero ($m=0$), the cnoidal wave equation provides waves that are equal to linear Airy waves. These cnoidal linear-like waves are denoted in this study as Airy-like waves. Up to a modulus of about $0<m<0.45$ the cnoidal waves are nearly linear and therefore are denoted as Airy-like. For a higher modulus up to about $0.45<m<0.95$ the cnoidal waves look like Stokes-theory waves and are denoted as Stokes-like waves. They are followed by cnoidal-like waves for a modulus up to $0.95<m<0.99$ and finally by solitary-like waves for even a higher modulus $m\geq0.99$.

For mathematicians and physicists this definition of *-like* waves might seem unnecessary. For coastal engineers that have grown up with the aforementioned four-category wave theory toolbox, this step is decisive to understand the real potential of the cnoidal wave equation. This *one cnoidal wave equation* can be applied to generate all *four* wave types that can physically occur in shallow water. Coastal engineers are generally taught that they need four different categorized wave theories, not just *one equation*. Furthermore, for coastal engineers the cnoidal wave theory is just one of these four approaches and is just used to fill the gap between weakly Stokes waves and extremely nonlinear solitary waves. Most probably, most coastal engineers never used the cnoidal wave theory, but applied numerical approaches such as the stream function theory. To overcome these restrictions in thinking, the term *cnoidal wave equation* is used in this thesis instead of the limiting term *cnoidal wave theory*.

Once the cnoidal wave equation is accepted to be sufficient to generate Airy-like, Stokes-like, cnoidal-like and solitary-like waves, the nonlinear mutual wave-wave interactions between the nonlinear waves have to be considered. Every time when nonlinear waves are superposed physically, then nonlinear wave-wave interactions occur that may significantly modify the shape of the free surface. If the cnoidal wave equation is written in terms of Jacobi θ-functions, then it is very easy to automatically obtain the nonlinear interaction by simple application of the Riemann Θ-functions. In theory, this fact seems trivial, but the numerical implementation is very complex and codes were not available. For the application of the KdV-NLFT within this study, the algorithms were successfully programmed 'from scratch' by numerical implementation of approaches and formulae that were available from publications on the IST and related topics. Now the nonlinear superposition of cnoidal waves and their nonlinear wave-wave interactions provides the correct free surface. This approach in general is called the inverse scattering transform. Since it is applied here to cnoidal waves which are solutions of the KdV equation, the procedure is denoted as inverse KdV-NLFT.

The next step is the implementation of the direct KdV-NLFT that decomposes a given signal into cnoidal waves as spectral basic components and their nonlinear wave-wave interactions. All determined basic components are cnoidal waves and, therefore, automatically solutions to the KdV equation. The shape and nonlinearity of each cnoidal wave can vary between linear Airy-like waves and extremely nonlinear soliton-like shape. Therefore, the KdV-NFLT is partly adaptive: the governing wave equation is pre-defined, but the nonlinear character of each cnoidal wave component is adaptive by variation of the modulus.

With the implemented direct and inverse KdV-NLFT a new method for the nonlinear analysis of nonlinear waves and nonlinear wave-wave interactions in shallow water is available. Although the IST is known for many decades and was improved and presented for the application to ocean surface waves in many publications by Alfred R. Osborne since the 1980's, it has not been used in coastal engineering at all since then. The main reasons surely are the mathematical complexity and the required computer power. The latter problem was solved in the last years by developments in computer hardware and techniques. The first problem is still present and will further persist in the future. In this study, the attempt is made to translate the mathematical and physical descriptions of the IST into the language of civil and coastal engineers and to establish it for the analysis of nonlinear wave problems in shallow water. The denotation KdV-NLFT is selected to illustrate the large similarities between the conventional FFT and the nonlinear Fourier transform that can easily be regarded to be a general extension of the FFT. The main differences between FFT and KdV-NLFT are the nonlinear spectral basis for the decomposition and hence the consideration of the nonlinear interactions. The main features like the decomposition of the signal into spectral components, the reconstruction of the original data by superposition of the basic components, the representation of the analysis results in amplitude-frequency and phase-frequency spectra are nearly identical to those of the conventional FFT. In case of only linear sinusoidal components in the original data and therefore no occurrence of nonlinear interactions, the results of the nonlinear KdV-NLFT reduce to the same as would be obtained from the conventional linear FFT. The denotation *NLFT* helps to bring out these similarities and to understand the KdV-NLFT approach.

7.1.2 Comparative analysis of cnoidal waves using the KdV-NLFT and the conventional methods FFT and HHT

The comparative analyses using the KdV-NFLT, the conventional fast Fourier transform (FFT) and the Hilbert-Huang transform (HHT) that are performed in this study that can be categorized as follows: (i) analysis of general spectral properties of cnoidal waves and (ii) comparative analyses of selected shallow-water wave problems. The results of (i) are discussed here, the results of the latter analyses are discussed in the next section.

The analysis of cnoidal waves using the KdV-NFLT, the conventional FFT and the HHT shows how the spectral basic components of the KdV-NLFT are represented in the different analysis methods. A cnoidal wave is generated by the cnoidal wave equation. By selecting one set of variables (amplitude, water depth and modulus as nonlinearity parameter) it contains of only one basic wave component. Therefore, a single cnoidal wave is determined in KdV-NLFT as only one wave. Nonlinear waves show specific characteristics such as narrower, higher crests and wider, shallower troughs than a linear wave with the same wave parameters. With further increasing nonlinearity, cnoidal waves finally end up in solitons.

The application of the conventional FFT to the cnoidal waves shows that the increasing nonlinearity in the original data is covered by an increasing number of higher-harmonic cosine components with increasing amplitudes. The higher the modulus of a cnoidal wave, the more cosine waves are required to return the original data. Even solitons can be generated by linear superposition of a large number of cosine waves. In the HHT, the nonlinear waves are considered to be nonlinear oscillation modes (IMFs). They are not decomposed into theory-based spectral basic components such as Airy, Stokes, cnoidal or solitary waves. It could be shown that the degree of nonlinearity DN that is proposed by Prof. Norden E. Huang to classify the nonlinear character of waves within the HHT approach is a logarithmic function of the Riemann matrix components B_{11} that represents the nonlinearity of the cnoidal waves. This relation might be used in future analyses to classify the cnoidal waves and to determine their modulus simply by determination of the degree of nonlinearity (DN).

7.1.3 Practical application of the KdV-NLFT to selected shallow-water wave problems and comparative analyses using FFT and HHT

The implemented KdV-NLFT was applied exemplarily to the following shallow-water wave problems: (i) the spectral analysis of soliton fission over and behind submerged reefs, (ii) the wave transformation in flumes and around submerged reefs and (iii) the propagation of long-period waves in very shallow water. Furthermore, a short example shows how long-period primary ship waves are represented in the KdV-NLFT.

The most important conclusion of the different analysis results is that all examined processes can be traced back to the same phenomenon: *Long waves in shallow water are transient dispersive waves.* Wave transformation is caused by dispersion effects and phase-depending changes of the nonlinear wave-wave interaction. The KdV-NLFT has proved to be able (i) to correctly predict the number and properties of the nonlinear cnoidal basic components, (ii) to analytically calculate the evolution of these components in time and space without the need for numerical simulations and (iii) to consider the water depth as a very important governing parameter on the analysis results.

The propagation of waves in shallow water with $kh<1.36$ is governed by the KdV equation. Cnoidal waves are solutions to this equation. Therefore, they are stable waves in shallow water and propagate in constant depth in time and space without changes in shape (if energy dissipation is neglected). Water waves or wave packages that are *not* solutions to the KdV equation are *not* stable waves but are *transient waves* that are composed by two or more other basic components *and* their nonlinear interactions. The 'toolbox' of waves that are stable in a given water depth and that are available for the reconstruction of the original data in the KdV-NLFT is strongly dependent on this water depth. Each surface shape that is not a solution of the KdV equation disperses into its underlying stable basic components which can be soliton-like (in very shallow water) and harmonic oscillatory cnoidal waves. Each of these cnoidal waves propagates as free wave with its own celerity and emerges from collision and overtaking processes without changes in the wave properties (except the phase shift after overtaking processes of solitons). This is the most important reason why long waves propagation in shallow water generates secondary wave crests (harmonic generation). Strictly speaking, these secondary crests are not *generated* during the wave propagation. They already exist right from the beginning as higher-order wave components that are part of the transient wave, but they are hidden by the superposed nonlinear interaction modes. Due to dispersion the crests of these higher-harmonic waves become visible. At the same time, the phase-dependent nonlinear interactions change and do not cover the formerly hidden crests any longer. In the literature it was shown that harmonic generation is not observed in KdV-NLFT analyses. This could be confirmed by means of KdV-NLFT analyses of numerical simulation data. Harmonic generation is shown to be not a strictly physical phenomenon but rather a consequence of the inability of the conventional linear FFT to consider the nonlinearity of the true shallow-water waves and their nonlinear interactions.

The assumption of transient long waves in shallow water provides the explanation to soliton fission over and behind submerged reefs, to the problem of harmonic generation, to the transformation of periodic oscillatory waves around submerged reefs and to the decomposition of long-period waves in shallow water. In each of these cases, a transient wave or wave package is the reason for wave transformation processes.

In case of harmonic generation, a wave is generated that is inappropriate for the given water depth. Therefore, this wave is subject to nonlinear dispersion.

In case of soliton fission over a submerged reef, a stable solitary-like cnoidal wave propagates onto a submerged reef. Now the water depth has changed and the formerly stable wave is now - due to the change of water depth - a transient wave over the reef. In very shallow water, this transient wave disintegrates into solitons and short-period oscillatory waves because these components are solutions to the KdV equation in this very shallow water depth. If the water depth over the reef is larger, then no solitons are generated and the initial soliton disperses into oscillatory waves. So soliton fission is just a special case of dispersion of long-period solitons in shallow water. Note that additionally, two other effects may occur at the same time. Due to wave reflection at the reef front, the wave shape of the transmitted incident soliton changes. Both reflected and transmitted waves have to adapt to the new conditions so that dispersion effects may occur. In shallow water depths over the reef, the initial soliton breaks and generates a water package that propagates over the reef. Again, this package is not a solution of the KdV equation and therefore disintegrates into solitons and/or oscillatory waves.

Finally, the KdV-NFLT is applied to the problem of long-period wave propagation in very shallow water. The results show that the phenomena that are observed can be categorized as a special case of harmonic generation or of soliton fission. The initial long cosine wave again is not a solution of the KdV equation and therefore disperses. Due to the small water depths, the 'toolbox' of the KdV-NLFT contains only solitons and very short-period waves. Hence, the long sine wave disperses into a train of solitons, exactly as observed for the bore disintegration in soliton fission.

The given examples of transient wave dispersion in shallow water are very good examples for clear answers to the initial questions from the motivation of this study: *If different methods provide different spectral representations, do these representations provide different results? And if the analysis results differ, how does that affect our understanding and interpretation of the physical processes?*

The answer is: *Yes, the interpretation of different types of spectra provides strongly different results and conclusion. The transient character of long-period waves in shallow water cannot be determined by application of FFT and HHT. Furthermore, the application of FFT leads to misinterpretations such as the effect of harmonic generation and unnecessary approaches such as the phase-locked or bound harmonics which are not required in the KdV-NLFT representation of nonlinear waves.*

7.2 Applicability and limitations of the implemented KdV-NLFT

The KdV-NLFT is implemented within this study on the basis of the available publications. Unfortunately, not all relevant details have been published, so that some general or specific problems still have not been completely solved. All results of the direct or inverse KdV-NLFT within study are - unless otherwise noted - determined with the implemented algorithms. The code has proofed its ability for qualitative analyses, and in most cases also for quantitative reliability. Within the last years, the direct KdV-NLFT has been applied successfully for synthetically generated signals, data from hydraulic model tests and field measurements. Nevertheless, the numerical existing code for the implementation of the inverse KdV-NLFT has to be significantly improved in the future. Especially the calculation of the cnoidal wave phases for solitons and of the calculation of the Riemann Θ-functions for long signals still represent serious problems that have to be solved. Numerical limitations of the implemented code exist due to the enormous number of interaction terms that have to be calculated and superposed. These problems might be solved in the future by parallelized calculations and faster computers.

Besides the limitation of the current version of the implemented code or computer power, the KdV-NFLT has physical restrictions that have to be considered when this method is applied for data analysis. First, the KdV-NLFT provides the solution of the KdV equation which is valid for shallow water with $kh<1.36$. Within this relative limit the KdV-NLFT provide reliable results. Outside this limit, for $kh>1.36$, this method provides mathematical results that do not correctly consider the nonlinear properties of the surface waves. Within the given limit, the cnoidal waves and their nonlinear interactions are governed by the KdV equation. Therefore, any arbitrary surface shape is considered to be generated as a transient wave by superposition of cnoidal waves and nonlinear interactions. Outside the KdV limit, the wave propagation and the nonlinear interactions are governed by the nonlinear Schrödinger (NLS) equation.

In the NLS-NLFT (the nonlinear Fourier transform based on the NLS equation) the basic components are solutions to the NLS equation. These waves are oscillatory nonlinear waves in deeper water and therefore provide different nonlinear interactions such as group effects. The KdV-NLFT is not able to correctly consider these physical effects and therefore attempts to represent the original data my means of KdV-governed shallow-water waves and their shallow-water wave-wave interaction. Therefore, the results of the KdV-NLFT outside the given limit of validity will be mathematically correct, but without correct physical relevance.

The implemented KdV-NLFT is a two-dimensional analysis method for $\eta(x,t)$, just as the NLS-NLFT is for deeper water. For the analysis of three-dimensional waves $\eta(x,y,t)$ in shallow water the inverse scattering transform of the Kadomtsev-Pethviashvili (KP) equation has to be implemented (denoted as KP-NLFT), for deeper water the Davey-Stewartson (DS) equation (denoted as DS-NLFT). Furthermore, the KdV-NLFT does not consider wave breaking.

7.3 Future research issues

This study has significantly improved the available knowledge on the nonlinear properties, analysis and propagation of surface waves in shallow water. Within this study, the KdV-NLFT was implemented for the first time for the application in civil and coastal engineering. The new method has proved to be a powerful analysis tool that shed light on different problems in coastal engineering that were disposed in general as *nonlinear effects* because the existing conventional analysis methods were not sufficient to really provide the necessary insight in the underlying processes. This study is the very first step of introducing the nonlinear Fourier transform to the civil and coastal engineering community. It will take the role of a pioneer to explore and apply the KdV-NLFT to the various problems in the world of coastal and ocean engineering. Finally, appropriate problems have to be indentified for which the additional effort of the KdV-NLFT in comparison to the conventional FFT is justifiable due to the improved understanding of the underlying nonlinear processes.

The most important future research issues can be categorized in four groups: (i) improvement of the implemented code and the understanding of the analysis algorithms and procedures, (ii) comparative analysis of further coastal and shallow-water wave problems, (iii) systematic analysis of suitable coastal and shallow-water wave problems and (iv) introduction and dissemination of the method in order to establish it as a standard analysis method for future nonlinear water wave problems within the coastal engineering community.

First, for a more extensive improvement of the implemented code and the understanding of the analysis algorithms and procedures further comparative analysis with simple synthetic signal, single cnoidal waves and selected numerical and hydraulic model test data should be performed. Systematic parameter studies will lead to the definition of analysis parameters that will help to predefine internal parameter in order to optimize the KDV-NLFT procedures and accelerate the analyses. Future research has to validate and verify the implemented code and the applicability of the method itself to different classes of problems. Furthermore, the implemented code should be extended for three-dimensional wave data analysis using the KP-NLFT.

Second, selected coastal and shallow-water wave problems should be studied qualitatively and quantitatively in more detail and more systematically using the implemented KdV-NLFT as well as the conventional methods fast Fourier transform (FFT), wavelet transform (WT) and Hilbert-Huang transform (HHT) in order to demonstrate more clearly the advantages and limitations of the KdV-NLFT.

Third, the KdV-NLFT should be applied systematically to more candidate shallow-water wave problems in coastal engineering in order to better identify those applications for which this method provides significant improvements compared to the conventional approaches such as FFT and HHT. Once these applications are identified, further detailed studies should be performed on these problems.

Forth, the KdV-NLFT should be introduced and disseminated within the civil and coastal community. This method has proved within this study to be a promising tool for the analysis of nonlinear wave problems that has the potential to become the future standard analysis method for the analysis of nonlinear shallow-water wave problems. After solving the remaining numerical problems and after the successful performance of further systematic studies using the KdV-NLFT, this method should be actively promoted and disseminated by means of publications, conference presentation, compact courses, lectures and seminars.

References

Ablowitz, M.J.;Kaup, D.J.;Newell, A.C.; Segur, H. (1974): The Inverse Scattering Transform - Fourier Analysis for Nonlinear Problems. *Stud. Appl. Math.*, 53, 4, pp. 249-315.

Ablowitz, M.J.; Segur, H. (1981): Solitons and the Inverse Scattering Transform. Philadelphia: SIAM, 425 pp.

Airy, G.B. (1845): Tides and waves. *In: Smedley, E.;Rose, H.J.;Rose, H.J. (eds.): Encyclopaedia Metropolitana*, London, pp. 241-396.

BAW (2012): Schiffserzeugte langperiodische Belastung zur Bemessung der Deckschichten von Strombauwerken an Seeschifffahrtsstraßen, Glossar. Bundesanstalt für Wasserbau (BAW), Abt. Wasserbau im Küstenbereich, Referat Ästuarsysteme I (K2), Hamburg, 8 S.

Bleck, M. (2003): Hydraulische Wirksamkeit künstliche Riffe am Beispiel einer rechteckigen Strukur. Ph.D. thesis, *Dissertation, Fachbereich Bauingenieurwesen, Leichtweiß-Institut für Wasserbau, Technische Universität Braunschweig*, Braunschweig, Germany, 144 S.

Bleck, M.; Oumeraci, H. (2002): Hydraulic performance of artificial reefs: global and local description. *Proceedings 28th International Conference Coastal Engineering (ICCE)*, ASCE, Volume 2, Cardiff, U.K., pp. 1778-1790.

Boussinesq, J. (1871): Théorie de l'intumescence liquide appelée onde solitaire ou de translation, se propageant dans un canal rectangulaire. *Comptes rendus hebdomadaires des séances de l'Académie des sciences*, 72, pp. 755-759.

Boussinesq, J. (1872): Théorie des ondes et des remous qui se progagent le long d'un canal rectangulaire horizontal, en communiquant au liquide contenu dans ce canal des vitesses sensiblement pareilles de la surface au fond. *J. Math. Pures Appl.*, 17, pp. 55-108.

Brauer, K. (2004): The Korteweg-de Vries Equation: History, exact Solutions, and graphical representation. https://www.usf.uni-osnabrueck.de/uploads/media/KdV.pdf, 16 pp., last access: .

Bronstein, I.N.;Semendjajew, K.A.;Musiol, G.; Mühlig, H. (2001): Taschenbuch der Mathematik. Frankfurt am Main: Verlag Harri Deutsch, 5., überarbeitete und erweiterte Auflage.

Brorsen, M. (2007): Non-linear waves. Aalborg University, Department of Civil Engineering, 40 pp.

Brühl, M.; Oumeraci, H. (2010): Analysis of soliton fission over a submerged structure using 'Nonlinear Fourier Transform (NLFT)'. *Proceedings of the International Conference on Coastal Engineering (ICCE 2010), No. 32(2010)*, Paper #: waves.59, Shanghai, China, 12 pp. Retrieved from http://journals.tdl.org/ICCE/.

Brühl, M.; Oumeraci, H. (2011): Application of 'nonlinear Fourier transform (NLFT)' for the analysis of soliton fission behind submerged reefs with finite width. *Proceedings of the ASME 2011 30th International Conference on Ocean, Offshore and Arctic Engineering (OMAE 2011)*, OMAE2011-49668, June 19-24, 2011, Rotterdam, The Netherlands, 8 pp.

Brühl, M.; Oumeraci, H. (2012): Nonlinear decomposition of transmitted wave trains from soliton fission using "Nonlinear Fourier transform (NLFT)": The spectral basic components. *Proceedings of the ASME 2012 31st International Conference on Ocean, Offshore and Arctic Engineering (OMAE 2012)*, OMAE2012-83418, July 1-6, 2012, Rio de Janeiro, Brasil, 10 pp.

Camassa, R.; Holm, D. (1993): An integrable shallow water equation with peakon solitions. *Phys. Rev. Lett.*, 71, 1661-1664.

Camassa, R.; Holm, D. (1994): An new integrable shallow water equation. *Adv. Appl. Mech.*, 31, 1-33.

Christov, I. (2009): Internal solitary waves in the ocean: Analysis using the periodic, inverse scattering transform. *Mathematics and Computers in Simulation*, 80, (1), pp. 192-201.

Cohen, L. (1995): Time-Frequency Analysis. Englewood Cliffs, New Jersey, US: Prentice Hall PTR, 299 pp.

Dalrymple, R.A. (1974): A finite amplitude wave on a linear shear current. *J. Geophys. Res.*, Vol. 79, No. 30, pp. 4498-4504.

Dalrymple, R.A.; Cox, J.C. (1976): Symmetric finite amplitude rotational water waves. *J. Phys. Ocean.*, Vol. 6, No. 6.

Daubechies, I. (1992): Ten lectures on wavelets. Philadelphia, US: Society for industrial and applied mathematics, 357 pp.

Dean, R.G. (1965): Stream function representation of nonlinear ocean waves. *J. Geophys. Res.*, Vol. 70, No. 18, pp. 4561.4572.

Dean, R.G.; Dalrymple, R.A. (1991): Water Wave Mechanics for Engineers and Scientists. *Advanced Series on Ocean Engineering - Volume 2*, Singapore: World Scientific, 353 pp.

Dingemans, M.W. (1997a): Water wave propagation over uneven bottoms. Part 1 - Linear wave propagation. *Advances Series on Ocean Engineering, Volume 13*, World Scientific, 471 pp.

Dingemans, M.W. (1997b): Water wave propagation over uneven bottoms. Part 2 - Non-linear wave propagation. *Advances Series on Ocean Engineering, Volume 13*, World Scientific, 496 pp.

Dubrovin, B.A.; Novikov, S.P. (1975): Periodic and conditionally periodic analogs of the many-soliton solution of the KdV-equation. *Soviet Physics JETP*, 40, 6, 1058-1063.

Flandrin, P. (1999): Time-frequency/time scale analysis. San Diego: Academic Press, xii, 386 p.

Flandrin, P.;Rilling, G.; Goncalvés, P. (2004): Empirical Mode Decomposition as a Filter Bank. *IEEE Signal Processint Letters*, 11, 2, pp. 112-114.

Flaschka, H.; McLaughlin, D.W. (1976): Canonically Conjugate Variables for the Korteweg-de Vries Equation and the Toda Lattice with Periodic Boundary Conditions (1st page only). *Prog. Theoret. Phys.*, 55, pp. 438ff.

Fourier, J. (1822): The analytical theory of heat, Englisch edition of original work from 1822. New York: Dover Phoenix Edtions, 1955.

Gardner, C.S.;Greene, J.M.;Kruskal, M.D.; Miura, R.M. (1967): Method for solving the Korteweg-deVries equation. *Physical Review Letters*, 19, 19, 1095-1097.

Germain, J.P. (1984): Coefficients de réflexion et de transmission en eau peu profonde. Instytut Budownictwa Wodnego, Report No. 46, Gdánsk, Poland, pp. 5-13.

Goda, Y. (2000): Random seas and design of maritime structures. River Edge, NJ, USA: World Scientific Publishing, 2nd edition, 464 p.

Goda, Y.;Okazaki, K.-I.; Kagawa, M. (1999): Generation and evolution of harmonic wave components by abrupt depth changes. *Proc. of Coastal Structures*, pp. 649-658.

Hammack, J.L.; Segur, H. (1974): The Korteweg-de Vries equation and water waves. Part 2. Comparison with experiments. *J. Fluid Mech.*, Vol. 65, Part 2, pp. 289-314.

Huang, N.E.;Lo, M.-T.;Wu, Z.-H.; Chen, X.-Y. (2013): Method for quantifying and modeling degree of nonlinearity, combined nonlinearity, and nonstationarity. Pub. No. US 2013/0080378 A1, Mar. 28.2013, Publication, U.S.P.A., ed., 48 pp.

Huang, N.E.;Shen, Z.; Long, S.R. (1999): A new view of nonlinear water waves: The Hilbert Spectrum. *Annual Review of Fluid Mechanics*, vol. 31, pp. 417-457.

Huang, N.E.;Shen, Z.;Long, S.R.;Wu, M.C.;Shih, H.H.;Zheng, Q.;Yen, N.-C.;Tung, C.C.; Liu, H.H. (1998): The empirical mode decomposition and the Hilbert spectrum for

nonlinear and non-stationary time series analysis. London: *Proceedings of the Royal Society of London A*, vol. 454, pp. 903-995.

Jacobi, C.G.J. (1828): Suite des notices sur les fonctions elliptiques. *Journal für die reine und angewandte Mathematik*, Band 1828, Heft 3, Seiten 403-404.

Johnson, R.S. (1972): Some numerical solutions of a variable-coefficient Korteweg-de Vries equation (with applications to solitary wave development on a shelf). *J. Fluid Mech.*, Vol. 54, Part 1, pp. 81-91.

Kabbaj, A. (1985): Contribution à l'étude du passaga des ondes de gravité et de la génération des ondes internes sur un talus, dans le cadre de la théorie de l'eau peu profonde. Ph.D. thesis, *Université Scientifique et Médicale de Grenoble*, Grenoble, France.

Karpman, V.I. (1975): Non-linear Waves in Dispersive Media. Oxford: Pergamon.

Korteweg, D.J.; deVries, G. (1895): On the change of form of long waves advancing in a rectangular canal, and on a new type of long stationary waves. *Philos. Mag. Ser.*, 5, 39, pp. 422-443.

Lara, J.L. (2005): A numerical wave flume to study the functionality and stability of coastal structures. *PIANC Magazine AIPCN*, No. 121, 25 p.

LeMéhauté, B. (1976): An introduction to hydrodynamics and water waves. Springer-Verlag.

Lin, P. (2004): A numerical study of solitary wave interaction with rectangular obstacles. *Coastal Engineering*, Vol. 51, pp. 35-51.

Losada, I.J.;Lara, J.L.;Guanche, R.; Gonzales-Ondina, J.M. (2008): Numerical analysis of wave overtopping of rubble mound breakwaters. *Coastal Engineering*, vol. 55, no. 1, pp. 47-62.

Losada, I.J.;Patterson, M.D.; Losada, M.A. (1997): Harmonic generation past a submerged porous step. *Coastal Engineering*, 31, pp. 281-304.

Losada, M.A.;Vidal, C.; Medina, R. (1989): Experimental study of the evolution of a solitary wave at an abrupt junction. *Journal of Geophysical Research*, Vol. 94, No. C10, pp. 14,557-14,566.

Madsen, O.S.; Mei, C.C. (1969): The transformation of a solitary wave over an uneven bottom. *J. Fluid Mech.*, Vol. 39, Part 4, pp. 781-791.

Madsen, P.A.;Fuhrman, D.R.; Schäffer, H.A. (2008): On the solitary wave paradigm for tsunamis (Presentation). *ICCE*, Hamburg, 14 pp.

Mansard, E.P.D.; Funke, E.R. (1980): The measurement of incident and reflected spectra using a least square method. *Proceedings 17th International Conference Coastal Engineering (ICCE)*, ASCE, Volume 1, Sydney, Australia, pp. 154-172.

Massel, S.R. (1983): Harmonic generation by waves propagating over a submerged step. Amsterdam, The Netherlands: Elsevier Science Publishers, *Coastal Engineering*, Vol. 7, pp. 357-380.

Massel, S.R. (1996): Ocean surface waves: Their physics and prediction. *Advances Series on Ocean Engineering, Volume 11*, World Scientific, 491 pp.

MathWorks (2006): Wavelet Toolbox for use with MATLAB - User's Guide. Natick, USA: The Math Works, Inc., March 2006, 1032 pp.

McKean, H.P. (1981): Boussinesq's equation on the circle. *Commun. Pure Appl. Math*, 34, 599-691.

McKean, H.P.; Trubowitz, E. (1976): Hill's Operator and Hyperelliptic Function Theory in the Presence of Infinitely Many Branch Points. *Communications on Pure and Applied Mathematics*, XXIX, pp. 143-226.

Mei, C.C.;Stiassnie, M.; Yue, D.K.-P. (2005): Theory and applications of ocean surface waves. Part 2: Nonlinear aspects. *Advances Series on Ocean Engineering, Volume 23*, World Scientific, 569 pp.

Mei, C.C.; Ünlüata, Ü. (1972): Harmonic generation in shallow water waves. *Waves on Beaches and Resulting Sediment Transport, October 11-13, 1971, Madison US*,

University of Wisconsin and the Coastal Engineering Research Center, U.S. Army, pp. 181-202.

Miles, J.W. (1980): Solitary Waves. *Annu. Rev. Fluid Mech.*, 12, pp. 11-43.

N.N. (2002): Coastal Engineering Manual (CEM). Engineer Manual 1110-2-1100. Washington D.C., USA: US Army Corps of Engineers.

Osborne, A. (2010): Nonlinear ocean waves and the inverse scattering transform. Amsterdam: Elsevier, 977 pp.

Osborne, A. (2011): Nonlinear Fourier transform. Lecture notes of a 4-days short-course at TU Braunschweig.

Osborne, A.R. (1991a): Nonlinear Fourier Analysis. *In: Osborne, A.R. (ed.): Nonlinear Topics in Ocean Engineering, Proceedings of the International School of Physics "Enrico Fermi", Course CIX, Varenna on Lake Como, 26 July - 5 August 1988*, Amsterdam: North-Holland, pp. 669-699.

Osborne, A.R. (1991b): Nonlinear Fourier Analysis for the Infinite-Interval Korteweg-de Vries Equation I: An Algorithm for the Direct Scattering Transform. *Journal of Computational Physics*, 94, 284-313.

Osborne, A.R. (1993a): The behaviour of Solitons in Random-Function Solutions of the Periodic Korteweg-deVries Equation. *Physical Review Letters*, vol. 71, no. 19, pp. 3115-3118.

Osborne, A.R. (1993b): Construction of Nonlinear Wave Train Solutions of the Periodic, Defocusing Nonlinear Schrödinger Equation. *Journal of Computational Physics*, 109, 1, 93-107.

Osborne, A.R. (1993c): Numerical construction of nonlinear wave-train solutions of the periodic Korteweg-deVries equation. *Physical Review E*, vol. 48, no. 1, pp. 296-309.

Osborne, A.R. (1993d): The Numerical inverse scattering transform for the periodic, defocusing nonlinear Schrödinger equation. *Physics Letters A*, 176 (1993), pp. 75-84.

Osborne, A.R. (1993e): The numerical inverse scattering transform: nonlinear Fourier analysis and nonlinear filtering of oceanic surface waves. *Proc. of the Aha Huliko's Hawaiian Winter Workshop*, University of Hawaii Press, pp. 161-183.

Osborne, A.R. (1994): Automatic Algorithm for the Numerical Inverse Scattering Transform of the Korteweg-de Vries Equation. *Math. Comp. Sim.*, 37, 4-5, pp. 431-450.

Osborne, A.R. (1995a): The Inverse Scattering Transform: Tools for the Nonlinear Fourier Analysis and Filtering of Ocean Surface Waves. *Chaos, Solitons & Fractals*, 5, 12, pp. 2623-2637.

Osborne, A.R. (1995b): Soliton physics and the periodic inverse scattering transform. *Physica D*, 86, 81-89.

Osborne, A.R. (1995c): Solitons in the periodic Korteweg-deVries equation, the Θ-function representation, and the analysis of nonlinear, stochastic wave trains. *Physical Review E*, vol. 52, no. 1, pp. 1105-1122.

Osborne, A.R.; Bergamasco, L.b.P.L. (1985): The Small-Amplitude Limit of the Spectral Transform for the Periodic Korteweg-de Vries Equation. *Il Nuovo Cimento*, 85 B, 2, pp. 229-243.

Osborne, A.R.; Bergamasco, L.b.P.L. (1986): The Solitons of Zhabusky and Kruskal Revisited: Perspective in Terms of the Periodic Spectral Transform. *Physica D*, 18, 26-46.

Osborne, A.R.;Kirwan, A.D.;Provenzale, A.; Bergamasco, L.b.P.L. (1986): The Korteweg-de Vries equation in Lagrangian coordinates. *Phys. Fluids*, 29, 3, pp. 656-660.

Osborne, A.R.;Petti, M.;Liberatore, G.; Cavaleri, L.b.P.L. (1988): Nonlinear Fourier Analysis of Laboratory Generated, Broad-banded Surface Waves. *In: Schrefler, B.A. and Zienkeiwicz, O.C. (eds.): Computer Modelling in Ocean Engineering, Proceedings of*

an International Conference on Computer Modelling in Ocean Engineering, Venice, 19-23 September 1988, Rotterdam: Balkema, pp. 99-105.

Osborne, A.R.;Provenzale, A.; Bergamasco, L. (1982a): Theoretical and Numerical Methods for the Nonlinear Analysis of Shallow-Water Wave Data. *Il Nuovo Cimento*, 5C, 6, pp. 633-648.

Osborne, A.R.;Provenzale, A.; Bergamasco, L.b.P.L. (1982b): Nonlinear Fourier Analysis of Localized Wave Fields Described by the Korteweg-de Vries Equation. *Il Nuovo Cimento*, 5 C, 6, pp. 612-632.

Osborne, A.R.; Segre, E. (1990): Numerical Solutions Of The Korteweg-deVries Equation Using The Periodic Scattering Transform μ-Representation. *Physica D*, 44 (1990), pp. 575-604.

Osborne, A.R.;Segre, E.;Boffetta, G.; Cavaleri, L. (1991): Soliton Basis States in Shallow-Water Ocean Surface Waves. *Physical Review Letters*, vol. 67, no. 5, pp. 592-595.

Ostrovsky, L.A. (1978): Nonlinear internal waves in a rotating ocean. *Oceanology*, 18, 119-125.

Prentice-Hall (1961): Ocean wave spectra. *Conference on Ocean Wave Spectra*, Prentice-Hall, Easton, Md., US, 357 p.

Provenzale, A.; Osborne, A.R. (1991): Nonlinear Fourier Analysis for the Infinite-Interval Korteweg-de Vries Equation II: Numerical Tests of Direct Scattering Transform. *Journal of Computational Physics*, 94, 314-351.

Riemann, B. (1857): Theorie der Abel'schen Funktionen. *Journal für die reine und angewandte Mathematik*, Bd. 54, Transcribed by D.R. Wilkins, Corrected version, April 2000, 101-155.

Seabra-Santos, F.J.;Renouard, D.P.; Temperville, A.M. (1987): Numerical and experimental study of the transformation of a solitary wave over a shelf or isolated obstacle. *J. Fluid Mech.*, Vol. 176, pp. 117-134.

Skjelbreia, L.; Hendrickson, J. (1961): Fifth order gravity wave theory. *Proc. 7th Conf. Coastal Eng.*, ASCE, pp. 184-196.

Sopper, R. (2012): Frequency domain analysis of ship waves from hydraulic model tests and field measurements using the nonlinear Fourier transform (NLFT). *Masterarbeit am Leichtweiß-Institut für Wasserbau, Fachbereich Bauingenieurwesen, Technische Universität BraunschweigDiplomarbeit am Leichtweiß-Institut für Wasserbau, Fachbereich Bauingenieurwesen, Technische Universität Braunschweig*, Braunschweig, Germany, 184 pp.

Sorensen, R.M. (2006): Basic coastal engineering. Springer, 3rd edition, 324 pp.

Stoker, J.J. (1957): Water waves : the mathematical theory with applications. New York: Wiley, 567 pp.

Stokes, G.G. (1847): On the theory of oscillatory waves. *Proc. Camb. Philos. Soc.*, 8, pp. 441-455.

Strusinska, A. (2011): Hydraulic performance of an impermeable submerged structure for tsunami damping. Ph.D. thesis, *Leichtweiß-Institute for Hydraulic Engineering and Water Resources, Dept. of Hydromechanics and Coastal Engineering, Technische Universität Braunschweig*, Braunschweig. ibidem-Verlag, Stuttgart, 224 pp.

Strusinska, A.; Oumeraci, H. (2008): Hydraulic performance of artificial reef for tsunami protection, Report No. 3: Laboratory experiments on solitary wave nonlinear transformation over a submerged structure of a finite width. Leichtweiß-Institute for Hydraulic Engineering and Water Resources, Dept. of Hydromechanics and Coastal Engineering, Technische Universität Braunschweig, Braunschweig, 241 pp.

Tappert, F.D.; Zabusky, N.J. (1971): Gradient induced fission of solitons. *Physical Review Letters*, Vol. 27, No. 26, pp. 1774-1776.

Van der Meer, J.W.; D'Angremond, K. (1991): Wave Transmission at Low-Crested Structures. *In: ICE (ed.), Proceedings of the Conference on Coastal Structures and Breakwaters*, London, U.K., 17 p.

Whitham, G.B. (1974): Linear and Nonlinear Waves. New York: Wiley, 635 pp.

Wiegel, R.L. (1960): A presentation of cnoidal wave theory for practical application. *J. Fluid Mech.*, Vol. 7, Pt. 2, pp. 273-286.

Wu, Z.; Huang, N.E. (2004): A study of the characteristics of white noise using the empirical mode decomposition method. The Royal Society, *Proceedings of the Royal Society of London A*, 460, pp. 1597-1611.

Yuen, H.C.; Lake, B.M. (1982): Nonlinear dynamics of deep-water gravity waves. *Adv. Appl. Mech.*, 22, 67-229.

Zabusky, N.J.; Kruskal, M.D. (1965): Interaction of 'solitons' in a collisionless plasma and the recurrence of inital states. *Physical Review Letters*, 15, 6, pp. 240-243.